Antennas for Frequency Reconfigurable Phased Arrays

Antennas for Frequency Reconfigurable Phased Arrays

Proefschrift

ter verkrijging van de graad van doctor
aan de Technische Universiteit Delft,
op gezag van de Rector Magnificus prof. ir. K. C. A. M. Luyben,
voorzitter van het College voor Promoties,
in het openbaar te verdedigen op donderdag 23 april 2015 om 12:30 uur

door

Syeda Nadia HAIDER

elektrotechnisch ingenieur
geboren te Comilla, Bangladesh.

This dissertation has been approved by the:

Promotor: Prof. DSc. A. G. Yarovoy

Composition of the doctoral committee:

Rector Magnificus
Prof. DSc. A. G. Yarovoy, promotor

Independent members:

Prof. Ir. F. Le Chevalier	Faculty Electrical Engineering, Mathematics and Computer Science, TU Delft
Prof. Dr. A. Neto	Faculty Electrical Engineering, Mathematics and Computer Science, TU Delft
Prof. Ir. P. Hoogeboom	Faculty of Civil Engineering and Geosciences, TU Delft
Prof. Dr. G. Gerini	Technische Universiteit Eindhoven
Prof. Dr. G. Vandenbosch	Katholieke Universiteit Leuven
Prof. Dr. J.-Y. Dauvignac	University of Nice Sophia Antipolis

The work in this thesis has been carried out at the Delft University of Technology, under the auspices of the research group MS3 (Microwave Sensing, Signals and Systems). This research is supported by the Sensor Technology Applied in Reconfigurable systems for sustainable Security (STARS) project.

Keywords: Reconfigurable antenna, wideband antenna, variable impedance matching, frequency reconfiguration, phased array

Printed by: Ipskamp Drukkers, the Netherlands

ISBN 978-94-6259-625-2

An electronic version of this dissertation is available at http://repository.tudelft.nl/

Author email: nadia@nadiahaider.nl

To my dear family

Contents

LIST OF ACRONYMS

AUT	Antenna Under Test
BV	Blind-Via
CMOS	Complementary Metal–Oxide–Semiconductor
CPW	Co-Planar Waveguide
CST	Computer Simulation Technology
CWD	Concealed Weapon Detection
DBF	Digital Beam Forming
DC	Direct Current
DSRC	Dedicated Short Range Communications
EM	ElectroMagnetic
FF	Far Field
FFT	Fast Fourier Transformation
FIT	Finite Integration Technique
FMCW	Frequency Modulated Continuous Wave
FNB	First Null Beamwidth
GSM	Global System for Mobile communications
HIS	High Impedance Surface
HPB	Half Power Beamwidth
IC	Integrated Circuit
IL	Insertion Loss
ITU	International Telecommunication Union
LTSA	Linear Tapered Slot Antenna
LC	Liquid Crystal
MEMS	Micro Electro-Mechanical Systems

MIMO	Multiple-Input-Multiple-Output
PCB	Printed Circuit Board
PIFA	Planar Inverted F Antenna
RA	Reconfigurable Antenna
RADAR	RAdio Detection And Ranging
RCS	Radar Cross Section
RF	Radio Frequency
SAR	Synthetic Aperture Radar
SATCOM	Satellite Communications
SLL	Side Lobe Level
SLR	Side Lobe Reduction
SMA	Surface Mount Assembly
SNR	Signal to Noise Ratio
SOA	State-Of-The-Art
SoC	System on Chip
S-Par	Scattering Parameter
STARS	Sensor Technology Applied in Reconfigurable systems for sustainable Security
TCDL	Tactical Common Data Link
TE	Transverse Electric
TEM	Transverse ElectroMagnetic
TM	Transverse Magnetic
TR	Transmit Receive
TSA	Tapered Slot Antenna
TTD	True Time Delay
TTW	Through-The-Wall
VSWR	Voltage Standing Wave Ratio
UAV	Unmanned Aerial Vehicle
UMTS	Universal Mobile Telecommunications System
UWB	Ultra-Wide Band

CHAPTER 1

INTRODUCTION

This chapter describes the research background, objective, focus and approach of the Ph.D. research project. The current chapter also reviews the developments of reconfigurable, wideband and multiband antenna technologies. The framework within which this research is conducted will be discussed in this chapter. In addition, an outline of the dissertation as a whole will be specified.

Parts of this chapter have been published in:

[J4] N. Haider, D. Caratelli, and A. G. Yarovoy, "Recent developments in reconfigurable and multiband antenna technology", *International Journal of Antennas and Propagation*, vol. 2013, Article ID 869170, pp. 1-14, Jan. 2013, *Special Issue on Wideband, Multiband, Tunable, and Smart Antenna Systems for Mobile and UWB Wireless Applications*.

1.1 BACKGROUND OF THE RESEARCH

OUR societies are repeatedly challenged by happenings such as natural disasters and catastrophes caused by (deliberate or unintended) human activities. While threats are increasing in number and variety, advances in science and technology have helped human society to build security systems to minimize or in some cases avoid calamities. Sensors and sensor networks are a good example of the contribution of technology to public safety, which can help to reduce the effects of natural and man-made disasters. They play an important role in every phase of safety and disaster management. Firstly, they provide situation awareness with functionalities such as weather forecast, airborne, coastal and harbour surveillance, observations during large-scale public events and classifications of targets. Secondly, they can demolish the source of impending disaster, for instance, by identifying threats and non-cooperative targets. Last but not least, sensor networks are important for post-disaster management, including monitoring the effects of disaster, assisting in search and rescue missions, detecting life signs, examining crowd movements and establishing emergency communications.

Microwave sensors, like radar (Radio Detection And Ranging), are playing an increasingly important role in advanced security systems. Remote sensing systems operating in microwave frequencies have signals with larger wavelengths compared to systems operating in infrared or visible lights. Consequently, they are day-and-night operational, more robust against weather conditions and can penetrate through clouds.

1.2 RESEARCH PROBLEM

FOR different scenarios, the requirements for security systems can change enormously and swiftly. For instance, an airborne-radar which has been observing a harbour may need to be relocated to a flooded area to monitor, first of all the disaster effects while communicating through space satellites. Afterwards, it may need to assist rescue teams in providing urgent medical and food supplies while acting as a communication relay for the isolated communities. These changes in situation often lead to the need for changes in a system's operational functions.

Current microwave and wireless systems are however designed for single pre-defined missions and hence incapable of reconfiguring their functionalities. Utilizing single-function systems, suitable only for a specific situation, is expensive. Integrating many of these separate systems into a single platform will create a complex

environment and hence performance may degrade. Furthermore, the requirements for these systems often cannot be pre-defined and the development of a new system is time consuming.

To overcome the limitations of conventional systems, use of reconfigurable (and multifunctional) systems appears to be the best approach to ensure sustainability of public security. The optimum solution will be a reconfigurable system where, instead of individual systems for each operation, one advanced system will perform multiple tasks.

Existing radar and communication systems are not entirely flexible and multi-functionalities, e.g. multi-band, multi-beam, dual-polarisation, are essential for future systems. Reconfigurable systems will reduce the size of ship-based or airborne radar systems and will be able to perform many operations such as long-range surveillance, short-range surveillance, tracking, detection and identification.

Reconfigurability is also becoming important for communication applications. For many modern communication systems, frequency and polarisation diversities are important to support different communication standards. Furthermore, the number of wireless systems is increasing tremendously, causing spectrum congestion and reducing the performance quality due to interference between different users. Reconfigurable functions will enable multiple high-speed communication links to operate simultaneously, hence utilizing the spectrum resources more efficiently. For advanced communication systems such as, frequency-hopping spread spectrum, software defined radio and cognitive radio, frequency and polarisation diversities are key issues to mitigate interference, jamming, multi-path fading in complex environment and to select the available spectrum.

It remains a difficult challenge to meet a good balance between the level of agility and reliability. Here, reliability is of utmost importance as system failure can lead to devastating consequences. To make a system reconfigurable, the entire functional chain needs to be adaptable. This requires reconfigurable front-end, digital signal processing, algorithms, software and methodology. Insufficient concept maturities, low technology readiness levels and gaps in our knowledge have so far prevented the realization of a complete reconfigurable system. However, current advancements in the field promise the accomplishment of such flexible systems without degrading the performance or the reliability of each separate function.

The analogue front-end is considered to be the least flexible part of a system. For multi-functional operations, the front-end should be quickly adapted according to the mission and needs adjustable components such as antennas, filters and amplifiers.

1.3 RESEARCH OBJECTIVE

THE objective of this research is to determine how we can ***realize antennas for reconfigurable sensors and sensor networks***.

Reconfigurability for an antenna can be defined as its capacity to change the fundamental properties, e.g. operating frequency, impedance bandwidth, polarisation, radiation patterns or a combination of a few of these characteristics. A single multi-function antenna can replace a number of single-function antennas, thereby reducing overall size, cost and complexity of the antenna system while improving total performance.

One of the main focuses of this research is frequency agile antenna elements for phased-array applications. In general, antenna elements operate in a single frequency band. Switching or tuning this operational band is a challenge and a major part of this research project is devoted to this particular issue. Among other research topics L-/S-band frequency reconfigurable phased-array antennas have been studied. A system which operates in both L and S bands can support many applications, such as L-band radar (1200 – 1500 MHz), S-band radar (2850 – 3500 MHz), weather surveillance and communication (e.g. GSM, UMTS). Other research scopes are the frequency reconfiguration within the X- and Ku-band. These frequency bands are particularly interesting for maritime surveillance, communication, weather radar, SATCOM (Satellite Communications) and TCDL (Tactical Common Data Link).

1.4 OVERVIEW OF ANTENNA TECHNOLOGIES FOR RECONFIGURABLE SENSORS

RECENTLY, reconfigurable antennas (RAs) have gained tremendous research interest for many different applications, e.g. cellular radio system, radar system, satellite communications, airplane and unmanned airborne vehicle (UAV) radar, smart weapon protection. In mobile and satellite communications, reconfigurable antennas are useful to support large number of standards (e.g., UMTS, Bluetooth, WiFi, WiMAX, DSRC), to mitigate strong interference signal and to cope with changing environmental conditions. On the other hand, in radar applications, reconfigurability

at antenna level is often needed for multi-functional operation. This feature is achieved by utilizing antenna array systems that can be quickly adapted according to the mission. Therefore, a control over operating frequency, beam pointing direction, polarisation and antenna radiation pattern is required.

In the past years, a variety of concepts has been proposed by different authors to achieve adaptable antenna properties. Key aspects of some outstanding concepts will be addressed in the following sections. In this discussion, focus is mainly on antenna designs with frequency agile capabilities. Some examples of antenna structures with polarisation and pattern reconfigurable property will be addressed as well.

There are basically three design approaches for achieving antenna array frequency agility:

1. Reconfiguration at element level: antennas integrated with electronic switches, mechanical actuators, tuneable materials;
2. Wideband antennas;
3. Reconfiguration at array level: shared-aperture antenna array, multi-layer antenna array;

1.4.1. Antenna systems with reconfiguration at element level

There has been a notable advancement in adaptable antenna technology recently. Many novel design concepts have been proposed [1]. Among them, utilizing the same antenna aperture for different frequencies will provide the most compact solution. Relatively narrow-band antennas with tuneable or switchable properties are an attractive solution when the aperture efficiency is an important issue. This approach also reduces the requirements on the front-end filtering properties compared to a wideband or multi-band antenna.

(a) Reconfiguration with RF switches

Frequency reconfigurability in antennas can be realized by employing micro electro-mechanical systems (MEMS) [2-11], varactors [12-16], or p-I-n diodes [17-26]. A dual-band tuneable slot antenna with MEMS was presented in [1]. In this design the frequency tuning was achieved by utilizing the RF MEMS variable capacitor on a stub. The resonance frequencies of the antenna were shifted from 10.22 GHz to 10.57 GHz and from 7.7 GHz to 8.7 GHz. A capacitive MEMS loaded PIFA antenna was studied in [3]. The outcome of this study confirmed that the antenna is capable of operating over a bandwidth of more than one octave while improving the

performance in terms of specific absorption rate. Another well known example of frequency tuning with MEMS is the pixel antenna concept which allows for switching in frequency band, polarisation and/or scan angle [4-5]. The disadvantage of this approach is the need of many switches which will increase the cost, the power loss, as well as the complexity of the biasing circuit. In [6] a reconfigurable microstrip antenna (on a quartz substrate) with RF-MEMS has been presented which has potential to be fabricated as an integrated antenna system on the chip (SoC). The results presented in [6] confirmed that the operational band of the antenna can be switched between 5.25 GHz and 5.6 GHz.

Integrating varactors in an antenna structure is another common way for achieving frequency agility [12-16]. In [12] the resonating microstrip radiator consisted of several smaller patches which were interconnected by varactors. These varactors were independently biased to change the electrical lengths of the corresponding patches and thereby changed the resonant frequency of the corresponding modes.

A differentially-fed microstip antenna with frequency tuning capability has been presented in [13] where varactor diodes were used to tune the operational band. In [16] adjustable high impedance surface (HIS) using varactor diodes were utilized in an active reflectarray.

Reconfigurable antennas are also designed by employing p-I-n diodes as the switching component [17-26]. In [17] a reconfigurable meander radiator is proposed. It has been demonstrated in this article that the resonant frequency can be tuned from 470 MHz to 1080 MHz. In [19] a polarisation reconfigurable slot antenna is discussed. Here, the antenna polarisation was switched between vertical and horizontal polarisation by changing the feeding structure from CPW (coplanar waveguide) to slot-line feed with p-I-n diodes.

(b) Mechanically reconfigurable antennas

The antenna topologies discussed above utilized lumped tuneable components. Recently, for applications where RF-switches are not desired due to the additional power losses in the switches and complexity of the bias lines, mechanically reconfigurable antennas are being investigated [27-29]. However, practical issues, such as the total size, switching speed, reliability and overall complexity of the system, needs to be considered here. In [27] a physically rotatable antenna has been designed for cognitive radio to tune the operational band from 2 to 10 GHz.

Mechanically reconfigurable antennas have also been used to achieve pattern diversity with a single radiating element. For systems which do not require fast pattern reconfiguration this approach might replace the need of expensive phased-array. In [28] a square ring antenna with a bendable parasitic plate has been used for machine-to-machine (M2M) communications.

(c) Frequency reconfigurability by tuneable materials

Reconfigurability with tuneable material is a very new research area and still facing challenges such as reliability, efficiency and proper modelling. However, in recent times many researches are carried out in this area and notable achievements have been reported [30-35]. Ferroelectric dielectric materials can be used for reconfigurable antennas as their permittivity change with the applied DC (direct current) bias voltage [30]. Disadvantage of this type of material is the large bias voltage required to change the dielectric constant and high losses of the material. In [31-32] plasma regions, which have relatively high electrical conductivity, were temporarily created inside a silicon substrate by injecting suitable DC current. In this way reconfigurable antenna aperture was created.

Another approach which has recently gained some research interest is the liquid crystal (LC) tuneable antennas. The permittivity of a liquid crystal can be varied with DC bias voltage. Researches of Sheffield University have demonstrated a tuneable liquid crystal microstrip patch antenna at 5 GHz [33] with a tuning range of 4-8%. However, due to the high losses in the current LC materials the antenna suffered from poor efficiency (20-40%).

Besides the above mentioned reconfigurable concepts, other promising research areas are emerging, such as the exploitation of microfluidics [36-47], optical controls [38-39] and graphene [40-41] in reconfigurable antennas.

1.4.2. Wideband antennas

In the previous section, some examples of reconfigurable antenna with tuneable or switchable components have been provided. Another approach is to use ultra-wideband or multiband antenna elements [42-53]. In this approach, one needs antenna solutions which feature good performance (e.g. good impedance matching, radiation pattern, gain) for the whole bandwidth of interest and a tuneable filter can be used to select the operational frequency band.

Numerous broadband antenna designs for different applications have been published. For instance, transversal electromagnetic (TEM) horn or dielectric filled waveguide antenna can provide extremely wide bandwidth with directive radiation pattern. End fire wideband antennas, such as, antipodal Vivaldi antennas and linear tapered slot antenna (LTSA) can also be used for phased array. Dual polarized Vivaldi antenna arrays [42] can be designed for more than 10:1 bandwidths while scanning 45˚ or more. An alternative solution is to place the filter in the radiating element itself. This will relax the pre-select filter requirements. An example of this design approach is provided by the reconfigurable Vivaldi antenna presented in [15], where a band-pass filter is integrated in the feeding line of the radiating structure resulting in a frequency switchable filtenna. Here, a varactor diode is inserted within the filter structure in order to provide frequency reconfiguration capability. In the study presented in [18] a switchable Vivaldi antenna has been demonstrated to provide either a narrow or wideband frequency response. Here, ring slots bridged by p-I-n diode switches have been inserted in the radiating element to obtain a narrowband resonating behaviour at different frequencies. On the other hand, the p-I-n diodes are deactivated wherein a wideband operation is desired. However, high mutual coupling between Vivaldi elements is a major limiting factor. Other potential candidates of UWB element are the 3D monopole antenna (fat monopole, tab monopole, cylindrical monopole) and dielectric resonator or dielectric lens antenna.

1.4.3. Antenna systems with reconfiguration at array level

In the two approaches detailed in the previous sections, the same radiating element is used for different frequency bands. An alternative solution is to employ different radiating elements for different antenna modes and then integrating them into the same array structure. The shared-aperture antenna is one example of the mentioned design concept [54-55]. In this approach the idea is to share the physical area of the antenna aperture between different sub-arrays. Here, interleaved matrices of radiators are used. This concept can be used for multi-frequency, multi-function and multi-polarisation applications. Advantages of this approach are the simple element configuration and frequency jumps can be extremely large. The main challenge related to shared-aperture antenna is in placing the elements on the same aperture while avoiding any physical overlapping. In [56] a dual-frequency circularly-polarized patch antenna array is introduced with large isolation. Here, the rectangular patch elements provide two orthogonally polarised frequency bands.

An alternative solution of shared-aperture antenna is multi-layer antenna array [57-59]. In [57] two planar arrays, having rectangular ring resonator and circular patches as the radiating elements, are incorporated for simultaneous S- and X-band

operation. [58] provides an example of dual frequency reflectarray using dual layers of radiating elements. Another notable example of multiband array is presented in [59]. Here, as S-band elements dipoles are used while square patches are used as the X-band element. One important design consideration for any multilayer array is that the antennas operating in different bands should be nearly transparent to each other to avoid performance degradation. Another disadvantage of this approach is the complex fabrication process due to many substrate layers.

1.5 RESEARCH CHALLENGES

THIS thesis is focused on frequency-reconfigurable phased-array antennas. Two types of reconfiguration are considered: switch between two radar bands and frequency tuning within a single frequency band. Multiple challenges are associated with such frequency reconfiguration and can be summarized as follows:

The realization of antenna elements with a large frequency coverage is very challenging. Similarly, for dual-band antennas it is extremely difficult to widely separate its operational bands. Although some multiband antennas with frequency ratio below 2:1 can be found in literature [60-64], designing dual-band antenna operating at bands separated more than an octave is extremely demanding. It remains difficult to achieve consistent performance, such as sufficient sub-bandwidth, good matching, high gain and stable radiation patters, in all operational bands. Furthermore, many antenna properties are vulnerable to frequency alteration and need to be carefully investigated.

The wide angle scanning capability forms another research challenge. The radiating element needs to fulfil strict requirements on its dimensions to permit wide scanning volumes. Large beam scanning also places high requirements on radiation patterns and coupling levels. These challenges become more intense for dual-band radiators. To avoid grating lobes at the higher frequency, the element needs to be placed very densely at the lower frequency. As a result, the coupling will increase and radiation efficiency may reduce. Hence, there is a clear trade-off between the maximum scan angle at the high frequency and the coupling in the low frequency band. This intricacy is greater for large separation between operational bands. While some wideband antenna systems with wide angle scanning capability have been demonstrated before [65-67], frequency reconfigurable antenna system with wide scan angles is still in research phase.

The combination of the above mentioned challenges makes the current research work an extremely complex task. Most reconfigurable antenna structures, discussed in section 1.4, are not suitable for L/S-band phased-array application, either due to the large size or the limited frequency coverage.

1.6 RESEARCH APPROACHES

THREE research approaches were studied to realize antennas suitable for reconfigurable sensors. A schematic overview of these research approaches is presented in Figure 1.1.

First, to treat the challenge of fine frequency tuning, wideband antennas are analyzed. Wideband antennas can cover a large frequency range and can be integrated with reconfigurable filter or T/R module to achieve frequency selectivity. Following this approach two planar wideband radiating structures with unidirectional radiation properties are investigated; (i) microstrip antenna with blind-via feed, (ii) quasi electric-magnetic radiating structure.

The second research focus was on a reconfigurable phased-array antenna design to switch the frequency between two (radar) bands. To answer this research question a reconfigurable antenna element incorporated with RF switches (p-I-n diode) was studied. To solve the challenge of large frequency ratio, the physical structure of the radiating element was modified by acting on the bias voltage of the diodes. Thereby, it was possible to shift the operational band from L- to S-band. To solve the challenge of wide angle scanning in both operational bands of the reconfigurable antenna, the multi-scale array topology was proposed and analyzed. In this array topology each reconfigurable L/S-band element was interleaved with an S-band element. Thereby, less than half-a-wavelength spacing was maintained for both operational modes. Within this research work the multi-scale array structure has been experimentally studied to investigate the scanning capabilities and the inter-element couplings.

In the third approach, frequency reconfiguration was achieved with variable-impedance matching. This approach is useful for both of the above mentioned research focus areas; fine frequency tuning and frequency reconfiguration over largely separated bands. In this approach frequency reconfiguration of a wide- or multi-band antenna can be achieved by an input-impedance tuneable RF-frontend. To overcome the challenge of frequency reconfiguration among two largely separated bands, a dual-band antenna structure (the E-slot element) was proposed. In this design a compact antenna profile and wide separation between the bands were targeted. The

input-impedance of this antenna was optimized in such a way that by varying the reference impedance, the operational band can be switched from L- to S-band. Within the (radar) L-band the input-impedance of the antenna varies almost linearly with the frequency and hence a fine frequency tuning within this band is achievable.

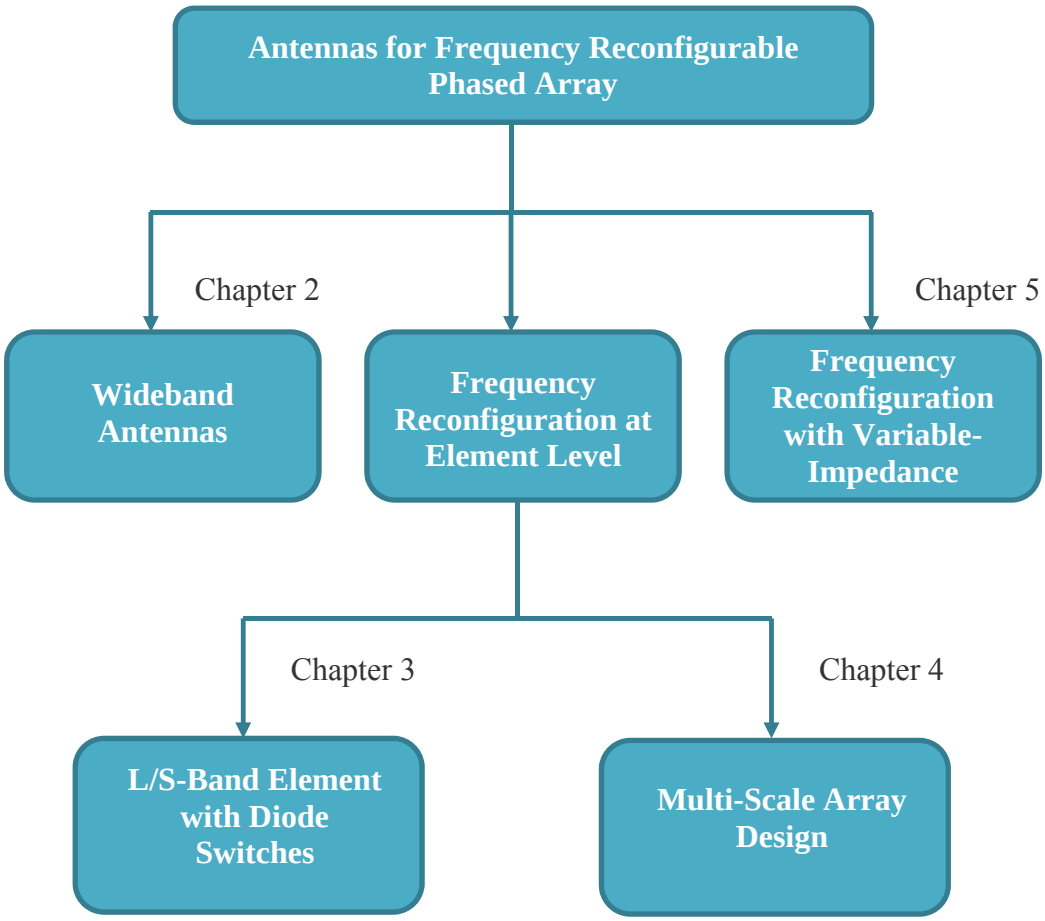

Figure 1.1 Schematic overview of the research

1.7 RESEARCH FRAMEWORK

THIS research is conducted as part of the Sensor Technology Applied in Reconfigurable systems for sustainable Security (STARS) project. The aim of this project is to develop knowledge and technology that can be used as a baseline for the development of reconfigurable sensors and sensor networks applied in the context of the security domain [68]. The duration of the STARS project is four and half years and both academic as well as industrial institutions from The Netherlands constitute the consortium, such as University of Twente, Delft University of Technology, Thales Netherlands, TNO and NXP.

1.8 OUTLINE OF THE THESIS

THIS dissertation is divided into six Chapters. Figure 1.1 gives a graphical illustration of the chapters.

Chapter 2 is devoted to wideband antenna designs. The design of a new feeding structure to enhance the operational bandwidth of planar antennas is presented here. The proposed feeding structure provides an effective means for flattening the input impedance of an antenna over a wide frequency range. As a result, the fractional bandwidth of a probe-fed planar antenna can be enhanced significantly, while reducing mutual antenna coupling and keeping stable radiation patterns over the frequency band in an array configuration. Furthermore, this chapter describes a uni-directional antenna for wideband radar applications. The antenna concept is based on the combination of the electromagnetic characteristics of a loop and a planar monopole. The antenna concept is used to develop X-band elements. In Appendix A, the proposed concept is further investigated for Ku-band applications and in Appendix B the X-band elements are used to design full-polarimetric antenna sub-arrays.

Chapter 3 presents a concept of a frequency reconfigurable L/S-band phased-array antenna element. The concept is based on changing the physical structure of the antenna by means of RF switches. The element has compact size and simple feeding structure. This chapter also presents a comprehensive analysis and implementable solution of the switching component on the frequency reconfigurable element. A concept to reduce the complexity of the biasing circuits is proposed and validated here.

In **Chapter 4** the multi-scale array structure is introduced. The developed array configuration is a unique solution to achieve wide scanning volumes in both operational bands of dual-band phased-array antennas. This method is particularly useful for scanning arrays with a large separation between the operational bands.

Chapter 5 is dedicated to the investigation of variable-impedance matching of antennas. It is proposed that variable-impedance matching between the antenna and the RF-frontend provides several potential advantages, including frequency reconfiguration, compensating for unintentional mismatch, improving scanning capability, and reducing noise level and interference signal. It is demonstrated that avoiding fix 50 Ω impedance transformation between the antenna and the RF-frontend will significantly reduce design restrictions and enhance total system performance.

Chapter 6 concludes this dissertation by summarizing the main achievements. The results of three investigated approaches are discussed along with their inherent benefits and challenges. Recommendations are provided for future research.

BIBLIOGRAPHY

[1] J. T. Bernhard, "Reconfigurable antennas", in Synthesis Lectures on Antennas, Morgan and Claypool Publishers, 2007.

[2] K. Topalli, E. Erdil, O. A. Civi, S. Demir, S. Koc, and T. Akin, "Tunable dual-frequency RF MEMS rectangular slot ring antenna", *Sensors and Actuators A*, vol. 156, no. 2, pp. 373–380, 2009.

[3] K. R. Boyle and P. G. Steeneken, "A five-band reconfigurable PIFA for mobile phones", *IEEE Trans. on Antennas and Propagat.*, vol. 55, no. 11, pp. 3300–3309, 2007.

[4] W. H. Weedon, W. J. Payne, and G. M. Rebeiz, "MEMS switched reconfigurable antennas", in *Proceedings of the IEEE International Symposium on Antennas and Propagation*, pp.654–657, 2001.

[5] A. Grau and F. De Flaviis, "A distributed antenna tuning unit using a frequency reconfigurable PIXEL-antenna", in *Proceedings of the 4th European Conference on Antennas and Propagation* (EuCAP '10), pp. 1–5, April 2010.

[6] A. Vasylchenko, X. Rottenberg, B. X. Broze, M. Nuytemans,W. De Raedt, and G. A. E. Vandenbosch, "A frequency switchable antenna based on MEMS technology", in *Proceedings of the 4th European Conference on Antennas and Propagation* (EuCAP '10), April 2010.

[7] J. Balcells, Y. Damgaci, B. A. Cetiner, J. Romeu, and L. Jofre, "Polarization reconfigurable MEMS-CPW antenna for mmwave applications", in *Proceedings of the 4th European Conference on Antennas and Propagation* (EuCAP '10), April 2010.

[8] A. Grau, J. Romeu, M. J. Lee, S. Blanch, L. Jofre, and F. De Flaviis, "A Dual-Linearly-polarized MEMS-reconfigurable antenna for narrowband MIMO communication systems", *IEEE Trans. on Antennas and Propagat.*, vol. 58, no. 1, pp. 4–17, 2010.

[9] S. Yang, H. K. Pan, A. E. Fathy, S. El-Ghazaly, and V. K. Nair, "A novel reconfigurable mini-maze antenna for multi-service wireless universal receiver using RF MEMS", in *Proceedings of the IEEEMTT-S International Microwave Symposium Digest*, pp.182–185, June 2006.

[10] C.-Y. Chiu, J. Li, S. Song, and R. D. Murch, "Frequency reconfigurable pixel slot antenna", *IEEE Trans. on Antennas and Propagat.*, vol. 60, no. 10, pp. 4921–4924, 2012.

[11] D. E. Anagnostou, G. Zheng, L. Feldner et al., "Silicon-etched re-configurable self-similar antenna with RF-MEMS switches", in *IEEE Antennas and Propagation Society Symposium*, vol. 2, pp. 1804–1807, June 2004.

[12] T. Korošec , P. Ritoša , and M. Vidmar, "Varactor-tuned microstrip-patch antenna with frequency and polarization agility", *Electronics Letters*, vol. 42, no. 18, pp. 1015–1016, 2006.

[13] S. V. Hum and H. Y. Xiong, "Analysis and design of a differentially-fed frequency agile microstrip patch antenna", *IEEE Trans. on Antennas and Propagat.*, vol. 58, no. 10, pp. 3122–3130, 2010.

[14] C. R. White and G. M. Rebeiz, "Single- and dual-polarized tunable slot-ring antennas", *IEEE Trans. on Antennas and Propagat.*, vol. 57, no. 1, pp. 19–26, 2009.

[15] Y. Tawk, J. Costantine, and C. G. Christodoulou, "A varactor based reconfigurable filtenna", *IEEE Antennas and Wireless Propagation Letters*, vol. 11, pp. 716–719, 2012.

[16] P. Ratajczak, J.-M. Baracco, and P. Brachat, "Adjustable high impedance surface for active reflectarray applications", in *Proceedings of the 2nd European Conference on Antennas and Propagation* (EuCAP '07), pp. 1–6, November 2007.

[17] F. Canneva, J. M. Ribero, and R. Staraj, "Tunable antenna for DVB-H band", in *Proceedings of the 4th European Conference on Antennas and Propagation* (EuCAP '10), pp. 1–3,April 2010.

[18] M. R. Hamid, P. Gardner, P. S. Hall, and F. Ghanem, "Switched band Vivaldi antenna", *IEEE Trans. on Antennas and Propagat.*, vol. 59, no. 5, pp. 1472–1480, 2011.

[19] Y. Li, Z. Zhang, W. Chen, and Z. Feng, "Polarization reconfigurable slot antenna with a novel compact CPW-to-slotline transition for WLAN application", *IEEE Antennas and Wireless Propagation Letters*, vol. 9, pp. 252–255, 2010.

[20] D. Piazza, N. J. Kirsch, A. Forenza, R. W. Heath, and K. R. Dandekar, "Design and evaluation of a reconfigurable antenna array for MIMO systems", *IEEE Trans. on Antennas and Propagat.*, vol. 56, no. 3, pp. 869–881, 2008.

[21] D. Piazza, P. Mookiah, M. D'Amico, and K. R. Dandekar, "Experimental analysis of pattern and polarization reconfigurable circular patch antennas for MIMO systems", *IEEE Trans. on Vehicular Technology*, vol. 59, no. 5, pp. 2352–2362, 2010.

[22] J. Ollikainen, O. Kivekäs , and P. Vainikainen, "Low-loss tuning circuits for frequency-tunable small resonant antennas", in *Proceedings of the 13th IEEE International Symposium on Personal, Indoor and Mobile Radio Communications* (PIMRC '02), vol. 4, pp. 1882–1887, September 2002.

[23] T.-Y. Han and C.-T. Huang, "Reconfigurable monopolar patch antenna", *Electronics Letters*, vol. 46, no. 3, pp. 199–200, 2010.

[24] D. Peroulis, K. Sarabandi, and L. P. B. Katehi, "Design of reconfigurable slot antennas", *IEEE Trans. on Antennas and Propagat.*, vol. 53, no. 2, pp. 645–654, 2005.

[25] S.-X. Cao, X.-X. Yang, B. Gong, and B.-C. Shao, "A reconfigurable microstrip antenna with agile polarization using diode switches", in *IEEE International*

Symposium on Antennas and Propagation (APSURSI ’11), pp. 1566–1569, July 2011.

[26] A. C. K. Mak, C.R. Rowell, and R.D. Murch, “Lowcost reconfigurable landstorfer planar antenna array”, *IEEE Trans. on Antennas and Propagat.*, vol. 57, no. 10, pp. 3051–3061, 2009.

[27] Y. Tawk, J. Costantine, K. Avery, and C. G. Christodoulou, “Implementation of a cognitive radio front-end using rotatable controlled reconfigurable antennas”, *IEEE Trans. on Antennas and Propagat.*, vol. 59, no. 5, pp. 1773–1778, 2011.

[28] S. J. Mazlouman, A. Mahanfar, C. Menon, and R. G. Vaughan, “Square ring antenna with reconfigurable patch using shape memory alloy actuation”, *IEEE Trans. on Antennas and Propagat.*, vol. 60, no. 12, pp. 5627–5634, 2012.

[29] J. T. Bernhard, E. Kiely, and G. Washington, “A smart mechanically actuated two-layer electromagnetically coupled microstrip antenna with variable frequency, bandwidth, and antenna gain”, *IEEE Trans. on Antennas and Propagat.*, vol. 49, no. 4, pp. 597–601, 2001.

[30] J. Modelski and Y. Yashchyshyn, “Semiconductor and ferroelectric antennas”, in *Proceedings of the Asia-Pacific Microwave Conference* (APMC ’06), pp. 1052–1059, Dec. 2006.

[31] Y. Yashchyshyn, J.Marczewski, K. Derzakowski, J.W.Modelski, and P. B. Grabiec, “Development and investigation of an antenna system with reconfigurable aperture”, *IEEE Trans. on Antennas and Propagat.*, vol. 57, no. 1, pp. 2–8, 2009.

[32] A. E. Fathy, A. Rosen, H. S. Owen et al., “Silicon-based reconfigurable antennas—concepts, analysis, implementation, and feasibility”, *IEEE Trans. Microw. Theory Tech.*, vol. 51, no. 6, pp. 1650–1661, 2003.

[33] L. Liu and R. J. Langley, “Liquid crystal tunable microstrip patch antenna”, *Electronics Letters*, vol. 44, no. 20, pp. 1179–1180, 2008.

[34] Y. Yashchyshyn and J. Modelski, “Reconfigurable semiconductor antenna”, in *Proceedings of the 9th International Conference: The Experience of Designing and Application of CAD Systems in Microelectronics* (CADSM ’07), pp. 146–150, February 2007.

[35] A. Gaebler, A. Moessinger, F. Goelden et al., “Liquid crystal reconfigurable antenna concepts for space applications at microwave and millimeter waves”, *International Journal of Antennas and Propagation*, vol. 2009, Article ID876989, 2009.

[36] D. Rodrigo, L. Jofre, and B. A. Cetiner, “Circular beam-steering reconfigurable antenna with liquid metal parasitics”, *IEEE Trans. on Antennas and Propagat.*, vol. 60, no. 4, pp. 1796–1802. Apr. 2012.

[37] S. A. Long and G. H. Huff, “A substrate integrated fluidic compensation mechanism for deformable antennas”, in *Proceedings of the NASA/ESA Conference on Adaptive Hardware and Systems* (AHS ’09), pp. 247–251, Aug. 2009.

[38] Y. Tawk, J. Costantine, S. Hemmady, G. Balakrishnan, K. Avery, and C. G. Christodoulou, “Demonstration of a cognitive radio front end using an optically

pumped reconfigurable antenna system (OPRAS)", *IEEE Trans. on Antennas and Propagat.*, vol. 60, no. 2, pp. 1075–1083, 2012.

[39] R. N. Lavallee and B. A. Lail, "Optically-controlled reconfigurable microstrip patch antenna", in *Proceedings of the IEEE International Symposium on Antennas and Propagation*, pp. 1–4, July 2008.

[40] I. Llatser, C. Kremers, D. N. Chigrin et al., "Characterization of graphene-based nano-antennas in the terahertz band", in *Proceedings of the 6th European Conference on Antennas and Propagation* (EUCAP '12), pp. 194–198, Mar. 2012.

[41] Y. Huang, L. S. Wu, M. Tang, and J. Mao, "Design of a beam reconfigurable THz antenna with graphene-based switchable high-impedance surface", IEEE Transactions on Nanotechnology, vol. 11, no. 4, pp. 836–842, 2012.

[42] M. Stasiowski and D. Schaubert, "Broadband array antenna", in *Proceedings of the Antenna Applications Symposium*, pp. 42–59, Sep. 2008.

[43] A. Kumar, "Monopole arrays are electronically steerable", *Microwaves & RF*, vol. 45, no. 9, pp. 88–94, 2006.

[44] S. Nikolaou, N. D. Kingsley, G. E. Ponchak, J. Papapolymerou, and M. M. Tentzeris, "UWB elliptical monopoles with a reconfigurable band notch using MEMS switches actuated without bias lines", *IEEE Trans. on Antennas and Propagat.*, vol. 57, no. 8, pp. 2242–2251, 2009.

[45] D. Manteuffel, M. Arnold, Y.Makris, and Z.N. Chen, "Concepts for future multistandard and ultra wideband mobile terminal antennas using multilayer LTCC technology", in *Proceedings of the IEEE International Workshop on Antenna Technology* (iWAT'09), pp. 1–4, Mar. 2009.

[46] G. M. Brzezina, L. Roy, and L. MacEachern, "LTCC ultrawideband antenna with transceiver integration capability", in *Proceedings of the European Microwave Conference*, vol. 3, pp. 2011–2014, Oct. 2005.

[47] R. Erickson, R. Gunnarsson, T. Martin et al., "Wideband and wide scan phased array micro- strip patch antennas for small platforms", in *Proceedings of the 2nd European Conference on Antennas and Propagation* (EuCAP '07), pp. 1–6, Nov. 2007.

[48] T. Aboufoul, A. Alomainy, and C. Parini, "Reconfigured and notched tapered slot UWB antenna for cognitive radio applications", *International Journal of Antennas and Propagation*, vol. 2012, Article ID160219, 2012.

[49] M. Martınez-Vazquez, O. Litschke, M. Geissler, D. Heberling, A. M. Martınez-Gonzalez, and D. Sanchez-Hernandez, "Integrated planar multiband antennas for personal communication handsets", *IEEE Trans. on Antennas and Propagat.*, vol. 54, no. 2, pp. 384–391, 2006.

[50] G. Srivatsun and S. S. Rani, "Compact multiband planar fractal cantor antenna for wireless applications: an approach", *International Journal of Antennas and Propagation*, vol. 2012, Article ID 839520, 6 pages, 2012.

[51] J. J. Heikkinen and M. A. Kivikoski, "Directive dual-band CP shorted ring-slot antenna", in *Proceedings of the IEEE International Symposium on Antennas and Propagation*, pp. 1–4, July 2008.

[52] N. Haider, D. Caratelli, D. P. Tran, and A. G. Yarovoy, "Directive electric-magnetic antenna for ultra-wideband applications", *IET Microwaves, Antennas and Propagation*, vol.7, no.5, pp. 381–390, Apr. 2013.

[53] G. Cappelletti, D. Caratelli, R. Cicchetti, and M. Simeoni, "A low-profile printed drop-shaped dipole antenna for wideband wireless applications", *IEEE Trans. on Antennas and Propagat.*, vol. 59, no. 10, pp. 3526–3535, 2011.

[54] C. I. Coman, I. E. Lager, and L. P. Ligthart, "The design of shared aperture antennas consisting of differently sized elements", ", *IEEE Trans. on Antennas and Propagat.*, vol. 54, no. 2, pp. 376–383, 2006.

[55] R. S. Chu, K. M. Lee, and A. T. S. Wang, "Multiband phased array antenna with interleaved tapered-elements and waveguide radiators", *in Proceedings of the AP-S International Symposium and URSI Radio Science Meeting*, vol. 3, pp. 1616–1619, Jul. 1996.

[56] A. B. Smolders, R. M. C. Mestrom, A. C. F. Reniers, M. Geurts, "A Shared Aperture Dual-Frequency Circularly Polarized Microstrip Array Antenna", *Antennas and Wireless Propagation Letters, IEEE* , vol.12, pp.120-123, Jan. 2013

[57] S. H. Hsu, Y. J. Ren, and K. Chang, "A dual-polarized planararray antenna for S-band and X-band airborne applications", *IEEE Antennas and Propagation Magazine*, vol. 51,no. 4, pp. 70–78, 2009.

[58] C. Han, C. Rodenbeck, J. Huang, and K. Chang, "A C/Ka dual frequency dual layer circularly polarized reflectarray antenna with microstrip ring elements", *IEEE Trans. on Antennas and Propagat.*, vol. 52, no. 11, pp. 2871–2876, 2004.

[59] X. Qu, S.-S. Zhong, and Y.-M. Zhang, "Dual-band dualpolarised microstrip antenna array for SAR applications", *Electronics Letters*, vol. 42, no. 24, pp. 1376–1377, 2006.

[60] S. Maci, G. Biffi Gentili, P. Piazzesi and C. Salvador, "Dual-band slot-loaded patch antenna", *Microwaves, Antennas and Propagation, IEE Proceedings*, vol.142, no.3, pp. 225-232, Jun. 1995.

[61] Z. N. Chen, "Suspended plate antennas with shorting strips and slots", *IEEE Trans. on Antennas and Propagat.*, vol. 52, no. 10, pp. 2525–2531, Oct. 2004.

[62] S. Maci and G. B. Gentili, "Dual-frequency patch antenna", *IEEE Antennas Propag. Mag.*, vol. 39, no. 6, pp. 13–20, Dec. 1997.

[63] L. Loizou, J. Buckley, B. O'Flynn, "Design and analysis of a dual-band inverted-F antenna with orthogonal frequency-controlled radiation planes", *IEEE Trans. on Antennas and Propagat.*, vol. 61, no. 8, pp. 3946-3951, Aug. 2013.

[64] A.I. Abunjaileh, I.C. Hunter, A.H. Kemp, "A circuit-theoretic approach to the design of quadruple-mode broadband microstrip patch antennas", *IEEE Trans. on Microw. Theory Tech.*, vol. 56, no. 4, pp. 896 - 900, Apr. 2008.

[65] D. Cavallo, A.Neto, G. Gerini, A. Micco, V. Galdi, "A 3- to 5-GHz wideband array of connected dipoles with low cross polarization and wide-scan capability", *IEEE Trans. Antennas Propag.*, vol. 61, no. 3, pp. 1148–1154, Mar. 2013.

[66] T.-Y.Yun,C.Wang,P.Zepeda,C.T.Rodenbeck,M.R.Coutant,M.Li, K. Chang, "A 1–21 GHz low-cost, multi-frequency and full-duplex phased array antenna system", *IEEE Trans. Antennas Propag.*, vol. 50, no. 5, pp. 641–650, May 2002.

[67] R. Erickson, R. Gunnarsson, T. Martin, L. G. Huss, L. Pettersson, P. Andersson, A. Ouacha, "Wideband and wide scan phased array microstrip patch antennas for small platforms", in *Proceedings of the 2nd European Conference on Antennas and Propagation* (EuCAP '07), Edinburgh, Nov. 2007

[68] STARS project, Sensor Technology Applied in Reconfigurable systems for sustainable Security. [Online] Available: www.starsproject.nl

CHAPTER 2

WIDEBAND ANTENNAS

This chapter is dedicated to the design of wideband antennas for reconfigurable sensors and sensor networks. To enhance the operational bandwidth of antennas two new concepts are studied and experimentally validated, (i) wideband blind-via feeding configuration and (ii) wideband quasi electric-magnetic radiating structure.

This chapter appeared in the following publication:

[J2] N. Haider, D. Caratelli, D. P. Tran, and A. G. Yarovoy, "Directive electric-magnetic antenna for ultra-wideband applications", *IET Microwaves, Antennas and Propagation,* vol.7, no.5, pp. 381–390, Apr. 2013.

IN chapter 1 (Section 1.6), three design approaches have been identified for realizing antennas for reconfigurable sensors and sensor networks. This chapter is devoted to the first research approach: *wideband antennas*. This approach requires antenna elements which provide good performances (e.g. good impedance matching, radiation pattern and gain) over a wide bandwidth. For frequency reconfigurability these radiators can be integrated with tuneable filters in order to select the operational frequency bands.

For wide scope of applications including surveillance, security, through-wall or rubble imaging, and medical diagnosis, wideband radar is needed. Wide operational bandwidth of such radars results in a high range resolution which helps to distinguish between closely spaced targets or distinguish targets from background clutters. Besides, ultra-wideband (UWB) radar provides low probability of interception, better target information recovery, non-interfering waveform and opportunity to perform time-domain analysis. The wide operational bandwidths of the antennas are crucial for the total system performance. A wide variety of wideband antennas have recently been designed, mainly for telecom applications [1-2]. However, the majority of the proposed antennas are not suitable for sensors or radar applications due to omni-directional (bi-directional) radiation patterns, high dispersion, high cross-polar component of the radiated field or a combination of these features. The choice of antenna types for wide- or multi-band arrays, where the antenna size and total volume are important, is even more limited. The most widely used radiators in this case are Vivaldi-like antennas [3]. However, Vivaldi-based arrays are characterized by a large volume (3D array). For systems implemented on a mobile platform, such as through-wall imaging (TWI) radar and radar systems for an unmanned aerial vehicle (UAV), planar antenna arrays are preferred to minimize the total weight. Therefore, the development of a planar wideband antenna element with back feeding, a size small enough to be integrated into a dense array, and unidirectional radiation patterns remains an attractive research problem.

In order to achieve the above mentioned requirements two aspects of an antenna structure are investigated: *the feeding section* and *the radiating structure*. In this chapter, these two features are analysed theoretically and experimentally. As the wideband feeding mechanism, the blind-via feeding structure and as the wideband radiating structure, an electric-magnetic antenna (combining a patch and a loop) is designed.

This chapter is organized as follows. Firstly, in Section 2.1 a new, simple and technology friendly feeding structure is presented which can increase the operational

bandwidth of planar antennas. Section 2.1.1 provides the concept of this wideband feeding structure. Design guidelines for the construction of the proposed blind-via feeding structure are presented in Section 2.1.2. Performance analysis and experimental verification of the feeding structure is treated in Section 2.1.3 while validation of the design guidelines is given in Section 2.1.4. Secondly, in Section 2.2 the concept of a wideband quasi electric-magnetic antenna is proposed. Antenna configuration is detailed in Section 2.2.1 followed by the X-band antenna design in Section 2.2.2. The experimental validations are demonstrated in Section 2.2.3. Finally, Section 2.3 ends this chapter with conclusions.

2.1 BLIND-VIA FENCE FOR BANDWIDTH ENHANCEMENT OF PLANAR PROBE-FED ANTENNAS

IN many applications, planar antenna elements are preferred due to their low profile, compact size, and ease of integration with the radio frequency (*RF*) front end [6]-[8]. While end-probe feeding is widely used in narrowband active phased arrays, because of its simplicity, compact size and ease of integration with the microwave front-end, it is typically replaced by more complicated feeding in wideband arrays due to its narrowband behaviour.

It is well known that the operational bandwidth of a planar antenna can be enhanced by increasing the substrate thickness [9-11]. However, such an approach results in an increase of the parasitic inductance of the probe feed which makes the antenna impedance matching over a large frequency band difficult. To reduce the feed inductance, ring gap can be etched between the feed probe and the patch [12]. However, more than 10% bandwidth enhancement remains challenging with this concept. Capacitive coupled feed, such as L-shaped [13-14] and T-shaped probe [15-16], are also extensively used to diminish feed reactance and thereby increase operational bandwidth to typically 20% to 35%. These approaches require bending the feed to construct the L-shape probe and therefore increase manufacturing complexity. The use of air dielectric layer also increases the size of the radiating element and makes it difficult to apply in a dense array environment.

In this section, a novel and simple feeding structure is presented which can increase the operational bandwidth of a planar antenna to 20-30% while reducing coupling level between radiating elements in an array. Unlike cavity-backed antennas

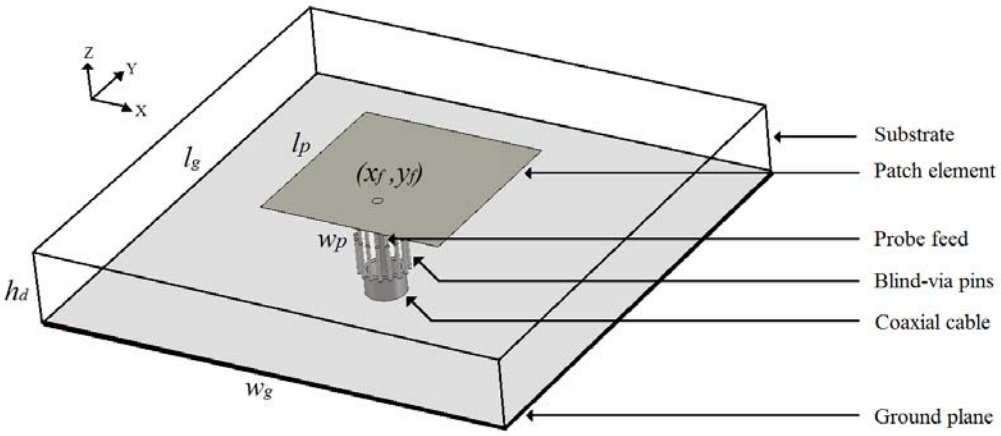

(a)

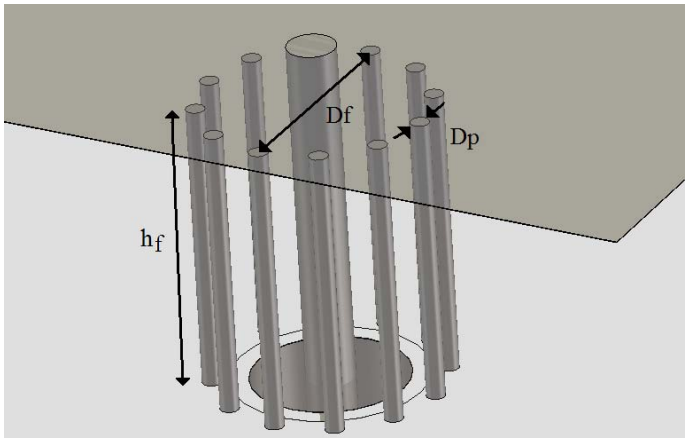

(b)

Figure 2.1 (a) Microstrip antenna with blind-via feeding printed on a dielectric substrate with relative permittivity ε_r=3.5. Geometrical characteristics of the structure: w_p=24mm, l_p=24mm, w_g=53mm, l_g=53mm, h_d=9.144mm, x_f=0mm, y_f=-5.5mm. The origin of the adopted coordinate system is located at the center of the radiating patch. (b) Characteristics of the feeding section: D_f=6mm, h_f=7.62mm, D_p=0.75 mm. The number of vias in the fence is 12, and the diameter of the center probe is 1.28mm.

[17], the proposed feeding structure does not increase the area occupied by each element. By avoiding air-substrate, compact radiating elements (smaller than quarter of the free-space wavelength at the centre frequency) are realized which allows them to be integrated into dense arrays.

In [18] a capacitively fed microstrip antenna element is introduced. The radiating element is excited by a smaller capacitor patch and the capacitor patch is then fed by a probe. In [19] the moment method is used to solve the integral equations describing the capacitively fed rectangular microstrip antenna element and in [20] a network model is given for the calculation of the effect of a capacitor patch on the impedance of a microstrip antenna.

While for a capacitively fed microstrip antenna element the probe inductance was cancelled by the capacitor patch, we propose below an alternative solution in which the inductive reactance of the probe is reduced by minimizing the effective length of the probe with the substrate integrated coaxial-like structure and by introducing parallel capacitance between the feeding probe and the via pins. In comparison with the capacitively fed patch the blind-via fence provides a larger bandwidth. However, the manufacturing cost can be also higher than the design presented in [18-20]. An advantage of using the blind-via structure is the possibility to bring the DC power to the radiating element, particularly useful for controlling the switch bias voltages of reconfigurable elements.

2.1.1. The blind-via fence and its operational principle

Probe-fed planar antennas printed on thicker substrates can have larger bandwidth if the feed inductance can be reduced by minimizing its effective length. To achieve this goal, a via-pin fence can be used to encircle the probe resulting in a coaxial-line-like section partly slipped in the antenna substrate. The proposed novel approach can reduce the reactance of the probe feed and significantly increase its operational bandwidth. The input impedances of the antenna element with and without blind-via fence are presented in Figure 2.2. These graphs demonstrate that the fence structure significantly reduces the antenna reactance and flattens the real part of the relevant input impedance. This results in the overall enhancement of the matching to the characteristic impedance $Z_0 = 50\Omega$ of the feeding line. For the blind-via fence the reactive part is reduced as a result of two physical aspects: reduction of the probe's effective length and partial cancellation of the probe inductance by the additional parallel capacitance. The surface current densities on the feeding probe and blind-via fence are illustrated in Figure 2.3. It can be seen that the currents in the inner part of the via pins flow in the opposite direction with respect to the current at the centre probe. These two currents resemble a *TEM* mode of a conventional coaxial line. As a result, the effective length of the probe reduces. However, it should be pointed out here that in contrast to an infinitely long coaxial cable here the via-pins has a finite length which causes some common-mode currents flowing in the same direction as the current at the centre probe. In Figure 2.3, these common-mode currents are visible on the external part of the via-pins.

To construct the coaxial line within the substrate material blind-via pins are more practical to impersonate the outer conductor than a continuous metal fence owing to its more robust structure and reduced manufacturing complexity. Blind vias, which do not go through the entire substrate material, can be created by mechanical or laser

drilling. Nevertheless, these methods are expensive and commonly not applicable for aspect ratio (the ratio between the height and the diameter of vias) larger than two. Alternatively, the substrate can be formed by attaching two dielectric layers. This allows the blind-vias to be constructed as through plated-holes in one of the layers before bonding them together. This process allows much larger aspect ratio and hence more suitable for the considered feeding structure.

The use of thick dielectric substrates usually can also result in a detrimental increase of the excitation level of surface waves. Consequently, the mutual antenna couplings increase, causing in phased arrays blind angles appearance, radiation efficiency decrease, and large impedance and gain variations during the scan. Therefore, reducing coupling levels in antenna arrays are important. In the proposed design, the use of blind-via fence also results in a favourable decrease of the antenna coupling level by minimizing the spurious radiation of the feeding probe. In the *H*-plane the influence of the via-fence is more persuasive where the probe radiation is the main cause of the coupling.

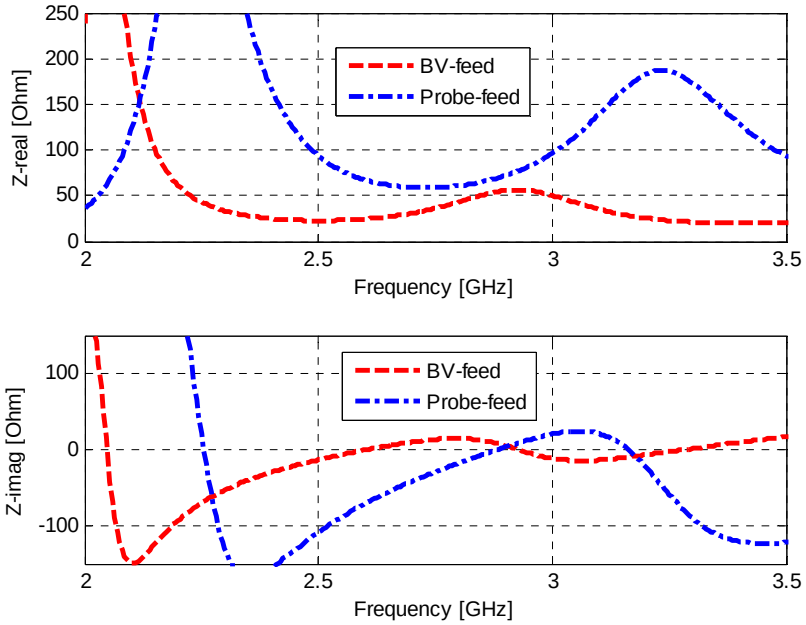

Figure 2.2 Input impedance of the microstrip antenna with the conventional probe feeding and by use of the blind-via fence.

To thoroughly analyse the operational principle of the blind-via fence, the surface current densities on the feeding probes and fences for the antenna elements forming a 3×3 planar array have been computed (Figure 2.3 - Figure 2.5). The experimental prototype of this array is presented in Figure 2.10(b). The element periodicity was selected to be half of the free-space wavelength at the centre operating frequency ($f_c = 2.8GHz$), which is a typical value in array design. The centre element (element

5) of the array was excited at the frequency of 2.9 GHz, whereas the other radiators were match terminated.

Figure 2.3 shows the surface current on the centre probe and on a blind-via pin of element 5 at 2.9 GHz. As mentioned earlier one can notice that there are two currents flowing on different parts of blind-via pin circumference: closer to the centre probe there is a strong current flowing in the opposite direction with respect to the current at the centre probe (these two currents resemble a *TEM* mode of a conventional coaxial line) and on the "external" part of the surface, a relatively small common-mode current flowing in the same direction as the current at the centre probe. The strength of the common-mode current is much smaller than the one of the transmission line current, which results in weaker electromagnetic field excited by this current in the substrate in comparison with the standard probe feeding. Furthermore, along the y-axis some asymmetry in the location of the common-mode current is observed, which can be explained by the influence of the patch and the off-set of the feeding section from the centre of the radiating patch. As a result, on the "external" surface of the via-pin the currents flow in two opposite directions (see Figure 2.3).

In Figure 2.4, the induced current on the feeding section of element 6 of the 3x3 array is shown for the same frequency. One can observe presence of two currents at the probe flowing in opposite direction (in contrary to the situation with conventional

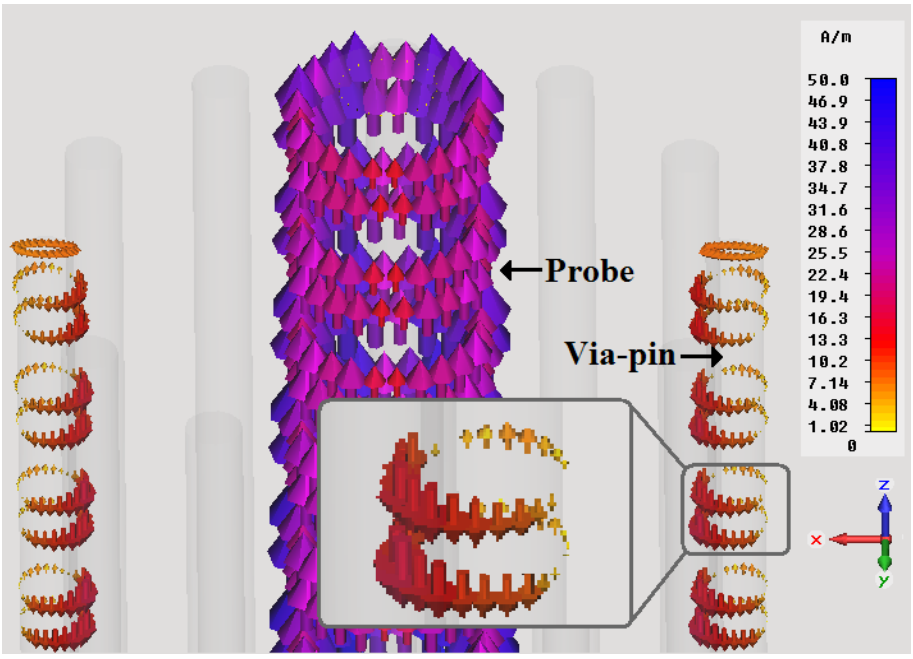

Figure 2.3 Surface current density distribution on the feeding section of element 5 in the array topology shown in Figure 2.10 at 2.9 GHz. Semi-transparent geometry is adopted for visualization purposes.

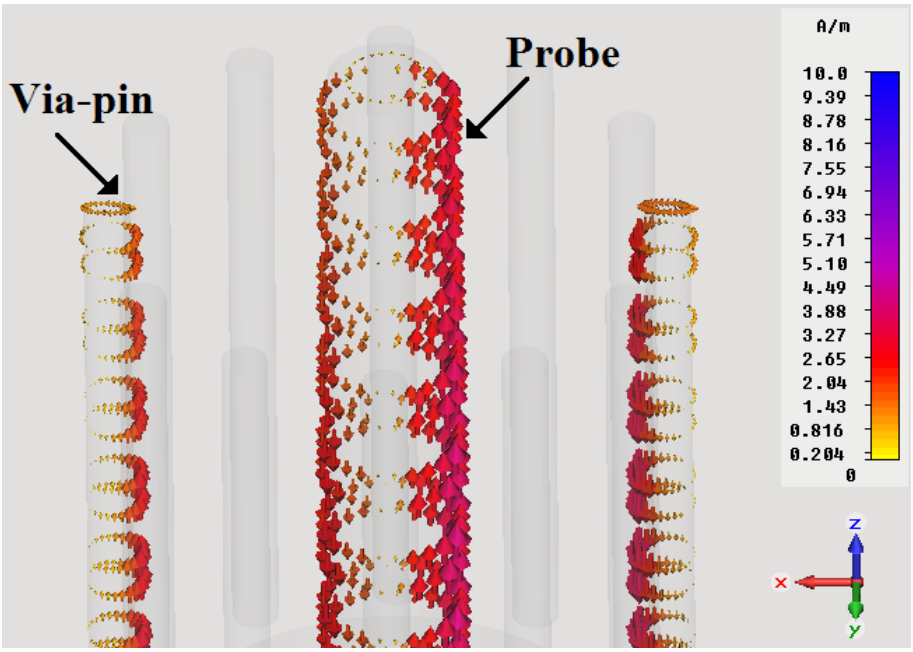

Figure 2.4 Surface (induced) current density distribution on the feeding section of element 6 in the array topology shown in Figure 2.10 at 2.9 GHz. Semi-transparent geometry is adopted for visualization purposes.

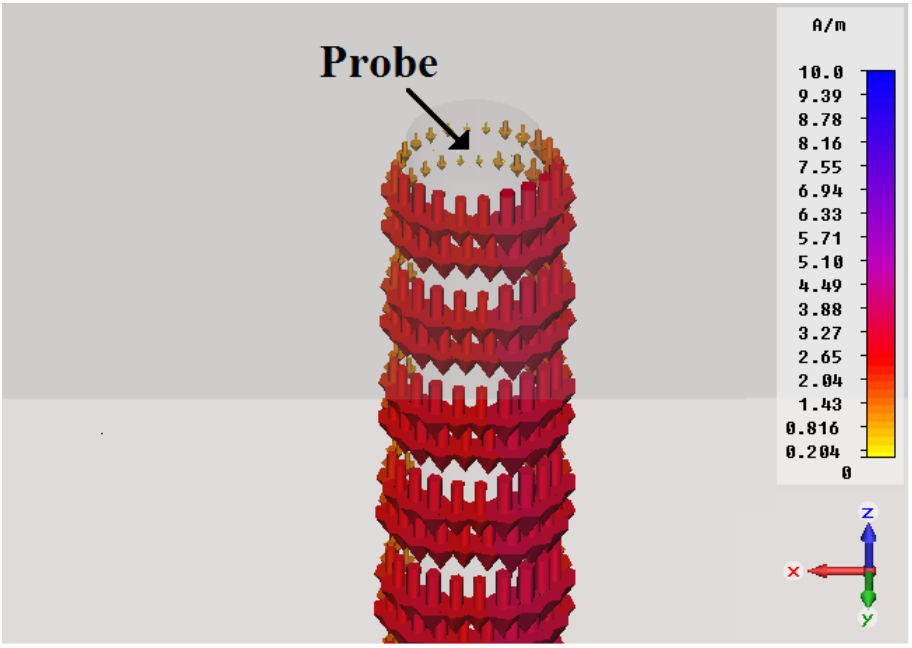

Figure 2.5 Surface (induced) current density distribution on the feeding section of element 6 for the probe-fed 3x3 array at 2.9 GHz. Semi-transparent geometry is adopted for visualization purposes.

probe feeding shown in Figure 2.5). As a result, susceptibility of the feeding structure to the electromagnetic field in the substrate is lower than that of the conventional one. Both effects (reduction of the excitation in the substrate field and reduction of the probe susceptibility to the external field) result in the reduction of the coupling.

2.1.2. Design guidelines

In the following sections, a general guideline to design the blind-via feeding section of a patch antenna is presented. In particular, the impact of the fence diameter, fence height, fence pin diameter and number of pins were studied. In this analysis, the values of all parameters, except of the one studied, were equal to those shown in Figure 2.1. The diameter of the feeding probe remains constant which is equal to the centre pin of the SMA (Surface Mount Assembly) connector. The following simulations results are obtained by using CST microwave Studio (which utilizes the Finite Integration Technique for computation) as the electromagnetic solver.

2.1.2.1. Fence diameter

The radius or, in this case, the distance between the centre probe and the via fence, should be such that the real-valued characteristic impedance of the structure, regarded as a truncated coaxial line with the substrate material as insulator, is close to the characteristic impedance of the feeding line. The characteristic impedance of a coaxial line is known as, $Z_c = \sqrt{\mu/\varepsilon}\ln(b/a)/2\pi$, where μ and ε are respectively the permeability and the permittivity of the dielectric material, and b (in this case D_f) and a are respectively the diameters of the outer and the inner conductors. The input reflection coefficient and the realized gain of the considered microstrip antenna as a function of the fence diameter are shown in Figure 2.6. It is evident from Figure 2.6(a) that the operational band of the microstrip antenna develops with the fence diameter from narrowband to wideband and finally splits into two bands. Variation of the characteristic impedance of the coaxial-like feeding structure with fence diameter increase plays here the dominant role.

For $D_f = 6\,mm$, the characteristic impedance of the fence section is close to the reference one $Z_0 = 50\,\Omega$ and, thanks to that, the radiating structure is found to be well-matched to the coaxial feeding line. The mentioned value of the parameter D_f has been selected as the optimal one for the considered antenna. In fact, a further increase of the fence diameter enhances the operational bandwidth as exemplified in Figure 2.6(a); however it also raises the range variability against frequency of the realized gain at the broadside. For D_f larger than $6\,mm$, the fence structure appears closer to the active radiating edge of the antenna element and interferes with the E-field distributions. This partly disruptive interference of the wave contributions relevant to the dominant resonant modes of the antenna causes the reduction of the gain. For the chosen value of the fence diameter less than $3\,dB$ variation in the realized gain has been observed within the operational band as revealed in Figure 2.6(b). Furthermore,

for D_f larger than $6\,mm$, the average value of the reflection coefficient over the operational band tends to increase, thus making the antenna prone to impedance mismatching due to manufacturing tolerances.

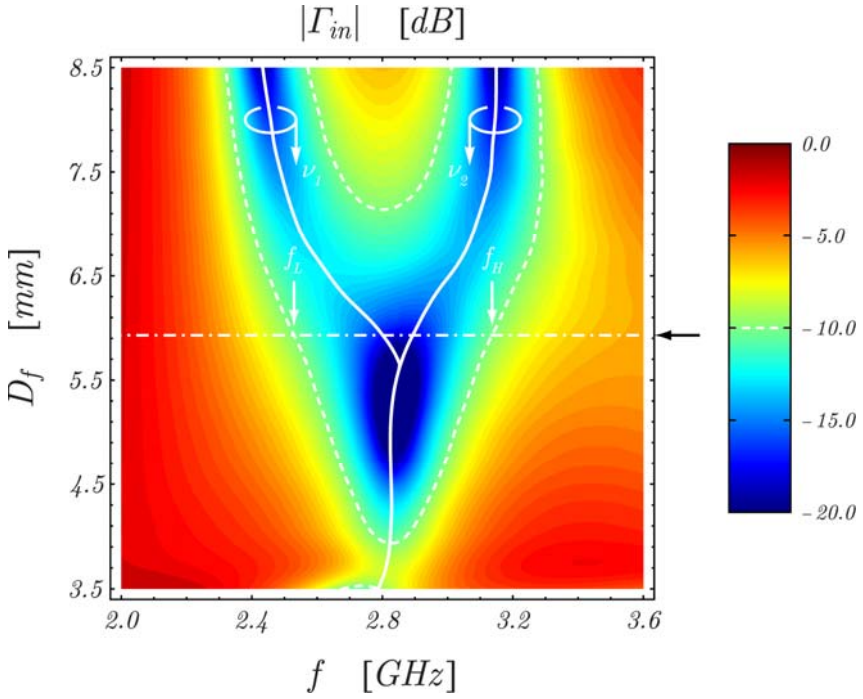

(a)

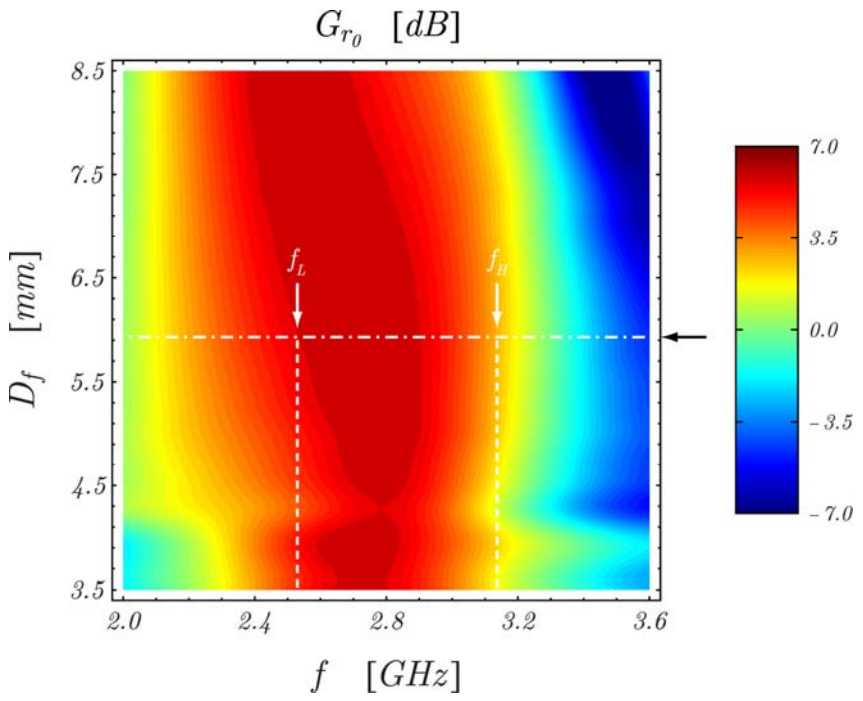

(b)

Figure 2.6 The input reflection coefficient (a) and realized gain (b) of the considered microstrip antenna as function of the fence diameter (D_f). The design value of D_f is indicated by a black arrow in both diagrams.

2.1.2.2. Fence height

For the proposed blind-via feeding, a proper selection of the fence height (h_f) is also crucial for the wideband performance. A sufficiently large height is needed to enhance the bandwidth, however placing the fence too close to the radiating element results in a detrimental influence of the surface current distribution excited along the metal patch. From the numerical simulation results it was observed that, wherein the substrate thickness is larger than $\lambda_d/6$, the largest operational bandwidth was achieved for:

$$h_f \approx 2\lambda_d/15, \tag{2.1}$$

where λ_d is the wavelength in the dielectric substrate at the centre frequency. Consequently, for the reference microstrip antenna shown in Figure 2.1, a fence height of 7.66 mm maximizes the operational bandwidth (see Figure 2.7).

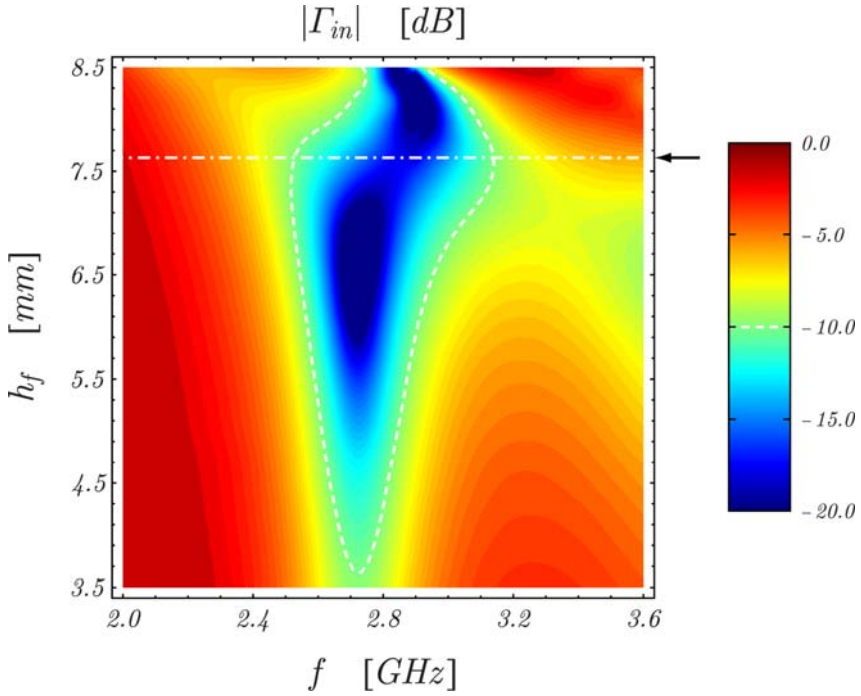

Figure 2.7 The input reflection coefficient as function of the height of the fence (h_f). The optimal design value of h_f is indicated by a black arrow.

2.1.2.3. Pin diameter

The effect of the diameter of each via-pin (D_p) is shown in Figure 2.4. Here, we notice that the operational band shifts towards the upper frequencies as the pin diameter increases. At this point, the effective diameter of the fence, namely the

distance from the inner coaxial probe to the fence, is reduced with the pin diameters (D_p) increase. This shift of the operational band can be estimated as follows:

$$\Delta f\big|_{MHz} \approx 340\,\Delta D_p\big|_{mm}, \tag{2.2}$$

where $\Delta D_p\big|_{mm}$ denotes the difference between the actual pin diameter and the reference one, that is $D_p = 0.5\,mm$. The printed-circuit-board (*PCB*) manufacturing process poses a limit on the minimum pin diameter.

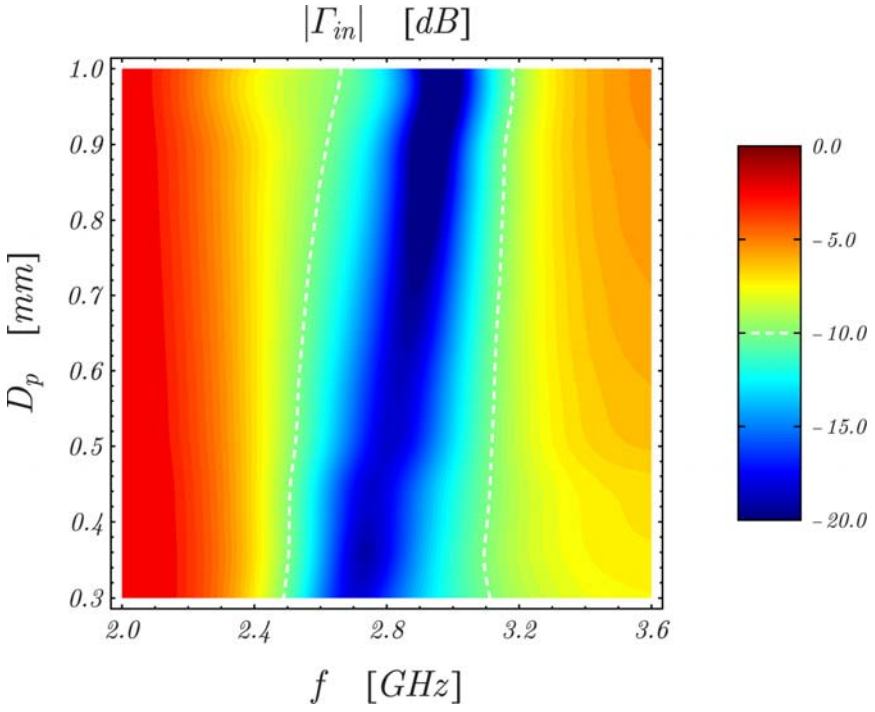

Figure 2.8 The input reflection coefficient as a function of the diameter of pins

2.1.2.4. Number of blind-via pins

In order to keep the characteristic capacitance of the feeding line similar to the coaxial one and to prevent the undesired radio frequency energy leakage in the dielectric substrate, a sufficient number of pins in the fence are needed. Nevertheless, manufacturing capabilities will limit the minimum distance between these pins. As a general guideline, the "same surface area" rule of thumb, introduced by A. C. Ludwig in [21], can be used and the number of pins forming the fence as well as their radius can be selected in such a way that the sum of the circumferences of each pin in a cross-section of the proposed feeding structure is equal to or larger than the inner circumference of the whole metal fence. Therefore, the minimum required number of pins n_p can be estimated as:

$$n_p \approx \left\lceil D_f / D_p \right\rceil, \tag{2.3}$$

where $\lceil \cdot \rceil$ denotes the usual ceiling function, D_f and D_p being the diameter of the metal fence and the via pins, respectively. Small variations in the total pin numbers have marginal effect on the reflection coefficient as shown in Figure 2.5. However, sufficient amount of pins are required in order to reduce antenna mutual couplings in an array (discussed in Section 2.1.3.2).

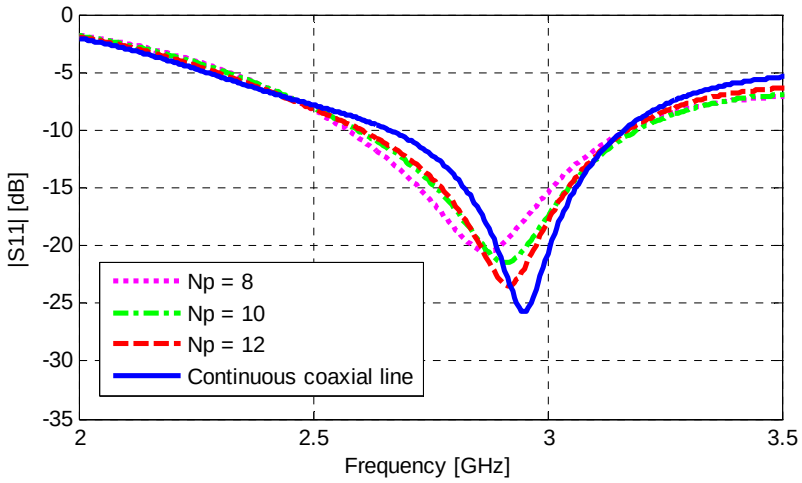

Figure 2.9 The input reflection coefficient of the considered microstrip antenna as a function of the number of pins in the probe fence.

2.1.3. Performance analysis and experimental verifications

In this section, the impact of the proposed feeding structure for a microstrip antenna (as shown in Figure 2.1) is demonstrated. Here, the substrate thickness was selected to be $0.085 \times \lambda_0$, λ_0 being the free-space wavelength at the centre working frequency ($f_c = 2.8 GHz$). Thereby, the thickness of the substrate is such that the cut-off frequency of the second propagation surface-wave mode (TE_1) is roughly two times larger than the upper operating frequency of the antenna. Therefore, only the fundamental mode (TM_0) contributes to the surface wave level excited in the structure. In order to experimentally validate the numerical results, a prototype was designed and fabricated (see Figure 2.10). The antenna is printed on a RO4003 substrate with relative permittivity $\varepsilon_r = 3.5$ and 17-µm-thick copper cladding.

2.1.3.1 Bandwidth enhancement

In Figure 2.11, the magnitudes of the reflection coefficient of the antenna with and without the blind-via fence are presented. As evident in Figure 2.11, the fence

increases the fractional bandwidth at 10-*dB* return-loss level of the considered S-band microstrip antenna to about 20%. In Figure 2.12, the realized-gain (accounting for the reflection at the feed location) is plotted and only 1 dB gain variation is observed between 2.4 GHz and 3 GHz. In this case, the 3-dB gain bandwidth is about 30%.

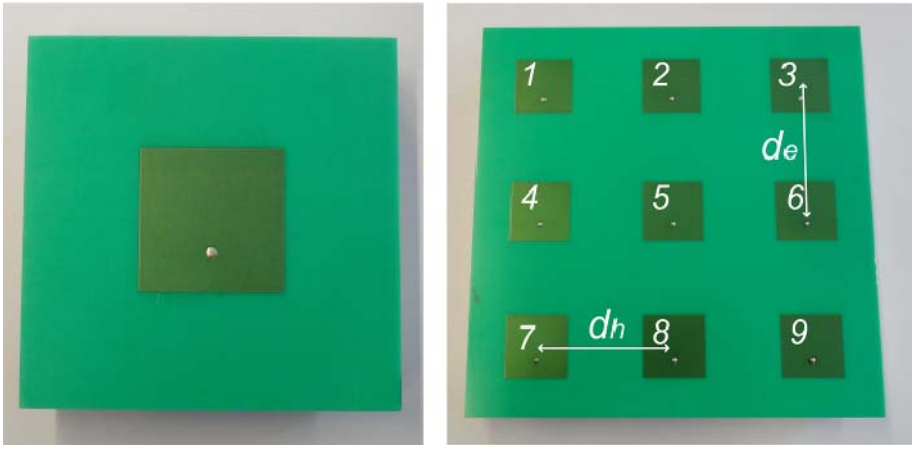

(a) (b)

Figure 2.10 Antenna prototypes: (a) isolated element, (b) 3x3 array, d_h=d_e=53mm

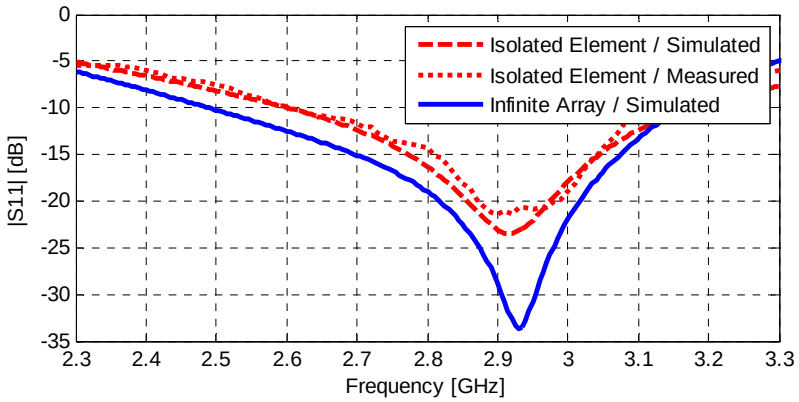

Figure 2.11 Reflection coefficient magnitude of the microstrip antenna

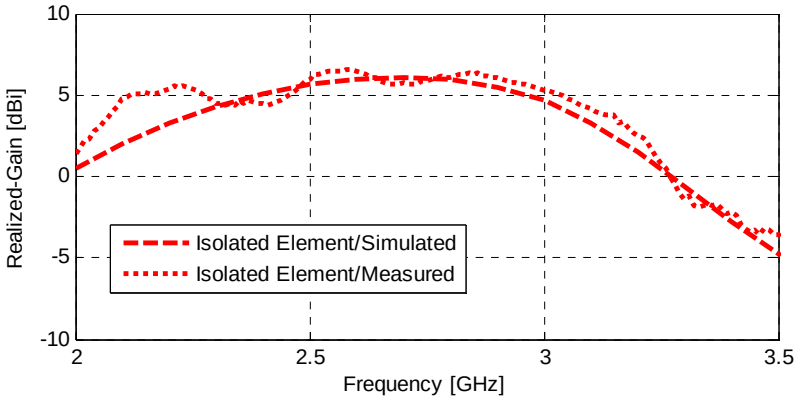

Figure 2.12 Broadside realized-gain against frequency for the blind-via fed microstrip antenna

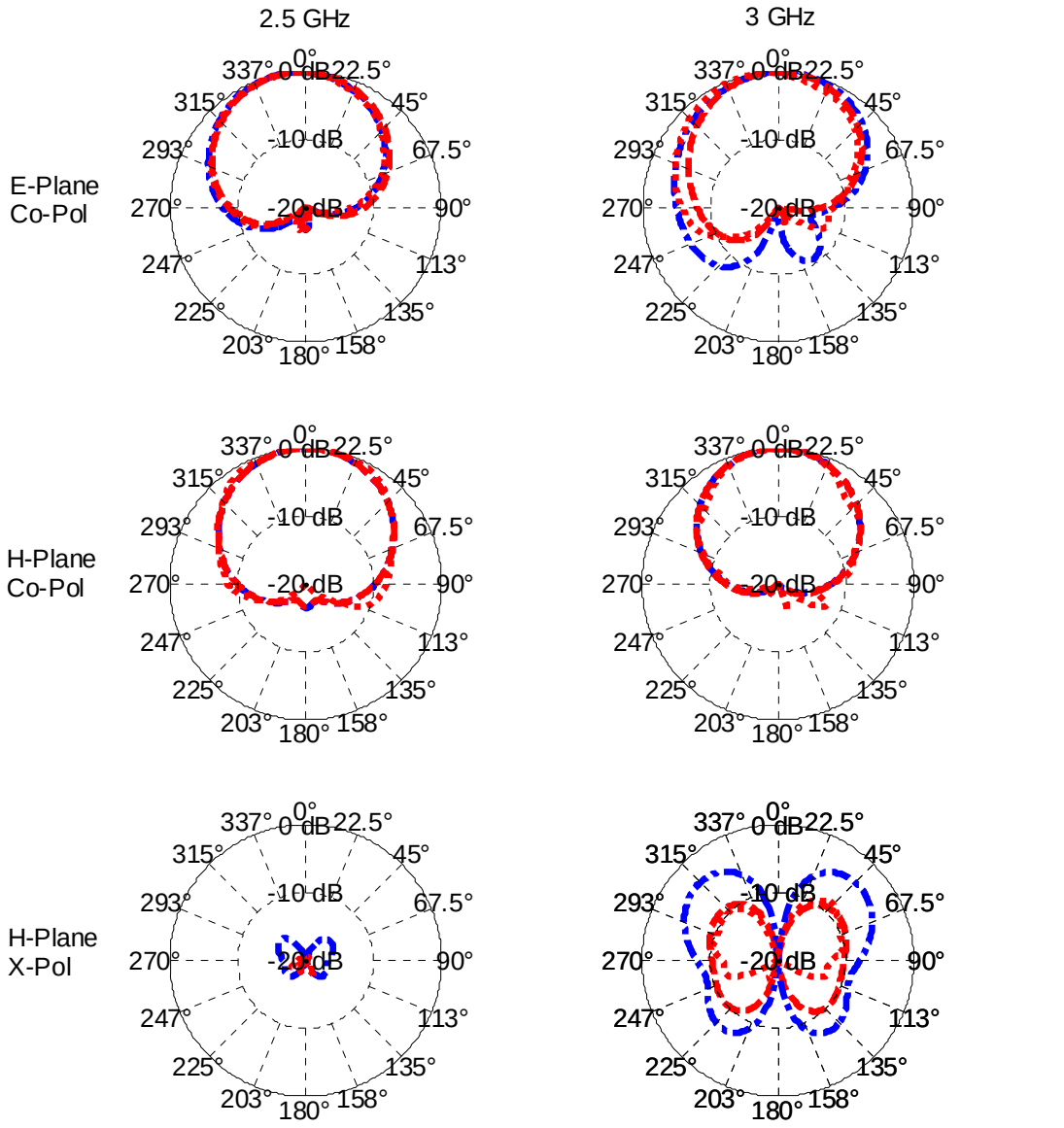

Figure 2.13 Normalized radiation patterns of the microstrip antenna for blind-via feeding and probe feeding at (a) 2.5 GHz (b) 3 GHz

The normalized radiation patterns of the microstrip antenna with the blind-via feeding and conventional probe feeding are illustrated in Figure 2.13. As it can be seen in these figures that the presence of the fence does not affect the co-polarized radiation patterns while the cross-polarization level decreases due to the reduction in the monopole-like radiation of the probe [22]. At 45° off boresight the cross-polarization level reaches its maximum value. Within the operational band, a

reduction of about 5 dB in the peak cross-polarization value is observed in the antenna configuration with blind-via feed. At higher frequencies, the substrate thickness is larger in terms of the wavelength which increases the monopole like radiation from the probe. To further reduce the cross-polarisation levels in the H-plane, sequential rotation can be applied in the array arrangement as discussed in Appendix B. This will also enhance the symmetry in E-plane patters.

2.1.3.2 Mutual coupling reduction

To investigate experimentally the impact of the via-pin fence on the mutual coupling, a 3×3 planar array configuration with square grid (see Figure 2.10(b)) was constructed. The element periodicity was selected to be half of the free-space wavelength at the centre operating frequency ($f_c = 2.8GHz$).

Generally, a probe-fed microstrip antenna with thick dielectric substrate couples strongly with its adjacent elements. The proposed concept can reduce the coupling level. In order to have correct comparisons of the electromagnetic isolations, the input reflection coefficients of the antennas were taken into consideration. The effect of the input impedance matching is separate from the coupling or isolation level by applying the well-known de-embedding method [23]-[24]:

$$C_{mn} \approx \frac{\left|S_{mn}\right|^2}{(1-\left|S_{mm}\right|^2)(1-\left|S_{nn}\right|^2)}, \tag{2.4}$$

where C_{mn} and S_{mn} are respectively the coupling and transmission coefficients while S_{mm} and S_{nn} are the input reflection coefficients of the corresponding ports.

In Figure 2.14 and Figure 2.15, the reduction in coupling level are demonstrated. Within the operational band, the average coupling level between adjacent elements along the *E*-plane is found to be 1.8 dB reduced in comparison with the setting without via pins, whereas a 3 dB reduction was observed along the *H*-plane. At the centre frequency the coupling level is improved by 3 dB and 20 dB along the *E*-plane and *H*-plane, respectively. The effect of the via-fence is more noticeable in *H*-plane for which the radiation from the probe is the main source of the coupling. Figure 2.15 shows that for the blind-via feed the coupling is extremely low around 2.9 GHz.

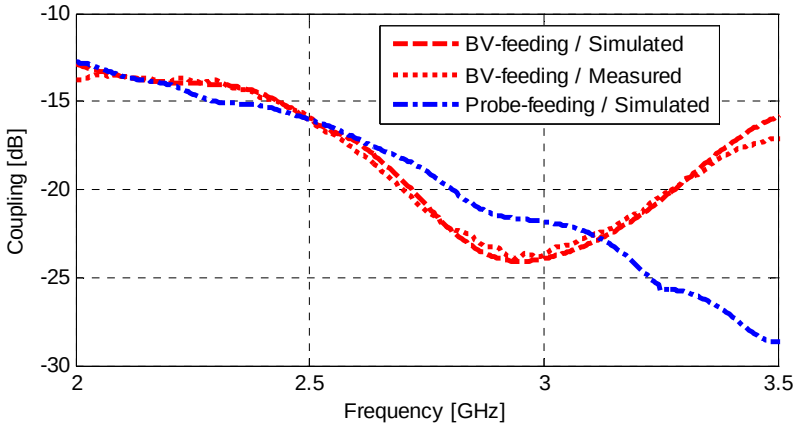

Figure 2.14 Coupling between two adjacent array elements along the *E*-plane

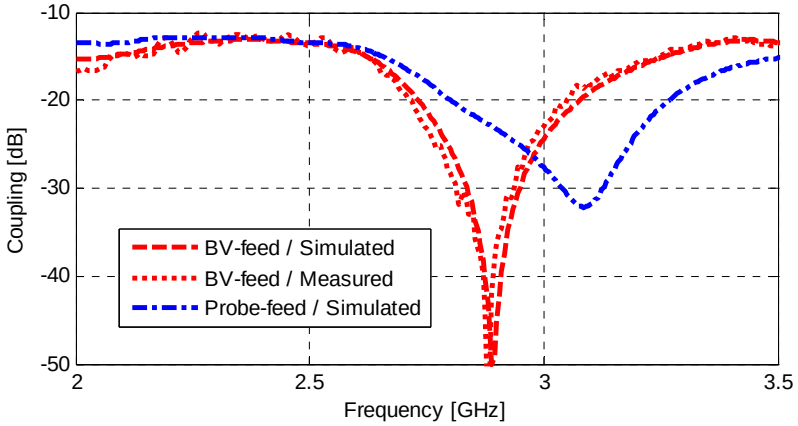

Figure 2.15 Coupling between two adjacent array elements along the *H*-plane

2.1.4. Validation of the design guidelines

To verify the applicability of the design guidelines presented in Section 2.1.2, the blind-via feeding structure was, also, applied to a *C*-band microstrip antenna. The geometrical characteristics of the feeding section follow directly from the guidelines provided in Section 2.1.2 and no further optimization was performed here. Similar to the previous design, here the fence diameter was set to 6 mm in order to bring the characteristic impedance of the fence section close to 50Ω. The height of the fence was set to 4.57 mm which was determined from equation (2.1), with λ_d denoting the wavelength in the dielectric substrate at the centre frequency ($f_c = 4.6 GHz$ in the considered test case). The reflection coefficient of the blind-via fed *C*-band element is plotted in Figure 2.16. The simulation results indicate that the fractional impedance bandwidth is about 30% for $|S_{11}| \leq -10 dB$.

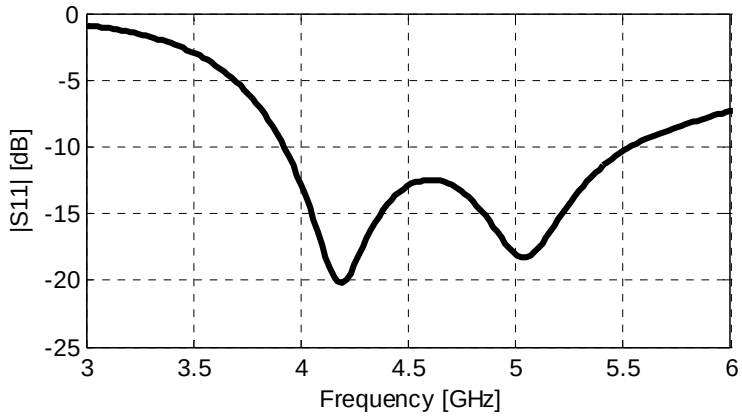

Figure 2.16 Reflection coefficient of the *C*-band microstrip antenna with blind-via feeding

2.2 WIDEBAND QUASI ELECTRIC-MAGNETIC ANTENNAS

THE feeding mechanism plays an important role for an antenna. In the previous section a wideband feeding technique is discussed which can significantly increase the operational bandwidth of planar probe-fed antennas. Besides the feeding topology, the radiating structure is a key feature of antennas in determining their overall performance. This section is devoted to the analysis of a wideband radiating structure.

2.2.1. Antenna concept

To obtain ultra-wideband radiation, it is important to combine proper excitation of both electric and magnetic fields [25]. An electric-magnetic antenna possesses less near-field reactive energy due to the cancellation of energy flow caused by the dual electric and magnetic configuration. This phenomenon can be used to match the antenna over a wide bandwidth [1, pp-247]. A need for proper combination of electric topologies has been discussed in [26]-[28]. Similar approaches have been used previously in [29]-[33]. Briefly, when the magnetic field of a radiator is orthogonal to the antenna plane over most of the antenna aperture, it can be denoted as the quasi-magnetic antenna. On the other hand, when the electric field is orthogonal to the antenna plane over most of the aperture, it is denoted as the quasi-electric antenna.

In the proposed antenna, we combine electric field radiator (patch) with a magnetic field radiator (loop around the patch). Both elements are elevated above the ground plane, which contributes to unidirectional radiation. A physical implementation of the antenna configuration is sketched in Figure 2.17.

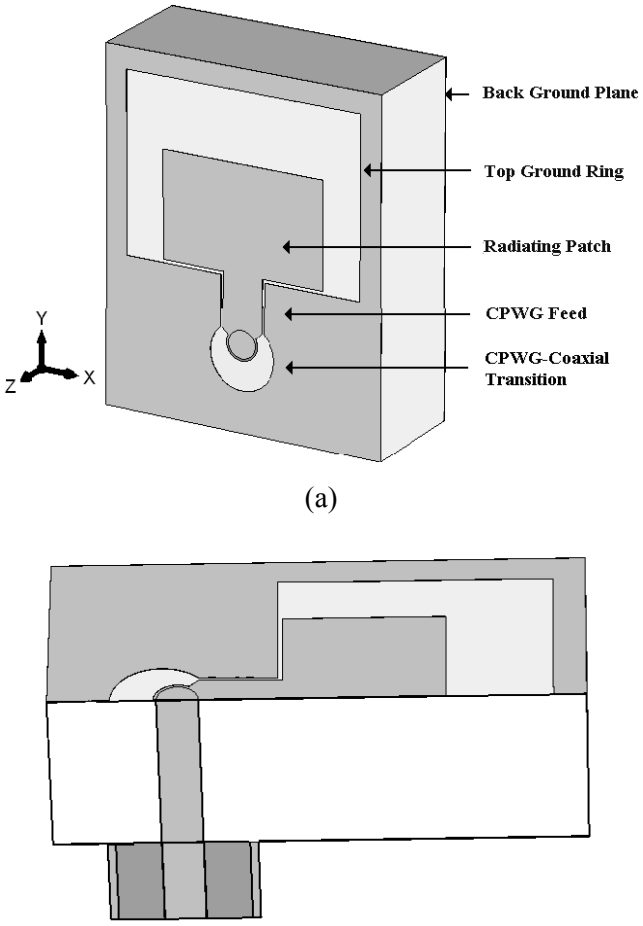

Figure 2.17 The basic antenna topology: (a) Front view, (b) Side view

In order to illustrate the operational principle of the antenna in Figure 2.18 the simulated magnetic-field and electric-field distribution at 10 GHz is presented. Let us define the top metal layer (XOY plane in Figure 2.17) as the antenna plane. For the proposed antenna the magnetic field lines are orthogonal (or the electric field lines are parallel) to this antenna plane in the slot regions as shown in Figure 2.18(a). A loop antenna is known as the purely magnetic antenna where all the magnetic fields within the loop region are orthogonal to the loop area. Here, the magnetic field lines are not allowed to be orthogonal to the antenna plane in the metal regions due to the well-known boundary condition of conducting material. Hence, the antenna is quasi-magnetic. In addition, this antenna can also be referred as quasi-electric antenna as the electric field lines in the metal radiating region are normal to the antenna plane due to the presence of the ground plane underneath the substrate (see Figure 2.18(b)). Consequently, we can denote that our antenna topology belongs to the quasi-electric-magnetic antenna group.

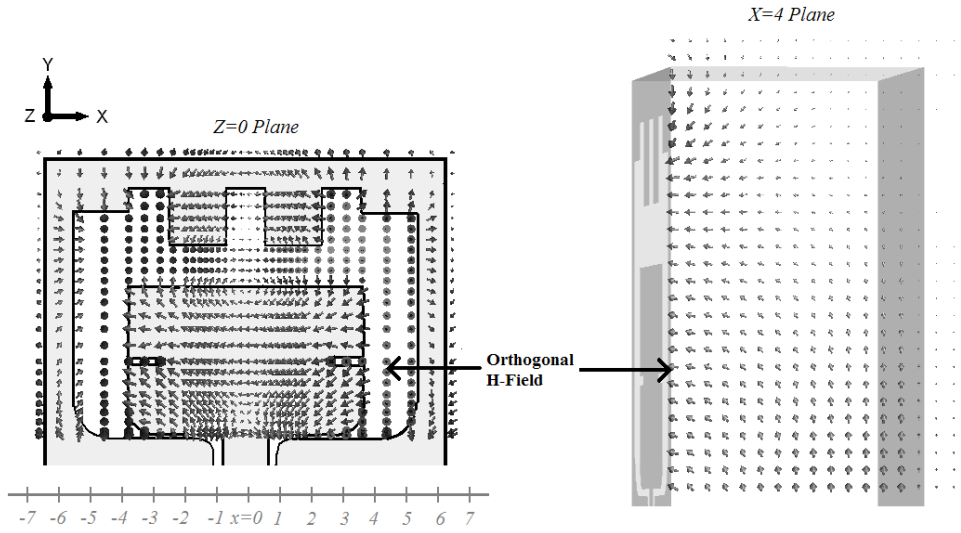

(a)

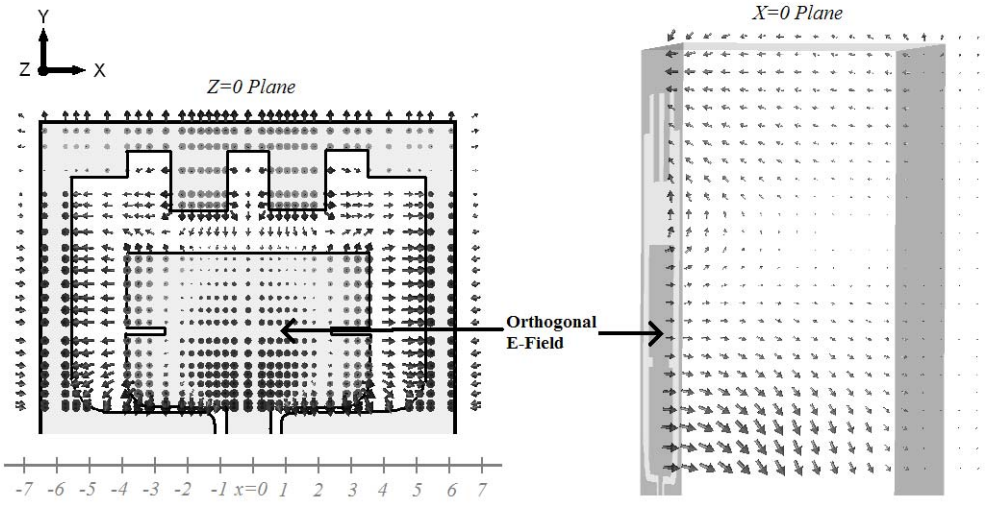

(b)

Figure 2.18 Simulated (a) magnetic field and (b) electric field distribution at 10 GHz. The origin of the adopted coordinate system is located at the centre of the radiating patch.

The proposed antenna consists of four major elements:

1) Radiating patch and the top ground ring;
2) CPWG feed;
3) Back ground plane;
4) CPWG-coaxial transition.

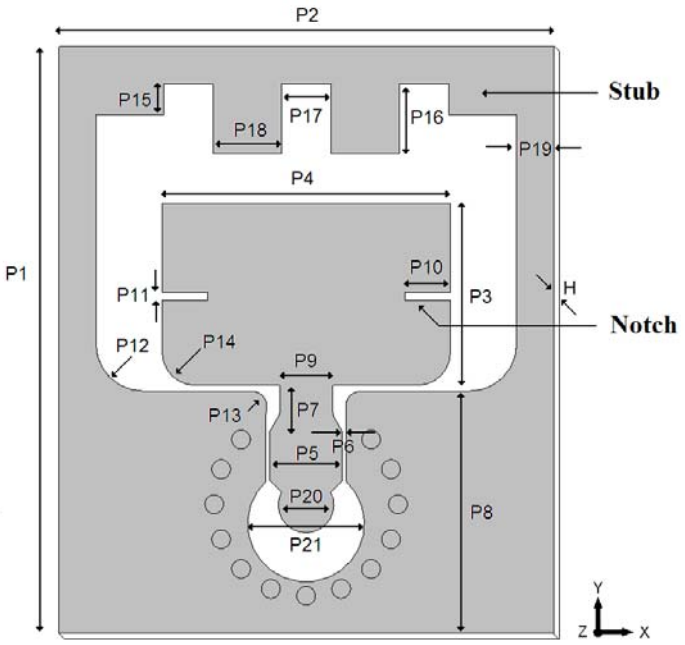

(*a*)

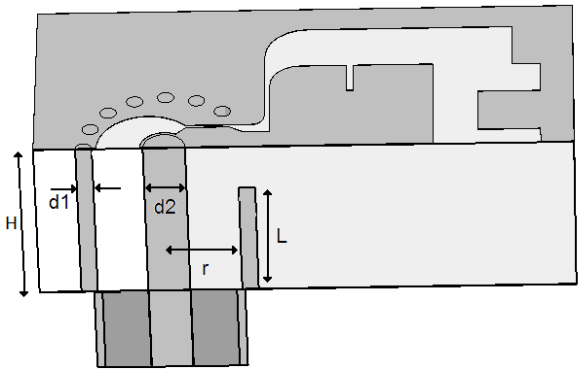

(*b*)

Figure 2.19 (*a*) The antenna architecture and its geometrical parameters, (*b*) Side view of the blind via placed beneath the coplanar waveguide

2.2.1.1. Radiating patch and the top ground ring

As demonstrated in Figure 2.17 and Figure 2.19, the antenna is formed by a radiating patch encircled by a loop. The inner patch contributes more to the radiation in the higher part of the operating band where the patch length becomes quarter to half of the guided wavelength. On the other hand, the perimeter of the loop is roughly one wavelength around the centre frequency. Due to the presence of the stubs (see Figure 2.19(a)), the actual loop perimeter will increase and hence the frequency band will expand towards the lower frequencies.

The top ground ring creates a magnetic slot which together with the patch is accountable for the radiation. Due to the presence of the ground ring, the surface electric field lines will be bounded in the slot area. By changing the loop geometry one can influence the slot area and thereby the field distribution inside the slot. This control over the field distribution is a great advantage of the proposed topology to satisfy various wideband characteristics. It can be noticed in Figure 2.17 that the proposed antenna structure exhibits symmetry along the y-axis. The symmetry is important for a symmetric radiation pattern in XOZ plane and for polarimetric purity (this will be demonstrated in section 2.2.3.3).

2.2.1.2. CPWG feed

A feeding technique has a major effect on the overall antenna performance. To concurrently feed the radiating patch and the loop, a grounded-coplanar-waveguide (CPWG) is the most appropriate choice. Moreover, it has been demonstrated in [34] that CPW feed structure has many advantages for wideband applications. Coplanar waveguide has simple structure, constant effective permittivity, low radiation and conductance losses, less dispersion and very wide operational bandwidth.

2.2.1.3. Back ground plane

The unidirectional radiation has been achieved by adding the ground plane. Ground plane or metal cavity is often used to achieve directional radiation from an omni-directional antenna element [35]. The effect of a ground plane can be seen as a short circuited transmission line connected to the antenna. The frequency for which the distance between the antenna and the ground plane is $\lambda/4$, there is a constructive interference between the incident wave and the wave reflected by the ground plane. For any other frequency this interference will not be entirely constructive and the reflection coefficient at the input port increases. Therefore, a floating ground plane generally degrades the impedance bandwidth. To compensate undesired influence of the ground plane on the antenna input-impedance, the ground plane is placed directly under the substrate at the initial design phase and antenna element has been modified accordingly to compensate the reduction of the antenna operational bandwidth due to the influence of the ground plane.

2.2.1.4. CPWG-coaxial transition

The end-launch geometry used in the initial design [discussed in Appendix A] has some practical disadvantages. Among them the most critical issue is the addition space required for the connector which will increase the total surface area required for each element. This additional space might not be available in an array environment

especially when strict element spacing has to be maintained. Therefore, a back feeding is required and a perpendicular transition of coaxial to coplanar transmission line is needed. Furthermore, such back-feed arrangement provides the possibility to design a planar array structure whereas only a linear array is realizable for the end-launch feeding configuration. The design process of the orthogonal coaxial-to-coplanar transition which can assure low transmission loss will be discussed in this section. The approach is closely related to the blind-via feeding structure presented in Section 2.1.

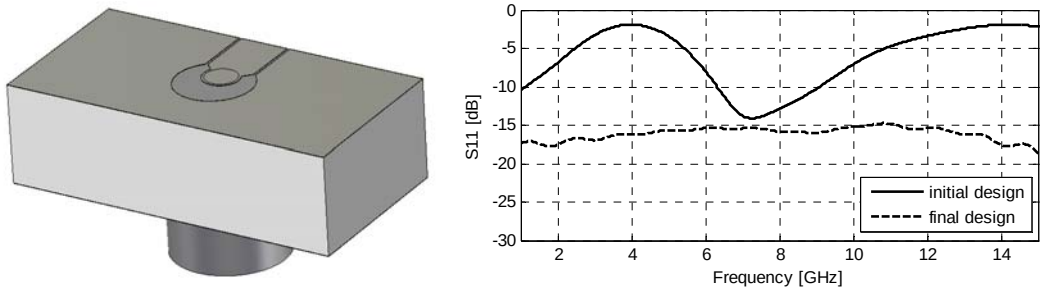

(a) (b)

Figure 2.20 (a) The orthogonal coax-to-coplanar transitions, (b) Simulated reflection coefficients

To investigate the back feeding structure separately, an orthogonal coax-to-coplanar transition was studied (see Figure 2.20(a)). Here, the centre pin of the SMA connector passes through the substrate and is soldered to the metal pad on the other side. In Figure 2.20(b), the reflection coefficient of the orthogonal transition is presented and it is clear here that for the initial design only within a very limited band the transmission loss is sufficiently low. The main reason for this narrow band behaviour is the discontinuity in the waveguide which causes undesired propagation in the substrate. The effect of the discontinuity is extreme in the proposed design due to the large substrate thickness.

To increase the bandwidth of the orthogonal transition, a coaxial waveguide between the connector and the coplanar line is needed. This transition has similar operational principle as the blind-via feeding section discussed in the previous section. The waveguide is realized by 16 via-pins as presented in Figure 2.19. The vias create the outer conductor and the centre pin the inner conductor. As the best transition is expected when the impedance of this coax line is around 50 Ω, the distance between the centre connector and the vias (r in Figure 2.19(b)) has been selected to bring the impedance close to 50 Ω.

To encircle the inner conductor completely blind-vias are placed underneath the coplanar waveguide as presented in Figure 2.19(b). To construct the coaxial-line-like section, sufficient number of pins is needed to achieve good impedance matching over a large frequency band as illustrated in Figure 2.21(a). However, as mentioned earlier

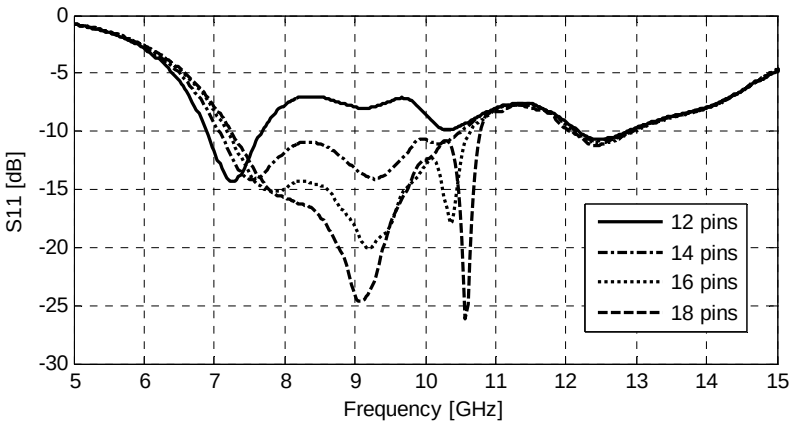

(*a*)

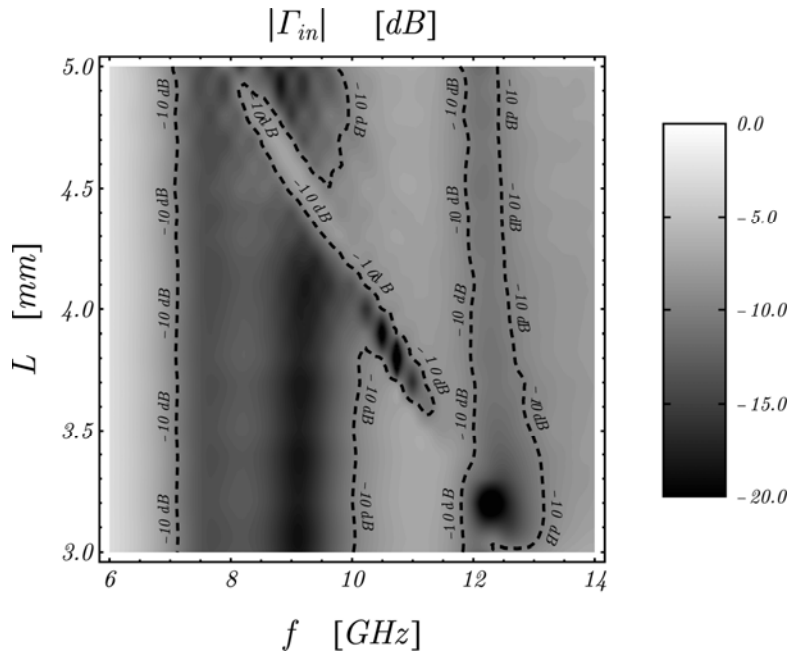

(*b*)

Figure 2.21 The reflection coefficient of the antenna as a function of the number (a) and the length (b) of the pins in the feeding section

the maximum number of pins is determined by the manufacturing process. For the X-band antenna element, described in the following section, 16 pins have been used.

A proper selection of the length of the blind-via pins (L in Figure 2.19(b)) is also crucial for wideband operation. A sufficiently large height is needed to prevent the

undesired radio frequency energy leakage in the dielectric substrate, however placing these pins too close to the coplanar line results in a detrimental influence. Consequently, a via-pin length of about 3.9 mm maximizes the operational bandwidth as demonstrated in Figure 2.21(b).

A small diameter of the pins (d1 in Figure 2.19(b)) is advantageous to reduce the gap between two pins and thereby the energy leakage. Here, the pin diameter is selected to be *0.5 mm*. Further reduction of this value limits the length of the blind-via pins due to current limitations in printed-circuit-board (*PCB*) manufacturing.

The proposed transition over performs the initial design: for the final design the return loss is less than -15 dB over the entire bandwidth of interest, while for the initial design it is less than -10 dB from 6 to 9 GHz (see Figure 2.20(b)).

2.2.2. X-band antenna design

Based on the antenna architecture discussed in the previous section, a radiating element to cover the complete X-band has been designed. The antenna is modelled numerically by using a commercially available simulation tool (CST MicroWave Studio) based on Finite-Integration-Technique (FIT). In Appendix A the design analysis of a Ku-band quasi electric-magnetic antenna is presented.

We have selected the total length and width of the radiator (P1 and P2 in Figure 2.19) to be equal to about half of λ_0 (where λ_0 is the free-space wavelength at the centre frequency). For the substrate we have selected Taconic TLY-5 material with ε_r = 2.2. The low dielectric constant value of the substrate material is advantageous for large bandwidth and good radiation performance. These outer dimensions of the antenna element we considered as fixed ones, while other parameters were optimized.

The shape and dimensions of the radiating patch are determined based on the following reasoning. It is well known that the length of a patch determines the resonant frequency and is about half of the guided wavelength for a microstrip patch antenna excited in its fundamental mode [36]. Due to the presence of the fringing fields at the edge of the patch, the physical dimension should be slightly lower. To decrease the patch length further, two notches are inserted in the patch geometry as depicted in Figure 2.19(a). As a result, the electrical length of the patch remains constant while P3 (see Figure 2.19(a)) decreases. Furthermore, four stubs are added to the upper side of the loop. The inner stubs are important for the lower resonance. These stubs are producing additional path length for the current and the operational band shifts towards the lower frequency as depicted in Figure 2.22(a). The length of

the outer stubs is important for the impedance match, especially for the centre frequency as shown in Figure 2.22(b). Some additional parametric analyses can be found in Appendix A.

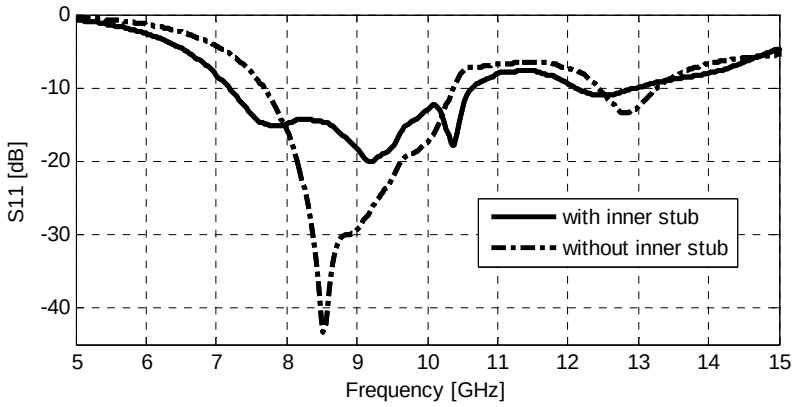

(*a*)

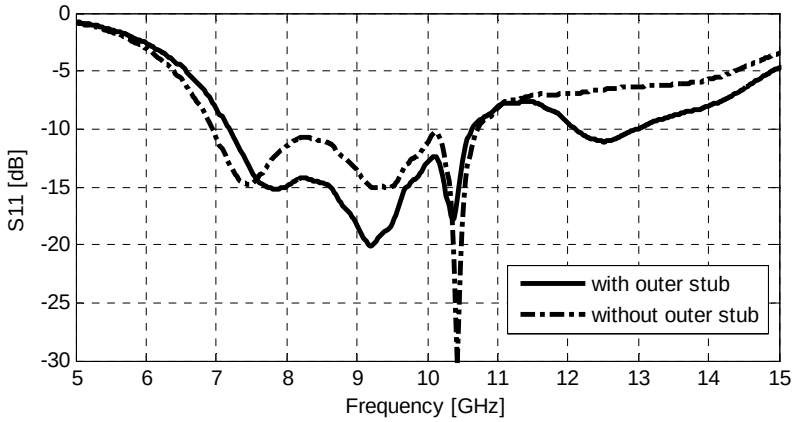

(*b*)

Figure 2.22 Effect of the inner stub length P16 (*a*), and the outer stub length P15 (*b*) on the input reflection coefficient of the antenna

Regarding the feeding, an impedance transformer is used to provide a good matching between the 50 Ω coplanar line and the radiating patch. The length (P7) and the width (P9) of this impedance transformer and the curve radius (P13) of the transition section are crucial values to obtain good matching over a large frequency band. To further minimize the impedance discontinuity, a smooth step has been realized in the central conductor of the CPWG line. The sharp corners of the top ground ring and the radiating patch have been blended to avoid strong diffractions. The curve radiuses of these blended sections are noted as P12 and P14 in Figure 2.19(a)).

A parametric study has been conducted to evaluate the influence of different parameters, e.g. patch, stub and notch lengths, and they have been optimized to

minimize the reflection coefficient. The final dimensions are listed in Table 2.1. The antenna matching achieved is shown in Figure 2.24 which exhibits that the antenna is well matched (VSWR < 2) to 50 Ω between 7 and 11 GHz.

Table 2.1 Geometrical dimension of the X-band antenna element

Symbol	Dimension in	Description
P1	16.35	Antenna length
P2	12.37	Antenna width
P3	4.95	Patch length
P4	7.81	Patch width
P5	1.94	Signal width of CPWG
P6	0.10	Gap width of CPWG
P7	1.057	Impedance transformer length
P8	3	Length of the feeding section
P9	1.44	Impedance transformer width
P10	1.23	Notch length
P11	0.21	Notch width
P12	1.28	Slot curve radius
P13	0.4	CPWG curve radius
P14	0.9	Patch curve radius
P15	0.84	Outer stub length
P16	1.9	Inner stub length
P17	1.33	Inner stub separation
P18	1.86	Inner stub width
P19	1	Ring width
P20	1.48	Inner transition diameter
P21	3.1	Outer transition diameter
H	5.52	Height of the substrate
d1	0.5	The diameter of each pin
d2	1.28	The diameter of the centre probe
R	2.2	The distance of the pins from the centre probe
L	3.96	The length of the blind-via pins

2.2.3. Performance analysis and experimental validation

To validate the suggested antenna topology, an X-band antenna prototype was manufactured and tested (Figure 2.23). The antenna is fabricated on Taconic (TLY-5) material having relative permittivity of 2.2, loss tangent of 0.0009 (at 10 GHz), and thickness of 5.52 mm (217.3 mil). The specified thickness was achieved by bonding two layers of 1.58 mm thick substrate on both side of a 2.36 mm thick TLY-5 substrate. As a bonding material fastRise-27 (ε_r =2.7) was used.

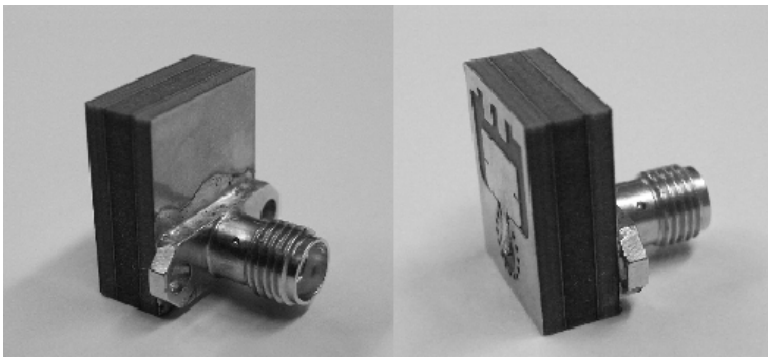

Figure 2.23 Experimental prototype of the back-fed X-band element

2.2.3.1. Impedance bandwidth

The impedance bandwidth of the proposed antenna structure has been experimentally analysed. The Agilent E8364B network analyzer was used for this measurement. The reflection coefficient of the back-fed X-band element is plotted in Figure 2.24. Simulation result indicates that an impedance bandwidth of about 40% is achieved for VSWR lower than 1.92 ($|S_{11}| \leq -10\,dB$) and an impedance bandwidth of

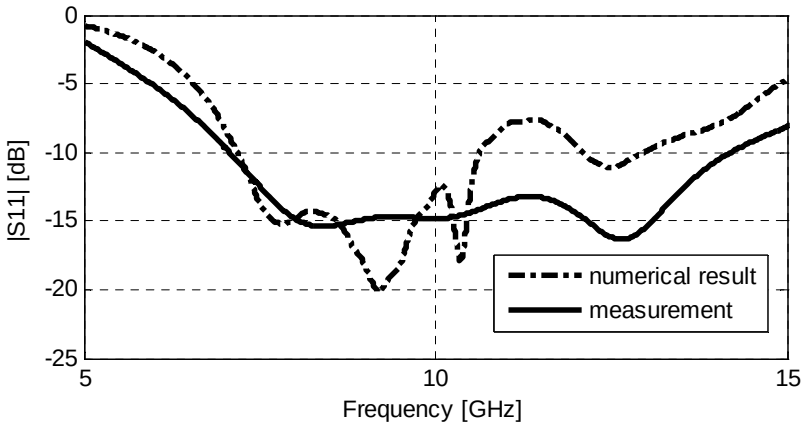

Figure 2.24 Simulated and measured reflection coefficients of the antenna element

about 67% is achieved for VSWR lower than 2.32 ($|S_{11}| \leq -8\,dB$). The experimental verification confirmed VSWR lower than 2 between 7 GHz and 14 GHz referring to a fractional bandwidth of 67% ($|S_{11}| \leq -10\,dB$). It is worth to point out that both numerical and experimental results presented here include the reflection caused by the antenna structure as well as the coplanar-to-coaxial transition.

2.2.3.2. Current distribution

In Figure 2.25, the current distributions at 7 GHz, 10 GHz and 12 GHz are shown (radiation patterns at these three frequencies are presented in Figure 2.27 and Figure 2.28). Here, a high current density along the edges of the top ground plane and the radiating patch is observed. From these figures the existence of different resonant harmonics is evident. In Figure 2.25(a) and Figure 2.25(b) two and in Figure 2.25 (c) three λ/2 current periods are visible on the half contour of the ground plane.

2.2.3.3. Radiation patterns

A three dimensional view of the far-field radiation patterns is presented in Figure 2.26. Evidently, the antenna element possesses a wide beam width. The half power beam width at 10 GHz is more than 80° along H-plane (xz-plane) while about 65° along E-plane (yz-plane) while the front-to-back ratio (FBR) is better than 12 dB. The back radiation can be further reduced by increasing the ground plane size. From Figure 2.26 we can conclude that while polarisation is extremely pure in the E plane (phi=90°), a high cross polarisation level is observed in the H plane (phi=0°).

In Figure 2.27 and Figure 2.28, the measured and simulated radiation patterns at three different frequencies are displayed as typical examples. These measurements were carried out in DUCAT (Delft University Chamber for Antenna Tests) using TEM horn (GZ0126ATP) as transmit antenna. A good agreement is observed between the simulated and the measured co-polarized radiation patterns while some disagreement in the cross-polarized radiation patterns has been noticed. These results verified stable radiation patterns over the operational band. Both simulation and measurement results confirm that the cross-polarized level is low in the broadside over the entire operational frequency band. Along the E-plane (yz-plane) the cross-polarisation level is very small over entire band (in practice, values around the numerical errors of simulations are observed) due to the antenna symmetry and therefore has not been plotted in Figure 2.28. However, along H-plane (xz-plane) for theta angle greater than 30 deg the cross-polarized level increases with the frequency (see Figure 2.27). The cross-polarisation in the H-plane levels can be decreased by using sequential rotation in the array arrangement as discussed in Appendix B. Another advantage of the sequentially rotated array arrangement is the improvement of pattern symmetry in E-plane.

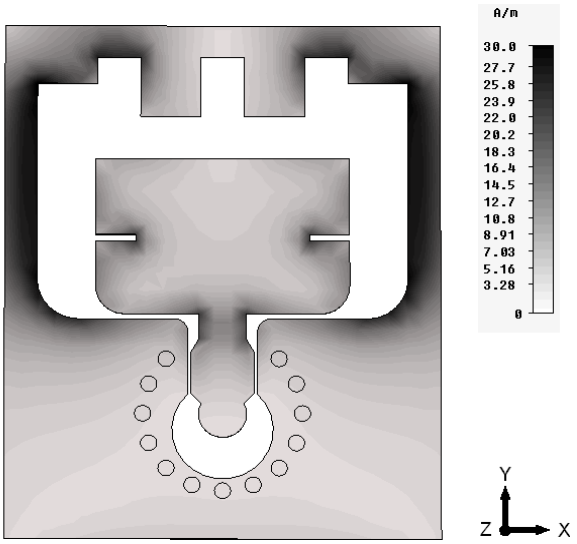

(*a*)

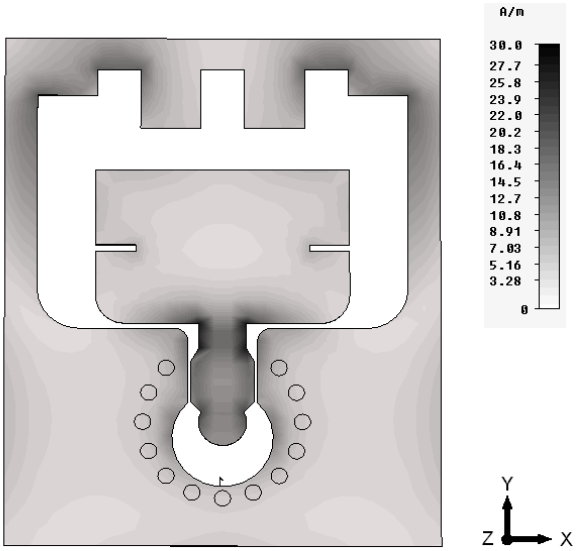

(*b*)

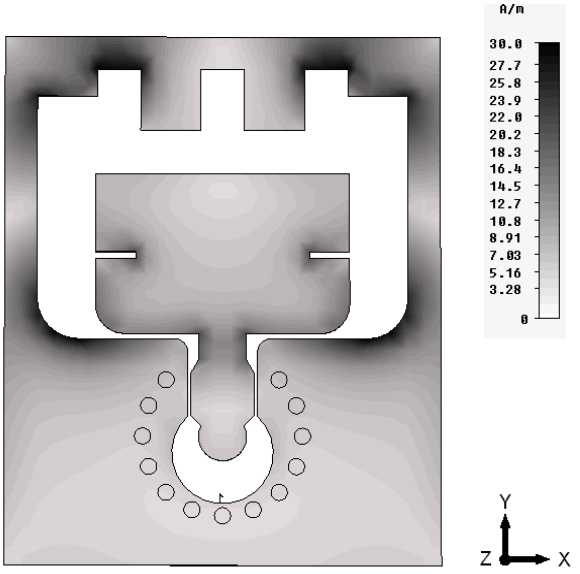

(*c*)

Figure 2.25 Simulated surface current distribution at 7 GHz (*a*), 10 GHz (*b*), and 12 GHz (*c*)

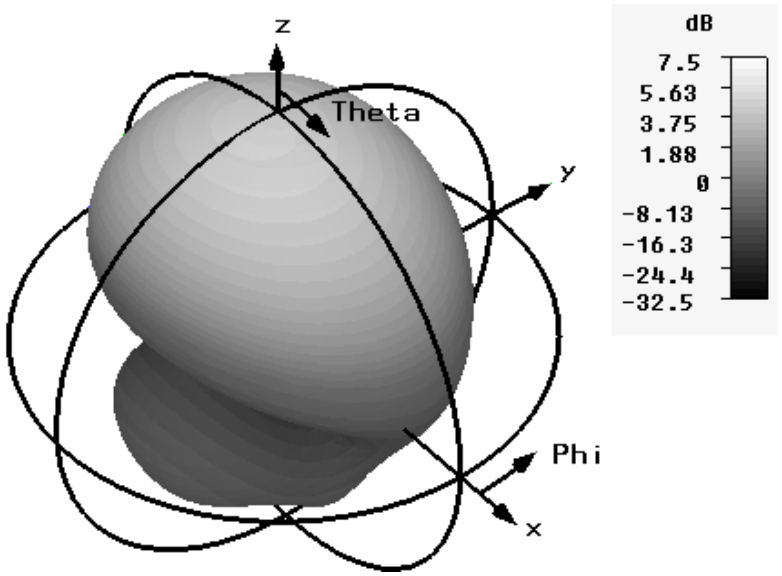

(*a*)

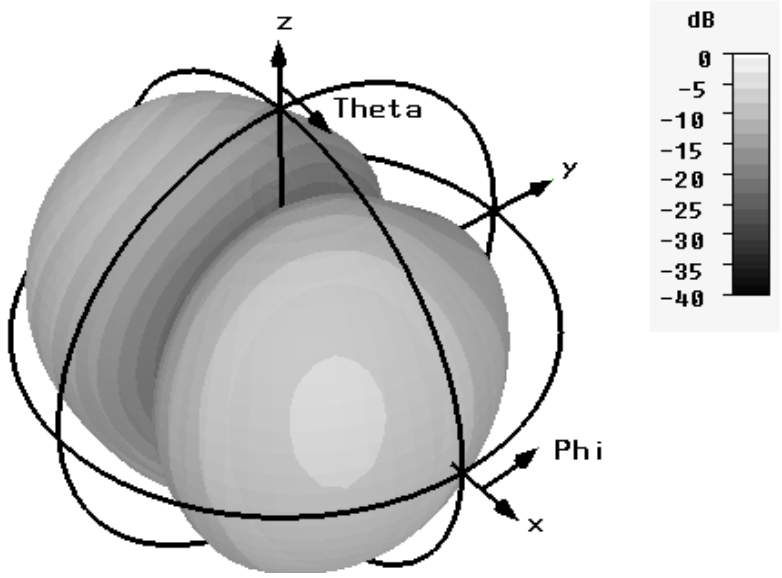

(*b*)

Figure 2.26 Far-field antenna gain at the centre frequency (10 GHz) of the X-band element, (*a*) co-polarized and (*b*) cross-polarized component

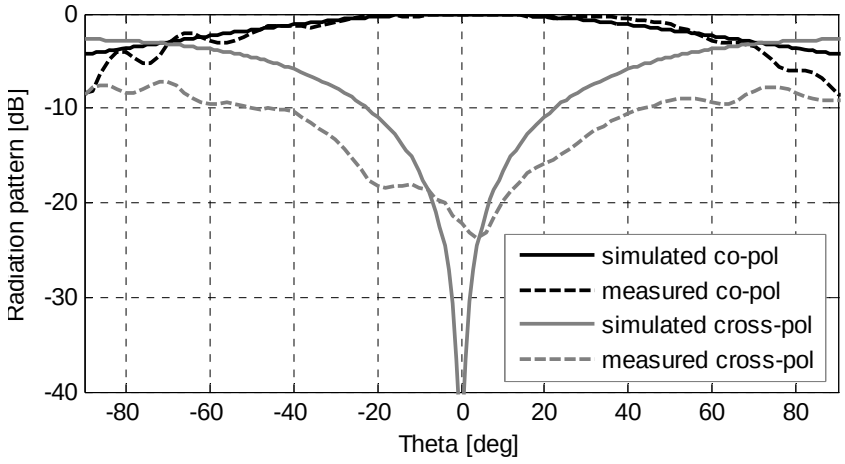

(*a*)

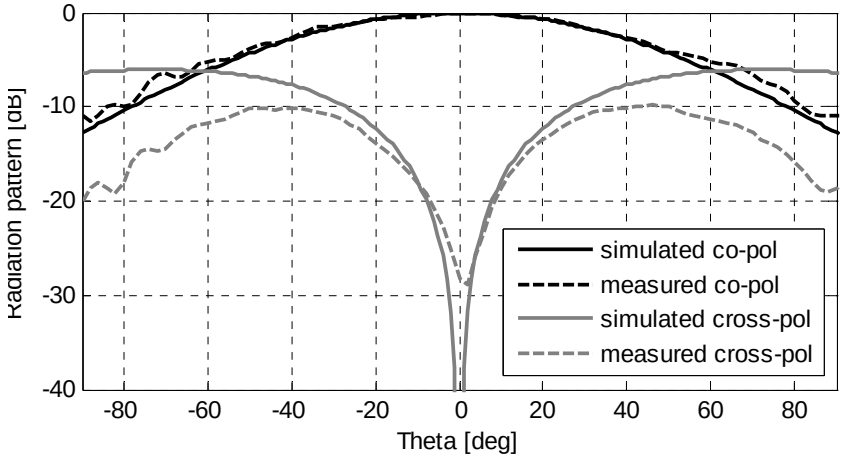

(*b*)

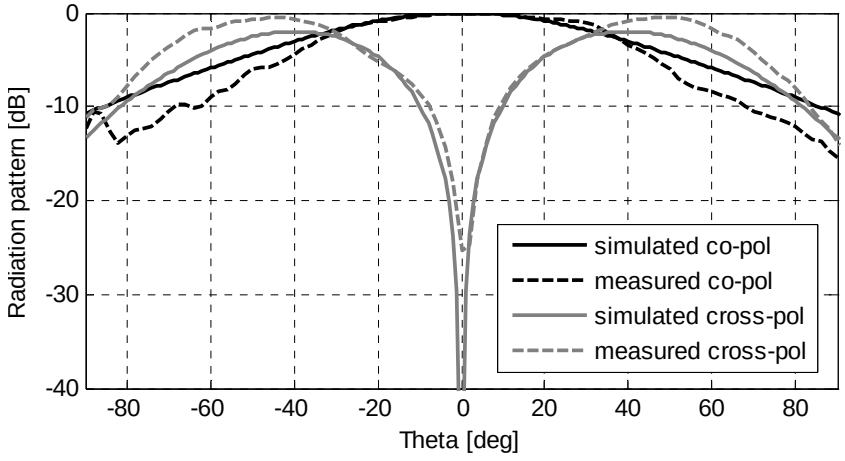

(*c*)

Figure 2.27 Normalized co-polarized and cross-polarized patterns for H-plane (XOZ plane) at (*a*) 7 GHz, (*b*) 10 GHz, and (*c*) 12 GHz

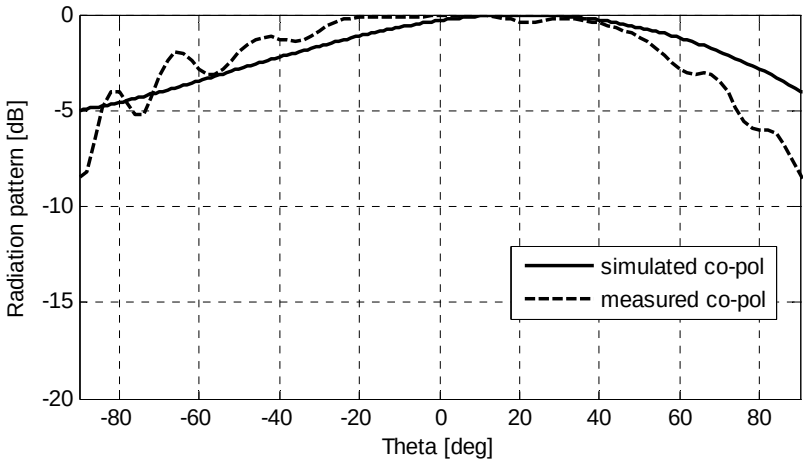

(*a*)

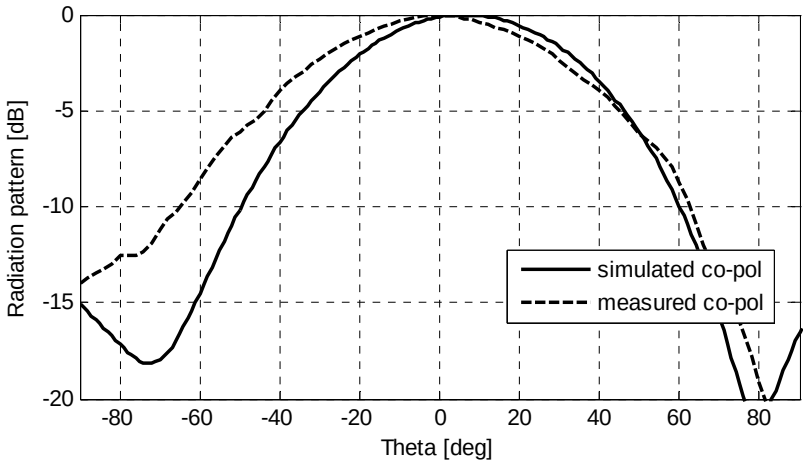

(*b*)

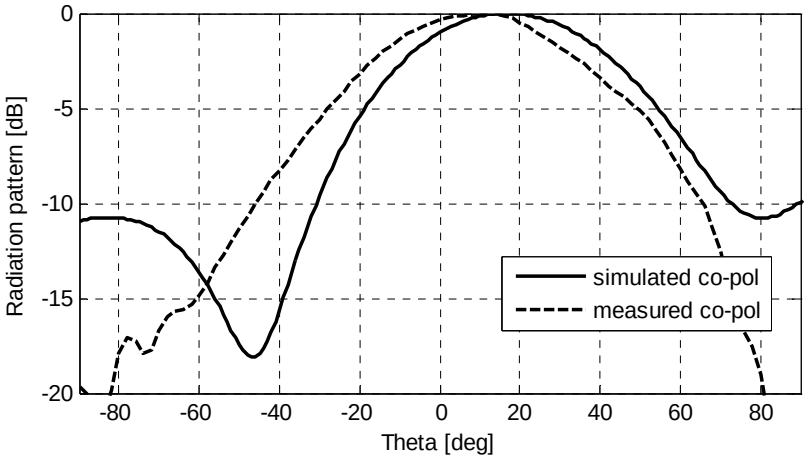

(*c*)

Figure 2.28 Normalized co-polarized and cross-polarized radiation patterns along the E-plane (XOZ plane) at (*a*) 7 GHz, (*b*) 10 GHz, and (*c*) 12 GHz

2.2.3.4. Group delay and antenna gain

In addition to the impedance bandwidth, the time-dispersive characteristic of an antenna structure is also of prime interest for UWB operation [37]. Deviations in the group delay should be much smaller than the duration of an actual or synthesized time-domain pulse fed to an antenna to conserve the shape of the radiated pulse. The group delay (τ_d) of the radiated field is the negative derivative of the far-field phase response (ϕ) with respect to frequency (f):

$$\tau_d = -\frac{1}{2\pi}\frac{\partial\phi}{\partial f}, \tag{2.5}$$

In Figure 2.29, the group delay in the boresight direction is presented for an observation point in the Far-field region. The phase characteristic of this antenna configuration is close to linear in the frequency band between 6 GHz and 10 GHz, and hence the deviations in the group delay curve are smaller than the duration of a synthesized pulse over this bandwidth (of about 250 ps). Due to the above mentioned resonances (at around 10 GHz and 12 GHz) the phase characteristic exhibits nonlinear behaviour around these frequencies, resulting in some variations of the group delay.

Besides the group delay, the antenna gain variation determines the pulse-preserving capabilities. From the system point of view, only the antenna realized-gain is of importance as it determines the field actually radiated by the antenna embedded into the system. Unlike standard IEEE gain, the realized gain (also known as modified gain) considers any reflection occurring at the feeding location.

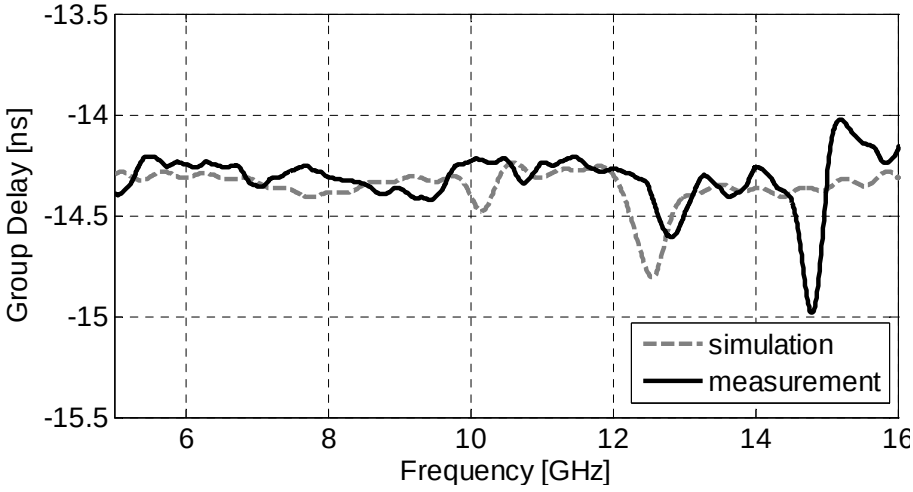

Figure 2.29 Group delay of the X-band antenna element

In Figure 2.30, the broadside antenna gain is plotted as a function of frequency. In this case, the measured gain is the realized-gain as the reflection of the feeding location is not calibrated. Figure 2.30 demonstrates that the measured co-polarized gain resembled very well the simulated result. The simulated cross-polarized gain in the broadside direction is extremely low (in practice, values around the numerical errors of simulations are observed) due to antenna symmetry and therefore has not been included in Figure 2.30. The broadside gain is larger than 3 dB over a frequency range of about 3 GHz and around 11 GHz the antenna gain reaches its maximum value of 7 dB.

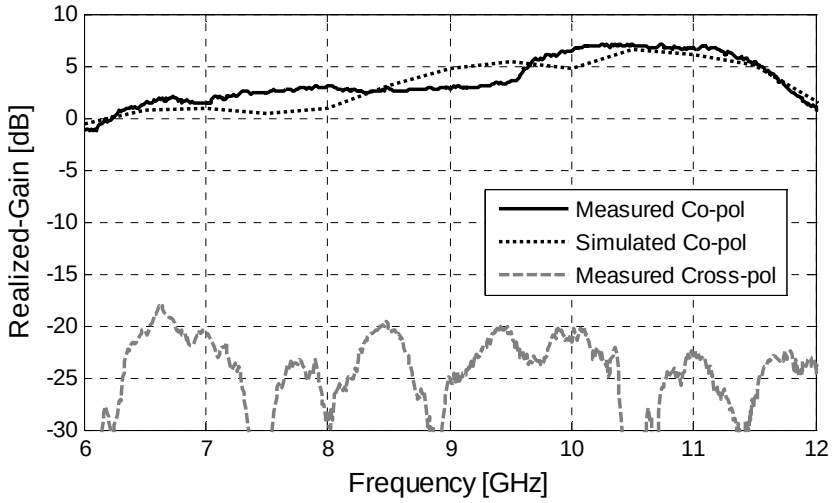

Figure 2.30 Broadside gain against frequency for the X-band element

2.3 CONCLUSION

IN this chapter, we have developed wideband antenna elements suitable for array applications. In order to achieve the wide operational band, two features were thoroughly investigated: *the antenna feeding section* and *the radiating structure*.

The proposed wideband feeding structure for a patch antenna is made of a via-pin fence. This fence encircles the feeding probe to reduce spurious feed inductance of planar antennas. The proposed feeding structure works very efficiently for planar antennas printed on thick microwave substrates and is an attractive solution for phased array applications in microstrip technology where the antenna elements should be fed directly from the back side of the ground plane. In comparison with a simple capacitively-fed patch [18-20], the blind-via fence provides a larger operational bandwidth. However, the manufacturing cost can be also higher. An advantage of using the blind-via structure is the possibility to bring the DC power to the radiating

element, particularly useful for controlling the switch bias voltages of reconfigurable elements. In comparison with other capacitive coupled feeds, such as L-shaped and T-shaped probe, the proposed concept reduces the realization complexity and thereby the manufacturing cost.

Impact of the fence diameter, height, number of pins and their diameters on the antenna performance were analysed and based on this analysis the design guidelines for the fence were proposed. The guidelines were verified on another patch antenna designed for a different frequency band. Results showed that the fence increases the fractional bandwidth of the considered narrow band microstrip antenna to more than 20% (for $|S_{11}| \leq -10dB$) and the relevant 3-dB gain bandwidth to about 30%, which is an enormous improvement of the bandwidth achieved by a conventional microstrip antenna.

Furthermore, mutual antenna coupling in an array configuration was shown to be decreased by at least 3-dB in H-plane and stability of the radiation patterns over the operational band was demonstrated. Last but not least, the geometrical parameters of the fence were proposed to be a design parameter to control the desired operational bandwidth.

In order to expand the bandwidth by influencing the radiating structure, a proper combination of the electric field radiator (patch) with a magnetic field radiator (loop around the patch) was exploited. A planar, directive antenna structure with large fractional bandwidth was introduced in this chapter. A detail discussion on the proposed antenna topology and its architecture was reported. In addition, a novel wideband orthogonal transition from the coaxial to the coplanar line was developed to realize the feeding. This back-feeding mechanism made the proposed design suitable for array applications.

The theoretical and experimental results are compared and it is demonstrated that the element features over 40% fractional impedance bandwidth (for $|S_{11}| \leq -10dB$), larger than 20% 3-dB gain bandwidth, unidirectional (with the front-to-back ratio of about 12 dB) and stable radiation patterns. Another distinctive feature of this design is its high time-dispersive quality. The variations of the group delay is less than 0.25 ns within the frequency band from 6 GHz and 10 GHz and less than 1 ns within the whole operational band. Therefore, the proposed radiator is an attractive candidate for radar-based sensors.

BIBLIOGRAPHY

[1] H. Schantz, *The Art and Science of Ultrawideband Antennas,* Norwood, MA, U.S.A.: Artech House, 2005.

[2] S. Hong, S. Kim, M.R. Coutant, C.T. Rodenbeck and K. Chang, "A multiband, compact, and full-duplex beam scanning antenna transceiver system operating from 10 to 35 GHz", *IEEE Trans. Antennas Propagat.*, vol.54, no.2, pp.359-367, Feb. 2006.

[3] D. H. Schaubert, A.O. Boryssenko, A. van Ardenne, J.G. Bij de Vaalte, and C. Craeye, "The square kilometer array (SKA) antennas", in *Proc. IEEE Intl. Symp. on Phased Array Systems and Technology,* Boston, MA, U.S.A., Oct. 14-17, 2003, pp. 3514-358.

[4] D. Tallini, A. Galli, M. Ciattaglia, L. Infante, A. De Luca, and M. Cicolani, "A new low-profile wide-scan phased array for UWB applications", *2nd European Conference on Antenna and Propagation (EuCAP)*, Edinburgh, UK, November 2007.

[5] R. Erickson, R. Gunnarsson, T. Martin, L. –G. Huss, L. Pettersson, P. Andersson and A. Ouacha, "Wideband and Wide Scan Phased Array Microstrip Patch Antennas for Small Platforms", *2nd European Conference on Antenna and Propagation (EuCAP)*, Edinburgh, UK, November 2007.

[6] R. Garg, P. Bhartia, I. Bahl, and A. Ittipiboon, *Microstrip Antenna Design Handbook,* Norwood, MA: Artech House, 2001.

[7] R. Azadegan, "A Ku-band planar antenna array for mobile satellite TV reception with linear polarization", *IEEE Trans. Antennas Propagat.*, vol. 58, pp. 2097–2101, June 2010.

[8] A. C. K. Mak, C. R. Rowell and R. D. Murch, "Low cost reconfigurable Landstorfer planar antenna array", *IEEE Trans. Antennas Propagat.*, vol. 57, pp. 3051–3061, Oct. 2009.

[9] W. S. T. Rowe and R. B. Waterhouse, "Edge-fed patch antennas with reduced spurious radiation", *IEEE Trans. Antennas Propagat.*, vol. 53, pp. 1785–1790, May 2005.

[10] Y. X. Guo, K. M. Luk and K. F. Lee, "L-probe proximity-fed annular ring microstrip antennas", *IEEE Trans. Antennas Propagat.*, vol. 49, pp. 19–21, Jan. 2001.

[11] K. S. Kona and Y. Rahmat-Samii, "Novel probe-feeding architecture for stacked microstrip antennas", *Microwave and Optical Tech. Letters*, vol. 38, pp. 467–475, Sep. 2003.

[12] M. Manteghi, "Wideband microstrip patch antenna on a thick substrate", *IEEE Antennas and Propagation Society International Symposium*, pp. 1-4, Jul. 2008

[13] K.-L.Wong and T.-W. Chiou, "Broad-band single-patch circularly polarized microstrip antenna with dual capacitively coupled feeds", *IEEE Trans. Antennas Propag*., vol. 49, pp. 41–44, Jan. 2001.

[14] C. L.Mak, K.M. Luk, K.-F.Lee, andY.-L. Chow, "Experimental study of a microstrip patch antenna with an L-shaped probe", *IEEE Trans. Antennas*

Propag., vol. 48, no. 5, pp. 777–783, May 2000.

[15] C. L. Mak, K. M. Lee, and K. M. Luk, "Broadband patch antenna with a T-shaped probe", Proc. Inst. Elect. Eng. Microwave Antenna Progation, vol. 147, pp. 73–76, Apr. 2000.

[16] P. H. Rao, V. F. Fusco, and R. Cahill, "Wide-band linear and circularly polarized patch antenna using a printed stepped T-feed", *IEEE Trans. Antennas Propag.*, vol. 50, no. 3, pp. 356–361, Mar. 2002.

[17] M. A. Gonzalez de Aza, J. Zapata, and J. A. Encinar, "Broad-band cavity-backed and capacitively probe-fed microstrip patch arrays", *IEEE Trans. Antennas Propag.*, vol. 50, no. 9, pp. 1266–1273, Sep. 2002.

[18] G. A. E. Vandenbosch and A. R. Van de Capelle, "Study of the capacitively fed microstrip antenna element", *IEEE Trans. Antennas Propagat.*, vol. AP-42, pp. 1648-1652, Dec. 1994.

[19] G. A. E. Vandenbosch, "Capacitive matching of microstrip antennas", *Electronics Letters*, vol. 31, no. 18, pp. 1535-1536, Aug. 1995.

[20] G. A. E. Vandenbosch, "Network model for capacitively fed microstrip element" *Electronics Letters*, vol. 35, no. 19, pp. 1597-1599, Sep. 1999.

[21] A. C. Ludwig, "Wire grid modeling of surfaces", *IEEE Trans. Antennas Propag.*, vol. AP-35, no. 9, pp. 1045–1048, Sep. 1987.

[22] A. Petosa, A. Ittipiboon, and N. Gagnon, "Suppression of unwanted probe radiation in wideband probe-fed microstrip patches", *Electron. Lett.*, vol. 35, pp. 355–357, Mar. 1999.

[23] I. E. Lager, and M. Simeoni, "Experimental investigation of the mutual coupling reduction by means of cavity enclosure of patch antennas", *1st European Conf. on Antennas Propag.*, Nice, Nov. 2006.

[24] J. Rahola, and J. Ollikainen, "Analysis of Isolation of Two-Port Antenna Systems using Simultaneousmatching, " *2nd European Conference on Antenna and Propagation (EuCAP)*, Edinburgh, UK, Nov. 2007.

[25] W. Runge, "Polarization diversity reception", U.S. patent 1892221, Dec. 1932.

[26] D.-H. Kwon, E.V. Balzovsky, Y.I. Buyanov, Y. Kim, and V.I. Koshelev, "Small printed combined electric-magnetic type ultrawideband antenna with directive radiation characteristics", *IEEE Trans. on Antennas and Propagat.*, vol. 56, pp. 237-241, Jan. 2008.

[27] E.G. Farr, C.E. Baum, W.D. Prather, and L.H. Bowen, "Multifunction impulse radiating antennas: theory and experiment", *Ultra-Wideband Short-Pulse Electromagnetics,* pp. 131-144, 1998.

[28] F.M. Tanyer-Tigrek, I.E. Lager, and L.P. Ligthart, "A CPW-Fed Printed Loop Antenna for Ultra-Wideband Applications, and its Linear-Array Performance", *IEEE Trans. on Antennas and Propagat.*, vol. 52, pp. 31-40, Aug. 2010.

[29] H.-C. Liu, T.-S. Homg, and N.G. Alexopoulos, "Radiation of printed antennas with a coplanar waveguide feed", *IEEE Trans. on Antennas and Propagat.*, vol. 43, pp. 1143-1148, Oct. 1995.

[30] P. Li, J. Liang, and X. Chen, "Study of printed elliptical/circular slot antennas

for ultrawideband applications", *IEEE Trans. on Antennas and Propagat.*, vol. 54, pp. 1670-1675, Jun. 2006.

[31] Y.-C. Lin and K.-J. Hung, "Compact ultrawideband rectangular aperture antenna and band-notched designs", *IEEE Trans. on Antennas and Propagat.*, vol. 54, pp. 3075-3081, Nov. 2006.

[32] F. Consoli, F. Maimone, and S. Barbarino, "Study of a CPW-fed circular slot antenna for UWB communications", *Microwave and Optical Techonology Letters,* vol. 48, pp. 2272-2277, 2006.

[33] D.P. Tran, F.M. Tanyer-Tigrek, I.E Lager, and L.P.Ligthart, "A Novel Unidirectional Radiator with Superb UWB Characteristics for X-band Phased Array Applications", *3rd European Conference on Antenna and Propagation: (EuCAP*), Berlin, Germany, 2009.

[34] R.N. Simons, *Coplanar Waveguide Circuits, Components and Systems*, New York: John Wiley & Sons, Inc., 2001.

[35] B. Munk and C. Larson, "A broadband cavity antenna with a steerable cardioid pattern", *Antennas and Propagate. Society Intl. Symp.* vol. 18, pp. 298-301, 1980.

[36] C.A. Balanis, *Antenna Theory, Analysis and Design,* Third Edition, New Jersey: John Wiley & Sons, pp. 819, 2005.

[37] D.-H. Kwon, "Effect of antenna gain and group delay variations on pulse-preserving capabilities of ultrawideband antennas", *IEEE Trans. on Antennas and Propagat.*, vol. 54, pp. 2208-2215, Aug. 2006.

CHAPTER 3

FREQUENCY RECONFIGURABLE L/S-BAND PHASED ARRAY ANTENNA ELEMENT

This chapter is devoted to frequency reconfigurable antennas with electronic switches. The antenna concept is based on changing the electrical size of the structure by means of p-I-n diode switches. The antenna element satisfies strict requirements on its frequency ratio, size, feeding structure and control lines to be integrated into a phased array system.

Parts of this chapter have been published in the following proceedings:

[C2] N. Haider, D.P. Tran, and A.G. Yarovoy, "A new concept for frequency reconfigurable phased-array element", *Proc. Loughborough Antennas and Propagation Conference (LAPC)*, pp.1-4, Nov. 2011.

[C4] N. Haider, A.G. Yarovoy, and D. Caratelli, "Frequency switchable L/S-Band antenna element", *Proc. 7th European Conference on Antennas and Propagation (EuCAP)*, Gothenburg, Sweden, Apr. 2013.

THIS chapter deals with the second research approach among the three approaches of reconfigurable elements addressed in chapter one (Section 1.6): *antenna systems with embedded switches*. The concept presented here can be used to switch the frequency between two (radar) bands and is complementary to the approach discussed in Chapter 2. The antenna element discussed in this chapter is capable of providing frequency reconfiguration by changing its electrical size. This change is realized by integrating electronic switches (p-I-n diodes) with the radiating structures. This approach reduces the requirements of the front-end filter compared to a wideband or multi-band antenna. Wideband antennas (discussed in Chapter 2) enforce severe requirements on the filters when frequency reconfiguration is desired. For frequency reconfigurable elements only the selected bands remain active at each time and therefore a diplexer to reject the non-active band is not required.

One of the aims of this study is to develop an antenna which can switch its operational bands according to the mission requirements of adaptive phased array radar systems. A low operational frequency usually allows a better coverage in range while a higher operating frequency can permit a better resolution. As the operating frequency bands of the antenna element, L- and S- radar bands were selected, which are separated over a very large frequency range with a frequency ratio of more than 2:1. Such an antenna element is required for future radar systems which will need the capability of both long and medium range surveillance. Maintaining good antenna performances in these broadly separated frequency bands brings major conceptual and design challenges.

Recently reconfigurable antennas (RAs) with RF-switches have gained high research interest for many different purposes [1-16] (a detailed state-of-the-art is discussed in Chapter 1). However, most of these antennas are not intended for array application. Furthermore, the frequency coverage of these antennas is not sufficient for an octave frequency ratio. Design of a frequency reconfigurable antenna element is a challenge on its own. Additional demands of a limited size (to be embedded into a phased array) and good antenna performance within (largely separated) multiple frequency bands make the problem very challenging. In this chapter the design of a frequency reconfigurable element, based on a novel adaptive antenna-aperture concept, is discussed. The proposed concept involves geometrical reconfiguration of each radiating cell of a phased array antenna with the use of RF-switches. The distinctive properties of the proposed approach are its array compatibility, extremely large frequency ratio and well defined radiation and circuital characteristics in both bands. Most reconfigurable antennas have highly complex dc bias arrangement.

Novelty of this work also lies in reducing this complication by controlling the switches by using the radiating structure itself to carry the DC biasing signals.

The chapter is structured as follows. Section 3.1 comments on the antenna concept used to realize frequency reconfiguration for a multi-band phased array. This section also contains the detailed parameter analysis. In this analysis the switches are modelled as ideal ones. In Section 3.2 the implementation of a real switch is carried out. The selection of the switch and the method of the numerical analysis of the switch are detailed in Sections 3.2.1 and 3.2.2, respectively. The DC-bias circuit is discussed in Section 3.2.3. Section 3.3 contains a description of the antenna prototype and highlights the measured results. Conclusions are stated in Section 3.4.

3.1 THE FREQUENCY RECONFIGURABLE L/S-BAND ANTENNA ELEMENT

RECONFIGURABLE antennas possess the properties to modify the relevant circuital characteristics and/or radiation properties in real time. The implementation of several functionalities on the same antenna requires topological reconfigurability. In particular, parameters such as the shape and the size of the antenna should be changed to adapt to the requirements set by the considered functionality. To design a frequency-reconfigurable antenna element for phased array

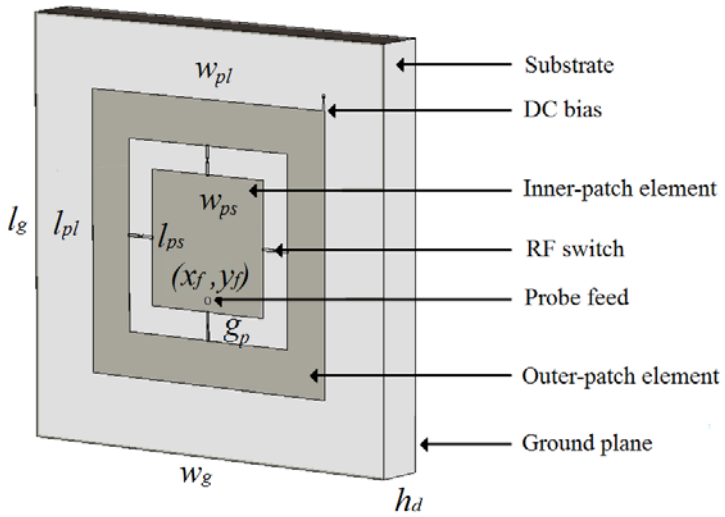

Figure 3.1 The geometry of the reconfigurable antenna. Geometrical characteristics of the structure: $w_{ps} = l_{ps} = 24$mm, $w_{pl} = l_{pl} = 50$mm, $l_g = w_g = 75$mm, $h_d = 9.144$mm, $g_p = 5$mm, $x_f = 0$mm, $y_f = -10$ mm.

application, a new concept is investigated and discussed in this section. In this methodology a square-ring loaded probe-fed patch antenna has been used. The following sections discuss the operational and design principles of this antenna.

Figure 3.1 illustrates the basic geometry of the structure. As can be seen from this figure, a dual-patch is used for frequency switch between L-band and S-band. The reconfigurability is realized by controlling the state of the RF switches and thereby changing the electrical size of the structure.

In Figure 3.2, the operational principle of the antenna is illustrated. When the switches are in CLOSED state the outer metal ring is connected to the inner patch and the antenna radiates in the lower frequency band (Figure 3.2(a)). When the switches are in OPEN state the metal ring is detached from the inner patch (Figure 3.2(b)) and it acts as a parasitic element. In this way, antenna operation in the higher frequency band is achieved.

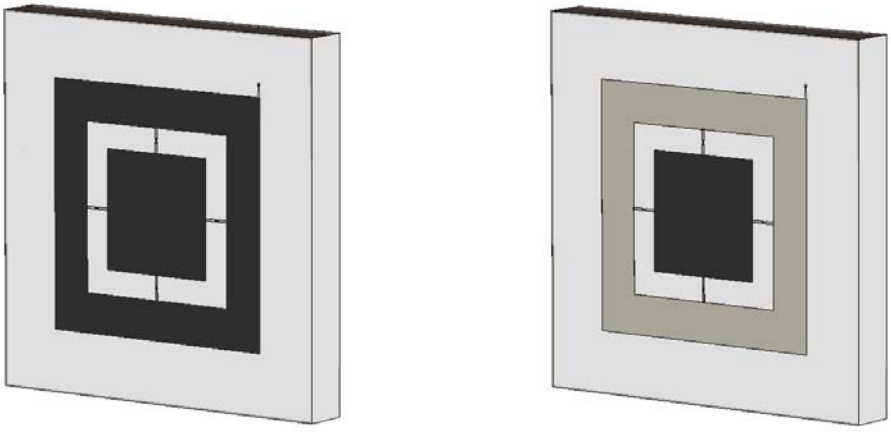

(a) (b)

Figure 3.2 The operation principle, (a) L-band operation mode, (b) S-band operation mode. Here, the black areas outline the radiating parts and the grey areas outline the non-radiating parts of the antenna element.

An inherent challenge associated with reconfigurable antennas is to achieve good antenna performance in various operational modes. As mentioned earlier, the challenge to meet this requirement becomes more intense for L/S-band phased array element due to the large separation between the radar bands. Therefore, dedicated analyses were carried out in order to investigate the effects of different geometrical parameters of the antenna structure, e.g. length, width and feed position. By careful optimization of the antenna structure the operational bands have been shifted within the allocated radar bands. The following section discusses the geometrical parameter analysis in detail. The antenna is modelled on RO4003C substrate having a relative

permittivity $\varepsilon_r = 3.5$. The thickness of the dielectric substrate has been set to $\lambda_{dh}/6$, where λ_{dh} is the wavelength in the dielectric material at the highest operating frequency. The simulations are performed by using CST microwave Studio which utilizes the Finite Integration Technique for electromagnetic computation.

3.1.1. The radiating structure

A microstrip antenna operating in S-band was selected as the radiating element for the higher operational band. The S-band patch length (l_{ps}) and patch width (w_{ps}) were selected to be roughly $\lambda_d/2.2$, where λ_d is the wavelength in the dielectric material at 3 GHz. The thickness of the dielectric material (h_d) was 9.144 mm.

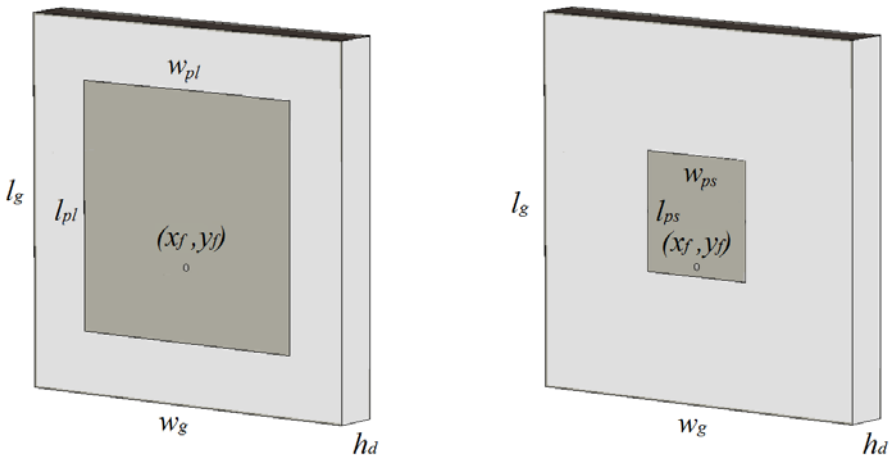

(a) (b)

Figure 3.3 Conventional microstrip antenna element, (a) L-band element, (b) S-band element. Geometrical characteristics of the structure: $w_{ps} = l_{ps} = 24$mm, $w_{pl} = l_{pl} = 50$mm, $l_g = w_g = 75$mm, $h_d = 9.144$mm, $x_f = 0$mm, $y_f = -10$ mm

For the lower operational band (L-band), a square ring encircling the inner-patch was used as shown in Figure 3.2 (a). When the RF switches are in CLOSED state this outer ring becomes a part of the radiating structure. This radiating structure then impersonates an L-band microstrip antenna incorporated with slots. It is worth mentioning here that both radiating structures are symmetric along the principal planes ($l_{ps} = w_{ps}$ and $l_{pl} = w_{pl}$). Such a design approach will ease the transformation to a dual-linearly polarised element by inserting a second feeding probe.

As opposed to a conventional microstrip antenna element (see Figure 3.3) here the S-band antenna element is accompanied by an outer parasitic metal ring. In

addition, the geometry of the L-band element diverges from a conventional microstrip antenna due to the presence of the RF switches and the slots between two patches. In this section the effect of these entities on the reflection coefficient and the radiation patterns are displayed and compared with the conventional microstrip antennas. The reference conventional microstrip elements had the same dimension as the reconfigurable antennas as outlined in Figure 3.3. Section 3.2 and Section 3.3 further discusses the effect of the RF-switches and their bias line on the antenna performance.

In Figure 3.4, the reflection coefficients of the conventional microstrip antennas (shown in Figure 3.3) and the reconfigurable antennas (shown in Figure 3.2) are compared. In Figure 3.4(a), we notice a slight shift of the dominant mode towards the lower frequency range in comparison with the conventional patch. This shift of the operational band is caused by the presence of the slots which create additional path lengths for the surface current. This helps to set the operating band within the intended radar L-band (1.2 – 1.4 GHz). On the contrary, for the reconfigurable element the bandwidth decreases from 80 MHz to about 50 MHz. For the reconfigurable antenna the optimal feeding location of the probe had to be compromised in order to have adequate matching for both operational modes. Furthermore, in Figure 3.4(a) we observe that the higher order harmonics of the L-band patches shifts towards the lower band because of the slots. Here, the second harmonic shifts from 2.8 GHz (for the conventional microstrip antenna) to 2.3 GHz. As a result, the higher order harmonic of the L-band remains outside the operational band of the S-band antenna.

In Figure 3.4(b), the reflection coefficients of the conventional S-band patch and the reconfigurable element are plotted. Similarly to the lower operation mode here the antenna bandwidth reduces for the reconfigurable element for the same reason discussed earlier. Here, the bandwidth reduces from 220 MHz to 170 MHz. We notice that the presence of the outer ring generates a dual-band matching in S-band. However, above 3.3 GHz the antenna element has poor radiation properties. Therefore, only the band close to 3 GHz is considered in the further analysis. Figure 3.4(b) also indicates an additional local minimum in the $|S_{11}|$ curve around 1.15 GHz due to the weak resonating effect of the parasitic L-band ring. The antenna structure was carefully optimized to bring this spurious radiation outside the lower operation band.

In Figure 3.5 and Figure 3.6, the radiation performances of the conventional microstrip antennas and the reconfigurable antennas are evaluated. Figure 3.5 presents

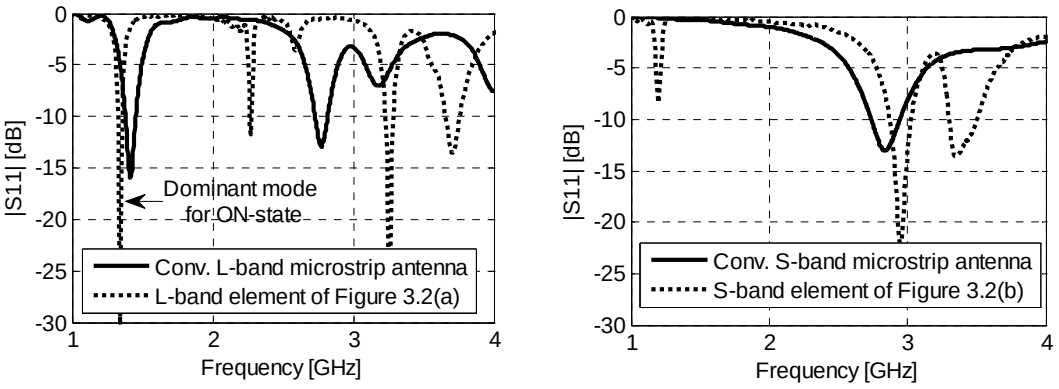

Figure 3.4 Reflection coefficients of conventional microstrip antennas and reconfigurable antennas for L-band operational mode (a) and for S-band operational mode (b).

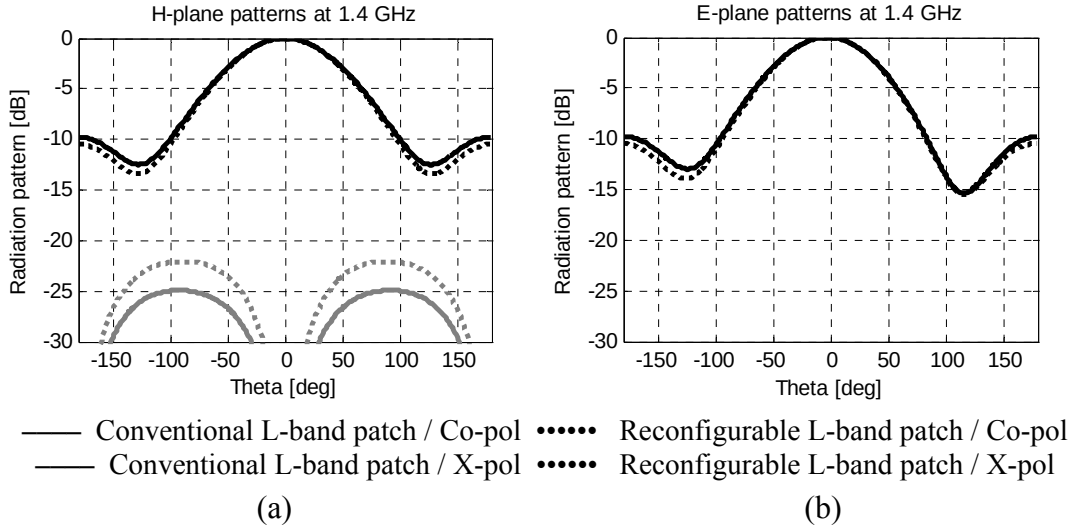

Figure 3.5 Radiation patterns for L-band operational mode, (a) H-plane, (b) E-plane.

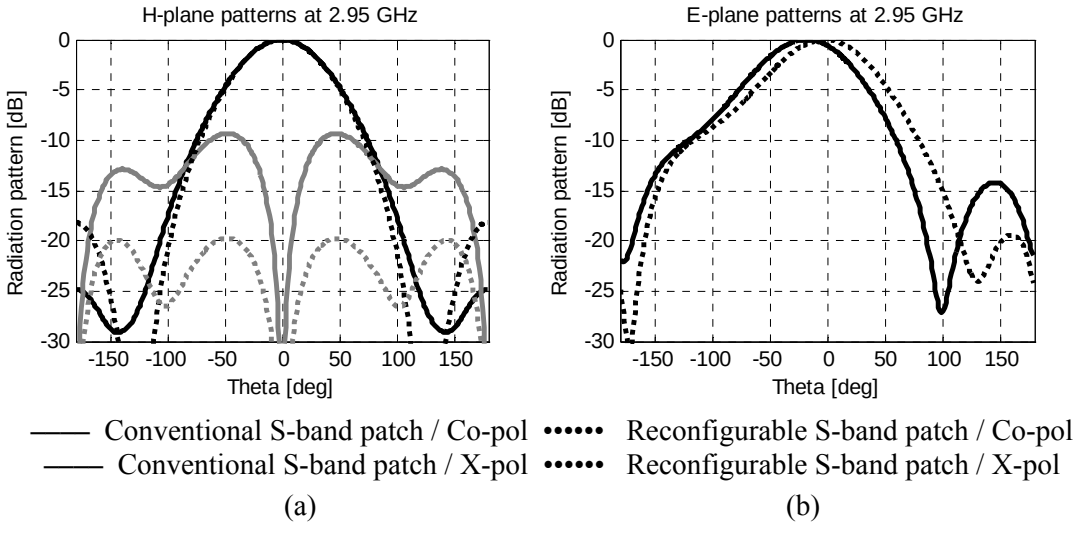

Figure 3.6 Radiation patterns for S-band operational mode, (a) H-plane, (b) E-plane.

the antenna radiation patterns in the lower band (L-band) and indicates that for the reconfigurable element the polarisation purity degrades slightly in the H-plane because of the diversion of the surface currents.

Figure 3.6 reveals the antenna radiation patterns in the higher band (S-band). In Figure 3.6(a), we observe that the conventional microstrip antenna has higher cross-polarisation level due to the monopole like spurious radiation of the probe feed (discussed in detailed in Chapter 2). In the E-plane this unwanted radiation introduces asymmetry in the radiation patter (see Figure 3.6(b)) [17]. For the reconfigurable element, the presence of the L-band ring partially suppresses the probe radiation. Therefore, the cross-polarisation level decreases along H-plane (about 10 dB reduction of the peak value) while the pattern symmetry improves along the E-plane.

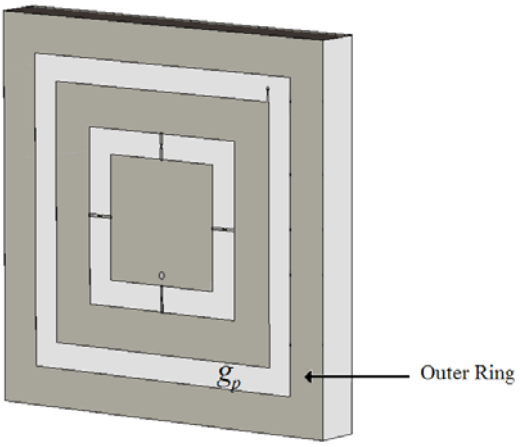

Figure 3.7 The reconfigurable antenna with ground ring

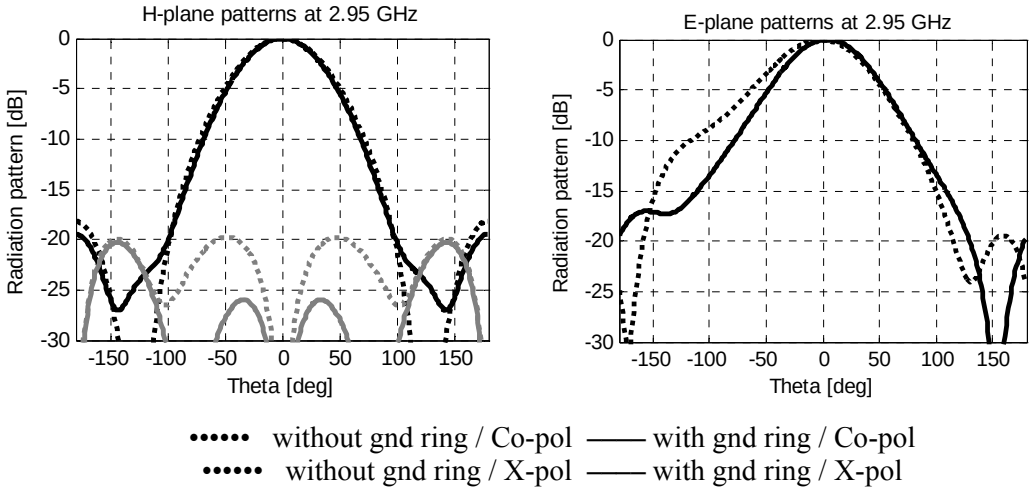

Figure 3.8 The effect of the floating ground ring on the H-plane (a) and the E-plane (b) radiation patterns of the reconfigurable S-band element

A further reduction of the probe effect can be obtained by an additional ground ring as shown in Figure 3.7. The gap between the L-band ring and this floating ground ring was set to g_p = 5 mm. Figure 3.8 illustrates this effect of the floating ground ring on the radiation patterns. Here, the peak cross-polarisation level decreases another 5 dB (see Figure 3.8(a)) and pattern symmetry further improves (see Figure 3.8(b)). Note that this outer ring had negligible effect on the input-reflection coefficients.

The gap between the patches (g_p in Figure 3.1) also affects the antenna performances. In Figure 3.9 and Figure 3.10, this effect is highlighted. A large gap size increases the deformation of the L-band patch from its conventional structure while decreasing this value increases the parasitic effect of the outer ring on the S-band element. The L-band ring acts as a parasitic structure during the S-band operation and weakly radiates. The amount and the frequency of this unwanted radiation are directly influenced by the gap (g_p) between the patches. Figure 3.9 illustrates that a larger gap width (g_p) favourably decreases the matching condition of this unwanted radiating band. In this case, a larger separation between the metal structures reduces the parasitically induced currents. In addition, a larger gap also shifts this parasitic resonating band towards the lower band owing to the increased electrical path of the fringing fields. This phenomenon has been exploited to move the unwanted radiating band outside the allocated radar L-band (1.2 – 1.4 GHz).

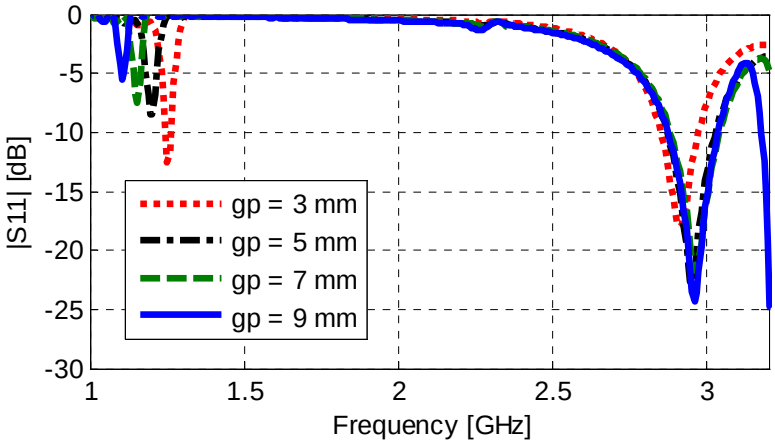

Figure 3.9 The effect of the gap width (g_p) on the input-reflection coefficient of for the S-band operational mode

The gap width (g_p) naturally also influences the radiation characteristics of the L-band operation during switch ON-state. Particularly, the cross-polarisation level increases with gap width due to the structural deformation as shown in Figure 3.10.

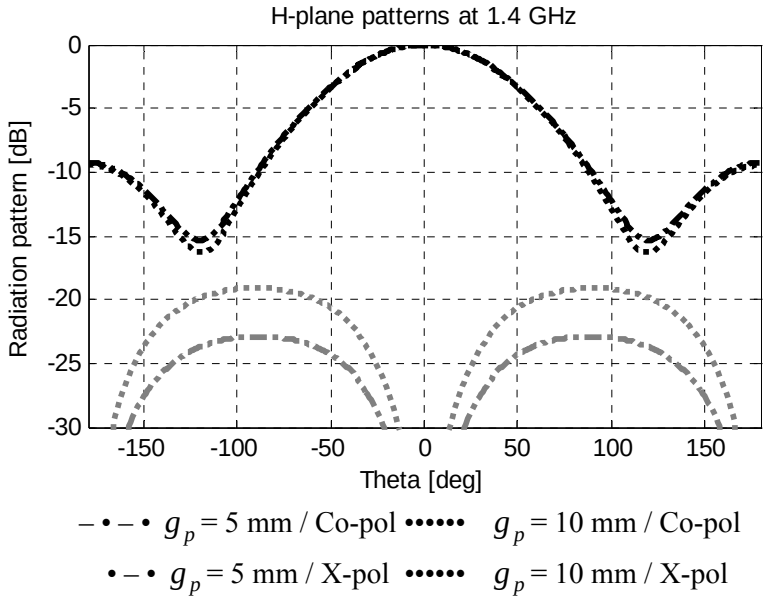

Figure 3.10 The effect of the gap width (g_p) on the polarisation purity of the L-band operational mode

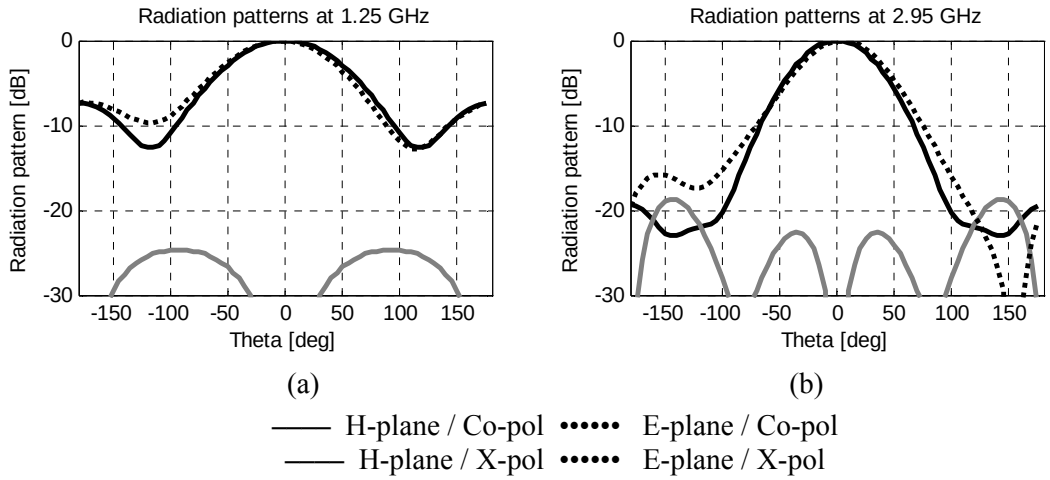

Figure 3.11 Radiation patterns of the reconfigurable element at OPEN state for $g_p = 3mm$ at 1.25 GHz (a) and 2.95 GHz

A gap width of 5 mm ensures a suitable trade-off between the above mentioned contradicting phenomena. For this gap width, the parasitic resonance of the S-band operation occurs at about 1.15 GHz while the cross-polarisation isolation of the L-band remains higher that 19 dB for the entire scan volume.

It is worth noting here that Figure 3.9 reveals the potentials of the considered reconfigurable antenna as a simultaneous dual-band radiating element with a single feeding structure. For such realization, a gap width (g_p) of 3 mm or smaller will assure sufficient radiation efficiency in both bands. In Figure 3.11, the radiation

patterns of the element are shown for $g_p = 3mm$. Here, we observe a stable radiation patterns for both operational bands.

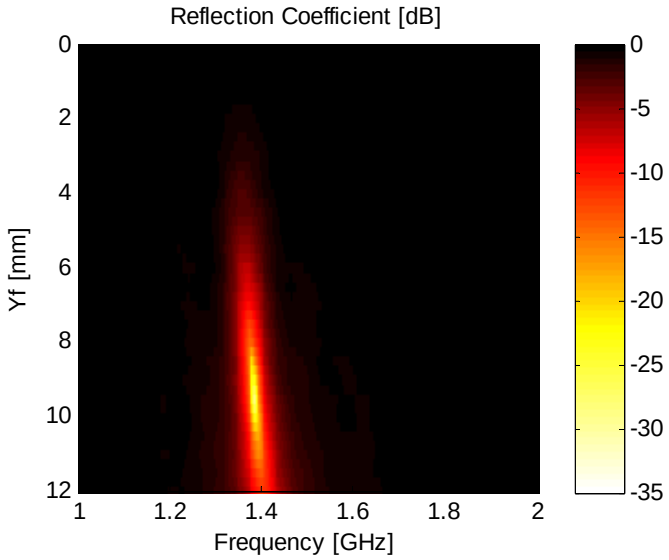

(a)

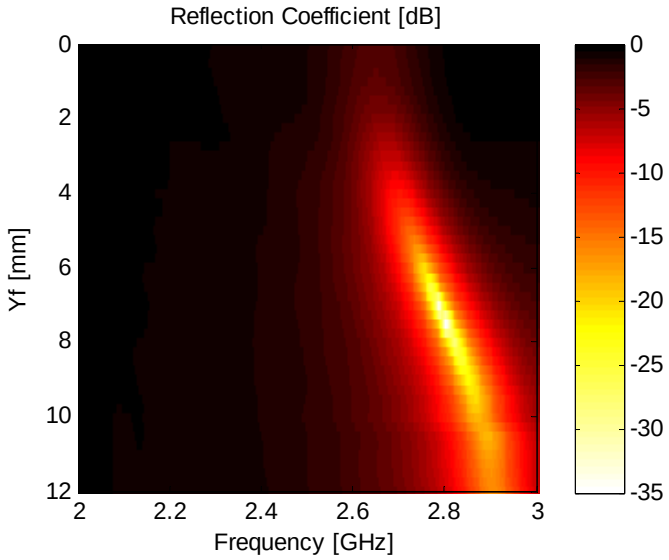

(b)

Figure 3.12 Frequency-domain behaviour of the input-reflection coefficient of the reconfigurable radiator as function of the feeding location (y_f) for L-band operational mode (a) and for S-band operational mode (b).

3.1.2. The feeding structure

For the proposed design, a coaxial probe feed is used as outlined in Figure 3.1. For the reconfigurable antenna the probe feeding mechanism is more suitable than an indirect electromagnetically coupled feed, such as proximity-coupled and aperture-coupled feed. The probe feed can be directly used for both feeding the antenna at radio frequency (*RF*) and controlling the DC-bias voltage affecting the state of the

switches. The use of the feeding probe to provide the DC-bias voltages is further discussed in Section 3.3. Here, the contribution of the probe in radio-frequency domain is presented.

For this study it is expected that the antenna will be directly attached to a RF-frontend having an input impedance of 50 Ω. This means no additional impedance matching steps were intended here and the input-impedance of the antenna needs to be as close as possible to the reference impedance (50 Ω) to satisfy an adequate matching condition. It is well known that the position of the feeding probe directly influences the input-impedance of the antenna [18]. For a dual-band antenna the challenge is to locate a feeding position which brings the input-impedance close to the reference value for both operational modes.

In Figure 3.12(a) and Figure 3.12(b), the parameter analyses of the feeding probe position are illustrated for L-band and S-band, respectively. Along the Y-axis the maximum deviation of the location of the probe from the centre of the inner patch were limited to 12 mm which is half of the length of the inner patch. Furthermore, the value of x_f is set to zero in order to maintain geometrical symmetry along the X-axis. Figure 3.12 clearly indicates that y_f value close to 10 mm ensures a minimum reflection coefficient around 1.38 GHz, while for the S-band mode, the operational bandwidth shifts towards the intended frequency range.

3.1.3. Number of RF switches

The number of the switching devices (N_{sw}) within the radiating structure also plays an important role. For minimum cost and complexity it is crucial to reduce the total amount of RF-switches in the antenna system. On the contrary, larger number of switching components will increase system redundancy and thus also the reliability. Furthermore, sufficient number of switches is needed to reduce alteration of the reconfigurable element structure (especially for the low-band operating mode) in comparison with a conventional microstrip antenna.

In Figure 3.13, the real part of the input-impedance is presented as a function of the total number of the switches for the low-band operational mode. When two switching components, are used the antenna shows very high input-impedance. Here, the input-impedance corresponds to a patch having an effective width of the inner-patch (which is about half of the conventional patch). The input-impedance is inversely proportional to the width. Therefore, a very high input-impedance is noticed for the reconfigurable element with two switching components. The impedance reduces when N_{sw} increases and this helped to match the antenna to the 50 Ω

reference impedance. In addition, numerical results predict minor shift in the resonance band. In this case, the resonating frequency increases with the number of switches due to the decreased current path. Having four switches (in comparison to eight switches) was helpful to shift the operational band below 1.4 GHz.

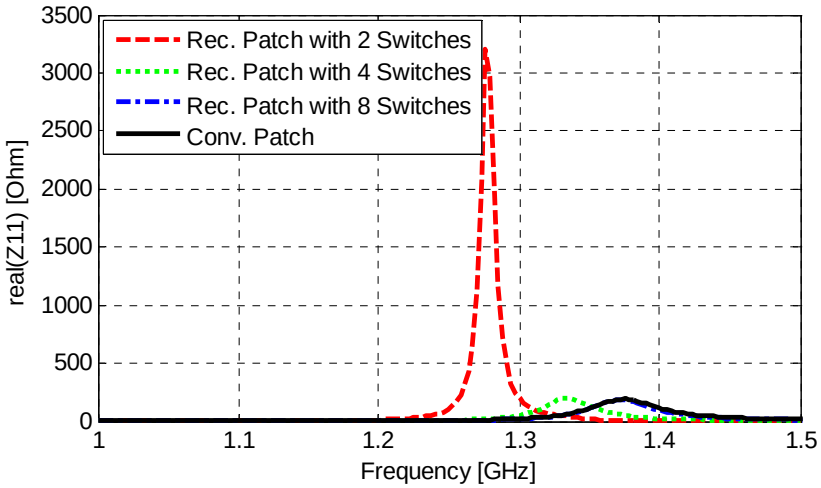

Figure 3.13 The input-impedance of the conventional L-band patch and the reconfigurable element with two, four and eight switches.

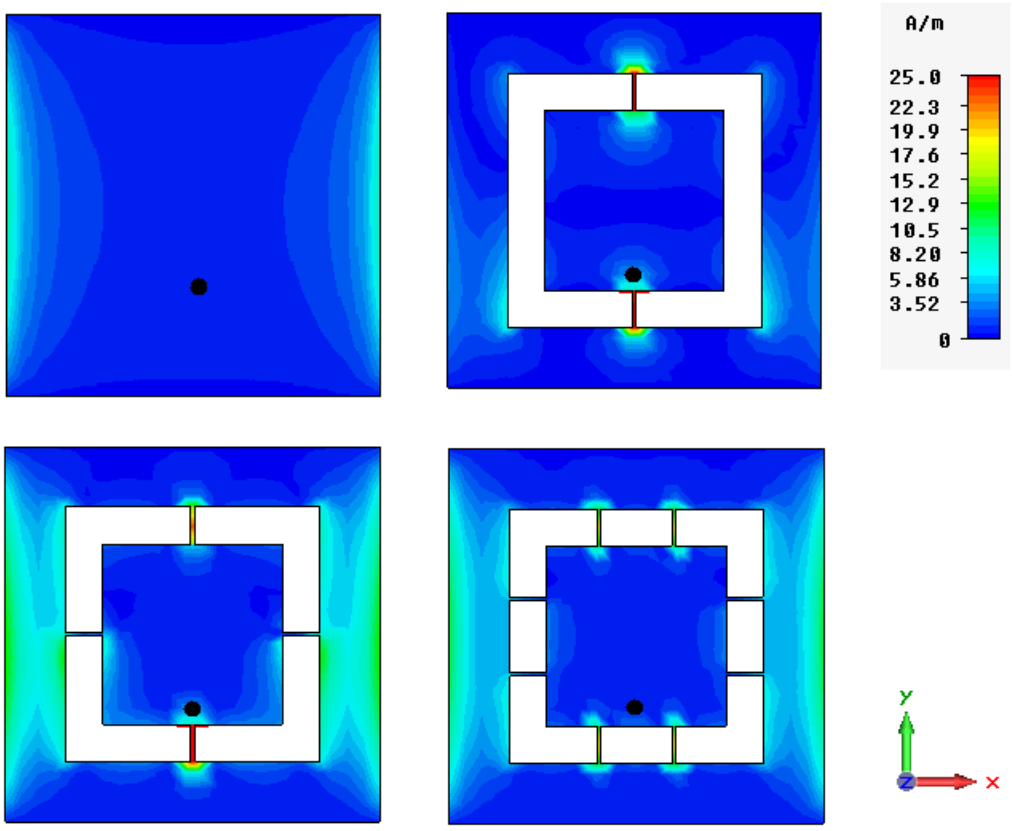

Figure 3.14 Surface current density (Y-component) on the conventional L-band patch and on the reconfigurable element with two, four and eight switches.

Figure 3.14 depicts the surface current density distribution on the antennas for the low-band operating mode. It is evident here that using two switches is not enough to impersonate the surface current distribution of the conventional microstrip patch due to its poor matching condition. With four or eight switching components the current density distribution of the reconfigurable element resembles better to the conventional patch. In the experimental validation of the concept, discussed in the following sections, four switches were used in order to simplify the prototype realization and to reallocate the low band beneath 1.4 GHz. However, it should be noted that increasing the number of switches to eight will enlarge the reliability of the antenna system in case of component failure.

3.2 RF SWITCH IMPLEMENTATION ON THE FREQUENCY RECONFIGURABLE ELEMENT

IN the investigations presented in the previous sections the RF-switches are considered as ideal ones. In this section, the analyses related to the RF-switches are discussed. In particular, the type of RF-switch, integration of these switches into the radiating structure, the DC bias circuit and the numerical model of the switches are addressed.

3.2.1 The selection of the RF switch

Reconfigurable antennas are often realized by employing radio frequency (RF) switches, such as micro electro-mechanical systems (MEMS), varactors and p-I-n diodes [1-14]. These technologies are especially suitable for antennas realized in printed technology. A radiating element in printed technology consists of a metallic surface to which an electric signal can be coupled through a guiding line. Switches, such as p-I-n diodes and RF MEMS, can electrically connect/disconnect metallic parts in order to introduce (discretized) changes in the geometry of the total radiating surface. Here, the power handling capability and the lifetime of the switches are important issues. MEMS switches have some advantages over p-I-n diodes, such as lower insertion loss, lower noise figure, higher quality factor, higher linearity, lower power losses and very little dc power consumption. However, they show higher actuation voltage and longer switching time. Recent advances in MEMS technology enable the realization of MEMS with improved switching speed and compact size (In [19], a switching time of 225 ns has been reported and in [20] MEMS with dimensions as small as few micrometer (μm) have been shown). Despite of many advantages of MEMS many designers still prefer to use semiconductor devices, mainly due to the lack of maturity in MEMS technology and their limited lifetime. Besides p-I-n diode

and MEMS, varactor diodes are often used in reconfigurable antenna designs. Varactors provide a capacitance that can be continuously tuned by acting on the diode bias voltage. In view of this they are typically used as a load to tune the resonance frequency of the antenna element [21], although their low dynamic range is a practical concern. MEMS with capacitance variable in a given range also represent a topic of research [22] but currently available prototypes are not yet sufficiently reliable.

Table 3.1 Comparison of switching components

Tunable Component	Advantages	Disadvantages
MEMS	Low insertion loss, very high isolation, extremely high linearity (IIP3 60–80 dBm theoretically), very low power losses (< 0.2 dB), consumes little or almost no dc power, wide bandwidth.	Poor reliability due to mechanical movement within the switch, slow switching speed (typically 1-300 μs), limited lifecycle, discrete tuning, low power handling capability (<1W), need high-control voltage (50-100 V), complex biasing circuit, expensive.
p-I-n Diode	Very reliable since there are no moving part, needs very low driving voltage (3–5 V), high tuning speed (1 – 100 ns), high isolation, low power losses (0.2-1.5 dB), simple biasing circuit, extremely low cost.	Needs high DC bias current in their on state (10-20 mA), nonlinear behaviour (IIP3 25–50 dBm), medium power handling capability (<10 W), discrete tuning.

A general comparison between MEMS and p-I-n diode switch is provided in Table 3.1. More comprehensive discussions can be found in [23-25]. Taking into account the reliability, switching speed, power handling capability and physical size, the p-I-n diode switches were implemented into the considered reconfigurable radiating element. The selection of the specific p-I-n diode is further discussed below.

The most important parameters that describe the p-I-n diode performance are isolation, insertion loss, power handling limitation, switching speed and maximum operational frequency. Besides, for practical reasons the size and the package type of the components are also important aspects. In view of the above mentioned criteria's two p-I-n diodes are selected for the antenna prototype- (i) GaAs (Gallium Arsenide) beamlead p-I-n diode (MA4AGBLP912 from MA-COM) and (ii) Silicon p-I-n diode (BAP64-02 from NXP).

The thermal resistance of GaAs is about three times higher than silicon. Therefore, the maximum power dissipation of a GaAs p-I-n diode is less than for a

silicon p-I-n diode. However, GaAs p-I-n diodes provide much faster switching speed and less parasitic capacitance. Another advantage of GaAs diode (MA4AGBLP912) is its maximum operational frequency which is above 20 GHz. For silicon diodes this value is usually below 3 GHz. In Table 3.2, a comparative analysis of these two diodes is presented. The silicon diode (BAP64-02) has better power handling capability while the GaAs diode (MA4AGBLP912) gives better isolation, faster switching speed and less parasitic capacitance.

The proposed reconfigurable antenna is primarily designed for digital beamforming on receive, with a maximum field strength of 200 V/m. For this the maximum power density becomes,

$$W_{rad} = \frac{1}{2\eta} * E^2 = \frac{1}{2*377} * 200^2 = 53W / m^2$$

The maximum received power for each radiator becomes, $P_{rec} = W_{rad} * A_{eff} = 53*2.5*10^{-3} = 132.5mW$. In this case, the maximum power handling capability of the GaAs diode (about 200 mW) is still sufficient. For other high-power applications, such as digital beamforning on transmit, RF switches with higher power handling capacity will be required. It should be pointed out here that the third-order-intercept (IP3) and the 1-dB compression point of the MA4AGBLP912 diode occurs above 35 dBm and 25 dBm, respectively. Therefore, a fairly linear behaviour of the diode can be expected within the intended power range.

Table 3.2 Comparison of the p-I-n diodes

Parameter	MA4AGBLP912	BAP64-02
Maximum frequency	20 GHz	3 GHz
Isolation (at 3 GHz)	30 dB	11 dB
Insertion loss (at 1.5 GHz)	0.25 dB	0.25 dB
Maximum incident power	200 mW	> 1 W
Maximum dissipated power	50 mW	715 mW
Switching speed	5 ns	1.55 µs
Parasitic capacitance under zero or reverse bias	0.02 pF	0.3 pF

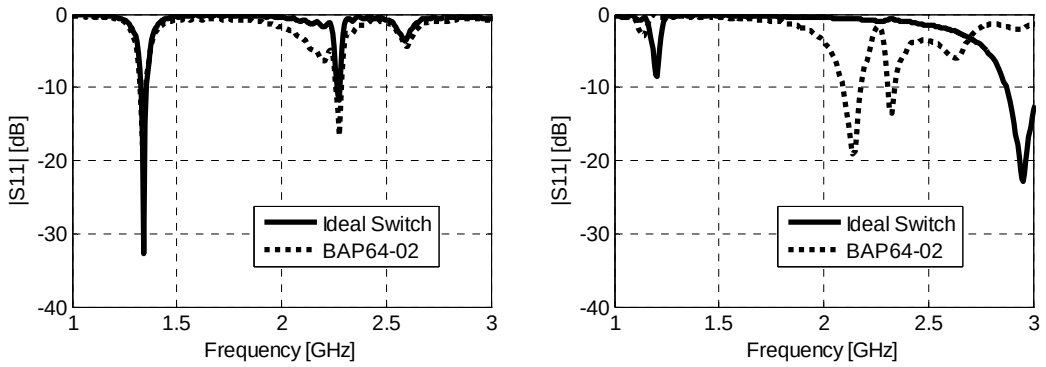

Figure 3.15 Magnitude of reflection coefficients for ideal switches and for BAP64-02 diode, (a) switch ON-state, (b) switch OFF-state.

In the initial numerical analysis of the reconfigurable antenna both diode types were implemented. However, for BAP64-02 the resonance frequency of the antenna in the higher band shifts considerably from 2.9 GHz to 2.15 GHz due to the higher parasitic capacitance of the diode under zero bias. This is clearly visible in Figure 3.15(b). Due to this detrimental effect of the silicon diode, the GaAs diode (MA4AGBLP912) was implemented in the antenna prototype and is discussed in detail in the following sections.

3.2.2 The numerical model of the diode switch

To transform the theoretical design of the reconfigurable antenna element into a prototype, the ideal OPEN and CLOSED circuit representations of the switches should be replaced by actual RF diodes. As mentioned in the previous section p-I-n diodes differ in their electrical characteristics. Therefore, the RF equivalent circuits of

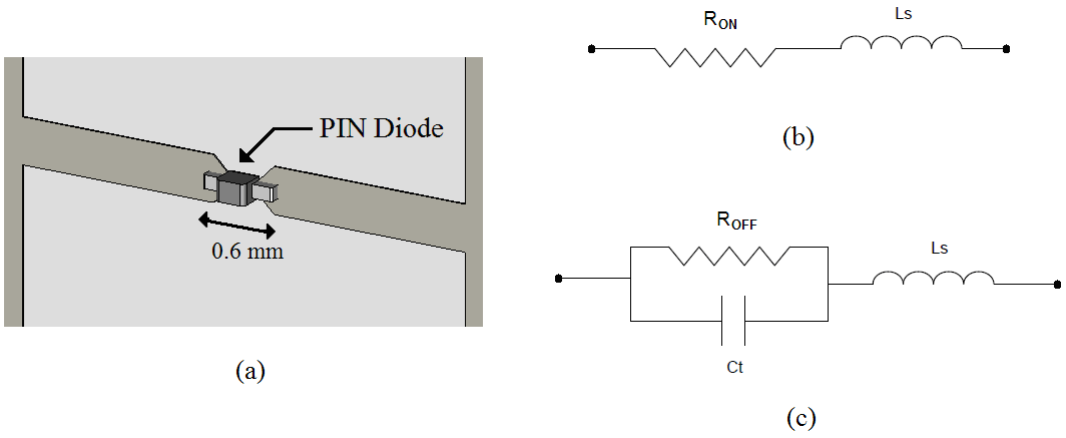

Figure 3.16 3D model of the p-I-n diode switch (a). RF equivalent circuit for the ON (b) and OFF (c) state of the MA4AGBLP912 diode: R_{ON}=4Ω, R_{OFF}=10KΩ, L_S=0.5nH, C_t=0.02pF.

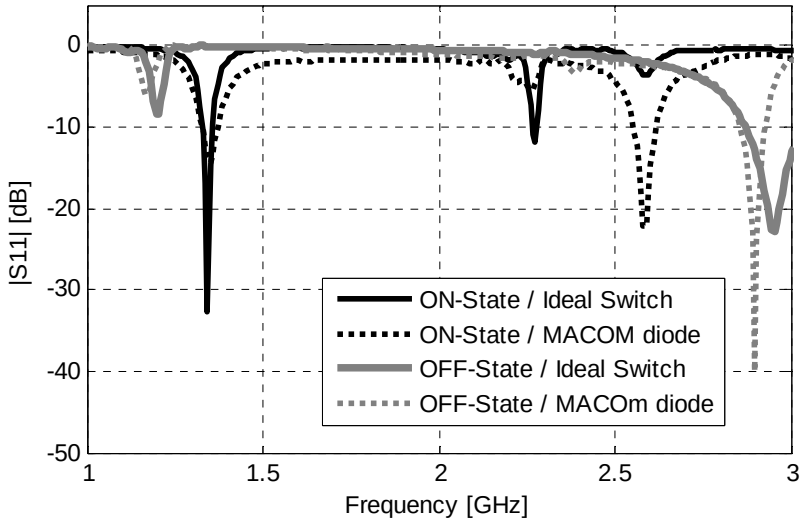

Figure 3.17 Magnitude of reflection coefficients for ideal switches and for MA4AGBLP912 diode

the diode needed to be integrated to the antenna's numerical model for a realistic analysis. In Figure 3.16, the RF equivalent circuits of the diode are shown which has been rigorously modelled in the full-wave electromagnetic analysis of the antenna. In Figure 3.17, the reflection coefficient of the antenna with lumped circuit components are presented. It is evident here that for MA4AGBLP912 the shift in the operating bands is significantly less. However, also here the parasitic capacitance of the diode influences the antenna performance in the OFF-state and reduces the bandwidth to about 70 MHz.

3.2.3 The realization of the DC bias circuit

For the proposed reconfigurable antenna, the implementation of the DC bias circuit was challenging as these elements are design for array application. Phased array antenna usually contains thousands of radiating elements. Therefore, placing additional lines in the antenna plane will drastically complicate the overall biasing network. To reduce such complexity, the DC control voltage was applied to the RF feed through a bias tee. DC ground was provided to the four p-I-n diodes using a single lumped inductor from Coilcraft (see Figure 3.18(a)). A plated-through hole then connects this inductor to the back ground plane. The discrete passive inductor is placed where the RF surface current density is minimal to reduce RF leakage. The relevant SPICE-like equivalent circuit of the inductor (see Figure 3.18) was included in the antenna model to analyse the impact of the packaging and parasitic effects of the device. In Figure 3.19, the measured S-parameters of the inductor are plotted. Here, we notice that the insertion loss at 1.35 GHz is only about 0.15 dB. For the

proposed antenna structure, the RF isolation will be further improved due to the inductive characteristic of the plated-through hole.

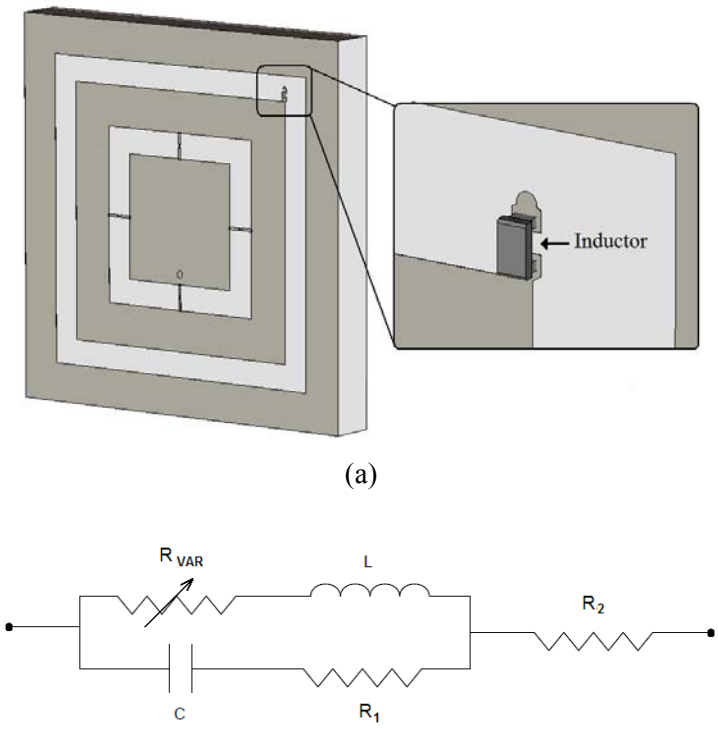

Figure 3.18 (a) Surface mount inductor (0603HP) placed on the reconfigurable antenna and (b) the RF equivalent circuit of the inductor. Circuit characteristics of the inductor: $L = 80nH$, $R_{VAR} = 1.2x10^{-4}\sqrt{f}$, $R_1 = 47\Omega, R_2 = 0.3\Omega$ and $C = 0.038\,pF$.

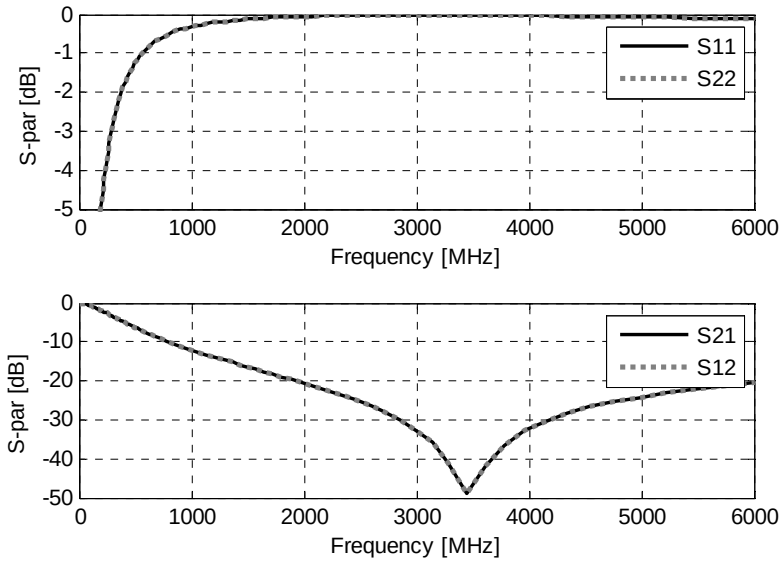

Figure 3.19 Measured S-parameters of the lumped inductor (data provided by the manufacturer)

3.3 THE EXPERIMENTAL VALIDATION

IN order to verify the theoretical results, experimental prototypes were designed and fabricated. The antenna is printed on Rogers high-frequency material, RO4003, with relative permittivity ε_r = 3.5 and 17-μm thick copper cladding. The antennas were manufactured at Printech Circuit Laboratories [26]. Photographs of the prototype are illustrated in Figure 3.20. The diode volume is 0.7x0.2x0.15 mm^3. Due to this extremely small size of the diodes, dedicated SMT (surface mount technology) component placement systems and hot-air soldering was used to attach them to the antenna surface. In the following sections the measured results of the reconfigurable antenna element with p-I-n diode switches are presented.

The reconfigurable element prototype and the measurement scheme are presented in Figure 3.20 and Figure 3.21, respectively. The PNA E8364B network analyzer from Agilent was used for the measurements. The forward voltage of about 1.35 V (minimum requirement 1.2 V) was applied to p-I-n diodes (MA4AGBLP912) through the internal bias tee of the network analyzer. The forward DC current was limited to about 40 mA (about 10 mA passing through each diode) by the 68 Ω resistor.

Figure 3.22 shows the magnitude of input-reflection coefficient for different operational modes. The experimental results and the theoretical predictions closely agree. At diode ON-state the antenna resonates at 1.33 GHz while it resonates at 2.95 GHz for the OFF-state. For the L-band and the S-band modes the measured bandwidths (at -10 dB reflection level) are 60 MHz and 70 MHz, respectively.

The antenna radiation measurements were carried out in DUCAT (Delft University Chamber for Antenna Tests) using a TEM horn (GZ0126ATP) as transmit antenna. In Figure 3.23, the measured and simulated boresight realized gains of the antenna are plotted. Here, we notice good out-of-band gain suppression while maintaining satisfying in-band gain. The measured peak gain is 4.7 dB at 1.36 GHz for diode ON-state while it is 6.1 dB at 2.95 GHz for diode OFF-state. The gain remains higher than 3 dB from 1.3 GHz to 1.38 GHz and from 2.5 GHz to 3.05 GHz for diode ON-state and OFF-state, respectively.

At diode OFF-state, the L-band outer ring performs as a parasitic element and causes spurious radiation in the lower band during the higher band operation. In the proposed design this undesired radiation was shifted below 1.2 GHz (comprehensive discussion in Section 3.2.1). Figure 3.23 demonstrates that the spurious radiation of the L-band patch (during the S-band operation) occurs around 1.15 GHz (outside the

frequency range of radar L-band). The measured results confirmed about 20 dB and 24 dB isolations between the bands at 1.35 GHz and 2.95 GHz, respectively.

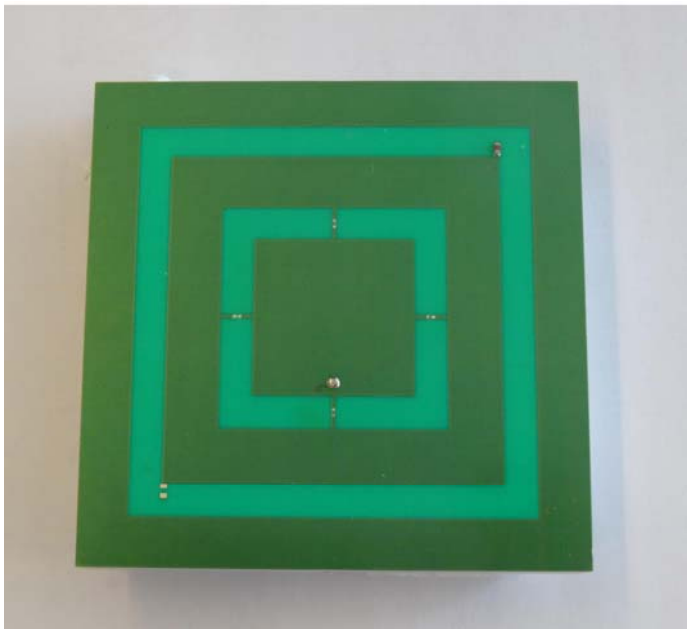

(a)

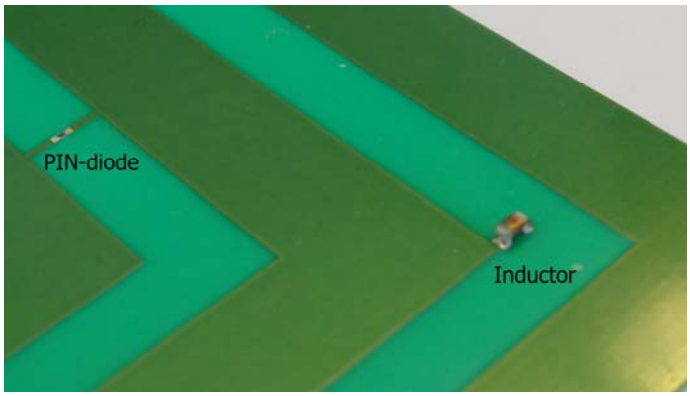

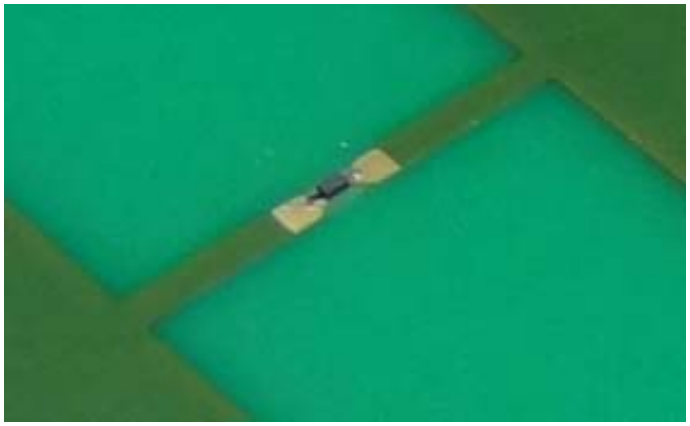

(b)

Figure 3.20 Photographs of (a) the L/S-band reconfigurable antenna prototype and (b) the p-I-n diode and the inductor attached on top of the radiating antenna

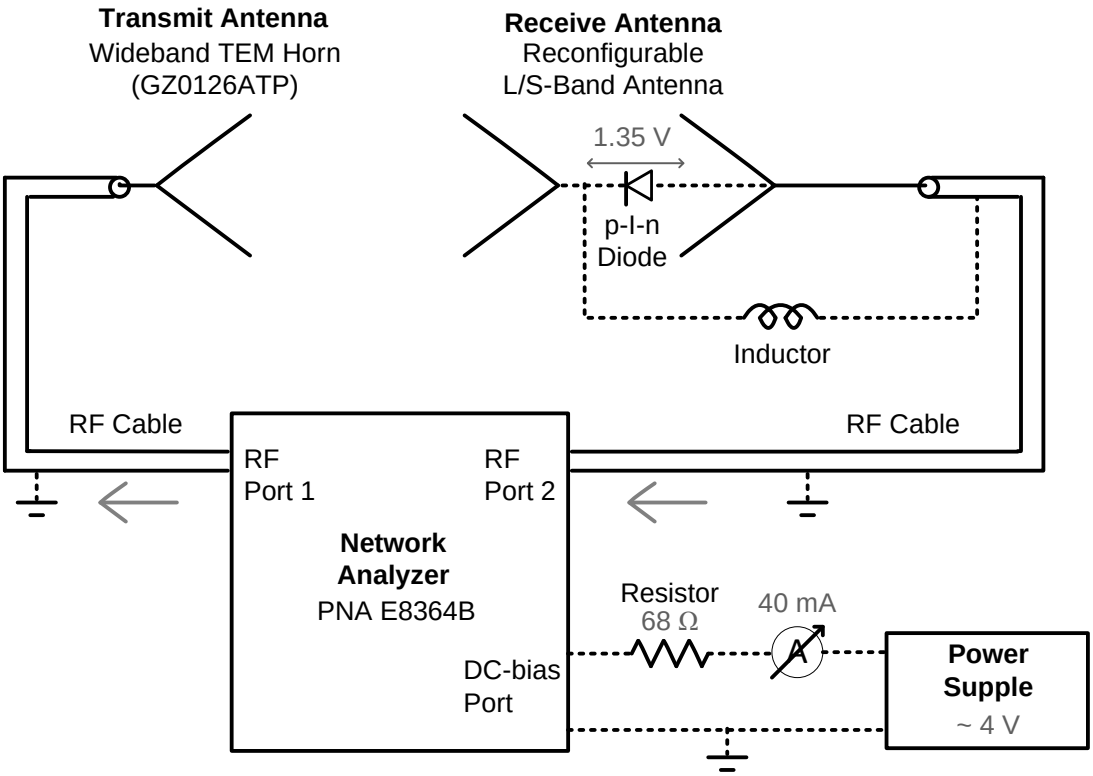

Figure 3.21 The measurement scheme

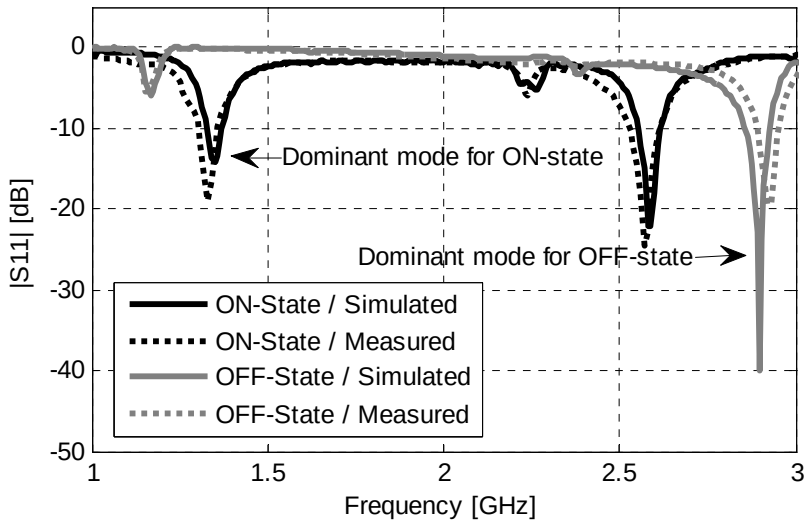

Figure 3.22 Magnitude of the input-reflection coefficient

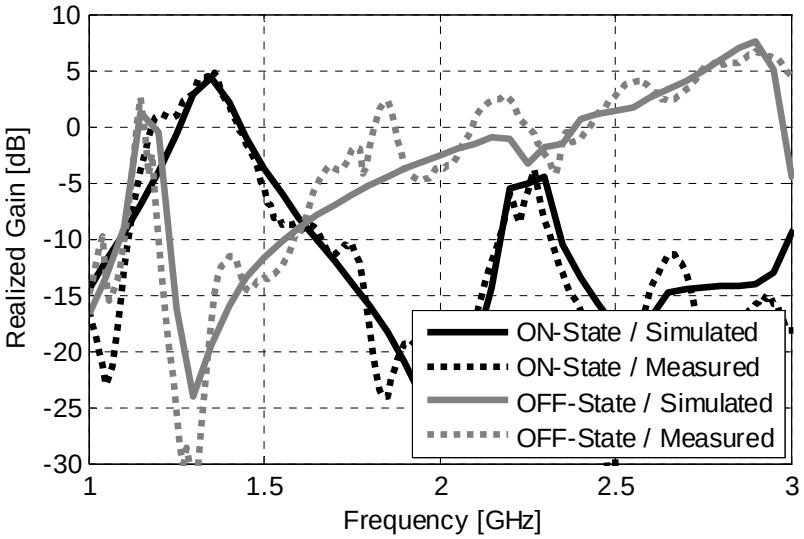

Figure 3.23 Boresight realized gain as a function of frequency

Figure 3.24 and Figure 3.25 show the antenna radiation patterns along the two principal planes. A good agreement is observed between the simulated and the measured radiation patterns. For the L-band mode, the half-power-beam-width (HPBW) is more than 100° along both principal planes. The measured cross-polar isolation within the scanning area (±60°) is more than 25 dB for E-plane. In the H-plane the polarisation purity reduces, but remains higher than 15 dB within the abovementioned scan volume. Furthermore, the measured results verify a symmetric radiation pattern along the H-plane and a quasi-symmetric pattern along the E-plane.

For the S-band mode, the antenna has more directive ration pattern (see Figure 3.25). Here, the half-power-beam-width (HPBW) is about 70° along both principal planes. Similarly to the L-band pattern, the antenna has a symmetric radiation pattern along the H-plane and a quasi-symmetric pattern along the E-plane. Along the E-plane the antenna element shows low cross-polarisation as expected. However, along the H-plane the polarisation purity degrades compared to an antenna with ideal open switch. This degradation of the polarisation was also predicted by the numerical model. Here, not only the diode but also the presence of the inductor causes higher cross-polarisation. However, Figure 3.25 demonstrates that the measured cross-polarisation isolation remains more than 13 dB within the scanning area (±60°) for H-plane.

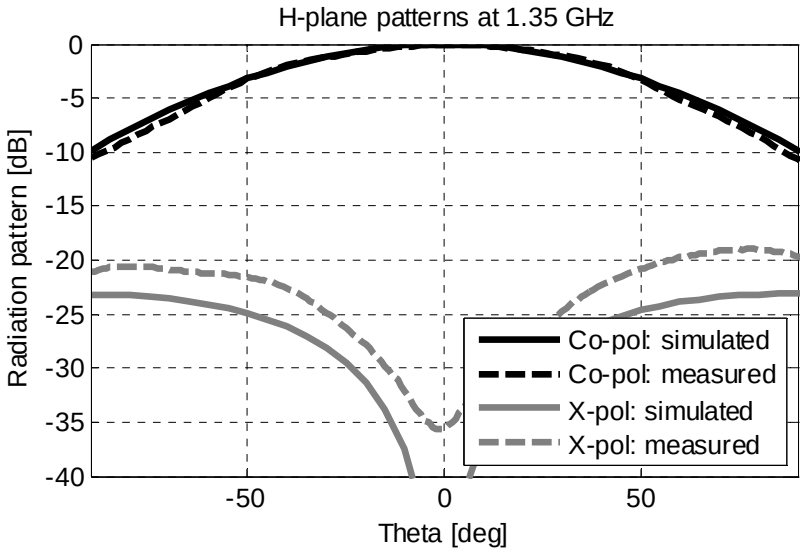

(a)

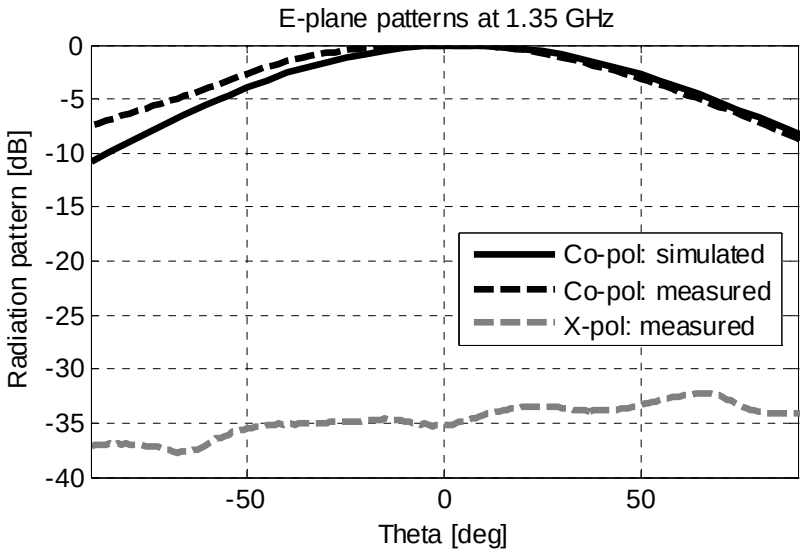

(b)

Figure 3.24 Normalized radiation patterns for diode ON-state along (a) the H-plane (b) E-plane

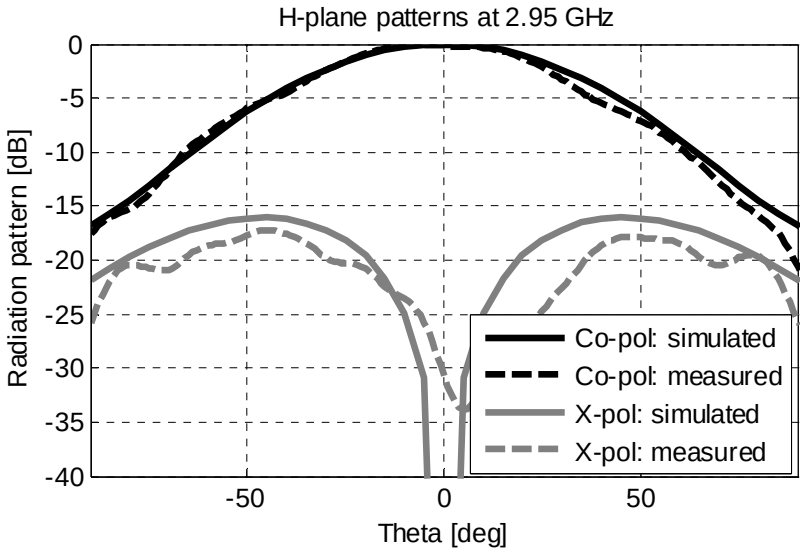

(a)

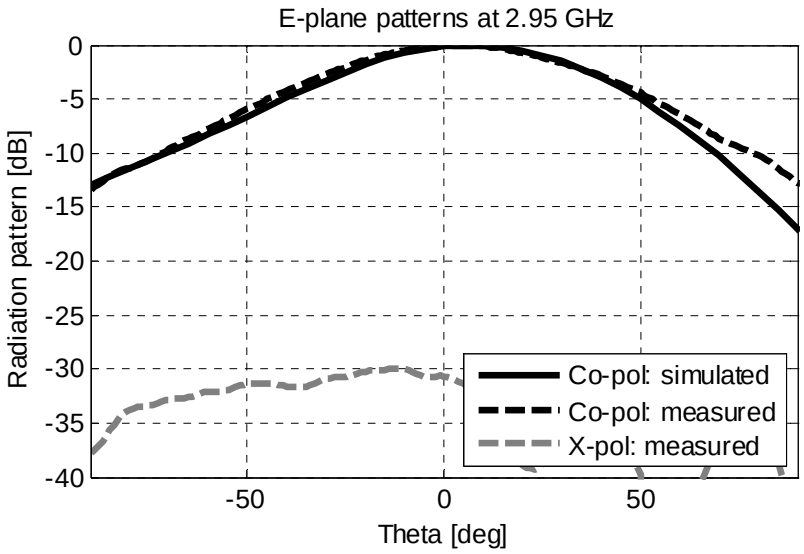

(b)

Figure 3.25 Normalized radiation patterns for diode OFF-state along (a) the H-plane (b) E-plane

For the proposed antenna topology the received power directly passes through the diodes during the ON-state of the switches. Consequently, there will be RF power losses. To experimentally verify the power loss through the p-I-n diodes in the ON-state, the diodes where replaced by metal connections as shown in Figure 3.26(a). Power loss was then evaluated by comparing the received power level of the antenna with metal connections with the received power level of antenna with diodes. Figure 3.26(b) presents this power loss caused by the diodes. Within the operational band of the antenna, the power loss varies between 1 and 1.7 dB.

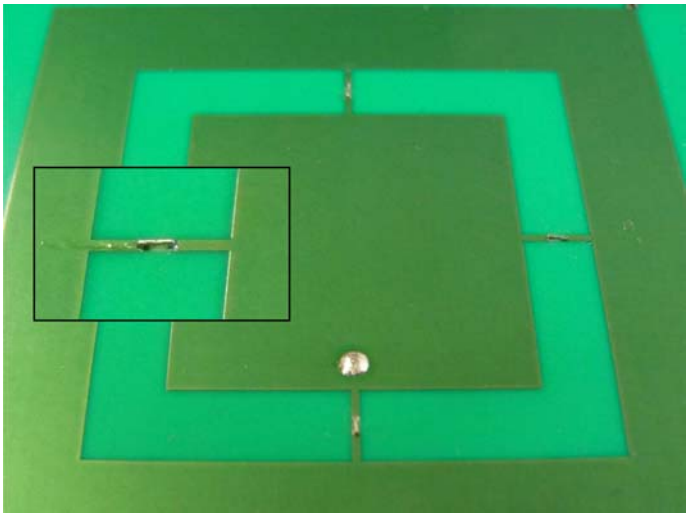

(a)

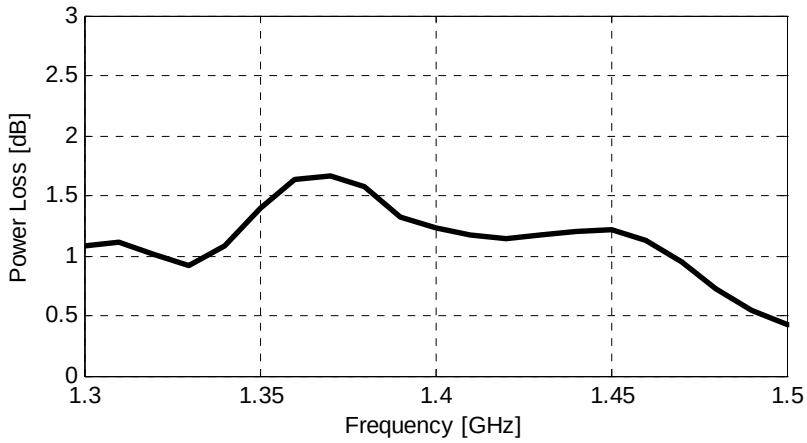

(b)

Figure 3.26 (a) Antenna element with metal lines (b) Measured power loss caused by the switching components (p-I-n diodes) of the reconfigurable antenna during ON-state

3.4 CONCLUSION

THIS chapter details the concept and the realization of a frequency reconfigurable phased array antenna based on modifying the element aperture. Here, the change of the electrical size of the antenna element was achieved by altering the state of the p-I-n diode switches placed on the radiating structure. The proposed concept provides a solution to accomplish frequency reconfigurability at the antenna element level, and therefore, considerably reduces requirements on the subsequent RF circuitry. Here, only a single operating band remains active at a time, discarding the non-active frequency spurious and the need of external diplexer.

To evaluate the reconfigurable antenna element independently of the RF-switch performance, the switches were initially considered as ideal components. Ideal open and metal connections were used in the numerical models to imitate the two switching states. Afterwards, a reliable numerical model of the RF switches was developed. The experimental verifications confirmed outstanding agreements between the numerical and measured results. These results predict that the proposed concept is applicable to frequency switch between L and S bands which refers to a frequency ratio of 2.2:1.

The antenna concept also contains a versatile biasing circuit for array configuration. Implementation of the biasing circuit is often a major complexity in the design of electronically reconfigurable antenna elements. For the antenna under investigation, this complexity had to be brought to a minimum stage due to its intended application in phased array systems. For the proposed antenna architecture this intricacy has been reduced considerably by controlling the DC bias voltage level through the RF feed.

The element has compact size of 50 x 50 mm² which makes it attractive for phased array application with large scanning volume in both frequency bands. The measured results verified 5 to 6 dB realized-gains with about 20 dB isolations between the bands. Furthermore, stable radiation properties were achieved in both operational bands with more than 13 dB cross-polar isolation within the entire scanning area. The antenna element also possesses sufficient bandwidths of 60 to 70 MHz. The main limiting factor of any reconfigurable antenna is the reduction of the radiation efficiency due to the power loss caused by the RF switches. In this work a p-I-n diode with low insertion loss was selected which resulted in a moderate level of power loss ranging between 1 and 1.7 dB within the operational band.

The results achieved from this work provided the prototype demonstration of a frequency reconfigurable radiating element and thereby significantly increased the technology readiness level of such antenna. To the author’s knowledge this work is one of the first published realizations of an L/S-band frequency reconfigurable antenna suitable for phased array application. In the following chapter, these antenna elements are arranged in an array structure to accomplish wide angle scanning in both frequency bands.

BIBLIOGRAPHY

[1] S. L. S. Yang, A. A. Kishk, and F. L. Kai, "Frequency reconfigurable U-slot microstrip patch antenna", *IEEE Antennas Wireless Propag. Lett.*, vol. 7, pp. 127–129, May 2008.

[2] J. T. Bernhard, "Reconfigurable antennas", in Synthesis Lectures on Antennas, Morgan and Claypool Publishers, 2007.

[3] K. R. Boyle and P. G. Steeneken, "A five-band reconfigurable PIFA for mobile phones", *IEEE Trans. on Antennas and Propagat.*, vol. 55, no. 11, pp. 3300–3309, 2007.

[4] A. Vasylchenko, X. Rottenberg, B. X. Broze, M. Nuytemans,W. De Raedt, and G. A. E. Vandenbosch, "A frequency switchable antenna based on MEMS technology", in *Proceedings of the 4th European Conference on Antennas and Propagation* (EuCAP '10), pp. 1–3, April 2010.

[5] A. Grau, J. Romeu, M. J. Lee, S. Blanch, L. Jofre, and F. De Flaviis, "A Dual-Linearly-polarized MEMS-reconfigurable antenna for narrowband MIMO communication systems", *IEEE Trans. on Antennas and Propagat.*, vol. 58, no. 1, pp. 4–17, 2010.

[6] C.-Y. Chiu, J. Li, S. Song, and R. D. Murch, "Frequency reconfigurable pixel slot antenna", *IEEE Trans. on Antennas and Propagat.*, vol. 60, no. 10, pp. 4921–4924, 2012.

[7] T. Korošec , P. Ritoša , and M. Vidmar, "Varactor-tuned microstrip-patch antenna with frequency and polarization agility", *Electronics Letters*, vol. 42, no. 18, pp. 1015–1016, 2006.

[8] S. V. Hum and H. Y. Xiong, "Analysis and design of a differentially-fed frequency agile microstrip patch antenna", *IEEE Trans. on Antennas and Propagat.*, vol. 58, no. 10, pp. 3122–3130, 2010.

[9] C. R. White and G. M. Rebeiz, "Single- and dual-polarized tunable slot-ring antennas", *IEEE Trans. on Antennas and Propagat.*, vol. 57, no. 1, pp. 19–26, 2009.

[10] Y. Tawk, J. Costantine, and C. G. Christodoulou, "A varactor based reconfigurable filtenna", *IEEE Antennas and Wireless Propagation Letters*, vol. 11, pp. 716–719, 2012.

[11] M. R. Hamid, P. Gardner, P. S. Hall, and F. Ghanem, "Switched band Vivaldi antenna", *IEEE Trans. on Antennas and Propagat.*, vol. 59, no. 5, pp. 1472–1480, 2011.

[12] T.-Y. Han and C.-T. Huang, "Reconfigurable monopolar patch antenna", *Electronics Letters*, vol. 46, no. 3, pp. 199–200, 2010.

[13] D. Peroulis, K. Sarabandi, and L. P. B. Katehi, "Design of reconfigurable slot antennas", *IEEE Trans. on Antennas and Propagat.*, vol. 53, no. 2, pp. 645–654, 2005.

[14] S.-X. Cao, X.-X. Yang, B. Gong, and B.-C. Shao, "A reconfigurable microstrip antenna with agile polarization using diode switches", in *IEEE International*

Symposium on Antennas and Propagation (APSURSI ’11), pp. 1566–1569, July 2011.

[15] M. Martınez-Vazquez, O. Litschke, M. Geissler, D. Heberling, A. M. Martınez-Gonzalez, and D. Sanchez-Hernandez, “Integrated planar multiband antennas for personal communication handsets”, *IEEE Trans. on Antennas and Propagat.*, vol. 54, no. 2, pp. 384–391, 2006.

[16] Y. Tawk, J. Costantine, K. Avery, and C. G. Christodoulou, “Implementation of a cognitive radio front-end using rotatable controlled reconfigurable antennas”, *IEEE Trans. on Antennas and Propagat.*, vol. 59, no. 5, pp. 1773–1778, 2011.

[17] A. Petosa, A. Ittipiboon, and N. Gagnon, “Suppression of unwanted probe radiation in wideband probe-fed microstrip patches”, *Electron. Lett.*, vol. 35, pp. 355–357, Mar. 1999.

[18] Z. Ning Chen and M. Y. W. Chia, “Broadband Planar Antennas: Design and Applications”, J. Wiley, 3rd edition, 2006.

[19] G. N. Nielson, M. J. Shaw, O. B. Spahn et al., “High-speed, sub-pull-in voltage MEMS switching”, SANDIA REPORT, SAND2008-0211, 2008.

[20] N. Biyikli, Y. Damgaci, and B. A. Cetiner, “Low-voltage smallsize double-arm MEMS actuator”, *Electronics Letters*, vol. 45, no.7, pp. 354–356, 2009.

[21] P. Ratajczak, J.-M. Baracco, and P. Brachat, “Adjustable high impedance surface for active reflectarray applications”, in *Proceedings of the 2nd European Conference on Antennas and Propagation* (EuCAP ’07), pp. 1–6, Nov. 2007.

[22] K. Topalli, E. Erdil, O. A. Civi, S. Demir, S. Koc, and T. Akin, “Tunable dual-frequency RF MEMS rectangular slot ring antenna”, *Sensors and Actuators A*, vol. 156, no. 2, pp. 373–380, 2009.

[23] G.M. Rebeiz, *RF MEMS theory, design, and technology*, Wiley, New York, 2003.

[24] P. D. Grant, M. W. Denhoff, and R. R. Mansour, “A comparison between RF MEMS switches and semiconductor switches”, in *Proceedings of the International Conference on MEMS, NANO and Smart Systems (ICMENS)*, pp. 515–521, Aug. 2004.

[25] I. Yeom,1 J. Choi, S. Kwoun, B. Lee, and C. Jung1, “Analysis of RF Front-End Performance of Reconfigurable Antennas with RF Switches in the Far Field”, *International Journal of Antennas and Propagation*, Volume 2014, Article ID 385730, 14 pages, Mar. 2014

[26] PCL, *Printed Circuit Boards*. [Online] Available: www.rfpcbs.com

CHAPTER 4

MULTI-SCALE ARRAY DESIGN FOR WIDE-ANGLE SCANNING OF DUAL-BAND ANTENNAS

In this chapter the multi-scale array topology is described and experimentally verified. The proposed methodology permits wide angle scanning in both operational bands of dual-band antenna arrays with large frequency ratio.

This chapter is based on the following publication:

[J1] N. Haider, D. P. Tran, A. G. Roederer, and A. G. Yarovoy, "Reconfigurable L/S band phased array," *Electronics Letters*, vol. 47, no. 23, pp. 1265 - 1266, Nov. 2011.

THE phased array antenna, where amplitude and phase distribution among the radiating elements are used to electrically steer the antenna beam, has great potentialities for adaptive system. As opposed to antenna structures with mechanical rotation, a phased array antenna can steer its beam in an order of magnitude faster while tracking multiple targets simultaneously. In the previous chapter the L/S-band frequency reconfigurable radiating element was discussed. It has been experimentally verified that the proposed element is able to switch its operational band from radar L-band to S-band (frequency ratio 2.2:1). The antenna elements are designed for phased array applications requiring large scanning capability in both frequency bands. It is well known that beam scanning places high requirements on antenna element and array design. The challenge to meet these requirements becomes more intense for dual band radiators. For wide angle scanning, a small element periodicity is vital in order to eliminate grating lobes in the visible region. To avoid grating lobes at the higher frequency of dual-band operations, the element needs to be placed very densely at the lower frequency. As a result, the coupling increases, which in the majority of cases, reduces the radiation efficiency and consequently the antenna gain. Hence, there is a clear trade-off between the maximum scan volume at the high frequency and the coupling in the low frequency band. This intricacy is greater for large separation between the operational bands and requires reconfigurability not only at antenna element level, but also at array topology level to correspondingly adapt the array spacing.

A glance to the scientific activities of the last decades reveals that only a very limited number of reconfigurable or dual-band antennas are designed for phased array application [1-11]. To date examples of multi-band antenna arrays which concurrently provide frequency ratio beyond 2:1 and 2-D scanning capability of more than ±45° in both bands are not present in open literature. For some antenna systems, multiple bands are achieved by sharing the same aperture among different single band radiating elements [6-11]. Most of these interleaved array structures are designed for SAR (Synthetic Aperture Radar) application where limited scan angles (typically < ±25°) are required. In this chapter, a novel multi-scale array topology is investigated where the elements were arranged in such a way that half wavelength element spacing is maintained in both frequency bands and hence provides wide angle scanning in both bands. The array geometry proposed in this work gives a unique solution for frequency reconfigurable phased array antenna with widely separated sub-bands (more than 2:1) as well as extremely wide (±60°) scanning capabilities in both of these bands.

The chapter is structured as follows. First, in Section 4.1 the shortcomings of the conventional regular grid for a dual-band antenna with a large frequency ratio are outlined. The multi-scale array topology is discussed in Section 4.2. The infinite array analysis of the proposed structure is presented in Section 4.3. Section 4.4 provides the numerical analysis and the experimental verification of the finite array. Section 4.5 ends this chapter with concluding remarks.

4.1 THE CONVENTIONAL DENSE ARRAY WITH REGULAR GRID

THE reconfigurable element structure, investigated in Chapter 3, can switch its operational band from 1.35 GHz to 2.95 GHz. The proposed radiating element was optimized for minimum protrusion. The width and the length of the element was only 50 mm which is $\lambda_{0L}/4.4$ where λ_{0L} is the free-space wavelength at the lowest operating frequency (1.35 GHz). This compact size of the element allows it to place within a dense grid.

After analysing the performance of the antenna as an isolated element (presented in Chapter 3), the antenna performance within the (finite and infinite) array was investigated. An equilateral triangular spacing was applied as the array grid. The triangular grid spacing allows reducing the total number of radiating elements by 15% compared to a square grid for the same array gain. As demonstrated in [12] for dense arrays the triangular grid is the optimal solution to suppress grating lobes adjacent to the main beam.

Figure 4.1 shows the dense array architecture with triangular grid. In this design an element periodicity of 75 mm was chosen which imply that the element periodicity

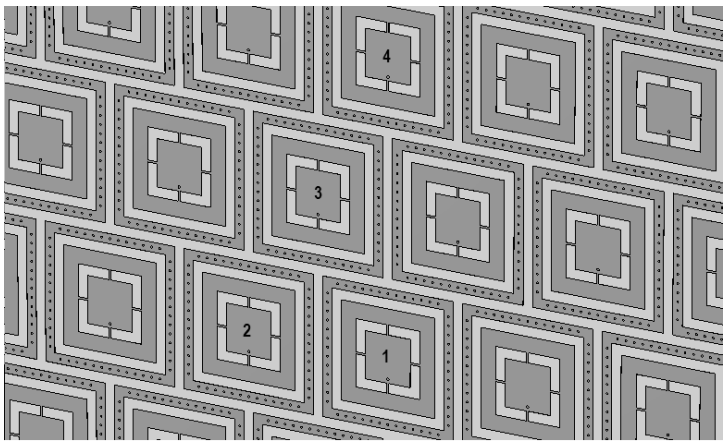

Figure 4.1 Dense array architecture with 75 mm element periodicity

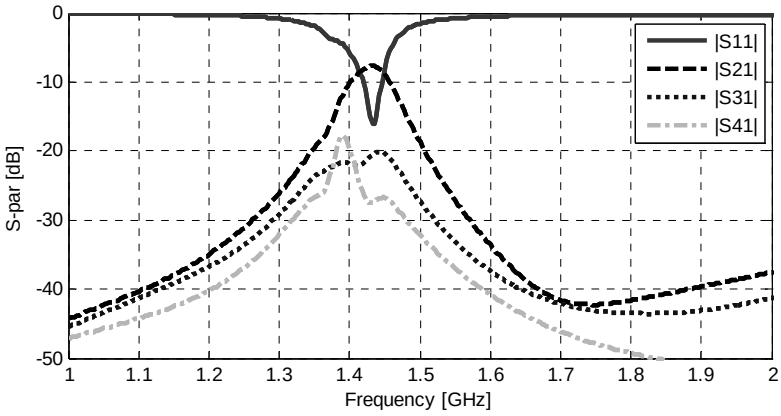

Figure 4.2 Reflection coefficient and coupling at the L-band for the dense array illustrated in Figure 4.1

at L-band is about $\lambda_{0L}/3$ (λ_{0L} being the free-space wavelength at 1.35 GHz). Due to this dense spacing, coupling at the lower band is large. Here, although a via-cavity enclosing each radiating element is used, coupling level as high as -7 dB is noticed as depicted in Figure 4.2. Even for this extremely dense grid the element periodicity for the high frequency becomes $\lambda_{0S}/1.4$ (λ_{0S} is the free-space wavelength at 2.95 GHz) which limits the maximum scan angle to less than 25° at S-band.

4.2 THE MULTI-SCALE ARRAY CONCEPT

FROM the results presented in the previous section we can conclude that for a dense array with regular grid one has to make a compromise between the maximum scan volume at the higher frequency band and the coupling level at the

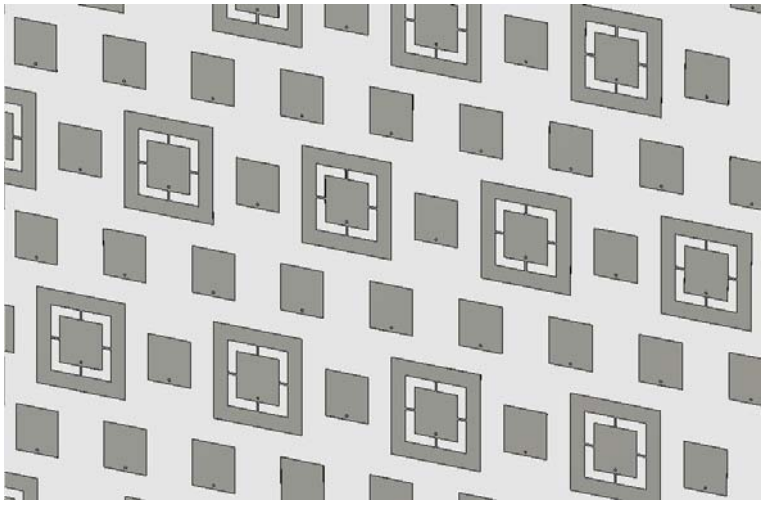

Figure 4.3 The multi-scale array architecture

lower band. This limitation of the dense array can be avoided by using a multi-scale array configuration. As illustrated in Figure 4.3 and Figure 4.4 each unit cell of this array will have one reconfigurable element (which can be switched to operate in either the high or the low frequency band) and three high frequency elements. In this array configuration, an equilateral triangular grid is used for both operational modes. The distance between two S-band elements is selected to be 50 mm and consequently the distance between two L-band elements turns to be 100 mm. Therefore, the inter-element spacing at both S-band and L-band becomes less than half of the free-space wavelength.

4.3 THE INFINITE MULTI-SCALE ARRAY ANALYSIS

IT is well known that an infinite array analysis can approximate antenna behaviour in large finite arrays with good accuracy [13-14]. The numerical investigation of antenna elements performance in an infinitely large array is a practical approach. Furthermore, the infinite array approach is useful to evaluate the active reflection coefficients. The amplitude and/or phase distribution among the excited radiating elements are modified to steer the main beam of phased array antennas. Consequently, the input impedances change with scan angle due to the mutual coupling among the radiating elements. This can cause parts of the incident power to reflect back at the input terminal which increases the scan loss. Reducing scan loss is one of the most

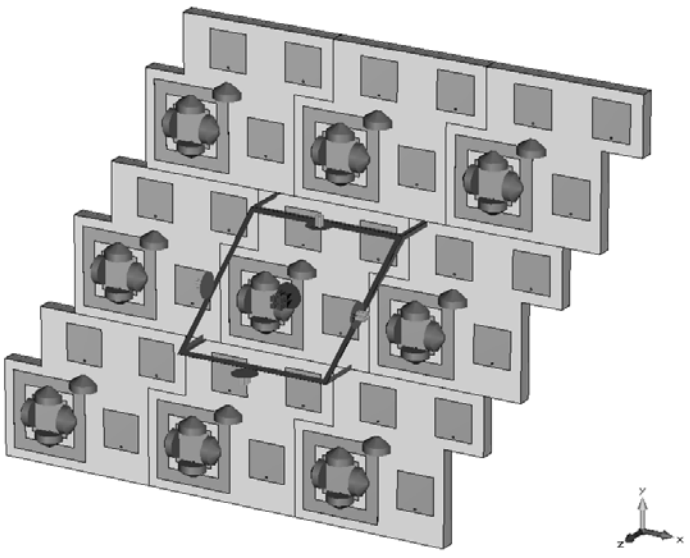

Figure 4.4 The numerical model of the infinite multi-scale array

difficult problems in phased array antenna design and requires dedicated antenna design with sufficiently low return losses for the entire scan volume.

The design of the unit cell is the first step for the numerical analysis of the infinite array. Figure 4.4 shows the investigated unit cell (containing one reconfigurable and three S-band elements) in the frequency domain solver of CST Microwave Studio. The adopted unit cell boundary condition periodically duplicates the antenna structure up to the infinity in the xy-plane and the absorbing Floquet ports are at some distance (along the z-axis) from the antenna aperture. As evident in Figure 4.4, the edges of the dielectric substrate within each unit cell have to be adjusted in order to construct the intended dual-band triangular grid. Furthermore, in these analyses, the RF equivalent circuits of the p-I-n diode and the inductor (discussed in detail in Chapter 3) were included in the simulation model.

Figure 4.5 reveals the active reflection coefficients for the L-band operational mode. The numerical results anticipate low active reflection coefficients. The variation of the active impedance as a function of the scan angle was more constrained in the E-plane. In this plane lower mutual coupling among the radiating elements was achieved due to the triangular grid. In the H-plane the deviation in the active input matching is slightly larger. Along the E-plane and the H-plane the active reflection coefficients were below -10 dB within a frequency band of 80 MHz and 50 MHz for scanning up to ±60°. For phased array antennas an active reflection coefficient of about -8 dB is usually accepted for the maximum scan angles. In Figure 4.5, it is evident that along the E-plane and the H-plane the active reflection coefficients remain below -8 dB over a frequency range of 105 MHz and 80 MHz, respectively.

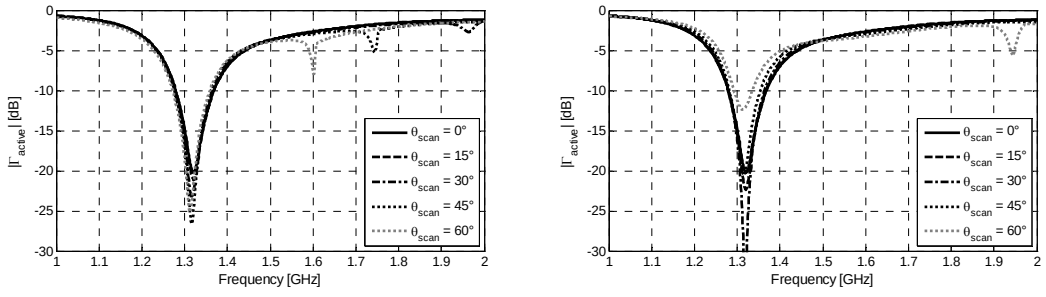

(a) (b)

Figure 4.5 The active reflection coefficients of the antenna within an infinite array for the L-band operation. The scan angle varies along (a) the E-plane and (b) the H-plane.

For the S-band operational mode, the unit cell of the multi-scale array topology is different from the conventional array or sub-array unit cell. Here, each cell contains four active radiating elements. Therefore, the active reflection coefficient for the diode ON-state was computed by applying the unit cell boundary condition in combination with true-time-delays (TTD) among the four elements within each cell.

In Figure 4.6, the active reflection coefficients for the S-band mode are presented. Also in this case numerical results predict tolerable variation within the scan volume. Active reflection coefficients lower than -8 dB was found over a frequency range of 102 MHz and 140 MHz for the E-plane and the H-plane scanning ($\max \theta_{scan} = \pm 60^0$), respectively. Here, values below -10 dB level were found within a frequency band of 60 MHz and 83 MHz for the E-plane and H-plane scanning, respectively.

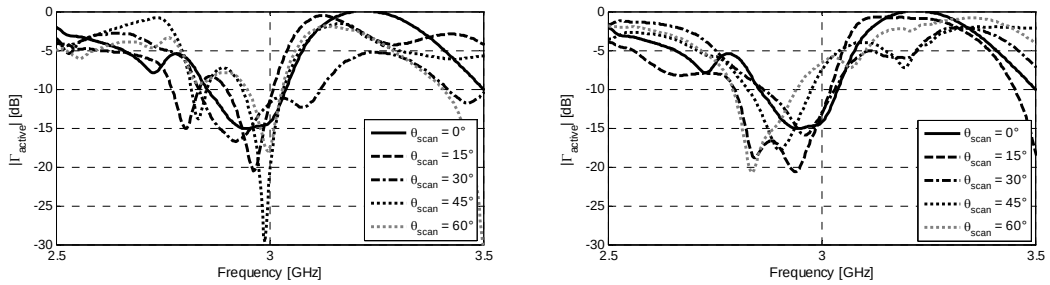

(a) (b)

Figure 4.6 The active reflection coefficients of the antenna within an infinite array for the S-band operation. The scan angle varies along (a) the E-plane and (b) the H-plane.

4.4 THE FINITE MULTI-SCALE ARRAY AND THE EXPERIMENTAL DEMONSTRATION

IN order to experimentally verify the concept an array demonstrator containing 72 radiating elements was designed, manufactured and measured. Figure 4.7 illustrates the numerical model of this 9x8 array structure. Photographs of this array prototype are shown in Figure 4.8. The overall size of this prototype is 56.5x45.7 cm. In this prototype the total number of rows had to be limited to eight in order to manufacture the prototype on standard 24"x18" dielectric panels. A dedicated array frame was made to place the AUT (antenna-under-test) on top of the turn table. The array demonstrator contains 18 reconfigurable elements and hence 72 diodes were needed to switch the bands. To ease the very demanding and time consuming

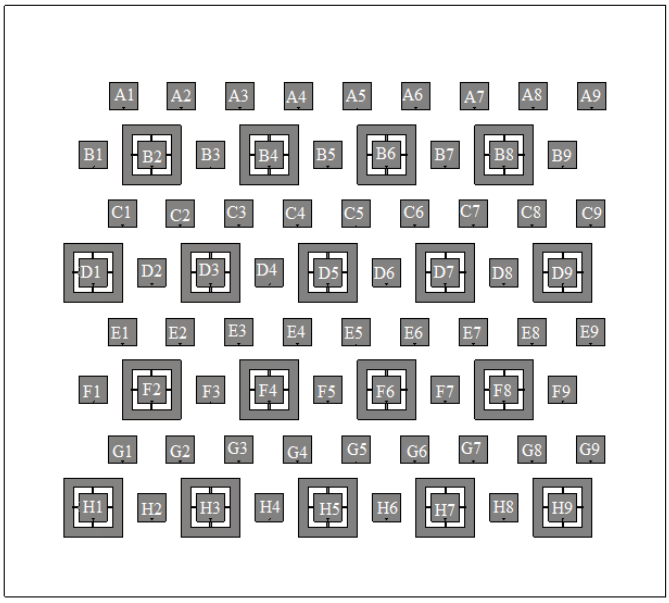

Figure 4.7 The numerical model of the 9x8 multi-scale array considered for the experimental verification.

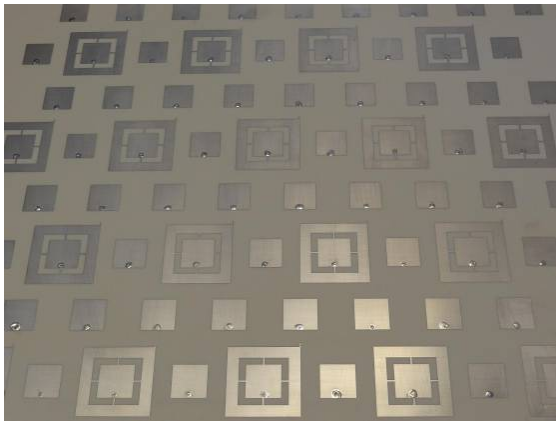

(a)

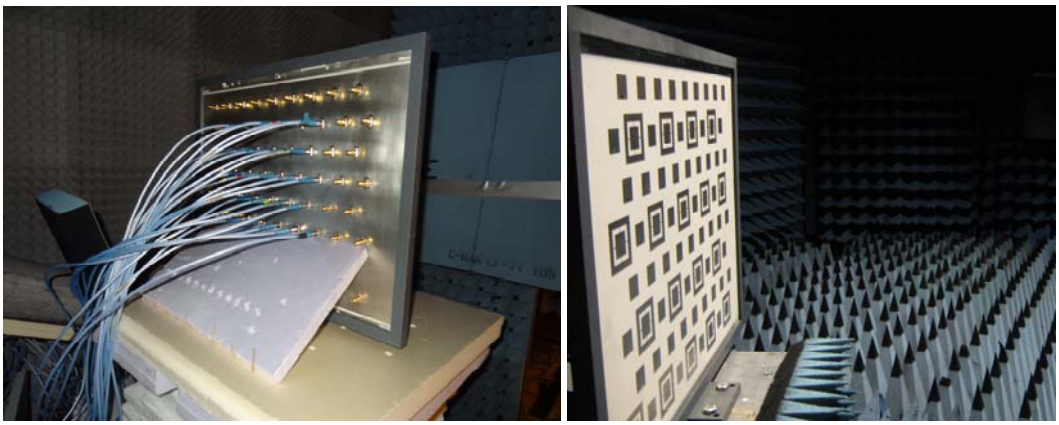

(b) (c)

Figure 4.8 The multi-scale antenna array demonstrator, (a) front-view, (b) back-view, (c) The AUT placed inside the anechoic chamber of Thales Nederland (Courtesy of Ufuk Yalcin and Pascal Aubry).

soldering process, the diodes in the antenna array prototype were replaced by ideal open and metal connections. It should be pointed out here that the influences of the diodes on the antenna performance were thoroughly investigated in Chapter 3 and in the preceding section. The simulated and measured performances of the finite multi-scale array in two operational bands are presented in this section.

4.4.1. The reflection coefficients

The embedded input reflection coefficients of the centre element in the finite 9x8 array were numerically investigated and verified with measurement results. In this case, other elements were match terminated. The embedded reflection coefficients of the centre element (D5 in Figure 4.7) during the L-band operation are shown in Figure 4.9 which reveal a good agreement between the simulated and the measured results. For the S-band operation, the reflection coefficients of both the centre reconfigurable element (D5 in Figure 4.7) and the centre S-band element (E5 in Figure 4.7) are studied and the results are presented in Figure 4.10. Also here, the measured results verified an excellent agreement with the simulated results. Furthermore, very similar return losses for the two types of S-band radiating elements (D5 and E5) are confirmed here.

Figure 4.11 and Figure 4.12 show the measured active reflection coefficients of the antenna for the L-band and S-band operation, respectively. Within the operational bands, the active reflection coefficients show acceptable matching levels. In the L-band and S-band, it remained below -8 dB over a frequency range of about 50 MHz and 100 MHz, respectively.

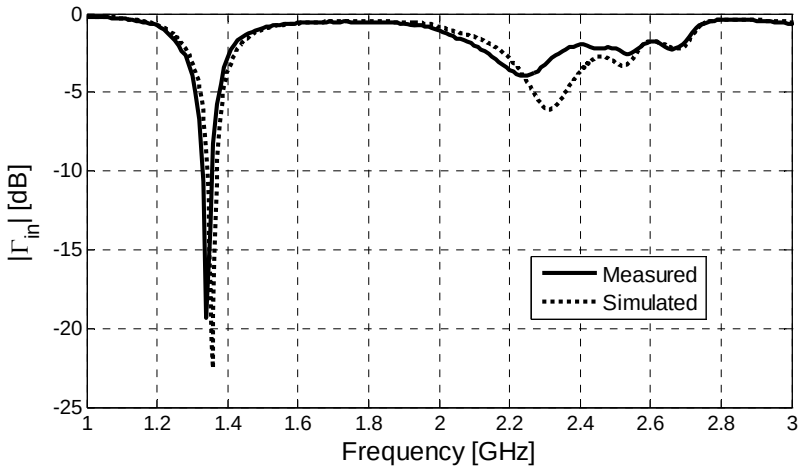

Figure 4.9 The embedded input reflection coefficient of the centre element (D5 in Figure 4.7) during L-band operation.

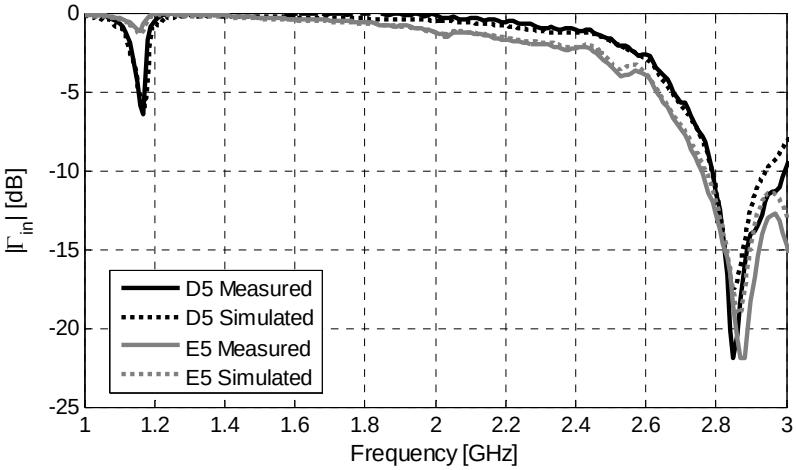

Figure 4.10 The embedded input reflection coefficient of the centre elements (D5 and E5 in Figure 4.7) during S-band operation.

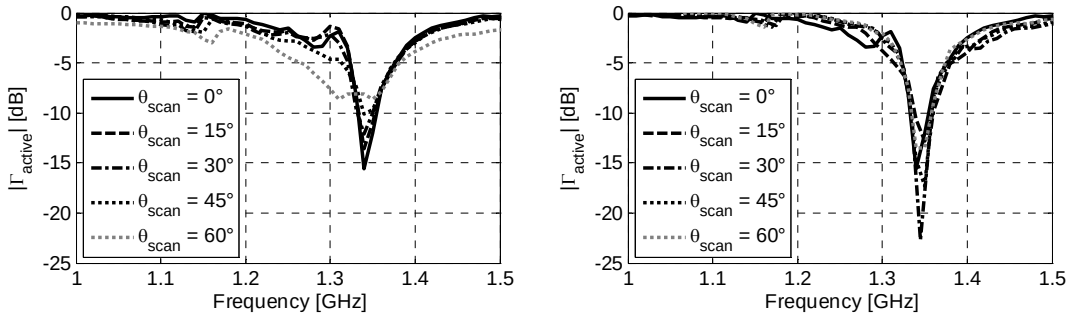

Figure 4.11 The measured active reflection coefficients of the antenna within the finite array for the L-band operation. The scan angle varies along (a) the E-plane and (b) the H-plane.

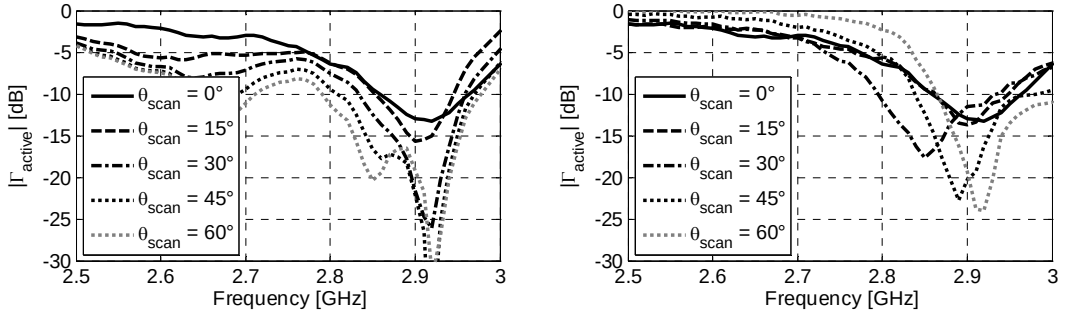

Figure 4.12 The measured active reflection coefficients of the antenna within the finite array for the S-band operation. The scan angle varies along (a) the E-plane and (b) the H-plane.

4.4.2. The mutual coupling levels

Figure 4.13 and Figure 4.14 display the measured mutual couplings of the centre element with three nearest elements. Owing to geometrical symmetry, same coupling levels are observed with the remaining adjacent elements. In the L-band and S-band

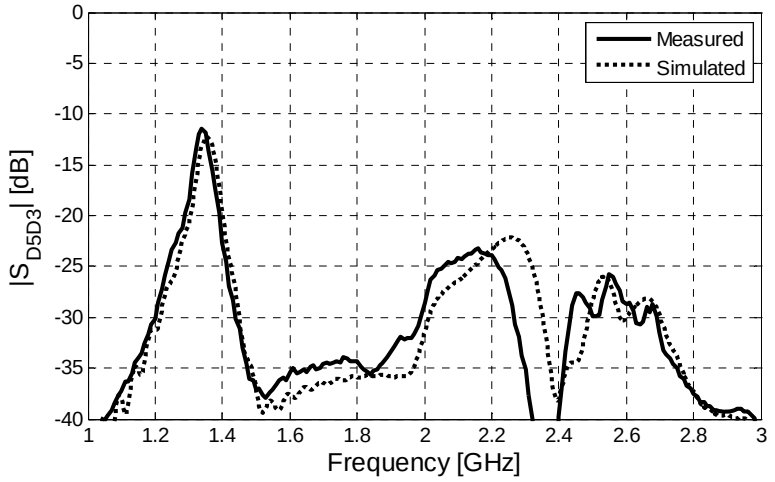

(a)

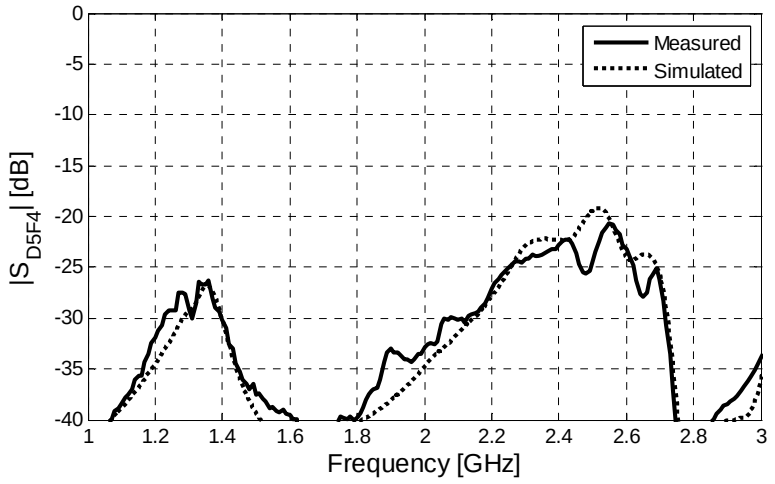

(b)

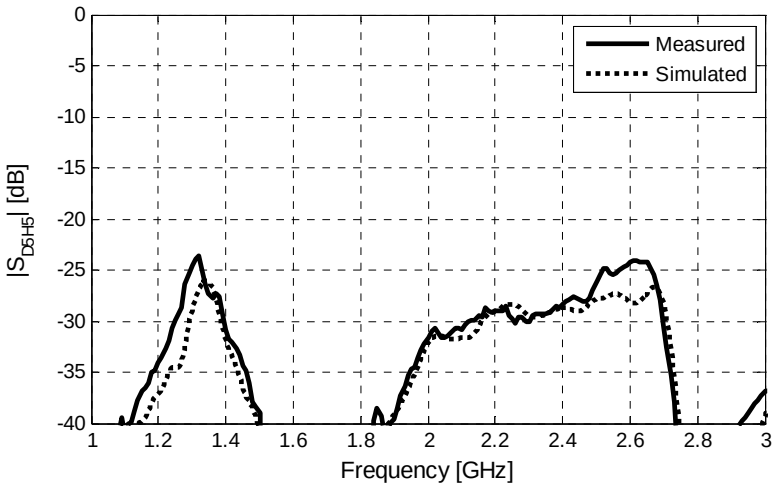

(c)

Figure 4.13 The coupling coefficient of the centre element (D5 in Figure 4.7) with (a) D3, (b) F4 and (c) H5 during L-band operation.

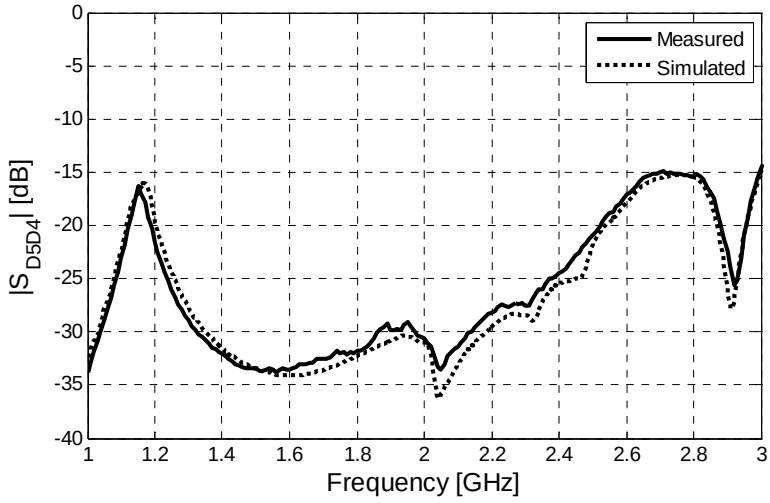

(a)

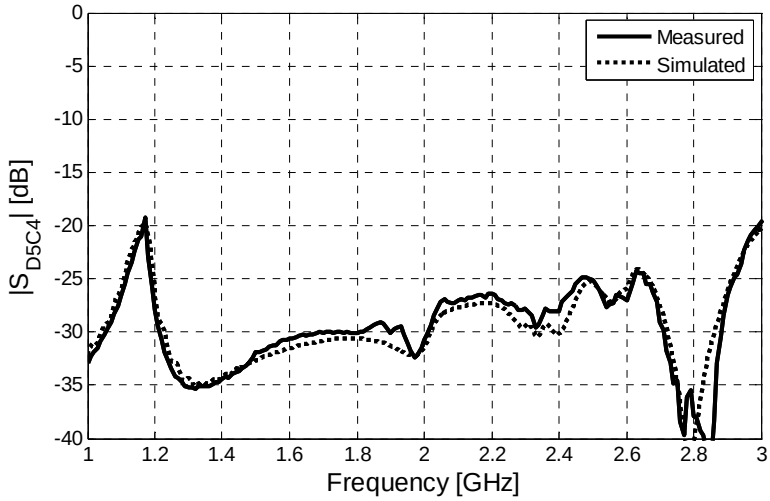

(b)

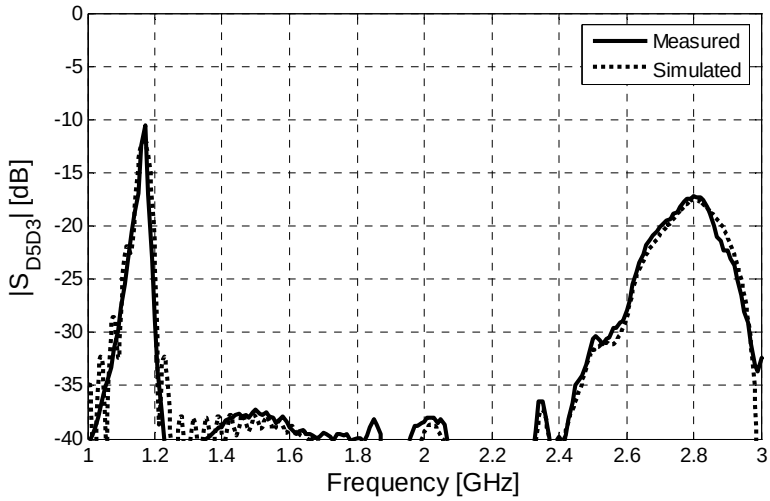

(c)

Figure 4.14 The coupling coefficient of the centre element (D5 in Figure 4.7) with (a) D4, (b) C4 and (c) D3 during S-band operation.

operation modes the coupling along the H-planes remains below -12 dB and -15 dB within the respective operational bands (see Figure 4.13(a) and Figure 4.14(a)). Moreover, due to the triangular spacing the coupling remains well below -25 dB among the elements placed along the diagonal planes (see Figure 4.13(b) and Figure 4.14(b)). Thanks to these adequate isolations expensive via cavities, which are usually required to reduce mutual couplings, were unnecessary for the proposed array architecture. It should be pointed out that the strong coupling of the L-band rings during the S-band operation (see Figure 4.14(c)) occurs below 1.2 GHz and hence remains outside the intended L-band frequency range.

In Figure 4.15, the total efficiencies (radiated and input power ratio) of the array element for both operational modes are shown. Mainly due to the mutual antenna couplings, surface-wave and return losses the element's efficiencies are about 70-80%.

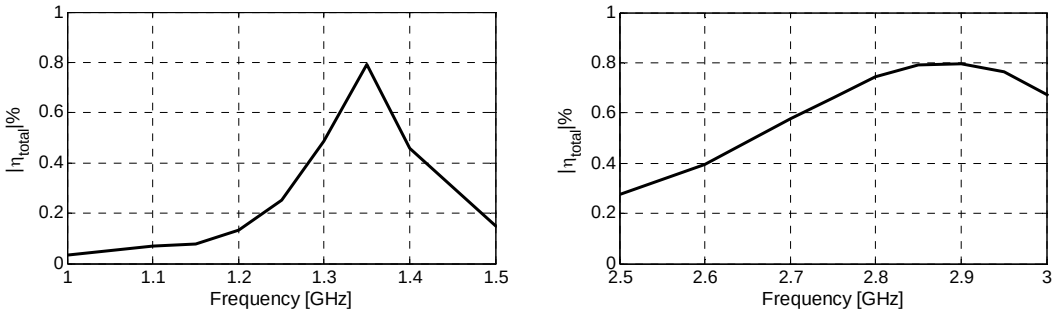

(a) (b)

Figure 4.15 Simulated total efficiency of the finite array element for (a) L-band mode and (b) S-band mode.

4.4.3. The scanning performance

In this section the scanning performance of the antenna array is discussed. For these investigations, the measured embedded element patterns are combined to synthesise the array radiation patterns. For the lower operational frequency embedded radiation patterns of 16 elements are used while for the higher frequency embedded patterns of 30 elements are used. Here, linear phase and uniform amplitude distributions are considered for the beam forming.

The measured H-plane scan patterns are depicted in Figure 4.16 and Figure 4.17 for the L-band and S-band mode, respectively. Due to less than half-a-wavelength element periodicity, a grating lobe free scanning performance was expected for the entire visible space scanning for both bands. The measured results confirmed this anticipation.

Figure 4.18 and Figure 4.19 provide comparisons between the theoretical and experimental H-plane scan patterns at 1.35 GHz and 2.95 GHz, respectively. These plots show that the measured patterns agree very closely with the numerically computed results. For the L-band the measured side lobe level (ratio between amplitudes of the main lobe and the maximum side lobe) varies from -13.75 dB to -10 dB while for S-band it rises from -14.25 dB to -9.76 dB as the scan angle shifts from broadside to ± 60°. Here, it is important to notice the absence of the grating lobes even for the maximum scan angles. It is worth pointing out that in the above investigation uniform amplitude distribution is considered and reduction of side lobe

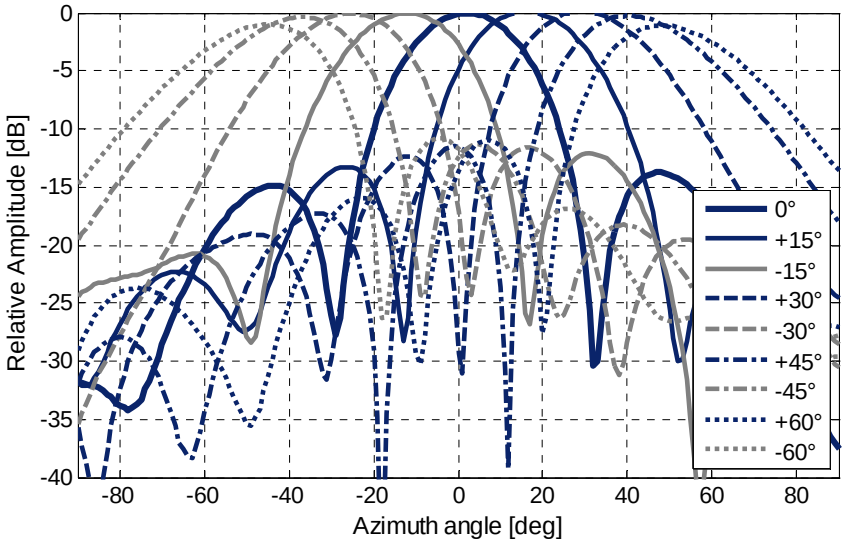

Figure 4.16 Computed from measured H-plane scan patterns at 1.35 GHz for 16 radiating elements

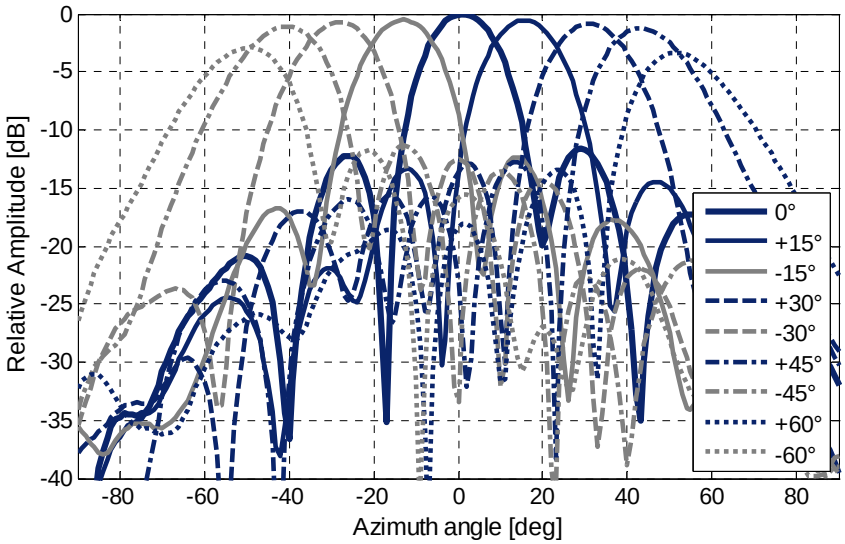

Figure 4.17 Computed from measured H-plane scan patterns at 2.95 GHz for 30 radiating elements

levels can be achieved by dedicated amplitude tapering, for example using binominal, Taylor, Chebyshev or other distributions [15-19].

In the proposed design, low scan loss is evident as presented in Figure 4.16 and Figure 4.17. The measured results verified that in the H-plane (beam steering up to ±60°) the variation in the relative amplitudes of the scan patterns remains below 3 dB and 5 dB at L-band and S-band, respectively. Consequently, deviation of the half-power-beamwidth (HPBW) is only 5.9° for L-band and 3.5° for S-band when the beam is steered from broadside to ±60°. This low variation has been achieved due to the element patterns with wide beamwidths.

Figure 4.18 and Figure 4.19 also demonstrates very symmetric scan patterns. A slight asymmetry in the pattern for large azimuth angles subsists due to unevenness in the edge-element arrangement along the x-axis as evident in Figure 4.7. For a larger array structures this asymmetry will diminish considerably.

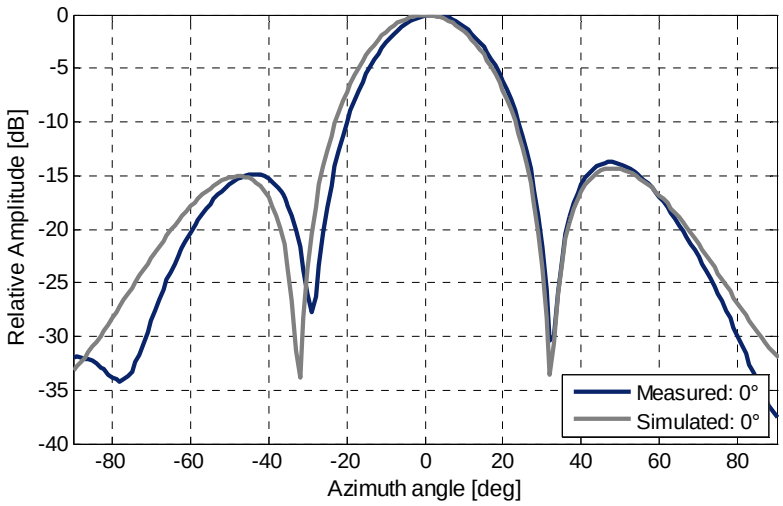

(a)

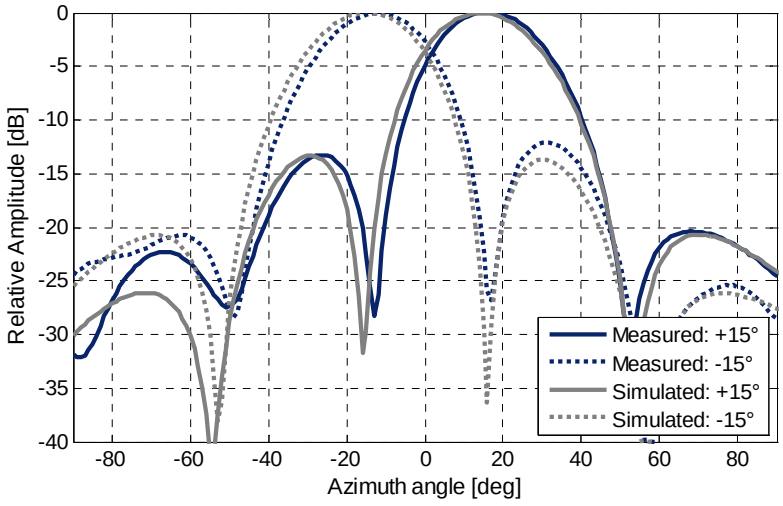

(b)

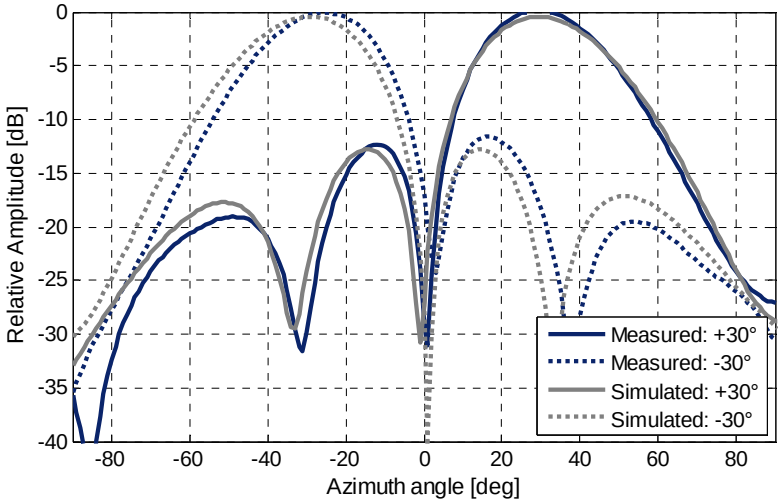

(c)

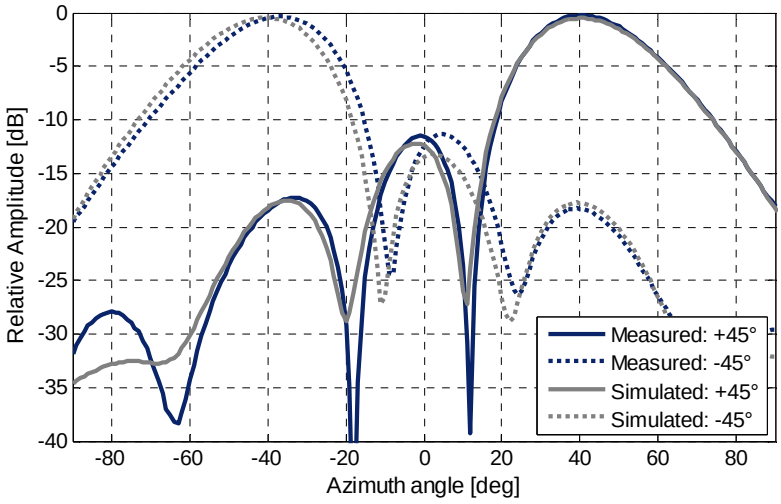

(d)

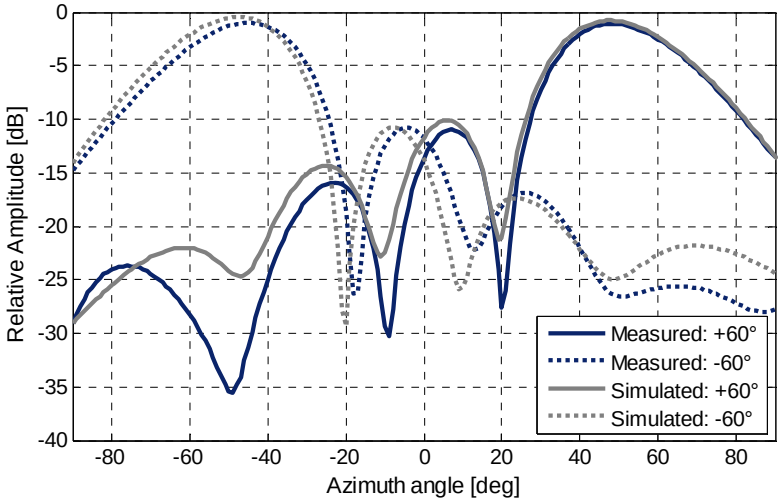

(e)

Figure 4.18 Comparison between the measured and simulated H-plane patterns at 1.35 GHz for 16 radiating elements, (a) 0° scan (b) ±15° scan, (c) ±30° scan, (d) ±45° scan, (e) ±60° scan

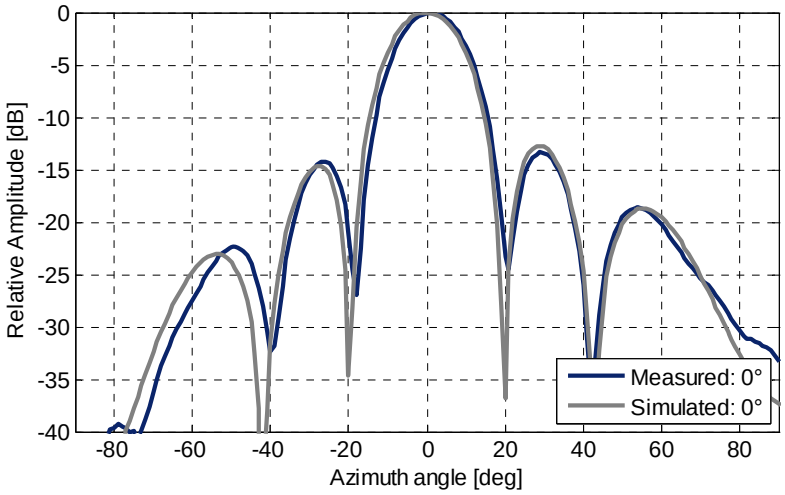
Relative Amplitude [dB]
Azimuth angle [deg]
Measured: 0°
Simulated: 0°

(a)

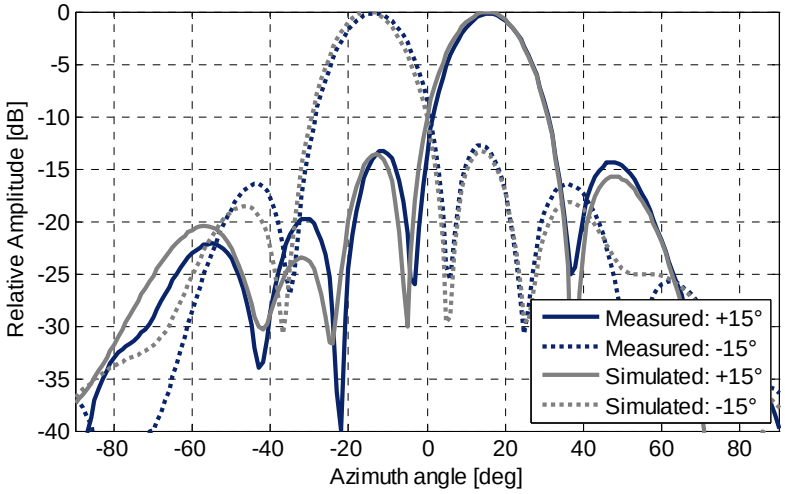
Relative Amplitude [dB]
Azimuth angle [deg]
Measured: +15°
Measured: -15°
Simulated: +15°
Simulated: -15°

(b)

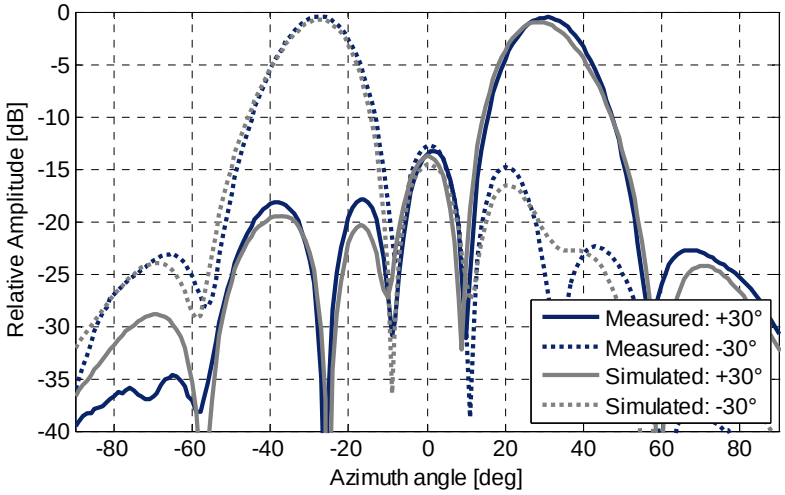
Relative Amplitude [dB]
Azimuth angle [deg]
Measured: +30°
Measured: -30°
Simulated: +30°
Simulated: -30°

(c)

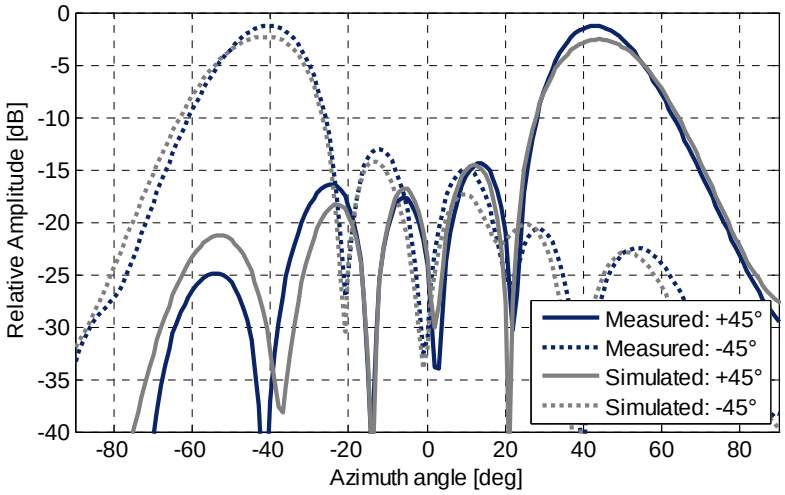

(d)

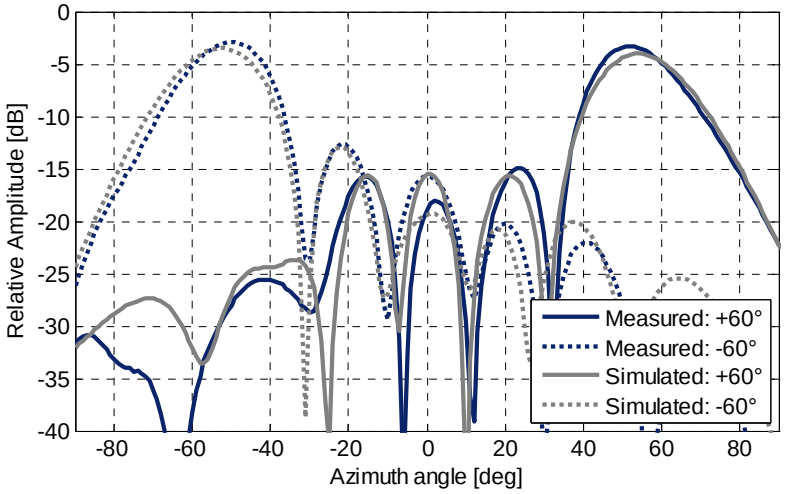

(e)

Figure 4.19 Comparison between the measured and simulated H-plane patterns at 2.95 GHz for 30 radiating elements, (a) 0° scan (b) ±15° scan, (c) ±30° scan, (d) ±45° scan, (e) ±60° scan

Figure 4.20 and Figure 4.21 show the simulated scan patterns along the E-plane for the L-band and the S-band mode, respectively. Since very good agreements between the measured and the simulated patterns were found in the H-plane, the E-plane patterns have been exclusively investigated with the numerical model. Similar to the H-plane patterns also in this case the array scan patterns remain grating-lobe free for both bands. As the scan angle changes from broadside to 60°, the maximum side lobe level along the E-plane increases from -13.9 dB to -7.6 dB for the L-band and from -12.1 dB to -7 dB for the S-band. Following figures also illustrate symmetric and consistent patterns for various scan angles.

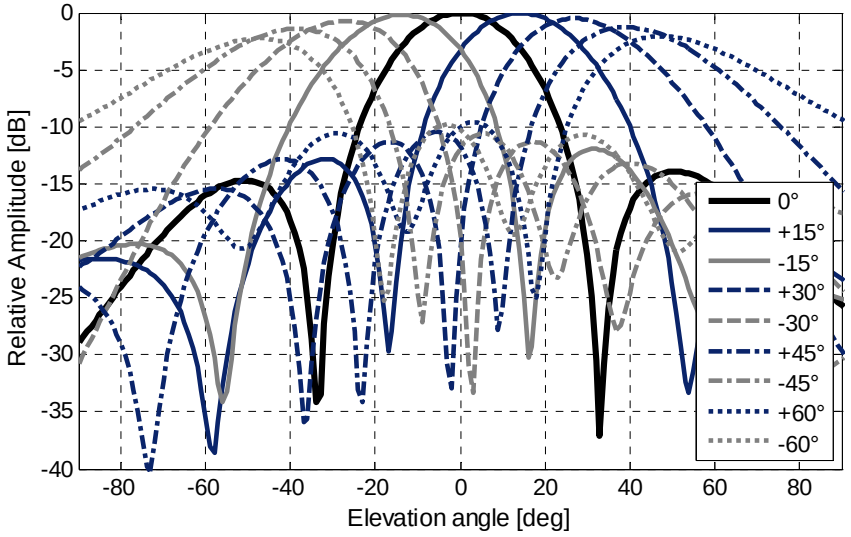

Figure 4.20 E-plane simulated scan patterns at 1.35 GHz for the 16 elements

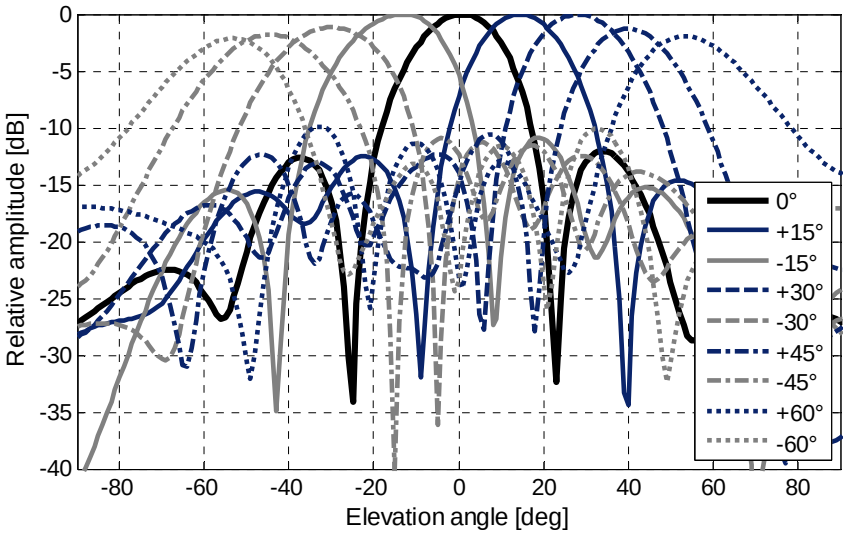

Figure 4.21 E-plane simulated scan patterns at 2.95 GHz for the centre 30 elements

4.5 CONCLUSION

IN this chapter the novel multi-scale array architecture is introduced which can evade the limitations of a dual-band dense antenna array. The radiating element introduced in Chapter 3 is suitable for dual-band phased array antenna. The antenna element operates in two bands which are separated over a frequency ratio of 2.2:1. This large frequency partition makes the proposed element practical for L/S-band phased array radar, but introduces major challenge in the array realization when wide angle scanning ($\max \theta_{scan} = \pm 60^0$) at both operating modes are desired. In this case, a

conventional dense array grid cannot assure low coupling at the lower frequency and large scanning volume at the higher frequency simultaneously. To overcome this drawback, the multi-scale array grid is proposed and investigated in this work. In this array architecture, an inter-element spacing of less than half of the free-space wavelength was maintained for both frequencies. Consequently, the grating lobes were fully shifted outside the visible space for the entire scan volume.

A planar 9x8 array demonstrator was designed and its performance was experimentally verified. In particular, the reflection coefficients, coupling levels and scan performances are experimentally demonstrated. In all cases good agreements between the measured and the simulated results were found. Outcome of this research work verified the advantage of the proposed array (as opposed to the regular-dense array) in increasing the scanning volume. While in the dense array arrangement the scan angle would be limited to ±25° for the higher operational frequency, the multi-scale array topology increases this scan volume to ±60°. For the lower operational frequency the effectiveness of multi-scale array in reducing the mutual element coupling was verified. Here, even without using any via cavity 5 to 6 dB less coupling was observed compared to the regular dense spacing with cavity cage.

Owing to the symmetric element patterns, the array beams also remained symmetric for off-boresight scanning not only along the H-plane but also along the E-plane. Moreover, the proposed antenna array shows consistent patterns when scanned along the H-plane and E-plane for both operational modes.

BIBLIOGRAPHY

[1] C. R. Liu, S. Q. Xiao, Y. X. Guo, Y. Y. Bai, and B. Z. Wang, “Broad-band circularly polarized beam-steering antenna array”, *IEEE Trans. Antennas Propag.*, vol. 61, no. 3, pp. 1475–1479, Mar. 2013.

[2] A. Thain, G. Peres, A. Hulzinga, H. Schippers, and H. Van Gemeren, “A dual-band low profile phased array antenna for civil aviation applications”, in *Proceedings of the 3rd European Conference on Antennas and Propagation*, Berlin, Mar. 2009.

[3] K. Lee, A. T. S. Wang, and R. S. Chu, “A dual band phased array using interleaved waveguides and dipoles printed on high dielectric substrate”, in *Proceedings of the IEEE AP-S Symp.*, vol. 2, pp. 886–889, Jun. 1984.

[4] O. H. Karabey, S. Bildik, C. Fritzsch, S. Strunck, A. Gaebler, R. Jakoby, and A. Manabe, “Liquid crystal based reconfigurable antenna”, in *Proceedings of the 32th ESA Antenna Workshop on Antennas for Space Applications*, Noordwijk, The Netherlands, 2010.

[5] M. A. Soliman, T. E. Taha, W. Swelam, and A. Gomaa, "3.5/5GHz dual-band 8x8 adaptive array antenna", *Progress In Electromagnetics Research C*, Vol. 34, pp. 85-98, 2013.

[6] L. Shafai, W. Chamma, M. Barakat, P. Strickland, and G. Seguin, "Dual-band dual-polarized perforated microstrip antennas for SAR applications", *IEEE Trans. Antennas Propag.*, vol. 48, no. 1, pp. 58–66, Jan. 2000.

[7] D. Isleifson and L. Shafai, "A Study on the Design of Dual-Band Perforated Microstrip Antennas for SAR Applications", *International Symposium on Antenna Technology and Applied Electromagnetics (ANTEM)*, Toulouse, Jun. 2012.

[8] E. Arnieri, L. Boccia, and G. Amendola, "A Ka-Band Dual-Frequency Radiator for Array Applications", *IEEE Antennas and Wireless Propagat. Letters*, vol. 8, Aug. 2009.

[9] Z. Sun, K. P. Esselle1, S.-S. Zhong, and Y. J. Guo, "Shared-Aperture Dual-Band Dual-Polarization Array Using Sandwiched Stacked Patch", *Progress In Electromagnetics Research C*, vol. 52, 183–195, Aug. 2014.

[10] S.-S. Zhong, Z. Sun, L.-B. Kong, C. Gao, W. Wang, and M.-P. Jin, "Tri-Band Dual-Polarization Shared-Aperture Microstrip Array for SAR Applications" *IEEE Trans. on Antennas and Propagat.*, vol. 60, no. 9, pp. 4157–4165, Sep. 2012.

[11] K. Naishadham, R. L. Li, L. Yang, T. Wu, W. Hunsicker, and M. Tentzeris, "A shared-aperture dual-band planar array with self-similar printed folded dipoles", *IEEE Trans. on Antennas Propag.*, vol. 61, no. 2, pp. 606–613, Feb. 2013.

[12] R. J. Mailloux, *Phased array antenna handbook, 2nd edition*, Artech House, Norwood, MA, 2005.

[13] H. J. Visser, *Array and Phased Array Antenna Basics*, John Wiley & Sons, Chichester, 2005.

[14] A. K. Bhattacharyya, *Phased Array Antennas: Floquet Analysis, Synthesis, BFNs and Active Array Systems*, John Wiley & Sons, New York, 2006.

[15] R. L. Haupt, "Reducing grating lobes due to subarray amplitude tapering", *IEEE Trans. on Antennas and Propagat.*, vol. 33, no. 8, pp. 846–850, Aug. 1985.

[16] R. L. Haupt, "Optimized weighting of uniform subarrays of unequal sizes", *IEEE Trans. on Antennas and Propagat.*, vol. 55, pp. 1207–1210, 2007.

[17] H. Wang, D. Fang, and Y. L. Chow, "Grating lobe reduction in a phased array of limited scanning", *IEEE Trans. on Antennas and Propagat.*, vol. 56, no. 6, pp. 1581–1586, 2008.

[18] L. Manica, P. Rocca, and A. Massa, "Design of Subarrayed Linear and Planar Array Antennas With SLL Control Based on an Excitation Matching Approach", *IEEE Trans. on Antennas and Propagat.*, vol. 57, no. 6, pp. 1684 – 1691, Jun. 2009.

[19] T. J. Brockett and Y. Rahmat-Samii, "Subarray Design Diagnostics for the Suppression of Undesirable Grating Lobes", *IEEE Trans. on Antennas and Propagat.*, vol. 60, no. 3, pp. 1373 – 1380, Mar. 2012.

CHAPTER 5

ANTENNA RECONFIGURATION WITH VARIABLE IMPEDANCE MATCHING

The concept of antenna frequency agility by variable-impedance matching is introduced. It is experimentally verified that by properly selecting the input-impedance of RF-frontend, the operating frequency of an antenna can be reconfigured. Other advantages of variable-impedance matching for phased array systems, such as sustain wider scan angles and minimize unwanted signal interferences coming from spurious directions, are also discussed in this chapter.

This chapter is based on the following publications:

[C5] N. Haider, M. S. Oude Alink, D. Caratelli, E. A. M. Klumperink, and A. G. Yarovoy, "Frequency-tunable antenna by input-impedance-tunable CMOS RF-frontend", *European Microwave Integrated Circuits Conference (EuMIC)*, Nuremberg, Oct. 2013.

[J5] N. Haider, D. Caratelli, and A. G. Yarovoy, "Frequency reconfiguration of a dual-band phased-array antenna with variable-impedance matching", *IEEE Trans. Antennas Propagat.* (accepted for publication).

IN the present chapter the concept of variable-impedance matching in realization of a reconfigurable antenna is introduced which belongs to the third of the three design approaches discussed in Chapter 1 (Section 1.6). Similar to the design approach presented in Chapter 3, the approach presented here is suitable for frequency reconfiguration between two (radar) bands. However, unlike the solutions presented in Chapter 3, in this case no switches are placed on the radiating element, thereby reducing the complexities and parasitic effects of the RF-switches and their control lines.

The concept and the advantages of variable-impedance matching for an antenna system are discussed in Section 5.1. The theory of power waves in the context of variable-impedance matching is presented in Section 5.2. In section 5.3 the concept has been experimentally verified with an input-impedance tuneable CMOS RF-frontend and a microstrip antenna. In Section 5.4 the concept of antenna frequency reconfiguration by variable impedance loading is applied to the dual-band E-slot antenna which has been exclusively developed to demonstrate the concept. Section 5.5 discusses the advantages of the proposed design concept for phased array antennas. Finally, the conclusions are drawn in Section 5.6.

5.1 THE CONCEPT AND THE ADVANTAGES OF VARIABLE-IMPEDANCE MATCHING FOR AN ANTENNA

TRANSMISSION lines and connectors with 50 Ω characteristic impedance are extensively used to provide a standard interface between antennas, RF-frontends and measurement equipment. This standardization, however, severely limits the flexibility for RF-frontend and antenna design. The 50 Ω reference impedance value has several practical advantages, but is neither dictated by any severe physical limit nor does it assure the best performance for an electronic system. Historically, this impedance value was selected as a compromise between the minimum attenuation at around 77 Ω and the maximum power handling capability at around 30 Ω of an air-filled coaxial-line or waveguide [1]. However, having the liberty to choose another impedance value increases the design flexibility for both antennas and RF-frontends, and can enhance the total system performance dramatically [2-7]. Possibility to select reference impedances other than the 50 Ω value reveals the opportunity to use antenna structures for which the inherent input impedance is not 50 Ω [4]. In addition, [6-7] demonstrate improvements in gain and noise factor when the impedance of the RF-frontend is not obliged to match a single value.

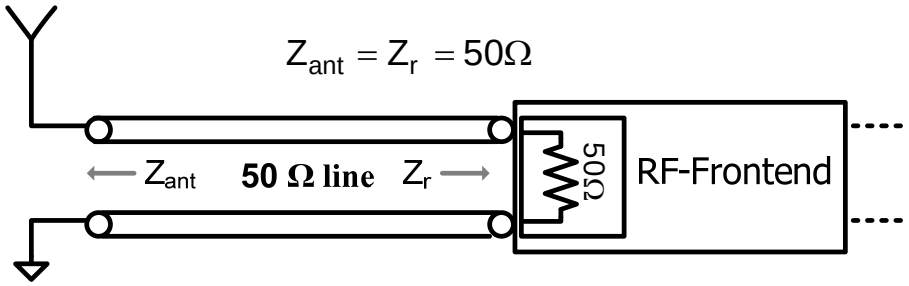

(a)

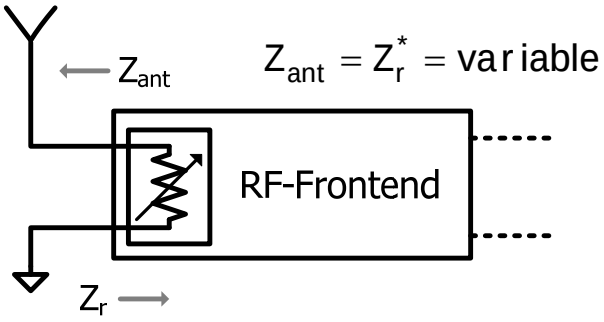

(b)

Figure 5.1 (a) Conventional impedance-matching and (b) variable-impedance matching between antenna and RF-frontend. Here, * notation represents complex conjugate.

To further increase the performance, variable-impedance matching can be utilized. This requires impedance tuneable RF-frontend with close integration with the antenna as illustrated in Figure 5.1(b). The variable-impedance matching can be achieved by a separate reconfigurable matching network [8-9] or it can be integrated in the RF-frontend chip. The latter is useful to reduce size and cost while producing a larger variety of resistance and reactance values.

The remarkable advancements of the cellular industry have initiated immense interest in multi-standard radio. For these systems, designers are challenged to provide fully integrated reconfigurable RF-frontends [10]. Among other requirements, tuneable input-impedance is a desired functionality. The study in [11] describes a 65 nm CMOS IC with on-chip low-ohmic switches for input-impedance control. In [12] a low-loss adaptive matching network implemented in silicon-on-glass technology was demonstrated. Recently, impedance-tuneable RF-frontends are also becoming commercially available [13-14].

These advancements in tuneable RF technology give the opportunity to develop antenna systems with variable-impedance matching and benefit from the high level integration between the antenna and the RF-frontend. Most of the above mentioned

examples are aimed for low-power cellular application. RF-Frontends designed for radar application on the contrary are required to meet large power handling capabilities. Moreover, in order to switch between two radar bands these frontends must operate over a wide frequency range (about 2:1). Therefore, the realization of such an input-impedance tuneable RF-frontend is highly challenging. Nevertheless, strong desire from radar industry will advance the development of concepts and components suitable to address the aforementioned requirements. Although reconfigurable antennas have recently been studied for wide scope of applications [16-17], the concept of frequency reconfiguration by variable input-impedance of the RF-frontend did not gain wide research interest yet. However, technological capabilities to tune the input impedance of RF modules are already available (e.g., the input impedance tuneable 65 nm CMOS RF-frontend is presented in [11]).

In Figure 5.1, the concept of variable-impedance matching is illustrated. Unlike conventional fixed-impedance matching (Figure 5.1(a)), here the input-impedance of the RF-frontend is tuneable (Figure 5.1(b)). Therefore, the input-impedances of both the antenna (Z_{ant}) and the RF-frontend (Z_r) are not obliged to be equal to a fixed value, typically 50 Ω, in order to minimize mismatch losses. Note that in Figure 5.1(b) the 50 Ω transmission line is not included. Here, any transmission line (connecting the antenna to the RF-frontend) is now becoming a part of the antenna and is included in Z_{ant} in Figure 5.1(b). This requires that this line length has to be known in advance. However, a small variation in this length (less than one twentieth of the wavelength) has in practice negligible influence on the antenna input-impedance.

This concept of variable-impedance matching has many fundamental advantages. For instance, many antenna elements show high radiation efficiency outside their instantaneous frequency band. As input impedances of most antennas are highly frequency dependent, a fixed 50 Ω impedance transformation only allows a good matching within a limited frequency range. For the concept presented in Figure 5.1(b), the input-impedance of the RF-frontend (Z_r) can be changed to match the antenna's input-impedance (Z_{ant}). In this way, frequency reconfigurable or tuneable antennas can be realized. This approach is useful to support communication standards, compensate for antenna mismatch losses due to aging or detrimental effects of objects in the close vicinity of the antenna (particularly important for hand-held cellular devices) or reduce any mismatch caused by manufacturing processes.

The approach can also be applied in selecting sub-bands of wideband or multi-band antenna systems. This can be achieved by matching the frontend to the corresponding impedance of a specific band while suppressing the signals from other bands through intentional mismatch. This will provide band selectivity, reduce the noise bandwidth and relax the constraints on the frontend filters. This approach avoids the use of switches in the radiating antenna element, and therefore reduces complexities and parasitic effects of RF-switches and their control lines. Furthermore, the proposed concept is helpful for phased array antennas to maintain good matching over large scan angles. This can increase the angular coverage of narrow-beam observations such as target tracking. In addition, angle dependent input-impedance matching provides the opportunity to perform spatial-filtering and thereby reduces interfering signal levels impending from accompanying angles.

Owing to these benefits there is a strong possibility that in future, variable-impedance matching will extensively be used for many applications, such as communications, cognitive radio, radio astronomy and radar.

5.2 THE THEORY OF POWER WAVES FOR VARIABLE IMPEDANCE MATCHING

IN this section the theoretical formulation backing the variable-impedance matching approach is described and discussed in detail.

In the theory of microwave circuit, the concept of travelling waves is a useful and straightforward method to provide physical explanation to many phenomena occurring in transmission lines. Travelling waves have been introduced by applying linear transformation to voltage and current and they provide a meaningful physical understanding of waves travelling along two opposite direction of a transmission line [18]. The travelling waves are defined as,

$$a_t = \frac{\sqrt{\mathrm{Re}\, Z_i}}{2\left|Z_i\right|}(V_i + Z_i I_i), \qquad b_t = \frac{\sqrt{\mathrm{Re}\, Z_i}}{2\left|Z_i\right|}(V_i - Z_i I_i) \tag{5.1}$$

Where, a_t and b_t are the travelling waves moving towards and from the i^{th} port respectively, while V_i and I_i are the voltage and current amplitudes flowing into the corresponding port. Z_i is the reference impedance or in other words the impedance seen from the i^{th} port looking towards the transmission line. Note that the value *2* in

the denominator has been included to represent the root-mean-square value of the voltages. From (5.1) it follows that if an antenna with input-impedance Z_{ant} is connected at i^{th} port, the reflection coefficient, as derived from the travelling wave formulation, is,

$$\Gamma_t = \frac{b_t}{a_t} = \frac{Z_{ant} - Z_i}{Z_{ant} + Z_i} \tag{5.2}$$

Now, for the situation depicted in Figure 5.1(b) the reference impedance Z_i can be replaced by the input-impedance of the RF-frontend Z_r.

$$\Gamma_t = \frac{Z_{ant} - Z_r}{Z_{ant} + Z_r} \tag{5.3}$$

$$\Gamma_t = \frac{Z_{ant} - Z_r}{Z_{ant} + Z_r} = \frac{\mathrm{Re}(Z_{ant}) + j\,\mathrm{Im}(Z_{ant}) - \mathrm{Re}(Z_r) - j\,\mathrm{Im}(Z_r)}{\mathrm{Re}(Z_{ant}) + j\,\mathrm{Im}(Z_{ant}) + \mathrm{Re}(Z_r) + j\,\mathrm{Im}(Z_r)}$$

where j is the imaginary unit which is defined as $j^2 = -1$. The time-average real power delivered to the antenna can be computed as,

$$P_{ant} = \frac{1}{2}\mathrm{Re}(V_i I_i^*) \tag{5.4}$$

From (5.1) we can derive,

$$V_i = \frac{|Z_r|}{\sqrt{\mathrm{Re}\,Z_r}}(a_t + b_t), \qquad I_i = \frac{|Z_r|}{Z_r\sqrt{\mathrm{Re}\,Z_r}}(a_t - b_t)$$

Placing these values of V_i and I_i into (5.4) follows,

$$P_{ant} = \frac{1}{2}\mathrm{Re}\left[\frac{|Z_r|^2\,(a_t + b_t)(a_t^* - b_t^*)}{Z_r^*\,\mathrm{Re}\,Z_r}\right]$$

$$P_{ant} = \frac{1}{2}\frac{|Z_r|^2}{\mathrm{Re}\,Z_r}\mathrm{Re}\left[\frac{Z_r(|a_t|^2 - |b_t|^2 + a_t^* b_t - (a_t^* b_t)^*)}{Z_r Z_r^*}\right]$$

$$P_{ant} = \frac{1}{2}\frac{|Z_r|^2}{\mathrm{Re}\,Z_r}\mathrm{Re}\left[\frac{(\mathrm{Re}\,Z_r + j\,\mathrm{Im}\,Z_r)(|a_t|^2 - |b_t|^2 + 2j\,\mathrm{Im}(a_t^* b_t))}{|Z_r|^2}\right]$$

$$P_{ant} = \frac{1}{2}\left(|a_t|^2 - |b_t|^2\right) - \frac{\mathrm{Im}\, Z_r \,\mathrm{Im}(a_t^* b_t)}{\mathrm{Re}\, Z_r} \tag{5.5}$$

$$P_{ant} \neq \frac{1}{2}\left(|a_t|^2 - |b_t|^2\right) \text{ if } \mathrm{Im}\, Z_r \neq 0 \tag{5.6}$$

From (5.5) and (5.6) we know that for a complex value of Z_r the total delivered power cannot be expressed straightforwardly as the difference in power carried by the incident and reflected travelling waves.

In order to allow for a more insightful analysis of the general case involving complex reference impedances, different formulations based on suitable linear transformations of port voltages and currents were proposed in [18-22]. The general form of the linear transformation of voltage and current can be expressed as,

$$a_0 = K_1 V_i + K_2 I_i, \quad b_0 = K_1 V_i - K_2^* I_i$$

Conversely, voltage and currents are,

$$V_i = \frac{K_2^* a_0 + K_2 b_0}{K_1 (K_2 + K_2^*)}, \quad I_i = \frac{a_0 - b_0}{K_2 + K_2^*}$$

By using this methodology, one can extract many linear transformations of voltages and currents. Among them, special attention is to be given to the concept of power wave which provides a more consistent description of the propagation of power in transmission lines and was introduced in [19-20] as,

$$a_p = \frac{V_i + Z_i I_i}{2\sqrt{\mathrm{Re}\, Z_i}}, \quad b_p = \frac{V_i - Z_i^* I_i}{2\sqrt{\mathrm{Re}\, Z_i}} \tag{5.7}$$

where, $Z_i = Z_r$. Therefore,

$$V_i = \frac{a_p Z_r^* + b_p Z_r}{\sqrt{\mathrm{Re}\, Z_r}}, \quad I_i = \frac{a_p - b_p}{\sqrt{\mathrm{Re}\, Z_r}}$$

Using the power waves in (5.4) gives,

$$P_{ant} = \frac{1}{2}\mathrm{Re}\left[\frac{(a_p Z_r^* + b_p Z_r)(a_p^* - b_p^*)}{\mathrm{Re}\, Z_r}\right]$$

$$P_{ant} = \frac{1}{2\,\mathrm{Re}\, Z_r}\mathrm{Re}\left[|a_p|^2 Z_r^* - |b_p|^2 Z_r + Z_r a_p^* b_p - (Z_r a_p^* b_p)^*)\right]$$

$$P_{ant} = \frac{1}{2\,\mathrm{Re}\,Z_r}\mathrm{Re}\left[\,|\,a_p\,|^2\,Z_r^* - |\,b_p\,|^2\,Z_r + 2j\,\mathrm{Im}(Z_r a_p^* b_p)\right]$$

$$P_{ant} = \frac{1}{2}\left(\left|a_p\right|^2 - \left|b_p\right|^2\right) + \frac{\mathrm{Re}(j\,\mathrm{Im}(Z_r a_p^* b_p))}{\mathrm{Re}\,Z_r} \tag{5.8}$$

The second term in (5.8) is zero for any real- or complex valued Z_r. Therefore, the total power delivered to the antenna can be expressed as the difference in power carried by the incident and reflected power waves.

$$P_{ant} = \frac{1}{2}\left(\left|a_p\right|^2 - \left|b_p\right|^2\right) \tag{5.9}$$

When the reference impedance (in this case Z_r) is complex, the power-wave definition of reflection coefficient is more meaningful than the more commonly used travelling-wave definition. The reflection coefficient for power waves can now be derived [20] as,

$$\Gamma_p = \frac{b_p}{a_p} = \frac{V_i - Z_r^* I_i}{V_i + Z_r I_i} = \frac{\dfrac{V_i}{I_i} - Z_r^*}{\dfrac{V_i}{I_i} + Z_r}$$

$$\Gamma_p = \frac{Z_{ant} - Z_r^*}{Z_{ant} + Z_r} \tag{5.10}$$

Equation (5.10) shows that Γ_p is zero when the antenna and the RF-frontend impedances are complex conjugates of each other. It this case, there is no reflected power wave (b_p) and maximum power will be delivered to the antenna for radiation. It is worth pointing out here that the travelling-wave definition of reflection coefficient, presented in (5.2) and (5.3), does not satisfy the above mentioned condition and hence fails to provide a physical meaning when the reference impedance is complex. In addition, as explained in [20] for the travelling-wave definition the magnitude of reflection coefficient can be larger than unity even for a passive system. On the other hand, the magnitude of the power-wave reflection coefficient is smaller than unity, that is $\left|\Gamma_p\right| < 1$, provided that the real parts of Z_{ant} and Z_r have the same signs, as always expected for passive devices.

Despite the fact that the theory of power wave has been introduced many decades ago, it is still not widely used by the antenna and microwave engineer community

(some applications of power wave method are seen for RFID tag design [23]). For commonly used fixed 50 Ω impedance-matching one can resort to the much simpler travelling wave theory. However, for a co-design of antenna with the RF-frontend where the impedance is not limited to any real values, a correct understanding of the power-wave theory is crucial.

5.3 THE EXPERIMENTAL VERIFICATION OF THE CONCEPT

PREVIOUS sections discussed the concept of variable impedance. This section is dedicated to the experimental verification of the concept of frequency tuning with variable-impedance matching. In this study, a microstrip antenna is selected as the reference antenna and a 65nm CMOS IC, designed at the University of Twente, as the input-impedance tuneable RF-frontend.

Figure 5.2 shows the implementation of two RF-frontends in a single 65nm CMOS IC. The receivers can be connected or disconnected by on-chip low-ohmic switches and thereby change their input-impedance. The two-receiver modes were designed to perform cross-correlation spectrum sensing (explained in detail in [11]). In [24] a brief description of the RF-frontend with regard to its variable impedance capability is presented.

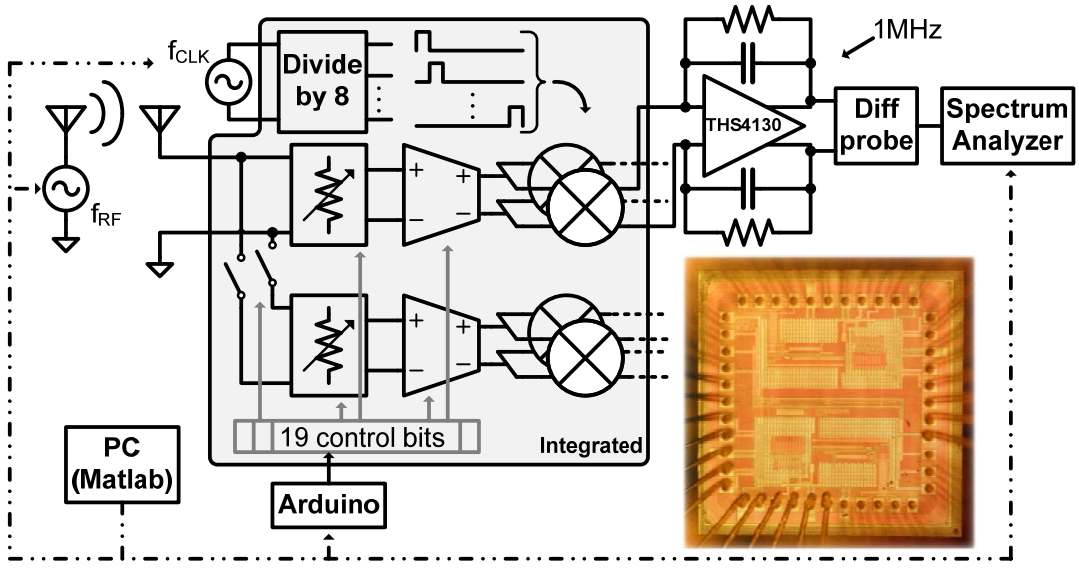

Figure 5.2 Block diagram of CMOS RF-frontend implementation and measurement setup (Courtesy of Mark S. Oude Alink)

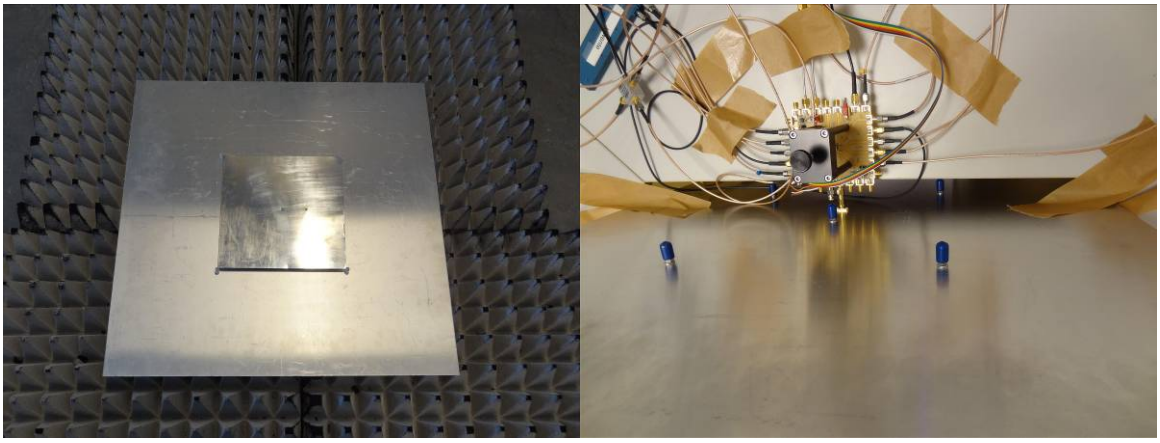

(a) (b)

Figure 5.3 (a) Antenna prototype, (b) CMOS chip attached at the back of the antenna

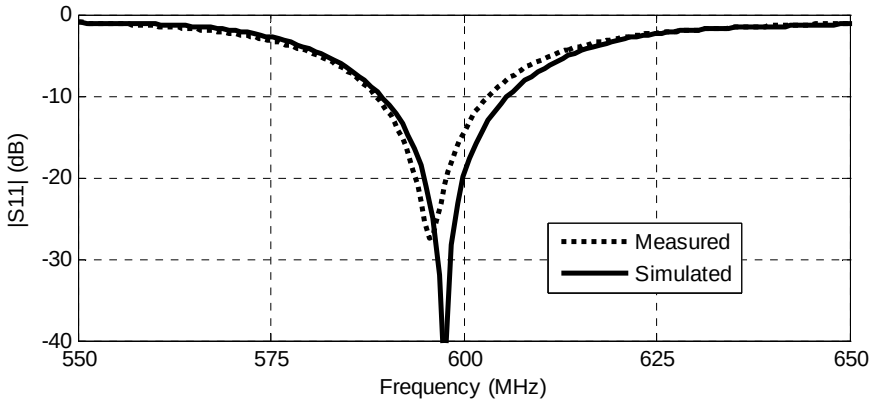

Figure 5.4 Numerical and measurement results of reflection coefficient (for 50 Ω reference impedance)

To verify the concept of variable-impedance matching experimentally, a narrowband microstrip antenna was used (see Figure 5.3(a)). The measurement setup is illustrated in Figure 5.2. Here, the dielectric wedge antenna of [25] was used as the transmit antenna while the microstrip antenna was used as the receive antenna followed by the impedance-tuneable RF-frontend. In this case a 50 Ω adapter was used (as shown in Figure 5.3(b)) to connect the antenna to the RF-frontend. The length of the adapter is less than one thirtieth of the wavelength at 600 MHz and hence in practice has no influence on the input impedance.

The reflection coefficient and the input impedances of the microstrip antenna are presented in Figure 5.4 and Figure 5.5, respectively. Good agreements are observed between the numerical and experimental results. The microstrip antenna radiates at 595 MHz with an instantaneous bandwidth of about 15 MHz ($|S_{11}| \leq -10\,dB$) for 50 Ω reference impedance. On the contrary, the antenna shows high absolute gain from 500

MHz to 700 MHz (see Figure 5.6) which implies that the antenna possesses sufficient radiation efficiency in this band; hence adequate radiated power can be expected within this band when properly matched to the reference impedance. Figure 5.6 reveals that for 50 Ω reference impedance the 3-dB gain bandwidth is limited to 50 MHz while a variable-impedance matching will give the opportunity to expand this value by a factor of four. It is worth pointing out here that only providing impedance match will not assure that the antenna will radiate efficiently and sufficient antenna gain over the whole tuneable-band is needed. Afterwards by changing the matching impedance, in this case the input- impedance of the CMOS RF-frontend, the operational band can be tuned.

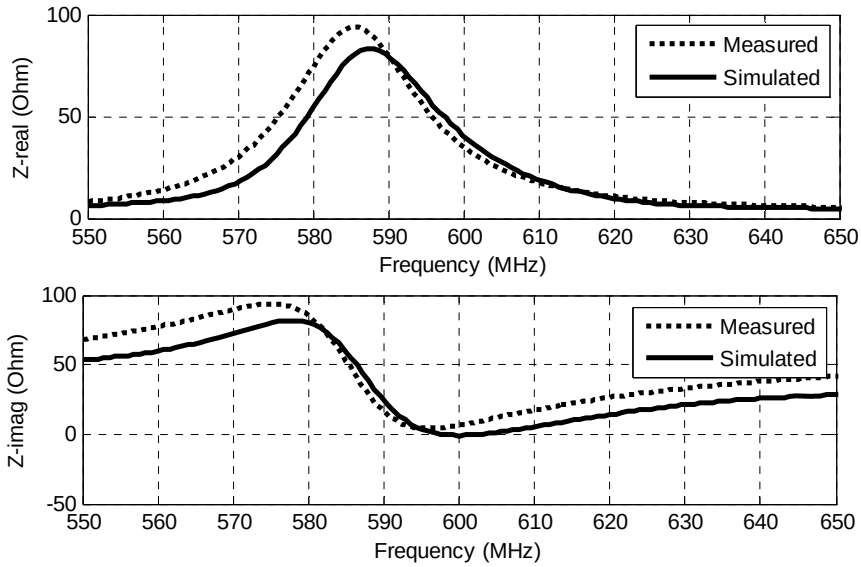

Figure 5.5 Input impedances of the microstrip antenna

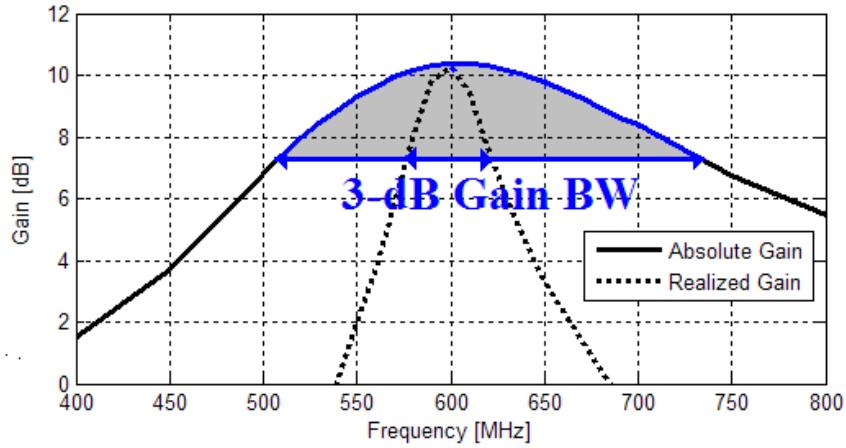

Figure 5.6 Broadside antenna gains against frequency

By using experimental results regarding the antenna input-impedance (see Figure 5.5) one can easily determine the input impedance of the CMOS chip needed for

optimal antenna driving. To tune the operational frequency band, the settings of the receiver module were altered (as explained in the previous section) in order to achieve these required impedance values.

In Figure 5.7 and Figure 5.8, the measured input impedance of the antenna are compared to the input impedance of the CMOS chip for two different settings as typical examples. For settings 1 and 2, the conjugated impedance matching occurs around 570 MHz and 600 MHz, respectively. In the frequency range between 560 and 580 MHz the antenna is highly inductive. As discussed in Section 5.3, maximum power will be delivered to the antenna when the impedance of the chip is complex conjugate of the antenna impedance. In order to achieve conjugate matching around 570 MHz, the impedance value of the chip is selected accordingly as shown in Figure 5.7. This brings the corresponding power-wave reflection coefficient, presented in (5.10), to its minimum value in the above mentioned frequency band. On the other hand, as depicted in Figure 5.9, the travelling wave reflection coefficient, defined in (5.3), will reach its minimum value at 625 MHz.

In Figure 5.10, the measured received signal levels are shown and we notice here that for impedance setting 1 the received signal strength reaches its highest value close to the frequency band predicted by power wave theory. Furthermore, as discussed in Section 5.3, here the travelling wave reflection coefficient magnitude is larger than 0 dB from 550 MHz to 590 MHz while for the power wave formulation this remains below 0 dB as expected for passive devices.

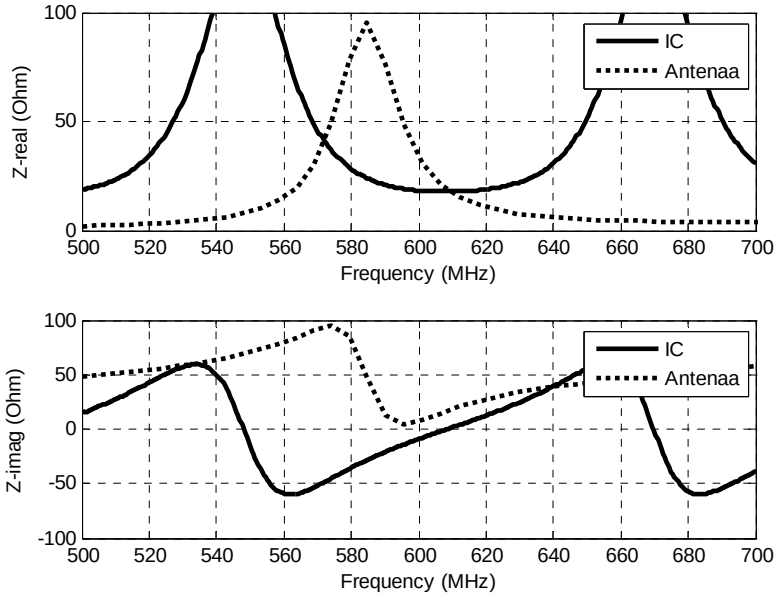

Figure 5.7 Impedance comparison of the antenna and the IC for setting 1

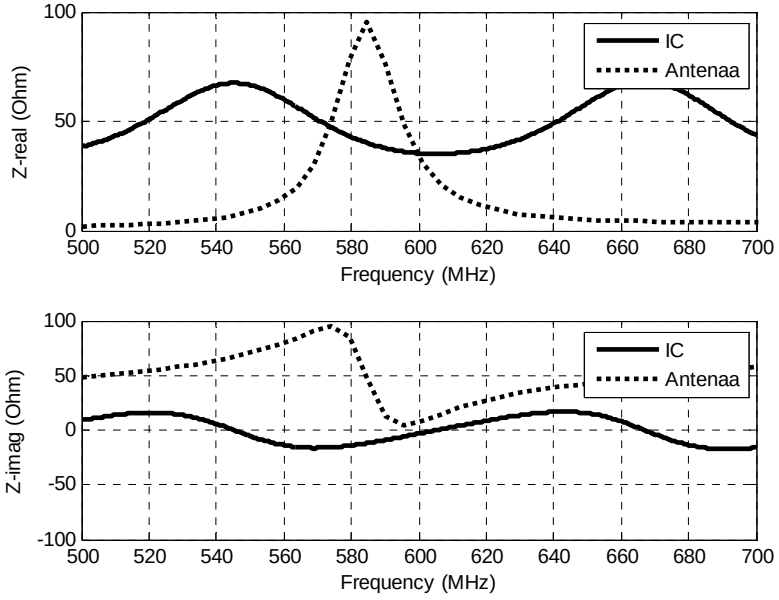

Figure 5.8 Impedance comparison of the antenna and the IC for setting 2

Similarly, to assure good matching around 600 MHz, an almost purely resistive 30 Ω (see Figure 5.8) input-impedance was selected, which in turn shifted the peak of the received signal to 600 MHz. In this way, the total operational bandwidth of the antenna increases from 10 MHz to more than 30 MHz.

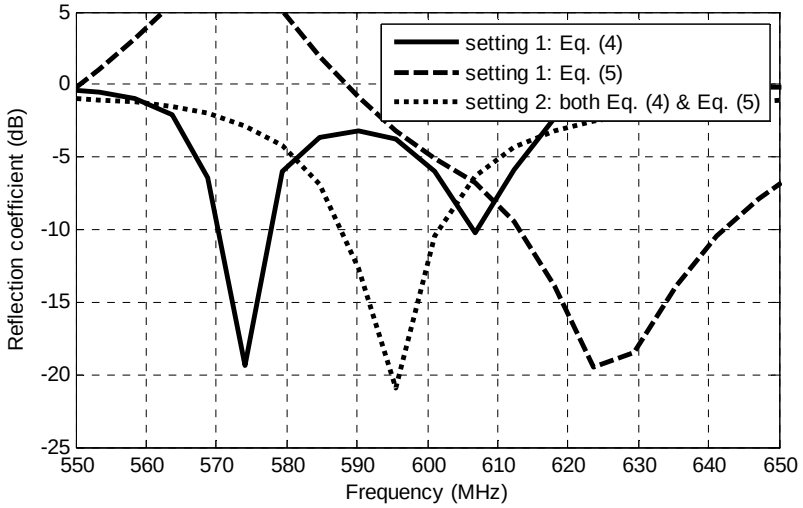

Figure 5.9 Power wave and travelling wave reflection coefficients

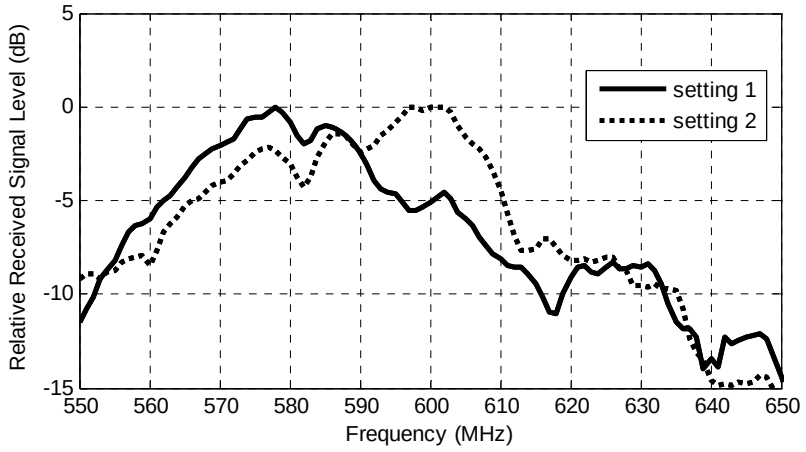

Figure 5.10 Received signal level for variable impedances

5.4 FREQUENCY RECONFIGURATION WITH VARIABLE IMPEDANCE MATCHING

SECTION 5.3 experimentally demonstrates the concept of variable-impedance matching on the basis of a simple microstrip antenna. In this section, the concept proposed is applied for antenna operational frequency tuning over a large frequency band. For dual- or multi-band antennas, an operational band can be selected by matching the frontend to the corresponding input impedances in the specific band while suppressing, in this way, the signals from other bands by deliberate mismatch. For this investigation, an E-slot microstrip antenna is presented for which the operating frequency can be shifted from L-band to S-band by using the variable-impedance matching approach discussed in the previous sections.

5.4.1. The antenna topology

The physical layout of the aforementioned dual-band E-slot antenna is sketched in Figure 5.11. The proposed antenna mainly differs from conventional microstrip antennas by containing the double E-slots and a blind-via feeding.

The dual-frequency operation has been achieved by inserting the E-slots in the radiating patch while the blind-via feeding section reduces the spurious reactance of the probe-feed. In the following sections these features are discussed in more detail. In Appendix C some additional findings are reported.

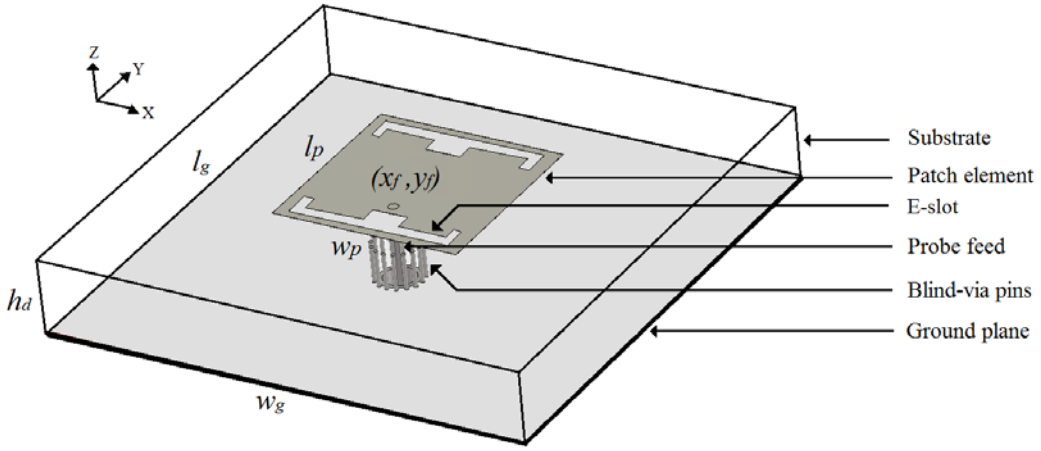

(a)

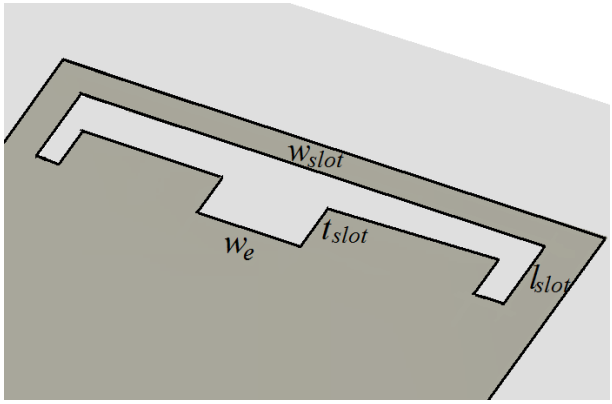

(b)

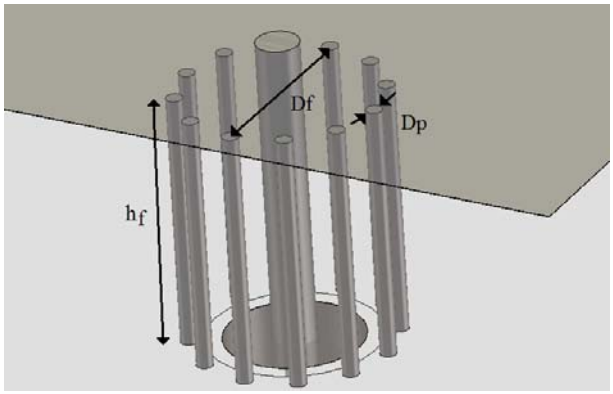

(c)

Figure 5.11 E-slot antenna (a), the slot section (b) and the feeding section (c). Geometrical characteristics of the structure: w_p=*34 mm*, l_p=35 *mm*, w_g=90 *mm*, l_g=90 *mm*, h_d=9.144 *mm*, x_f=0 *mm*, y_f=-5.5 *mm*, w_e=5 *mm*, w_{slot}=33 *mm*, l_{slot}=*6.5 mm*, t_{slot}=*4.5 mm*, D_f=5 *mm*, h_f=7.62 *mm*, D_p=0.5 *mm*. The number of vias in the fence is 11, and the diameter of the center probe is 1.28 *mm*. The origin of the adopted coordinate system is located at the center of the radiating patch.

5.4.1.1 The E-slot

Dual-band planar antennas are commonly realized by inserting slots in the radiating structure. This approach provides the opportunity to control the operating band of the TM_{030} mode and to transform the three-lobe radiation pattern of this mode to the desired single-lobe pattern.

In comparison with two parallel slots [26], the proposed E-slot structure separates the TM_{010} mode and the TM_{030} mode over a wider frequency band. The parameter w_e (see Figure 5.11(b)) influences the current path of the third mode due to high surface current distribution at these locations. Increasing this value leads to a shorter current path for the TM_{030} mode and thereby swifts the resonating frequency towards the higher band. On the other hand, the central slots only marginally affect the first mode (TM_{010}) as the current density of the subsequent mode is particularly low at the slot locations.

In Figure 5.12, the effect of the slot width (w_e) on the frequency ratios of the two aforementioned modes is depicted. By controlling the width of the central slot we can influence the frequency band of the TM_{030} mode. It is evident in Figure 5.12 that TM_{010} mode remains unaffected by the variations of this parameter.

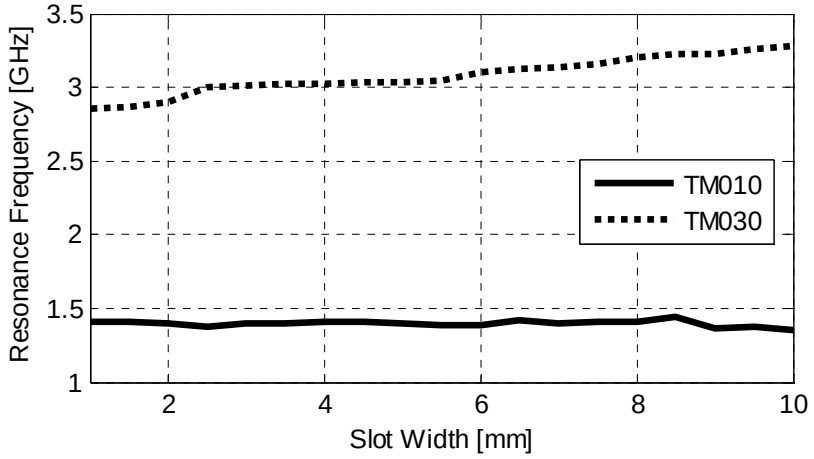

Figure 5.12 Simulated results of the resonance modes vs central slot width (w_e)

5.4.1.2 Blind-via feeding

The blind-via feeding section is shown in Figure 5.11(c). A detailed study of the proposed feeding structure for a single-band microstrip antenna is presented in

Chapter 2. The effect of the proposed feeding structure on the reference antenna element is discussed here for completeness.

It is known that the input impedance of an antenna element fed by a probe possesses a large reactive part. For the proposed E-slot microstrip antenna this reactive value is particularly high for the TM_{030} mode for which the thickness of the dielectric substrate relative to the wavelength is large compared to the TM_{010} mode. Here, the substrate thickness is about $0.09\times\lambda_0$, λ_0 being the free-space wavelength at 3 GHz.

High reactive input impedances (in particular capacitive values) of the antenna make it difficult to match the device to the RF-frontend. By minimizing the effective length of the probe-feed, the reactive part of the input impedance can be reduced. To achieve this goal, a via-pin fence can be used to encircle the probe resulting in a coaxial-line-like section partly slipped in the antenna substrate (see Figure 5.11(c)). The proposed approach can significantly reduce the spurious reactance of the probe-feed. In Figure 5.13, the simulated input impedance of the radiating element with and without blind-via (BV) fence is shown. The obtained results illustrate that the BV fence structure significantly reduces the antenna input reactance and flattens the antenna resistance around the TM_{030} mode. For the lower frequency band the via-pins

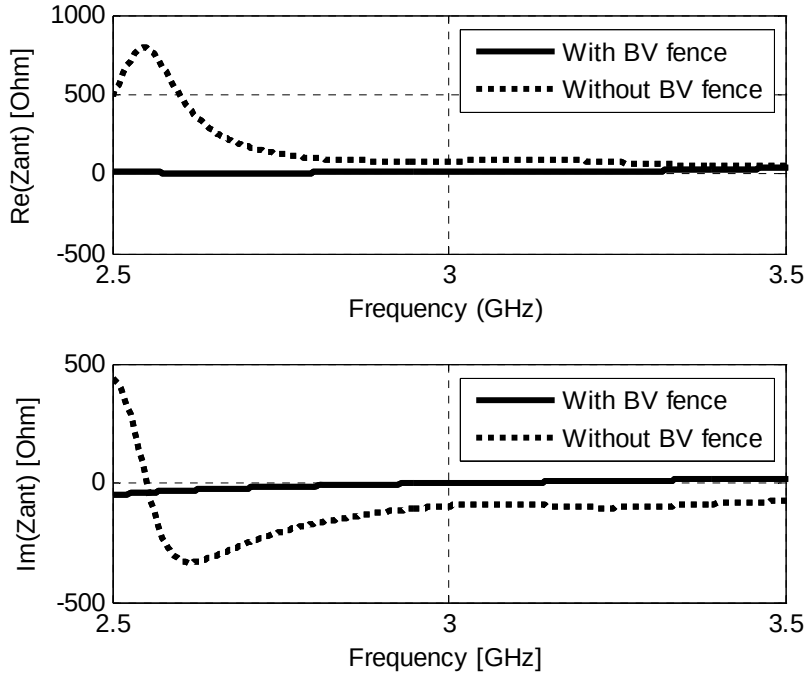

Figure 5.13 The effect of the blind-via fence on the impedance of the E-slot microstrip antenna

have negligible effect on the input-impedance. The geometrical parameters (in particular the fence diameter D_f) of the fence can be used to control the input impedance of the antenna.

5.4.2. The antenna performance

Based on the antenna architecture discussed in the previous section, an antenna element with high radiation efficiency in L- and S-radar bands (1.2-1.4 GHz and 2.9-3.5 GHz) was designed. The antenna is etched on Rogers high-frequency material, RO4003, with ε_r = 3.5. The prototype of the antenna is presented in Figure 5.14. For the experimental data the Agilent E8364B network analyser was used. The length and the width of the radiating element here are less than $\lambda_0/6$, λ_0 being the free-space wavelength of the first mode ($f_c = 1.4 GHz$). The size of the antenna element was reduced by avoiding air-substrate and by increasing the thickness of the dielectric substrate. This compact size makes it suitable for dense array environment.

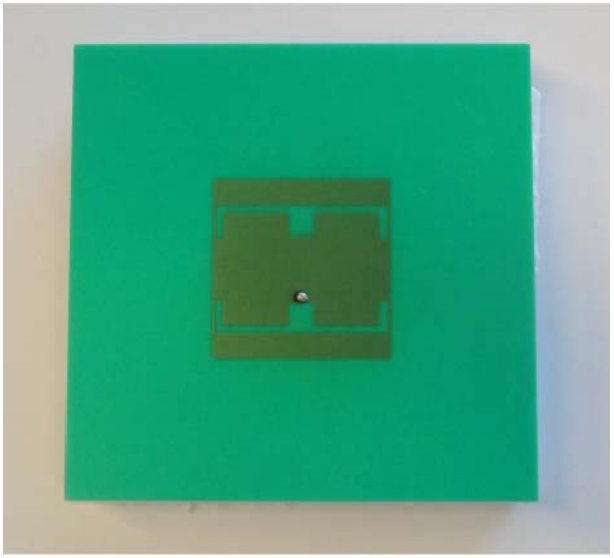

Figure 5.14 E-slot microstrip antenna prototype

The measured input impedance of the antenna is compared with the simulation results and a close agreement was observed (Figure 5.15). The fundamental mode (TM_{010} mode) resonates at 1.45 GHz. Around the fundamental mode we notice two circuitry resonances (peaks in the real part of the input impedance curve and zeros in the imaginary part) caused by loading the patch with complex-valued impedance of the slots. These resonances however do not correspond to excitation of new current modes on the patch. The second (TM_{020}) and the third (TM_{030}) harmonics are efficiently excited around frequencies of 2 GHz and 3 GHz, respectively. Due to the

presence of the E-slots, the higher order harmonics are shifted towards the lower frequency range.

The measured and simulated boresight absolute gains (which do not consider any reflection occurring at the feeding location) of the antenna are plotted in Figure 5.16. Around 1.45 GHz and 3 GHz the antenna's absolute gain reaches the local maxima as a result of radiation of the fundamental and the third harmonic modes, respectively. The measured absolute gain is 6.8 dBi at 1.47 GHz while it is 5.4 dBi at 3 GHz. It should be pointed out here that the absolute gain remains higher than 3 dBi from 1.05 GHz to 1.55 GHz and again from 2.7 GHz to 3.2 GHz. This indicates adequate radiation efficiencies at the aforementioned frequency bands. Here, the antenna gain values are slightly less than that for a conventional patch (about 6.0-6.5 dBi) due to the reduced antenna aperture at the lower band and the surface-wave loss at the upper band.

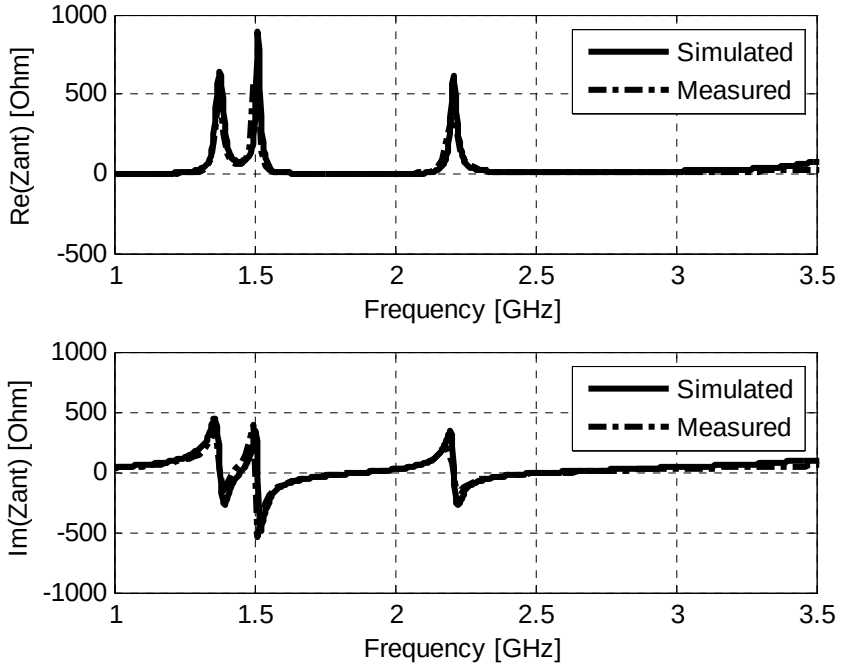

Figure 5.15 Input-impedance of the E-slot microstrip antenna

The measured and the simulated reflection coefficients of the antenna for two different input-impedance settings as typical examples are shown in Figure 5.17. In this example, the frequencies for which the absolute gain reaches its maximal values are selected. Here, the experimental data is measured for 50 Ω reference impedance and the input-reflection coefficient for other impedance values were extracted according to (4). Figure 5.17 reveals that by changing the reference input impedance from about 10 Ω to 75 Ω (both in simulations and post-processing of the experimental

results), the operating frequency can be shifted from L to S band. The realization and the details of an input-impedance tuneable RF-frontend are discussed in [11] and in [24].

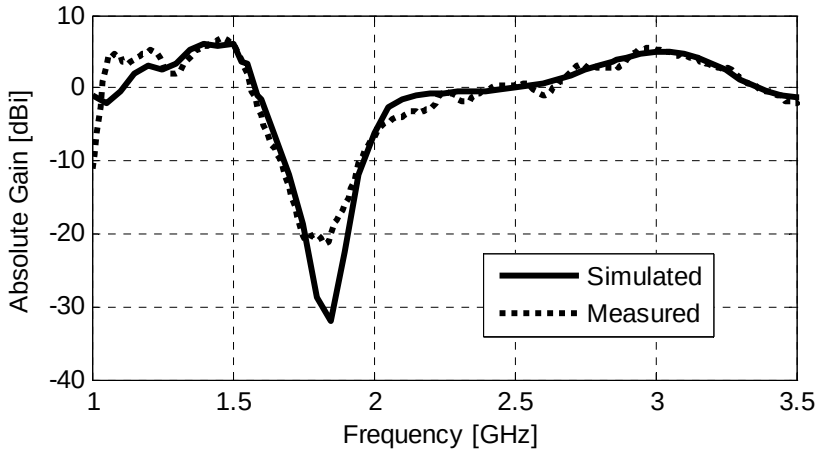

Figure 5.16 Boresight absolute gain as a function of frequency

Figure 5.15 shows that within the radar L-band (1.2 GHz – 1.4 GHz) the input-impedance varies with the frequency. This provides opportunity to tune the operational band by proper impedance matching. For the E-slot antenna, the input-impedance of the antenna is inductive within the aforementioned band. It is worth mentioning here that inductive antenna impedances are often advantageous for conjugate matching, since in an integrated circuit capacitive impedances are easier to synthesize compared to inductive ones. In Figure 5.18, it is shown that the operational band shifts towards the higher frequencies when the resistive part of the input impedance increases while the reactive part decreases.

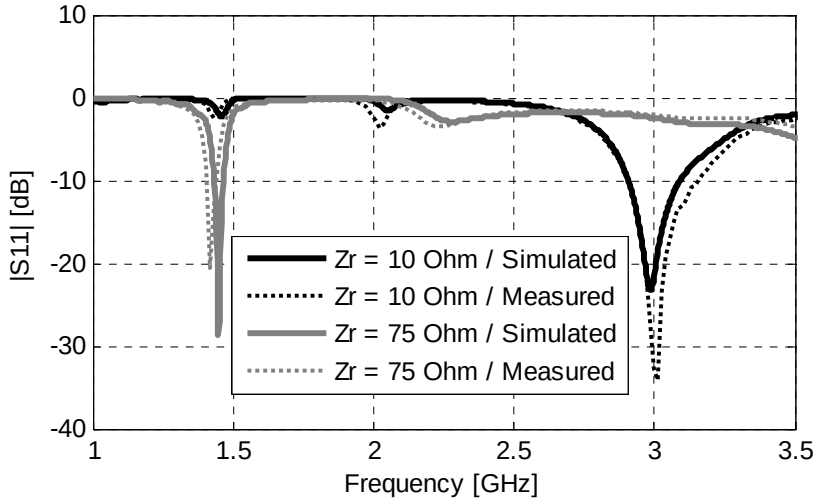

Figure 5.17 Simulated and measured power wave reflection coefficient for two different impedance settings

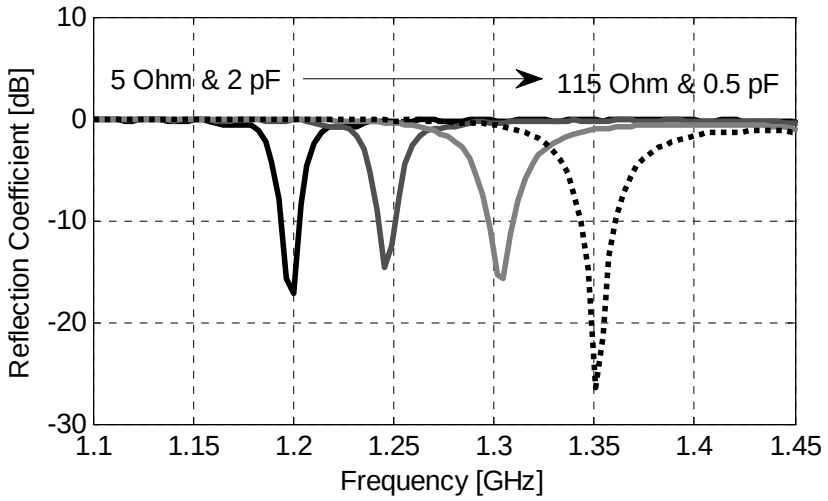

Figure 5.18 Power-wave reflection coefficient of the antenna for various complex reference impedance settings

The far-field radiation patterns are presented in Figure 5.19 and Figure 5.20. Measured and theoretical results indicate low cross-polarisation levels for the lower band. In the higher band the cross-polarisation levels increase for H-plane due to the larger electrical thickness of the dielectric substrate. Furthermore, symmetric radiation patterns for both upper and lower frequency bands are evident owing to the symmetrical geometry of the antenna.

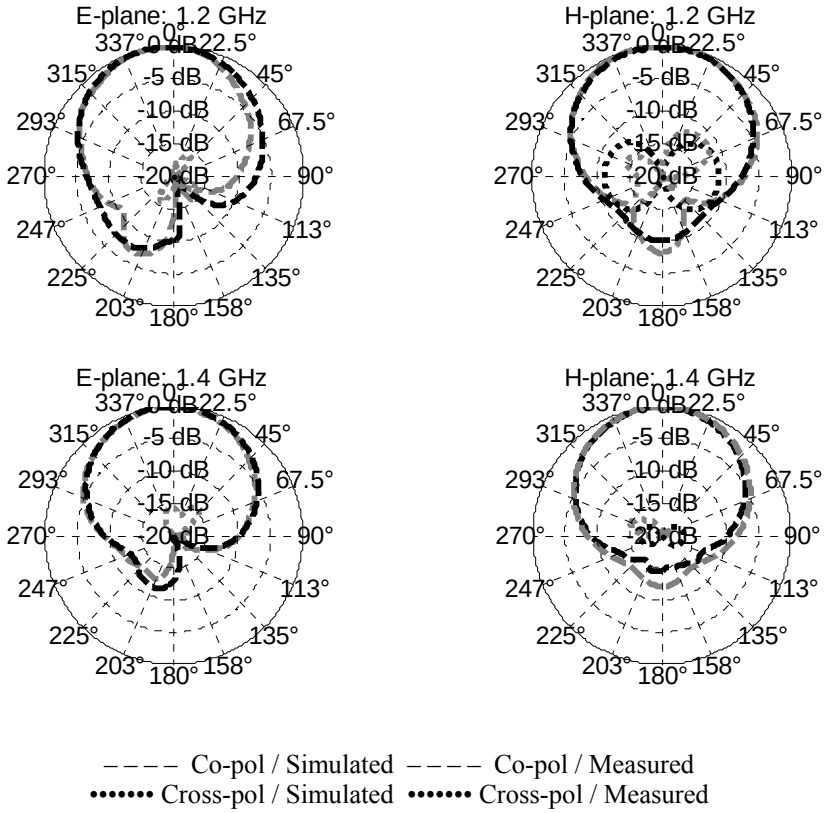

Figure 5.19 Normalized radiation patterns in L-band

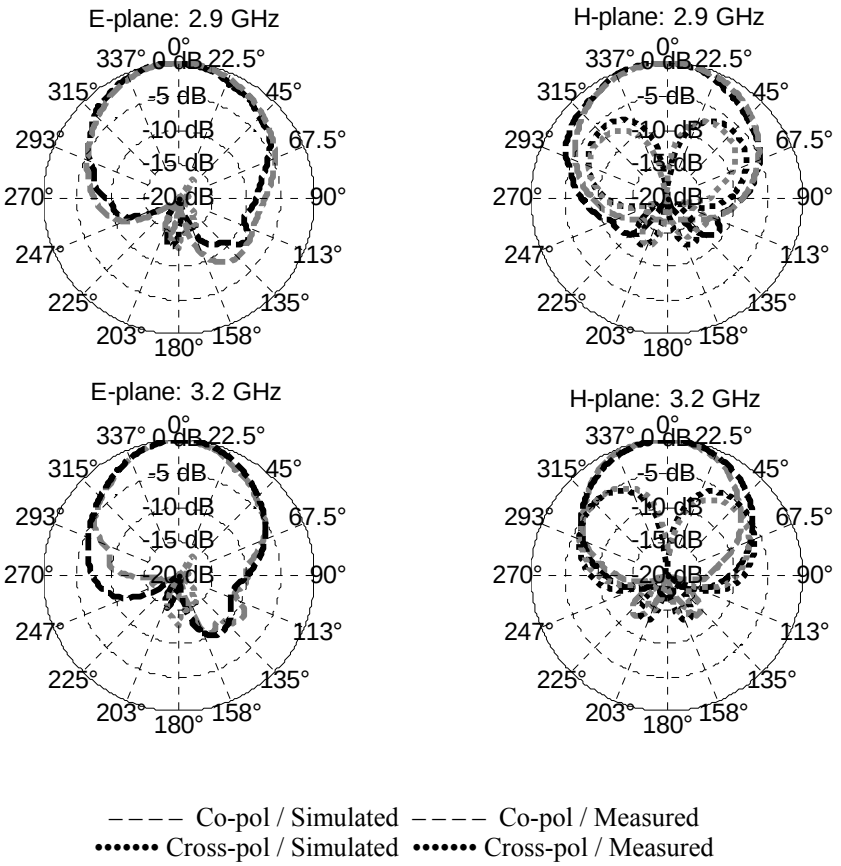

Figure 5.20 Normalized radiation patterns in S-band

5.5 VARIABLE-IMPEDANCE MATCHING FOR PHASED ARRAY ANTENNAS

IT is widely known that the active impedance of a phased array antenna varies with scan angle and the scale of this variation depends on the amount of the couplings between the radiating elements. As a result, a single predefined reference impedance value gives an optimal impedance matching for a single beam direction (usually for boresight scanning). For other directions the reflected signal increases due to impedance mismatch.

Generally variation of the active impedance is minimized by reducing the antenna mutual couplings with proper antenna design and optimization. However, the outcome of such approach is highly design specific. To eliminate this problem utterly, a scan dependent variable-impedance matching is desired [27]. This can be realized by changing the input-impedance of the RF-frontend not only as a function of the desired band, but also if needed, as a function of the scan angle.

To investigate the concept of scan dependent matching, an infinite array of E-slot elements with triangular grid was analysed. The numerical model of the infinite array is illustrated in Figure 5.12 where an element spacing of 53.6 mm was selected to allow ±60° grating-lobe free scan angle up to 3 GHz. The current work is done having in mind electrically very large arrays with thousands of radiating elements. The infinite array analysis is useful to evaluate the active-element impedances of such large arrays. However, it is worth mentioning here that the performances of elements close the edge of a finite array will be different from the element within an infinite array.

In Figure 5.22 and Figure 5.23, the active input impedances of the antenna are shown for different scan angles. Along the E-plane coupling with the adjacent elements are less due to the triangular array arrangement. Hence, the impedances remain more stable with the frequency within the operational bands. We notice in Figure 5.23 that along the H-plane the impedance variation is more for the L-band in comparison with the S-band (at lower frequency the electrical distance between the elements is less resulting in a larger coupling). The active impedance within the L-band is once more presented in Figure 5.24.

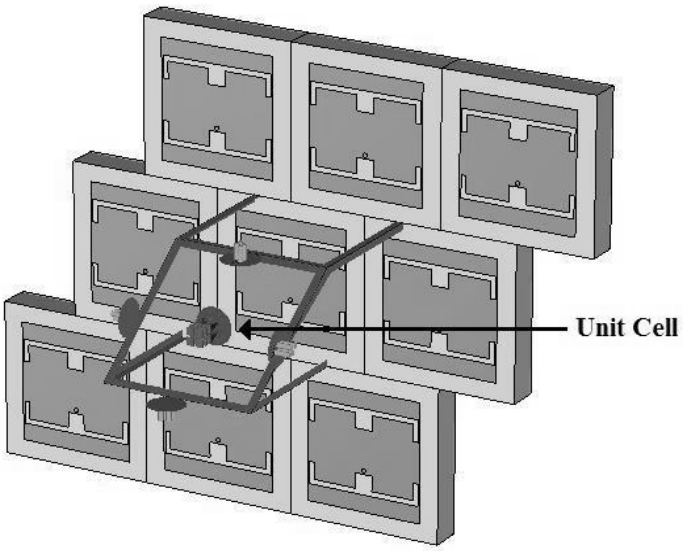

Figure 5.21 E-slot infinite array configuration with 53.6 mm element periodicity

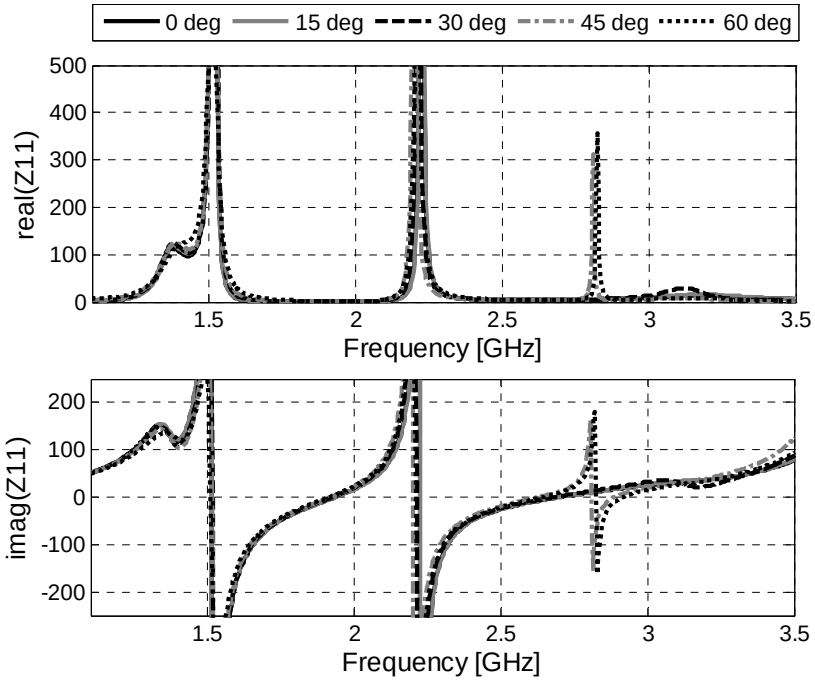

Figure 5.22 E-plane active input impedance versus frequency for various scan angles

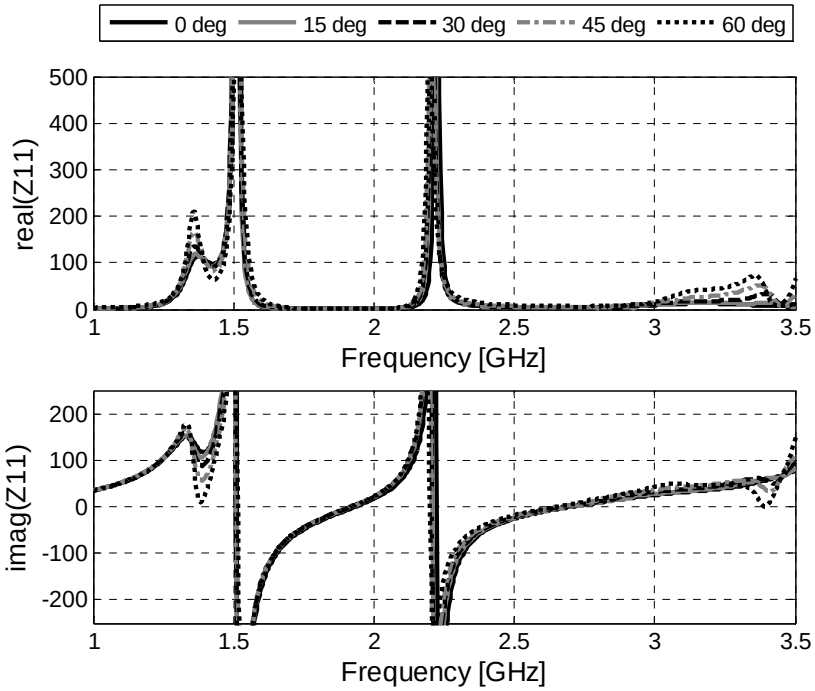

Figure 5.23 H-plane active input impedance versus frequency for various scan angles

The scan-angle (θ) dependency of the impedances can be expressed with polynomial functions as follows:

$$Z^{real}(f,\theta) = C_0^{real}(f) + C_1^{real}(f).\theta + C_2^{real}(f).\theta^2 + ... + C_N^{real}(f).\theta^N \tag{5.11}$$

$$Z^{imag}(f,\theta) = C_0^{imag}(f) + C_1^{imag}(f).\theta + C_2^{imag}(f).\theta^2 + ... + C_N^{imag}(f).\theta^N \tag{5.12}$$

where C_{0-N} are the polynomial coefficients and θ is scanning angle in degrees. As the variation in the impedances is not abrupt, a third order (N=3) polynomial function can estimate these values with about 0.97 correlation of determination. Note that the ability to analytically express the scanning behaviour of the antenna with polynomial functions will significantly reduce the total number of numerical analysis necessary for the co-design of the antenna and RF-frontend. To extract the equivalent mathematical expression, numerical active-impedances of only five scanning angles (0°, 15°, 30°, 45°, 60°) were used. Figure 5.25 shows the H-plane active input impedances as a function of the scanning angle at 1.37 GHz as a typical example. Here, we observe a nearly perfect fit to the data curve.

In Figure 5.26, the frequency-domain behaviour of the coefficients C_{0-N} of (5.11) and (5.12), conveniently expressed as 6th-order polynomial functions, is shown. For

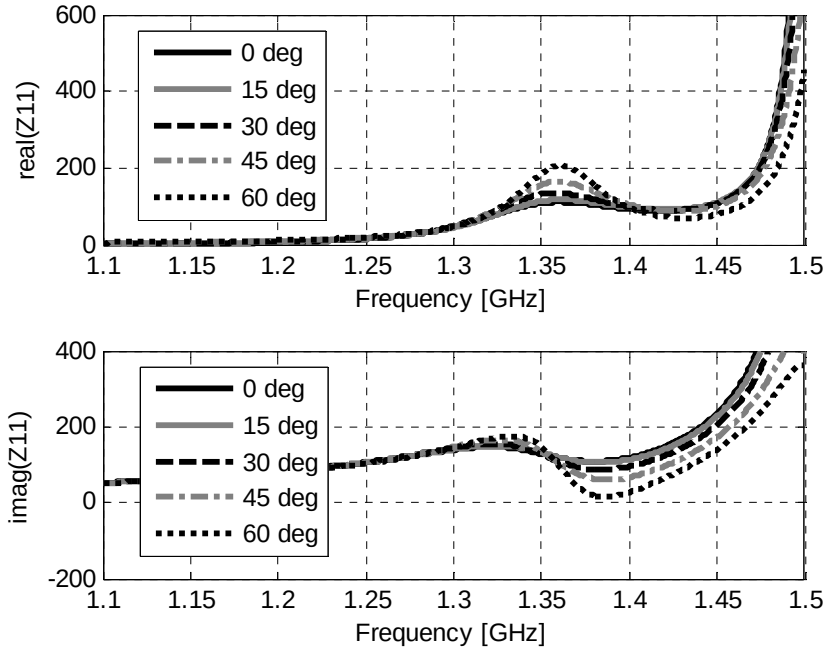

Figure 5.24 H-plane active input impedance versus frequency in L-band

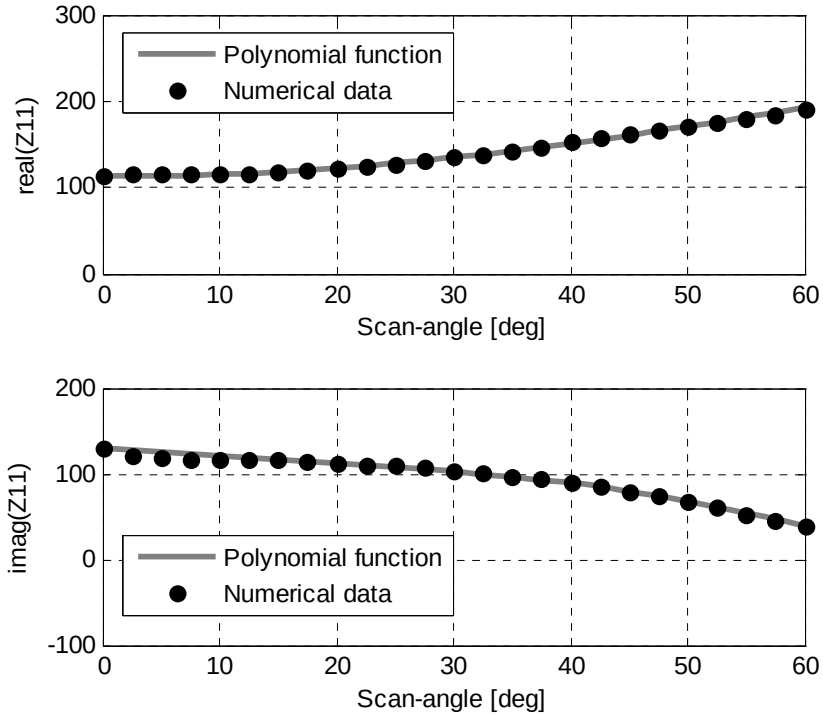

Figure 5.25 H-plane active input impedance versus scan-angle at 1.37 GHz

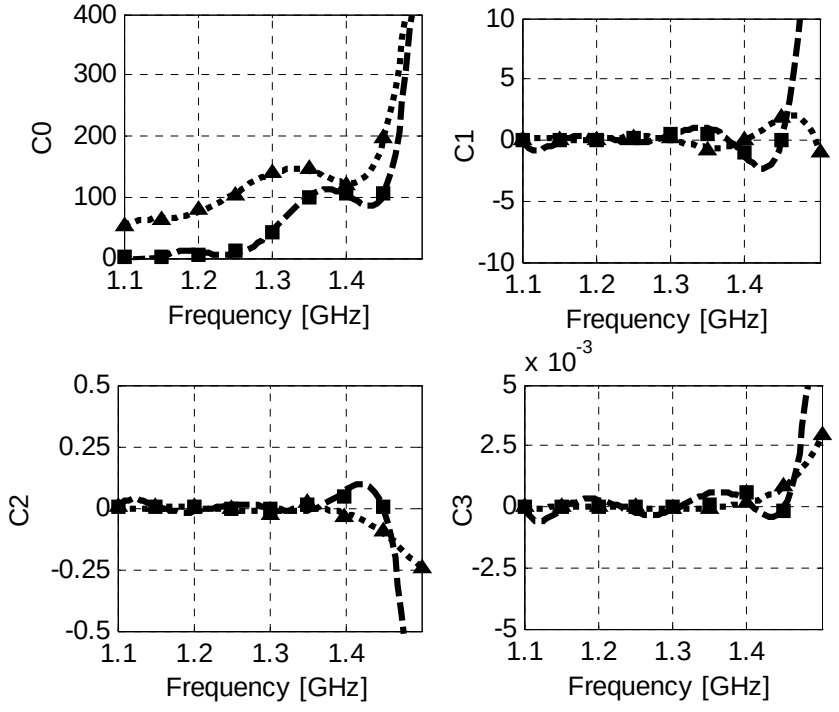

Figure 5.26 Polynomial coefficients of equations (5.11) and (5.12) for H-plane as a function of frequency

f < 1.3 GHz, the higher order coefficients become negligible (resulting in an almost constant value of impedances). On the contrary, for $f > 1.3\ GHz$ these coefficients increase and their impact cannot be neglected. In this context, it is worth noting that the c_0 coefficient reveals the frequency-domain behaviour of the antenna input-impedance for 0° scanning angle.

In Figure 5.27, the active reflection coefficients are illustrated. Here, these active reflection coefficients are computed according to (5.10). In Figure 5.27(a), the reference impedances were considered constant for all scan angles and were selected to provide an optimal matching condition for θ=0° angle at 1.37 GHz. Here, we notice that the reflection coefficient increases with the scan-angle. Note that within the operational bands, the highest variation in active impedance is around 1.37 GHz.

If further improvement of the matching condition is desired for the utmost scan angles, an impedance matching where the reference impedance will vary with the scan angle is required. Figure 5.27(b) provides an example of this approach. Here, the reference impedance is conjugate-matched to the corresponding active antenna impedances and hence a reduction of the active reflection coefficient is observed for off-boresight angles (the active-antenna impedances at 1.37 GHz are presented in Figure 5.25). In this example, the reference impedance is set to provide a minimum reflection at 1.37 GHz. As a result the realized gain is maximized. In this case, the realized gain of each element can be improved by 0.6 dB for θ=60°. Figure 5.27(b) reveals that the active-impedance bandwidth (at -10 dB level) is 50 MHz. This bandwidth can be improved at the expense of reduced matching, known from the Bode-Fano criterion [28-29].

This approach of scan dependent impedance matching is helpful for phased array antennas to maintain good matching over large scan angles. In addition to this advantage of sustaining better matching, the proposed approach has another potential for phased array systems. An angle dependent input-impedance matching provides the opportunity to perform some spatial-filtering. Any signal approaching from directions other than the main beam will undergo larger suppression. This will assist beam forming networks to minimize the interferences of unwanted signals impending from adjacent angles.

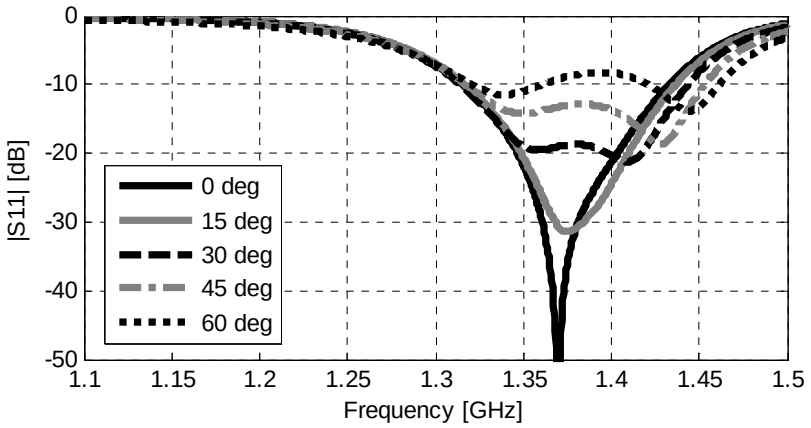

(a)

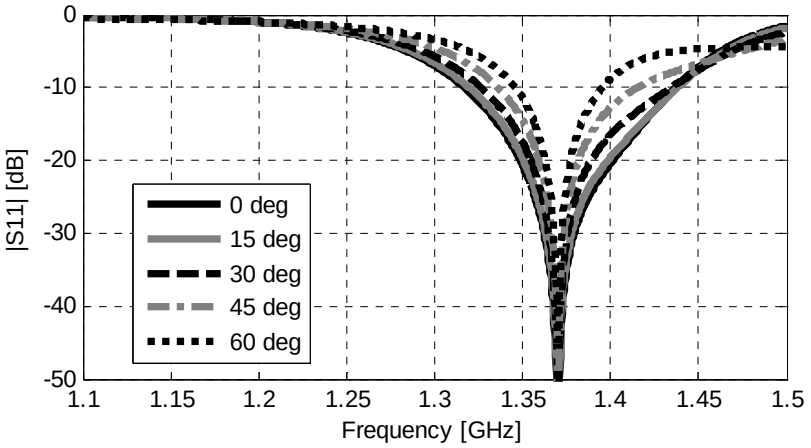

(b)

Figure 5.27 Magnitude of active reflection coefficient versus frequency along H-plane for (a) reference impedance match to the impedance value for θ=0° at 1.37 GHz (Z_r = 114 – 130j) and (b) reference impedance match to the corresponding active antenna impedances at 1.37 GHz

5.6 CONCLUSION

THE concept of antenna frequency agility by means of variable-impedance matching between the antenna and the RF-frontend was investigated in this chapter theoretically and experimentally on examples of two different antennas.

The theory of power waves has been applied to antenna and front-end circuit. The theory demonstrate possibilities to achieve antenna – front-end matching at an arbitrary (including complex-valued) value of the interface impedance. Usage of an arbitrary value of the interface impedance allows for power transfer to the antenna at

frequencies different from the conventional frequency band, which is defined by 50 Ω input impedance.

An initial analysis of tuning the antenna operational band by varying the input impedance of the RF-frontend was conducted by a patch antenna. A CMOS chip was used as a receiver with variable input-impedance. To tune the operational frequency band, the impedance settings of the RF-frontend was altered. Accordingly, the operational band shifted and we observed extension of the antenna's overall operational bandwidth. While for conventional 50 Ω loading the instantaneous bandwidth equals 10 MHz, a non-standard impedance matching increases the total bandwidth by a factor of three at least.

The concept of antenna frequency reconfiguration by variable-impedance matching was further investigated, in particular, by implementing it to an E-slot planar antenna. A novel E-slot antenna has been developed which is an attractive solution for frequency reconfigurable (phased-) array due to its ability to switch from L- to S- (radar) bands. The antenna element has a very compact dimension (35 x 34 mm²) which was needed for the phased array application with large scanning angle in both frequency bands. The proposed element also maintains geometrical symmetry along both E- and H- planes, allowing it to exhibit symmetric radiation patterns. Furthermore, the applied back feeding technique and the wide-angle scanning capabilities are distinctive features of this E-slot antenna. It was shown that the antenna's operational band can be switched from L- to S-band (about 2.5:1 frequency ratio) by changing the antenna loading impedance. Within the (radar) L-band the input-impedance of the antenna increases with the frequency and hence a fine frequency tuning of about 25% within this band is achievable.

Finally, in this chapter, the concept of scan dependent variable-impedance matching for a phased array system was, also, assessed by showing its effectiveness in retaining better matching over the whole scanning area. A scan-angle dependent impedance control of the RF-frontend will diminish the fundamental active-impedance matching problem and thereby increase the scan volume, particularly interesting for pencil beam observations used in tracking radars. At the same time a scan dependent matching will further enhance system performance and robustness by reducing interfering and jamming signals impinging from adjacent angles. Furthermore, it is well-known that elements close to the edge of an array have active impedance essentially different from those located in the centre. Dummy elements along the array borders are often used when a conventional 50 Ω impedance matching is applied. These dummy elements reduce the overall gain. An impedance-tuneable

RF-frontend can provide a particular impedance matching for these edge elements and thereby avoid the use of non-active dummy elements.

The concept of antenna frequency agility by means of variable-impedance matching between the antenna and the RF-frontend enables wide range of opportunities for frequency agile antennas and might be implemented with the current state of the art technology in active (integrated) antennas. The ideas developed and investigated in this chapter have been presented in [C5] and [J5].

BIBLIOGRAPHY

[1] D. M. Pozar, Microwave Engineering, 3rd ed., John Wiley & Sons, Inc, NJ, 2005, pp.130

[2] K.F. Warnick and M.A. Jensen, "Signal and noise analysis of small antennas terminated with high-impedance amplifiers", 2nd European Conf. on Antennas Propag., Edinburgh, Nov. 2007.

[3] V. Kaajakari, A. Alastalo, K. Jaakkola and H. Seppa, "Variable antenna load for transmitter efficiency improvement", IEEE Trans. Microw. Theory Tech., vol.55, no.8, pp.1666-1672, Aug. 2007.

[4] Formato, R.A.: 'Variable Z0 antenna device design system and method'. U.S. patent 0331436, Dec. 2012.

[5] S. Bagga, A.V. Vorobyov, S.A.P Haddad, A.G. Yarovoy, W.A. Serdijn, J.R. Long, "Co-design of an impulse generator and miniaturized antennas for IR-UWB", IEEE Trans. Microw. Theory Tech., vol. 54, no. 4, pp. 1656-1666, Apr. 2006.

[6] E.A.M. Klumperink, Qiaohui Zhang, G.J.M. Wienk, R. Witvers, J.G. bij de Vaate, B. Woestenburg and B. Nauta, "Achieving wideband sub-1dB noise figure and high gain with MOSFETs if input power matching is not required", IEEE Radio Frequency Integrated Circuits (RFIC) Symp., pp.673-676, Jun. 2007.

[7] M. Pelissier, et al, "LNA-antenna codesign for UWB systems", Circuits and Systems, 2006. ISCAS 2006. Proceedings. 2006 IEEE International Symposium on, May 2006.

[8] M.J. Franco and D. Dening, "Broadband reconfigurable matching network of reduced dimensions for the UHF military satellite communication band", in IEEE MTT-S International Microwave Symp. Dig., Jun. 2011.

[9] Yue Li, Z. Zhang, W. Chen, Z. Feng and M.F. Iskander, "A switchable matching circuit for compact wideband antenna designs", IEEE Trans. on Antennas Propag., vol.58, no.11, pp. 3450-3457, Nov. 2010.

[10] F. Agnelli et al., "Wireless multi-standard terminals: System analysis and design of a reconfigurable RF front-end", IEEE Circuits Syst. Mag., pp. 38–59, 1st Quarter, 2006.

[11] M. S. Oude Alink, E. A. M. Klumperink, A. B. J. Kokkeler, Z. Ru, W. Cheng and B. Nauta, "Using crosscorrelation to mitigate analog/RF impairments for integrated spectrum analyzers", IEEE Trans. Microw. Theory Tech., vol.61, no.3, pp.1327-1337, Mar. 2013.

[12] K. Buisman, L. C. N. de Vreede, L. E. Larson, M. Spirito, A. Akhnoukh, Y. Lin, X. Liu, and L. K. Nanver, "Low-distortion, low-loss varactor-based adaptive matching networks, implemented in a silicon-on-glass technology", in Proc. RFIC Symp., Long Beach, CA, pp. 389–392, Jun. 2005.

[13] IMEC, [Online] Available: http://www2.imec.be/content/user/File/NEW/Research/Wireless%20Communication/Analog%20R_F%20front-end/Scaldio%20leaflet.pdf

[14] STMicroelectronics, [Online] Available: http://www.st.com/web/en/resource/technical/document/datasheet/DM00033029.pdf

[15] O. García-Pérez, D. Segovia-Vargas, L. E. García-Muñoz, J. L. Jiméenez-Martín, and V. González-Posadas, "Broadband differential low-noise amplifier for active differential arrays", IEEE Trans. Microw. Theory Techn., vol. 59, no. 1, pp. 108–115, Jan. 2011.

[16] J. T. Bernhard, "Reconfigurable antennas", in Synthesis Lectures on Antennas, Morgan and Claypool Publishers, 2007.

[17] R. L. Haupt and M. Lanagan, "Reconfigurable antennas", IEEE Antennas Propag. Mag., vol. 55, no. 1, pp. 49–61, Feb. 2013.

[18] R. B. Marks and D. F. Williams, "A general waveguide circuit theory", J. Res. Nat. Inst. Standards Technol., vol. 98, no. 5, pp. 533-561, Sep. 1992.

[19] K. Kurokawa, "Power waves and the scattering matrix", IEEE Trans. Microw. Theory Tech., vol. MTT-13, no. 3, pp. 194–202, Mar. 1965.

[20] K. Kurokawa, An Introduction to the Theory of Microwave Circuits, Academic press, Inc, NY, 1969, pp.33-38.

[21] D. C. Youla, "On scattering matrices normalized to complex port numbers", Proc. IRE, vol. 49, no. 7, pp. 1221–1221, Jul. 1961.

[22] J. Rahola. "Power waves and conjugated matching", IEEE Trans. Circuits Syst. II, vol. 55, no. 1, pp.92-96, Jan. 2008.

[23] P.V. Nikitin, K.V.S. Rao, S.F. Lam, V. Pillai, R. Martinez and H. Heinrich, "Power reflection coefficient analysis for complex impedances in RFID tag design", IEEE Trans. Microw. Theory Tech., vol.53, no.9, pp. 2721-2725, Sep. 2005.

[24] N. Haider, M. S. Oude Alink, D. Caratelli, E. A. M. Klumperink and A. G. Yarovoy, "Frequency-tunable antenna by input-impedance-tunable CMOS RF-

frontend", *European Microwave Integrated Circuits Conference (EuMIC),* Nuremberg, Oct. 2013.

[25] A.G. Yarovoy, J.H. Zijderveld, A.D. Schukin, I.V. Kaploun and L.P. Ligthart, "Dielectric wedge antenna for UWB applications", in *Proc. IEEE Int. Conf. Ultra-Wideband, ICU*, Zurich, pp. 186-189, Sep. 2005.

[26] S. Maci, G. Biffi Gentili, P. Piazzesi and C. Salvador, "Dual-band slot-loaded patch antenna", Microwaves, Antennas and Propagation, IEE Proceedings, vol.142, no.3, pp. 225-232, Jun. 1995.

[27] P. W. Hannan, D. S. Lerner, and G. H. Knittel, "Impedance matching a phased array-antenna over wide scan angles by connected circuits", IEEE Trans. Antennas Propag., vol. AP-12, pp. 28–34, Jan. 1964.

[28] H. W. Bode, Network Analysis and Feedback Amplifier Design, Sec. 16.3, Van Nostrand, New York, 1945.

[29] R. M. Fano, "Theoretical limitations on the broadband matching of arbitrary impedance", J. Franklin Institution, vol. 249, pp. 57-83, Jan. 1950.

CHAPTER 6

CONCLUSIONS AND RECOMMENDATIONS

This chapter recapitulates the main scientific findings of this thesis. The novelty and focal contributions emerging from this research activity is discussed. Recommendations are provided for future research in the field of antenna design for reconfigurable sensors.

6.1 MAJOR RESULTS AND NOVELTIES

THE aim of this thesis was to answer the key research question: ***how we can realize antennas for reconfigurable sensors and sensor networks?***

Three approaches were investigated to answer the main research question during the course of the study presented in this thesis. Firstly, wideband antennas covering the desired frequency bands were investigated. Such an antenna, which covers the bands of interest simultaneously, should be followed by reconfigurable filter or T/R module to achieve frequency selectivity. In the second approach, frequency reconfiguration was achieved at the antenna element level by placing RF-switches on the radiating structure. Finally, in the third approach the operational band of an antenna was tuned by impedance tuneable RF-frontend.

A multi-band sensor can operate via an UWB or multi-band antenna whose operational bandwidth covers all required frequencies of the sensor. The concept of such wideband antennas were extensively analyzed during this research study. The focus was made towards planar structures which are suitable for implementing in planar arrays. In order to realize antenna elements suitable for array environment planar structures were chosen. Two aspects of an antenna structure play very important roles for the wideband characteristic: *the feeding section* and *the radiating structure*. These two features have been analyzed independently and in combination.

A highly frequency-dependent behaviour of a feeding section in planar antennas, in particular patch antennas, makes it very challenging to achieve wide operational bandwidth. For example, a probe feed shows large frequency-dependent reactive-part which increases with the thickness of the substrate material. In order to reduce this reactive part, a novel blind-via feeding structure was developed. The proposed substrate-integrated feeding section is an effective mean to minimize the reactive part of the probe and thereby extensively increase operation bandwidth of planar radiating structures while reducing coupling and cross-polarisation levels. In a particular case, the bandwidth expansion of narrowband microstrip antennas to 20-30% was demonstrated which is a substantial improvement compared to less than 10% fractional bandwidth of a conventional microstrip antenna. Furthermore, mutual coupling and cross-polarisation levels were reduced by about 3 dB and 5 dB, respectively.

Besides a proper feeding mechanism, an appropriate radiating structure is important for wide operational bandwidth. Proper combination of both electric and magnetic fields in primary antenna radiators helps in achieving large operational bandwidth. Realization of this antenna concept by combination of a magnetic loop and electric monopole backed by a ground plane was used to develop an X-band radiator with more than 40% fractional bandwidth. A wideband orthogonal transition from the coaxial to the coplanar line was developed to realize the feeding section of the antenna. Due to its unidirectional radiation, compact size and back feeding structure, the element is a suitable candidate for array environment.

In the second approach, a frequency adaptive antenna was realized by changing the physical structure of the radiator. A novel concept of a patch antenna with switchable electrical length was proposed. In order to realize a frequency reconfigurable antenna for L/S-band radar, a new type of radiating structure with p-I-n diode switches and an array compatible bias network was designed. The complexity of the biasing circuit was considerably reduced by utilizing the RF feed for DC bias. Here, in order to provide DC ground to four p-I-n diodes only a single inductor and via connection to the ground was needed. The benefit noticed for this approach was the larger frequency coverage in comparison with wide or multiband antennas. The developed antenna was able to switch its band over about 2.2:1 frequency ratio with 5 to 6 dBi antenna gain and very stable radiation properties. The element has a compact size of 50 x 50 mm^2 which makes it attractive for phased array application.

In order to develop antenna arrays with wide angle scanning in both operational bands of the proposed element a novel multi-scale array topology was introduced where reconfigurable elements are interleaved with high frequency elements. Consequently, dense element spacing was maintained for both operational modes. A planar 9x8 antenna array demonstrator of this L/S-band array was built, thoroughly investigated and compared with a regular dense array. Two major benefits of the multi-scale array in comparison with conventional array topology were verified. First of all, results assure that the array structure increases the total scan angle in S-band to ±60° opposed to less than ±25° for the array with conventional topology. Next, the reduction of coupling levels in L-band by at least 5 dB was demonstrated. This innovative array configuration makes wide-angle scanning possible in both operational bands of a dual or multi-band antenna system.

In the third approach, the operational band of an antenna was tuned by variable-impedance matching. This approach also reduced the requirements of the front-end

filter compared to the UWB or multi-band approach. In this novel concept we have avoided the standard 50 Ω matching, which has been used for many decades, and demonstrated many potentials of variable-impedance matching. Theoretical and experimental results verified the frequency tuning of a narrowband microstrip antenna by an input-impedance tuneable CMOS RF-frontend. The concept was further implemented for the realization of an L/S-band reconfigurable antenna element. For this purpose a dedicated dual-band E-slot antenna was designed. The distinctive features of this novel element are its large frequency switching capability from radar L-band to S-band (frequency ratio of about 2.5:1), very compact size of 35 x 34 mm^2 and symmetric radiation patterns along all principle planes. Furthermore, fine tuning capability within the allocated radar L-band was demonstrated. The advantage of a scan dependent variable-impedance matching for a phased array system was addressed by revealing its effectiveness in retaining better matching over the whole scanning area of ±60°.

The main novelties of this research study (discussed in detail in the preceding subsections) can be summarized as follows:

- A novel multi-scale array configuration for dual-band reconfigurable antenna systems is proposed and experimentally verified (Chapter 4).
- An array compatible novel frequency reconfigurable antenna element with electronic switches and minimal number of control lines is designed (Chapter 3).
- A novel principle of frequency reconfiguration by input-impedance tuneable RF-frontend is introduced (Chapter 5).
- A dual-band antenna element with novel E-slots is designed (Section 5.4).
- A new feeding arrangement based on a substrate integrated blind-via feeding structure is proposed to enhance the operational bandwidth of planar antennas (Section 2.1).
- A wideband electric-magnetic antenna with unidirectional radiation and back-feeding mechanism is introduced (Section 2.2).

6.2 DISCUSSION AND RECOMMENDATIONS

THE insight achieved from this research study can be interpreted as follows:

Among the three aforementioned research approaches, *(i) wideband or*

mulitband antennas integrated with tuneable filters, (ii) reconfigurable antenna elements integrated with electronic switches, and (iii) reconfiguration by variable-impedance matching, the optimal solution will depend severely on the intended application. The first approach is the most mature and commonly used approach for non-reconfigurable wide- or multi-band systems for which the range of frequency coverage is not significantly large. This concept imposes stringent requirements on the filters if implemented for frequency agile systems. Consequently, one of the main design challenges for the RF-frontend becomes the realization of filters with high out-of-band suppression capabilities. In the second approach, frequency reconfigurability is acquired at antenna element level and thus reduces the constraint imposed on the filters. Such reconfigurable antenna elements also provide the best solution for systems requiring extensive frequency coverage. On the other hand, this approach needs sophisticated design and analysis of the frequency reconfigurable antenna. Furthermore, additional ohmic losses of the control switch (up to 1–2 dB) and consequently reduction of maximal power are limiting factor here. The third approach gives a good compromise of the earlier two. This approach requires impedance tuneable RF-frontend with close integration with the antenna. It is an attractive alternative solution which can provide frequency range close to a reconfigurable element while reducing the design complexity by eliminating the electronic switches. Moreover, this concept may provide most flexibility in the selection of the operation sub-bands.

The study presented in this thesis gives rise to some new research questions and directions. The following studies can be recommended for subsequent researches.

1. For the L/S-band reconfigurable element (discussed in Chapter 3) the antenna's operational band in the switch off-state is highly dependent on the parasitic capacitance of the diode switch. A high parasitic capacitance (under zero bias) undesirably shifts the operational band towards the lower frequency range. This prohibited the use of standard p-I-n diodes (such as silicon diodes) for which the parasitic capacitances are usually ten times larger than the required value. Therefore, a (GaAs) diode with extremely low parasitic capacitance value (~0.02pF) was used to minimize the frequency shift. However, the maximum power handling capabilities of such diodes are limited. In order to overcome this problem one can physically reduce the size of the inner-patch of the reconfigurable antenna to compensate for the frequency shift caused by the diode. However, in this case the antenna input-impedance

in two operational modes will largely differ from each other due to the large difference in two patch sizes and it is unlikely that both modes can be well match to 50 Ω. At this point, a variable-impedance control (discussed in Chapter 5) will help to restore the impedance matching.

2. In Chapter 3 and Chapter 4, the frequency reconfigurable antenna element was studied. This antenna is capable of switching between two bands. The proposed antenna covers a portion of the total radar L- and S-band. As the input-impedance of the antenna varies consistently with frequency, frequency tuning within the aforesaid bands is foreseen. Analysis of the antenna configuration in order to provide flexible bandwidth is an interesting research topic. Furthermore, it might be possible to increase the functionality of the antenna by adding an additional metal ring and thereby generate three switchable bands covering a frequency range of 3:1. In order to get wide scanning in all bands, 3rd order multi-scale array topology can be applied.

3. In Chapter 5 of this dissertation the concept of frequency reconfiguration of an antenna by variable-impedance matching was proposed. Developing a dedicated L-/S-band input-impedance tuneable RF-frontend for the dual-band E-slot antenna can be interesting continuation of the current research work.

6.3 IMPACT OF THE RESEARCH

THE research activities as presented in this dissertation have led to solid understanding of how we can realize frequency reconfigurable antennas for adaptive sensors. The work presented here has provided novel antenna demonstrators for frequency reconfigurable active phased array systems. The outcomes of this research will be particularly valuable in developing future narrow or wide beam radar systems with frequency reconfiguration and angular filtering capabilities. This research work is presented to the scientific community in more than 15 publications in recognized international journals, conference proceedings and book chapters.

APPENDIX A

ADDITIONAL ANALYSES OF THE QUASI ELECTRIC-MAGNETIC ANTENNA

In Chapter 2 of this thesis the electric-magnetic antenna, based on a combination of a patch and a loop, is introduced. In this section some additional findings of this element will be addressed. Among other topics the Ku-band antenna design, the surface feeding construction and the polarimetric array structures are discussed here.

A.1. The Ku-band element

An X-band quasi electric-magnetic antenna and its performance were discussed in detail in Section 2.3. To further investigate the applicability of the concept a Ku-band electric-magnetic antenna has been also constructed and experimentally studied. Here the emphasis is put on the enhancement of the impedance bandwidth and size reduction of the element, as well as the relevant experimental verification. Furthermore, a detailed analysis of the antenna performance as a function of the main geometrical parameters is presented.

The results presented in this section have been published in:

[J3] N. Haider, D. Caratelli, and A. G. Yarovoy, "Circuital characteristics and radiation properties of an UWB electric-magnetic planar antenna for Ku-band applications", *Radio Science.* DOI: 10.1002/rds.20015, vol. 48, pp. 13–22, Jan. 2013.

[C1] N. Haider, B. Yang, D.P. Tran, and A.G. Yarovoy, "UWB antenna element for a full-polarimetric antenna array," *Proc. 4th European Conference on Antennas and Propagation (EuCAP)*, Barcelona, Spain, Apr. 2010.

The geometry of the Ku-band antenna is shown in Figure A.1. As it can be noticed here, the antenna may be regarded as the combination of a loop and patch antennas. This in turn is essential for wideband behavior in terms of input impedance matching and gain.

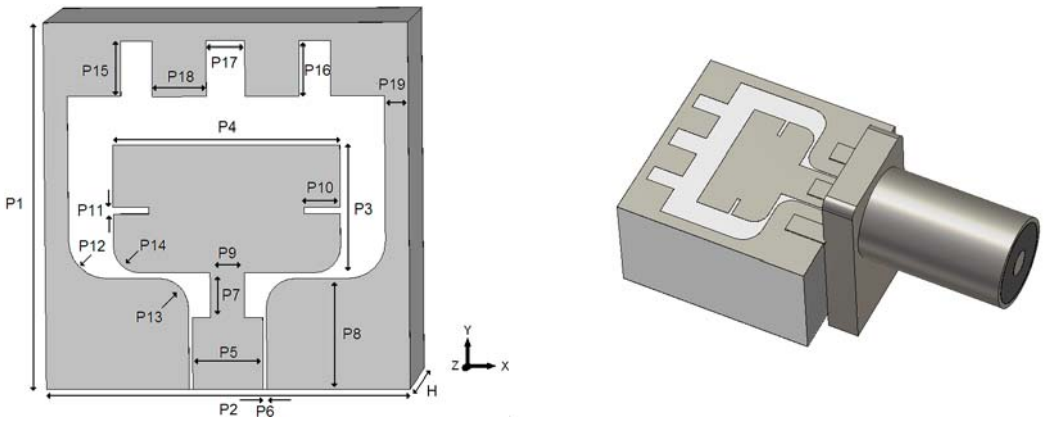

(a) (b)

Figure A.1(a) The antenna architecture and relevant geometrical parameters, (b) The numerical model of the antenna and the connector

To concurrently feed the radiating patch and the loop a grounded-coplanar-waveguide (CPWG) is applied. However, in this way antennas cannot be connected to the measurement system. The measurement of these antennas can only be performed with a coaxial measurement system. Therefore, there is an unavoidable need of coaxial-to-coplanar transition which can assure minimum transmission loss for a wideband. Here a surface feeding arrangement is used for the transition of coaxial to coplanar where the axis of the coaxial connector is aligned with the end of the coplanar line. The inner connector of the coaxial cable is connected with the centre signal line of the coplanar waveguide and the outer connector with the coplanar ground plates as shown Figure A.1 (b).

To expand the impedance bandwidth both the patch and the loop geometry have been optimized. In the following section a comprehensive parametric study is presented.

A.2. Parameter analyses

A parametric analysis has been carried out by evaluating the effect of the variation of geometrical parameters on the element performance. In this section the impact of the key geometrical parameters of the antenna is analyzed and discussed thoroughly. In doing so, only one parameter value has been changed at a time while keeping the others unaltered.

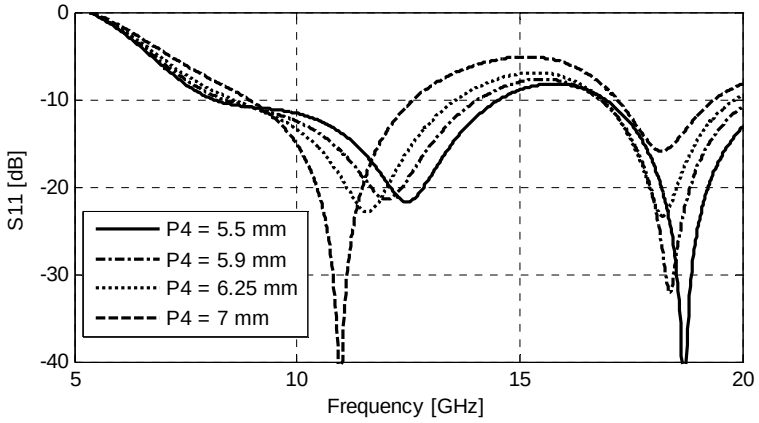

Figure A.2 The effect of the patch width (P4) on the input reflection coefficient of the antenna

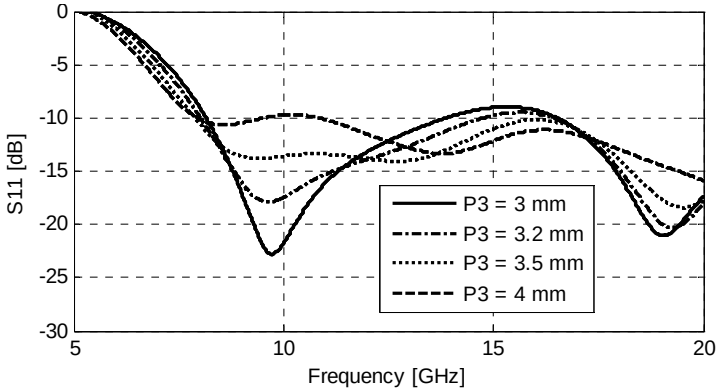

Figure A.3 The effect of the patch length (P3) on the input reflection coefficient of the antenna

In Figure A.2 the effect of the patch width (P4) on the impedance bandwidth is illustrated. The patch width has a clear balancing effect between the lower and higher frequency bands. When P4 is reduced to less than 6 mm, a strong resonance around 18 GHz is observed. On the other hand, a patch width larger than 6.6 mm results in a strong resonance around 11 GHz. This parametric analysis shows prospective of the proposed structure as a frequency reconfigurable antenna element. For a wide operational band, it is essential to maintain balance between the resonances and hence P4 = 6.25 mm has been chosen. The patch length (P3) has been varied from 3 to 4 mm and the effect is shown in Figure A.3. When P3 is larger than 4 mm, it has been found out that the return loss level in the lower frequency band increases. On the other hand when the length is decreased, the antenna shows two clear separate resonances around 10 GHz and 18 GHz.

In Figure A.4, the effect of the outer stub length (P15) is illustrated. This study shows that P15 has a negligible impact on the total bandwidth. On the other hand, it plays an important role for the antenna matching condition in the centre frequency

band. The impact of the curve radius P13 is analyzed in Figure A.5. The obtained numerical results clearly show that a smooth transition from the input coplanar waveguide (CPWG) to the radiating patch, namely a larger value of P13, results in an enhanced return-loss response in the frequency spectrum of interest.

The purpose of the impedance transformer is to provide a good matching between the 50 Ω coax cable and the antenna input impedance over a large frequency band. Figure A.6 shows that the transformer width (P9) has most effect on the centre frequency. This study shows that maximizing the transformer width will provide good balance in the return loss. The influence of other parameters, e.g. patch inner stub length, notch length, have been studied and fine tune to achieve a wide bandwidth (VSWR lower than 2 between 8 GHz and 24 GHz). The performance of this element is further discussed in Section A.3.

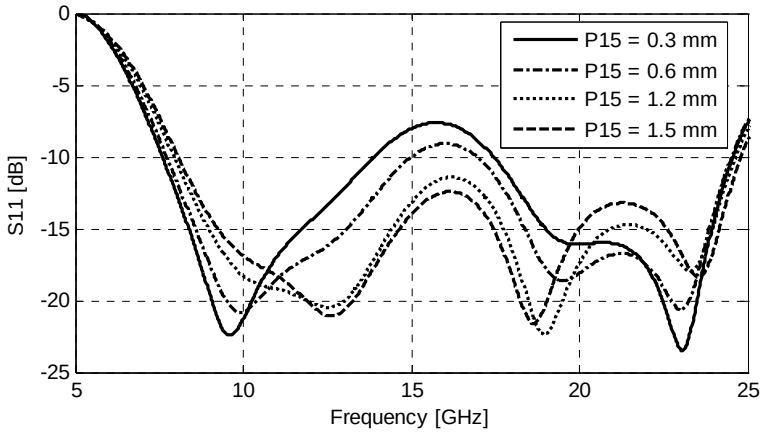

Figure A.4 The effect of the outer stub length (P15) on the input reflection coefficient of the antenna

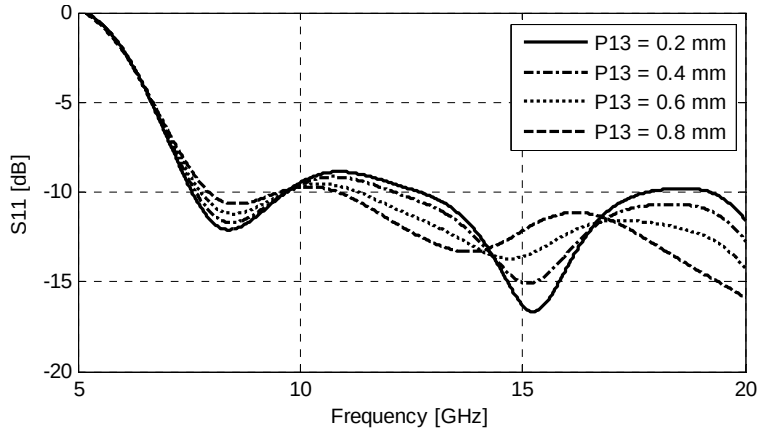

Figure A.5 The effect of the transition curve radius (P13) on the input reflection coefficient of the antenna

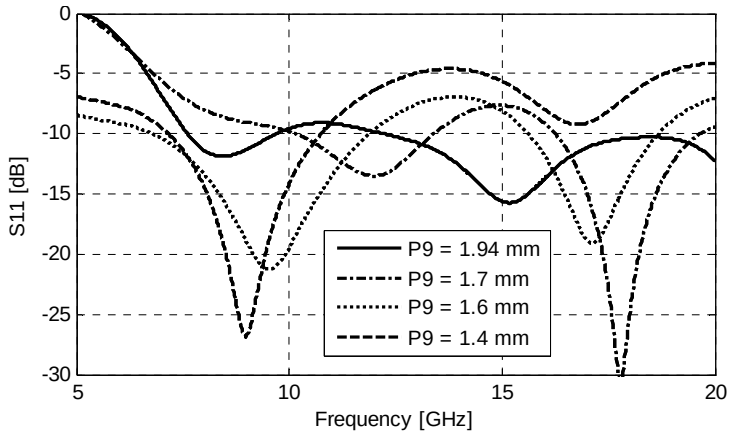

Figure A.6 The effect of the transformer width (P9) on the input reflection coefficient of the antenna

A.3. Performance analysis and experimental verification

In order to verify the theoretical results presented in the previous sections, an experimental prototype has been designed and fabricated (see Figure A.7). Similar to the X-band element, the Ku-band element is printed on a Taconic (TLY-5) substrate with relative permittivity $\varepsilon_r = 2.2$ and 17-μm-thick copper cladding.

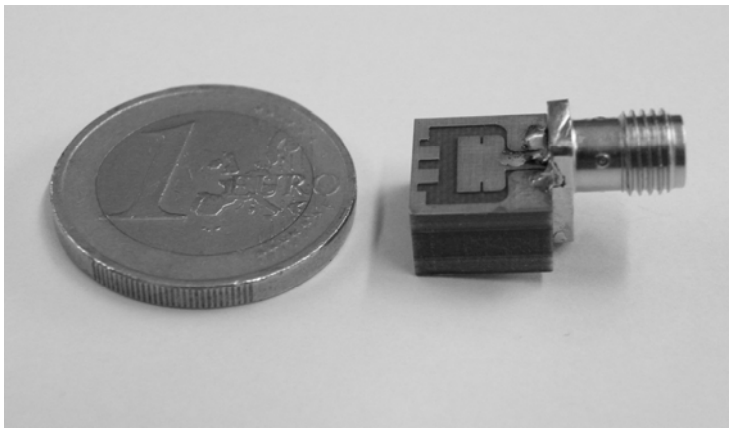

Figure A.7 Experimental prototype of the Ku-band element with the SMA connector

A.3.1 Impedance bandwidth

The impedance bandwidth of the proposed antenna structures has been experimentally analyzed. The frequency-domain behaviour of the input reflection coefficient in X/Ku band is shown in Figure A.8, and a reasonably good agreement between the experimental and theoretical results can be noticed. In both cases a good impedance matching (with respect to 10-dB return-loss level) is predicted in the frequency range from 8 to 24 GHz, corresponding to a fractional bandwidth of 100%. The differences in the measured and simulated results are possibly caused by the additional parasitic of the SMA connector.

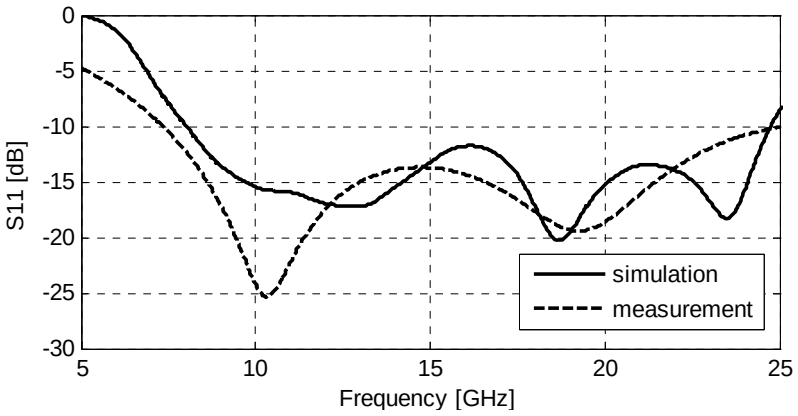

Figure A.8 Simulated and measured input reflection coefficient of the antenna element shown in Figure A.7

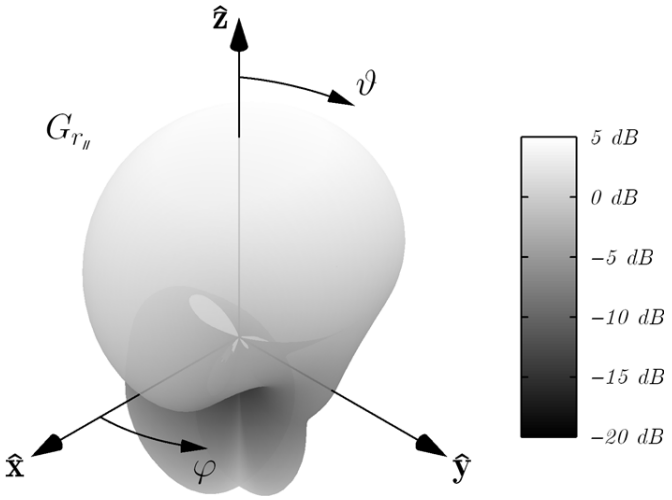

(a)

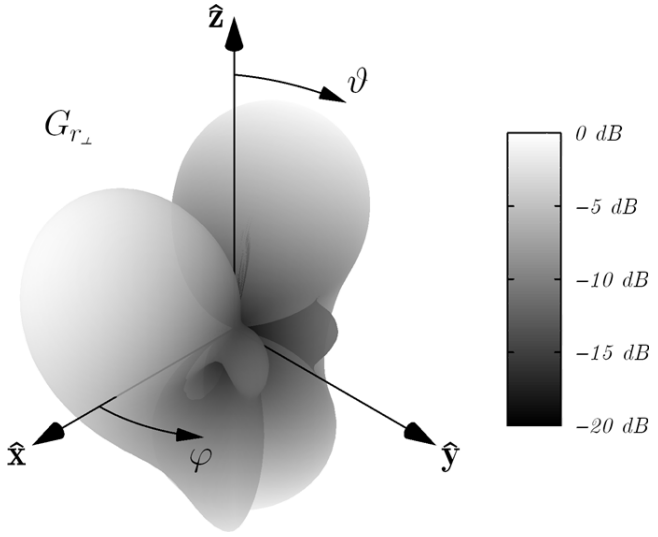

(b)

Figure A.9 Realized gain of the antenna at 15 GHz: (a) co-polarized and (b) cross-polarized component

A.3.2 Radiation pattern

A thorough investigation of the radiation properties of the antenna has been, also, carried out. In Figure A.9 the three-dimensional view of the realized gain pattern at the centre frequency f=15 GHz is shown. The antenna element possesses uni-directional radiation pattern with about 10 dB front-to-back ratio (FBR). The FBR can be further improved by extending the ground plane size. The half power beam width (HPBW) at 15 GHz is about 65° in E-plane and about 90° in H-plane. Furthermore, as expected from theory, Figure A.9 reveals that the cross polarization level is minimum in the E-plane ($\varphi = 90°$) and maximum in the H-plane ($\varphi = 0°$).

The normalized radiation patterns along the H-plane (xz plane) and E-plane (yz plane) of the antenna at three different frequencies are shown in Figure A.10 and Figure A.11, respectively. The measurements were carried out in DUCAT (Delft University Chamber for Antenna Test) by using a reference TEM horn (GZ0126ATP) as the transmit antenna. The radiation pattern of the antenna is moderately stable over the frequency range of interest with 2-6 dBi maximum realized gain level. At lower frequencies the radiation pattern is tilted in the E plane due to the presence of the SMA connector as predicted by the numerical analysis (see Figure A.11). To obtain a symmetrical E plane pattern the SMA connector needs to place at the back of the radiating structure by applying the back feeding configuration proposed in Section 2.3. Along the E plane the cross-polarization level is very small over entire band (in practice, values around the numerical errors of simulations are observed) due to the antenna symmetry and therefore has not been plotted in Figure A.11.

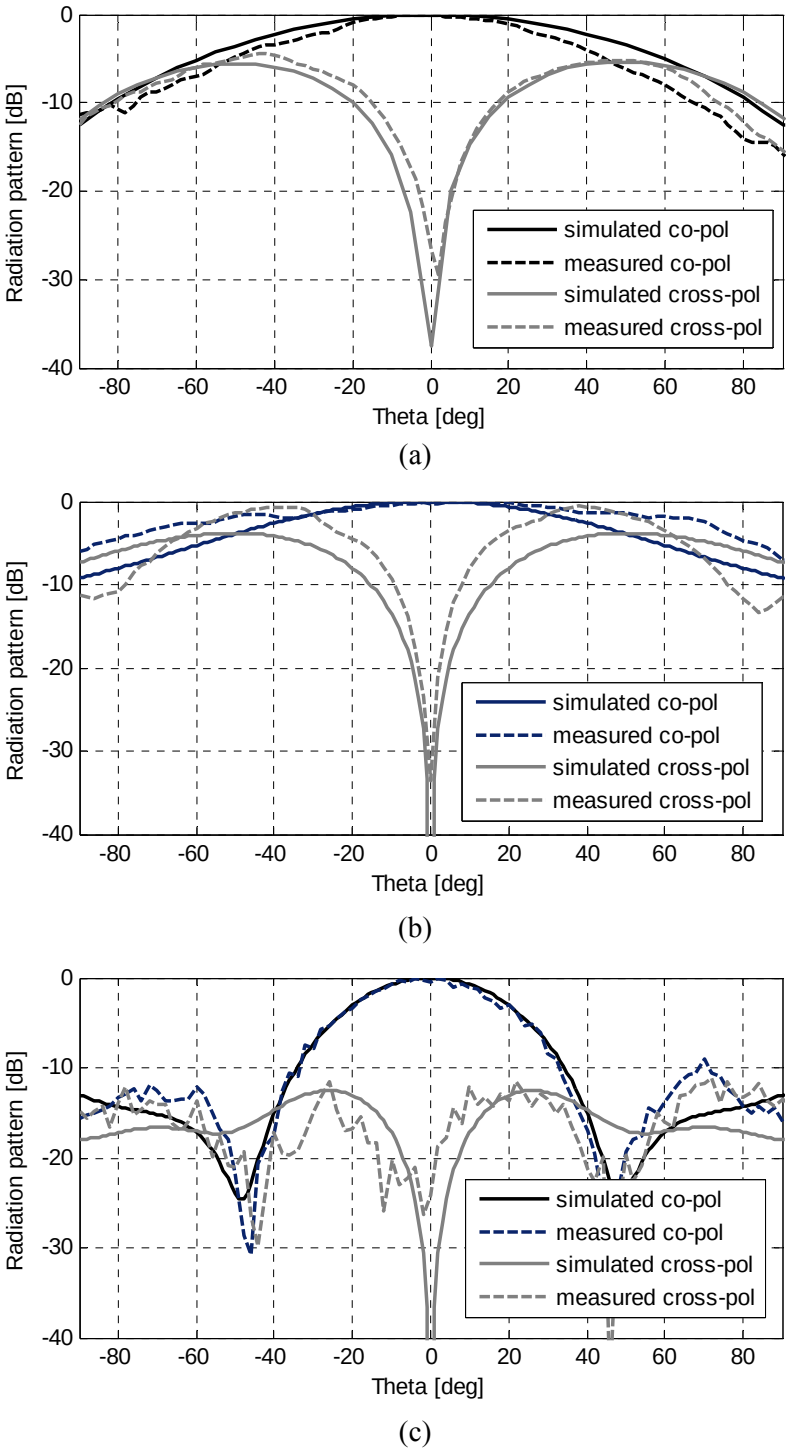

Figure A.10 Normalized co-polarized and cross-polarized patterns for H-plane (XOZ plane) at 10 GHz (a), 15 GHz (b), and 25 GHz (c). The SMA connector has been included in the numerical model.

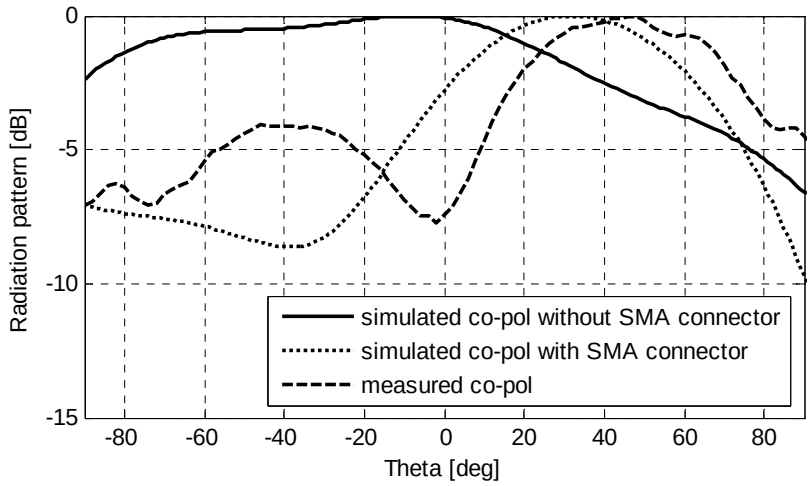

(a)

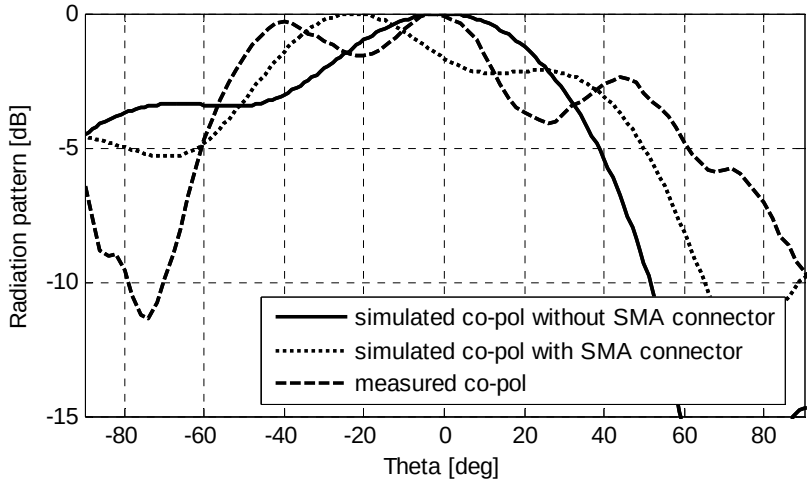

(b)

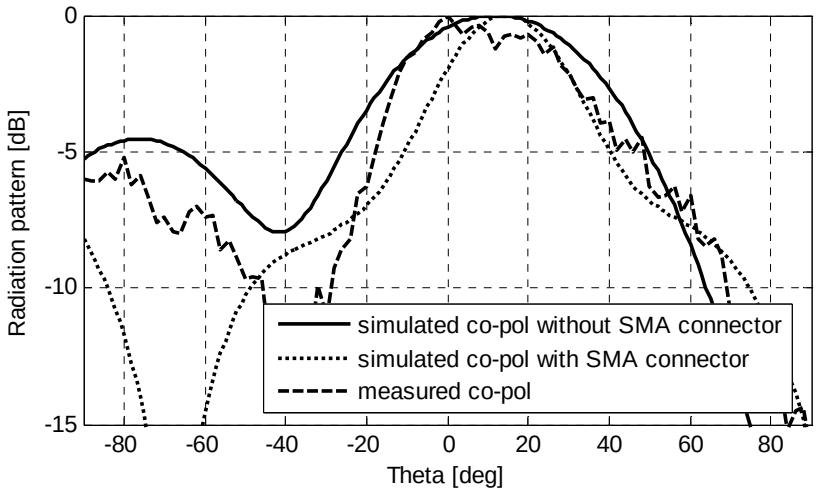

(c)

Figure A.11 Normalized co-polarized patterns for E-plane (YOZ plane) at 10 GHz (*a*), 15 GHz (*b*), and 25 GHz (*c*)

A.3.3 Poynting's vector flow

In order to investigate the near field behaviour of an antenna usually surface current distribution, electromagnetic field strength, or Poynting's vector flow is analyzed. The Poynting's vector indicates how the energy of the radiated wave propagates around the antenna. In Figure A.12 the distribution of the z-component of the Poynting's vector is depicted. It is clear from this figure that the Poynting's vector flow is dominated by the loop-like radiation contribution at the lower frequencies while the inner patch contributes more in the upper part of the operational band of the antenna.

A.3.4 Time-domain behaviour

The performance of an UWB system is heavily dependent on the time domain behaviour of the radiated and received pulse [1]-[2]. In this section, the time-domain characteristics of the element are investigated. To this end, the mono-pulse fired by the pulse generator (GZ1117DN-25), shown in Figure A.13, has been used in all the measurements. For numerical simulations the same transmit pulse has been used as the excitation signal. The duration of the pulse is 0.1 ns for a level of 10% of the peak amplitude. The power spectrum density (*PSD*) of the pulse is shown in Figure A.14. At 25 GHz the PSD is about -30 dB with respect to the maximum.

In order to estimate the radiated electric field distribution, two identical elements have been used in the measurement set-up. In this way, the receiving transfer function of the individual antenna, $h_R(j\omega)$, for a fixed position can be extracted from the measured coupling coefficient $S_{21}(j\omega)$ between the radiating elements by applying the following relation [3]-[5]:

$$h_R(j\omega) = \sqrt{\frac{2\pi c_0 R S_{21}(j\omega)}{j\omega} e^{j\beta R}}, \tag{A.9}$$

where R is the distance between the antennas, β is the propagation constant and c_0 denotes, as usual, the speed of light in free space. Afterwards, the normalized incident electric field strength, $e^{inc}(j\omega)$, can be expressed in terms of the normalized received voltage, $V_r(j\omega)$, as:

$$e^{inc}(j\omega) = -\frac{V_r(j\omega)\sqrt{\eta_0}}{h_R(j\omega)}, \tag{A.10}$$

η_0 being the wave impedance of the medium. By doing so, the magnitude of the co-

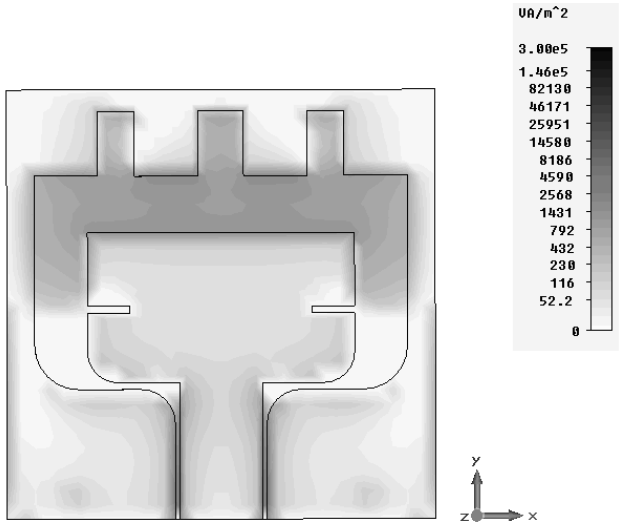

(a)

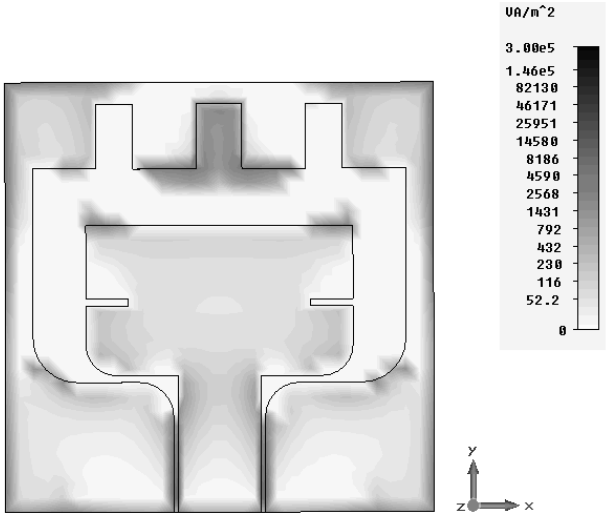

(b)

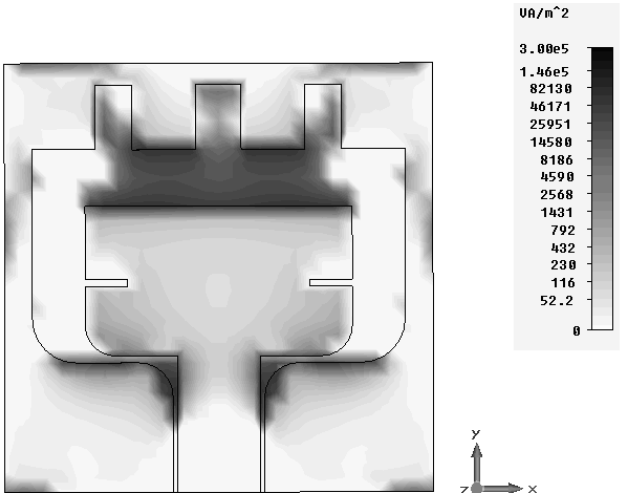

(c)

Figure A.12 Simulated z-component of the Poynting's vector flow at 8 GHz (a), 16 GHz (b), and 25 GHz (c)

polarised component of the electric field has been evaluated for different scan angles. As it can be noticed in Figure A.15, a good agreement between the experimental measurements and the numerical results has been achieved. A marginal disagreement in the amplitudes of the peaks has been noticed due to tolerances in the antenna manufacturing.

It is worth noting that the proposed antenna features a reasonably good fidelity factor [6] varying between 0.6 and 0.8 for different scan angles. Such performance is particularly important in UWB imaging applications where a reduced signal distortion in the scanning field of view (FOV) is needed in order to increase the radar detect ability of the target.

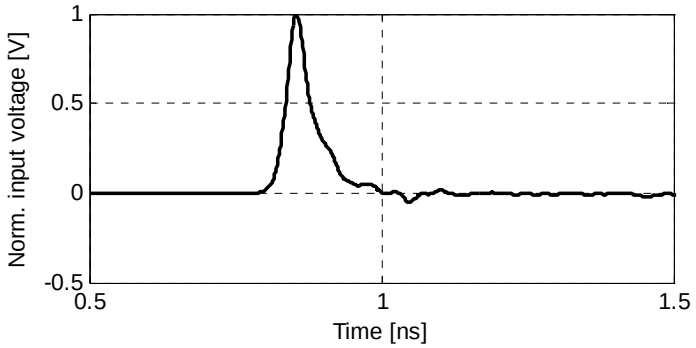

Figure A.13 Time-domain behaviour of the generated pulse

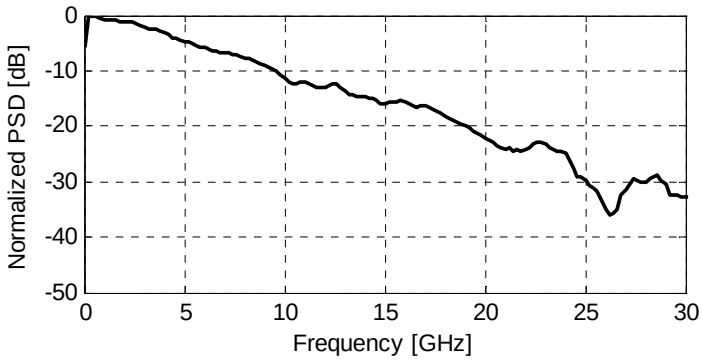

Figure A.14 The power spectrum density (*PSD*) of the generated pulse

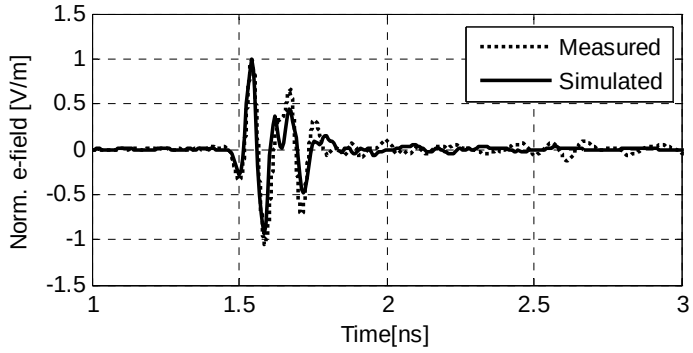

(a)

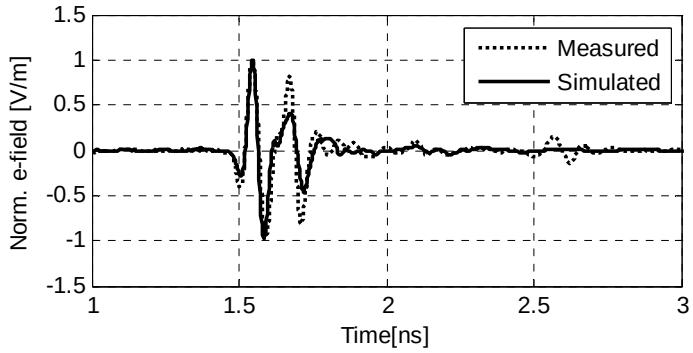

(b)

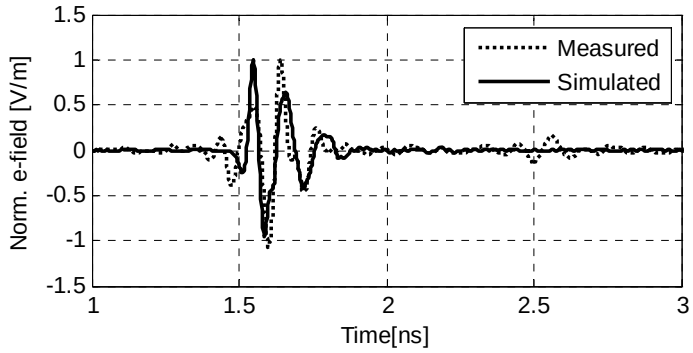

(c)

Figure A.15 Time-domain behaviour of the radiated electric field along the H-plane for R=1 m and (a) $\vartheta = 0°$, (b) $\vartheta = 45°$, (c) $\vartheta = 90°$

A.4. Conclusion

An UWB antenna topology has been utilized in the development of an antenna element with 3:1 impedance bandwidth. A parametric study is presented to investigate the effect of the antenna geometrical parameters on its performance. This investigation confirms that proper combination of electric and magnetic topologies can increase the impedance bandwidth of planar antennas. In addition, the proposed antenna is planar and compact in size (half of the free-space wavelength at the centre frequency). Therefore, the proposed design is attractive for UWB imaging sensors.

BIBLIOGRAPHY

[1] T.P. Montoya, G.S. Smith, “A study of pulse radiation from several broad-band loaded monopoles”, *IEEE Trans. on Antennas and Propagat.*, vol. 44, pp. 1172-1182, 1996.

[2] D. Caratelli, and A. Yarovoy, “Unified time- and frequency-domain approach for accurate modeling of electromagnetic radiation processes in ultra-wideband antennas”, *IEEE Trans. Antennas Propagat.*, vol. 58, pp. 3239-3255, 2010.

[3] J. S. McLean, R. Sutton, A. Medina, H. Foltz, and J. Li, “The experimental characterization of UWB antennas via frequency-domain measurements”, *IEEE Antennas and Propagation Magazine*, vol. 49, pp. 192-202, 2007.

[4] S. Licul, and W. A. Davis, “Unified frequency and time-domain antenna modeling and characterization”, *IEEE Trans. on Antennas and Propagat.,* vol. 53, pp. 2882-2888. 2005

[5] E. G. Farr, and C. E. Baum, “Extending the definitions of antenna gain and radiation pattern into the time domain”, *Sensor and Simulation Notes*, SSN 350., 1992

[6] D. Lamensdorf, and L. Susman, “Baseband-pulse-antenna techniques”, *IEEE Antennas and Propagation Magazine*, vol. 36, pp. 20-30, 1994.

APPENDIX B

WIDEBAND ELECTRIC-MAGNETIC ANTENNA FOR POLARIMETRIC APPLICATIONS

As discusses in Chapter 2, UWB imaging radar serves as a very important tool for many surveillance and security applications, for instance, concealed weapon detection (CWD), earthquake rubble imaging, through-the-wall (TTW) imaging during fire evacuation or hostage situation. For these situations high resolution 3D imaging in real-time operation is essential and requires real-aperture data acquisition to increase the speed of data collection. To increase the resolution of real-aperture UWB radar, large aperture sizes are needed. Hence, oppose to dense array architecture, sparse array configuration becomes more suitable in order to avoid unrealistically high cost and to reduce the complexity of data collection. An example of such a sparse Multiple-input-multiple-output (MIMO) array with UWB radiating elements developed at Delft University is illustrated in Figure B.1.

The results presented in this section have been published in:

[C8] N. Haider, D. Caratelli, D.P. Tran, and A.G. Yarovoy, "Wideband Electric-Magnetic Antenna for Polarimetric Applications," *Proc. 8th European Conference on Antennas and Propagation (EuCAP)*, The Hague, The Netherlands, Apr. 2014.

Figure B.1 Example of sparse antenna array for UWB near-field imaging (Courtesy of Yu-Che Yang) [1]

The performance of UWB systems, such as imaging radars, can be further improved by applying polarimetric diversity. A dual-polarized system receives two co-polar and two cross-polar scattering data of the target. Therefore, it has additional information regarding the scattering behaviour of objects compare to a single polarized system. Then the polarimetric signature of objects can be used to enhance the quality of target recognition [2]. A system which combines UWB performance with full-polarimetric imaging will have the capability to provide very fine resolutions together with better target classification ability. Nonetheless, to realize such a system we need a suitable dual-polarized UWB antenna.

The desired features for such an antenna will be dual linear or circular polarization, sufficient polarimetric isolations, large fractional bandwidth (> 25%), uni-directional and frequency-stable radiation patterns, low dispersion, sufficient gain, planar structure and compact size (about λ at the centre frequency). In practice, it is extremely challenging to fulfil all these desired properties. A review of current state-of-the-art (SOA) UWB antennas shows that some of the dual-polarized antennas can also provide ultra-wide bandwidth, for example, dual-polarized horn, Vivaldi or tapered slot antennas (TSA) [3]. Nevertheless these antenna elements are not suitable for short-range UWB sparse arrays (illustrated in Figure B.1) due to their 3D volumetric structures. Realization of a fully planar polarimetric wideband antenna element is discussed in this section.

To design dual polarized antennas two fundamental approaches are often considered. Firstly, dual-polarized antenna elements are used. In this case the polarimetric diversity is achieved from each radiating elements capable of radiating fields in both polarization. Alternatively, single polarized antenna elements are

arranged in a group such that together they provide dual polarization. The first approach provides a more compact solution while the second approach often gives a better polarimetric isolation and larger operational bandwidth. As sparse array configurations are considered here, the second topology was more beneficial. Following sections discuss the realization of such dual-polarized (sub) arrays with linearly polarized elements.

B.1 The polarimetric array concepts

In order to extend the applicability of the linearly polarized antenna presented in the section B.3 and Section 2.3, the X-band electric-magnetic elements were arranged in sub-array configurations. For this study, four elements were used in each sub-array to overlap the phase centers of both orthogonal linear polarizations.

Two sequentially rotated array configurations were studied: the conventional element arrangement shown in Figure B. 2(a) and the Huang array [4-5] arrangement as illustrated in Figure B. 2(b). Appropriate phase distribution will enforce these sub-arrays to radiate either in circular or in dual-linear polarization.

The elements of the same polarization are physically rotated to simplify the feeding mechanism. The required phase difference between two opposite ports is introduced by the 1-26.5 GHz 180º hybrid coupler from Krytar [6]. A benefit of having differentially fed array is the low level of cross polarization along the H-plane and more symmetry in the array radiation pattern even along the E-plane.

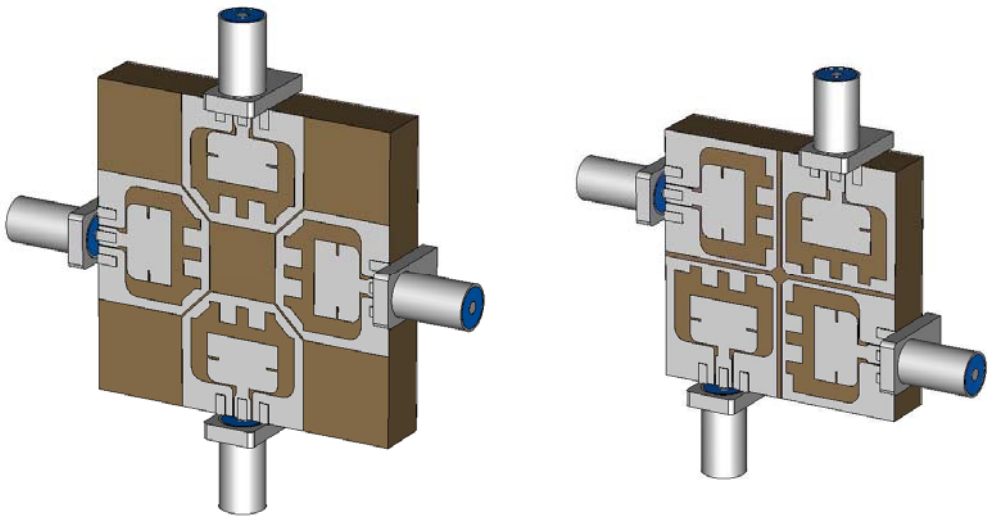

(a) (b)

Figure B.2 Simulation models of the sequentially rotated polarimetric arrays; (a) conventional array and (b) Huang array

The advantage of the Huang array is the possibility to bring the antenna elements closer than in a conventional arrangement and this reduces the total size of the array. A small size for each antenna element or sub-array is crucial for array architectures which require moderate element periodicity. Here, the size of the 2x2 conventional array illustrated in Figure B.2 is 32 x 32 mm² (element periodicity is about 0.7λ at the centre frequency). The length and the width of the Huang array are 26 mm (element periodicity is about 0.4λ at the centre frequency).

On the other hand, the conventional array provides a simpler configuration and better polarization purity. The phase and polarization imbalances are greater for the Huang array due to its specific element arrangement. This causes higher cross-polarization levels. Another advantage of the conventional array is the comparatively smaller coupling level due to the larger distance between adjacent elements. In section B.4.2, the aforementioned properties of both arrays are demonstrated with experimental results.

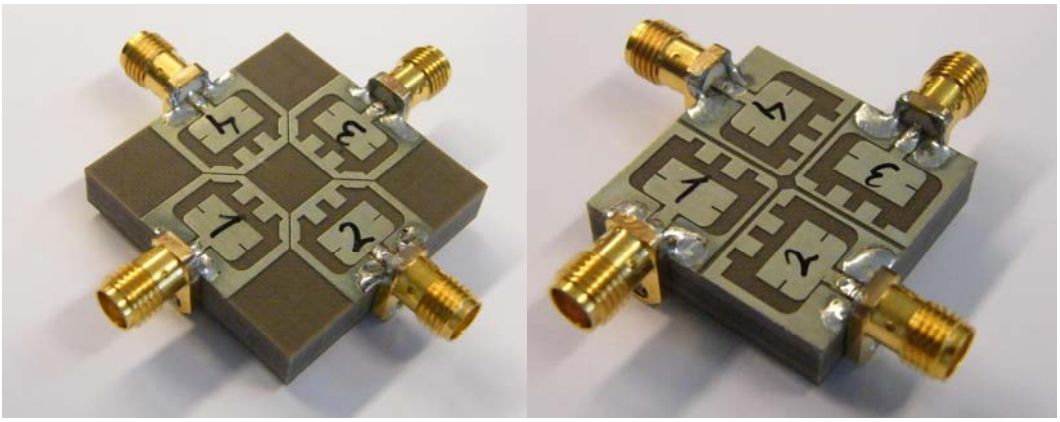

(a) (b)

Figure B.3 Antenna prototypes, (a) Conventional array, (b) Huang array

B.2 Performance analysis and experimental verifications

To validate the suggested antenna topologies, array prototypes (shown in Figure B.3) are fabricated and tested. The obtained numerical results and the experimental verification presented in Figure B.4 confirm that the fractional bandwidth is close to 40% for both considered array topologies.

Figure B.5 illustrated that within the operational band the broadside realized-gain varies between 2 dB and 7 dB. It is worth mentioning here that both numerical and experimental results presented here include the effects of the reflection caused by the antenna structure as well as the coplanar-to-coaxial transition. Figure B.6

demonstrates the coupling levels between the adjacent elements. The Huang array shows about 5 dB higher coupling level compared to the conventional array due to its compact element arrangement.

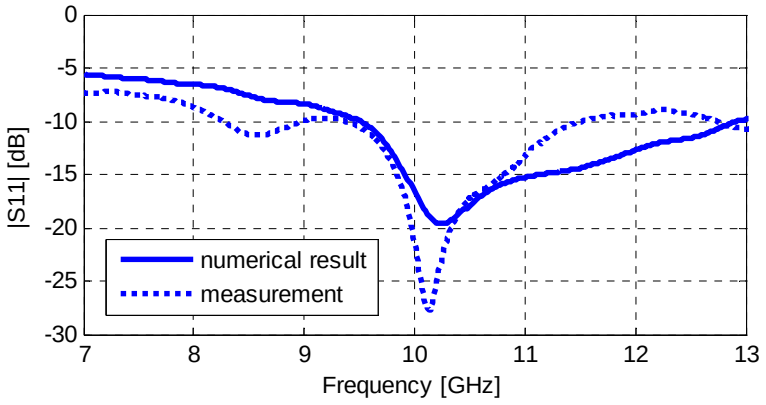

(a)

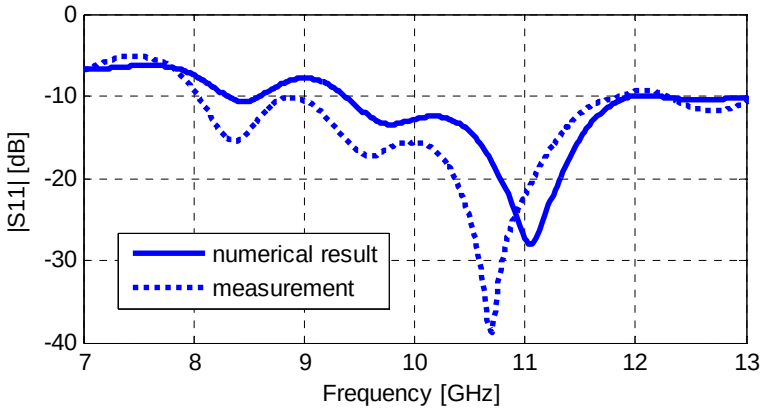

(b)

Figure B.4 Input reflection coefficient magnitude of (a) the conventional array and (b) the Huang array

The normalized radiation patterns at 10 GHz are shown in Figure B.7. Here we plotted the measured radiation patterns when two opposite elements having the same polarization are excited simultaneously. Due to the relative element arrange of the arrays, we observe notable differences in the radiation patterns. Firstly, we notice discrepancy in the co-polarized beam patterns. For the conventional array a narrower beam is observed along the E-plane (in comparison with the H-plane pattern) due to the two element arrangement along this plane. For the Huang array the patterns along the E-plane and H-plane are similar as the elements are placed along the diagonal plane here.

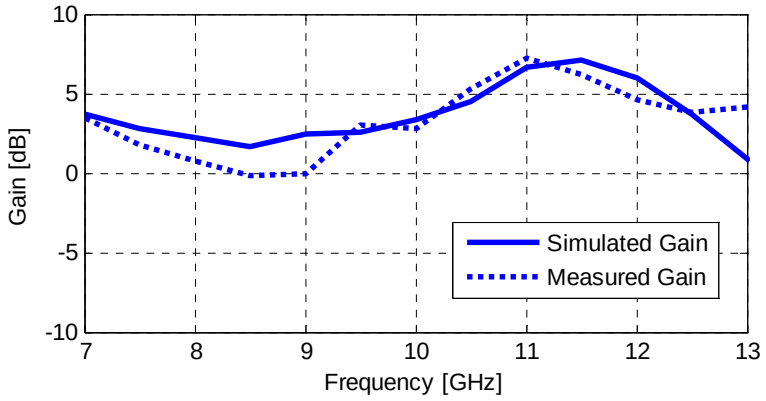

(a)

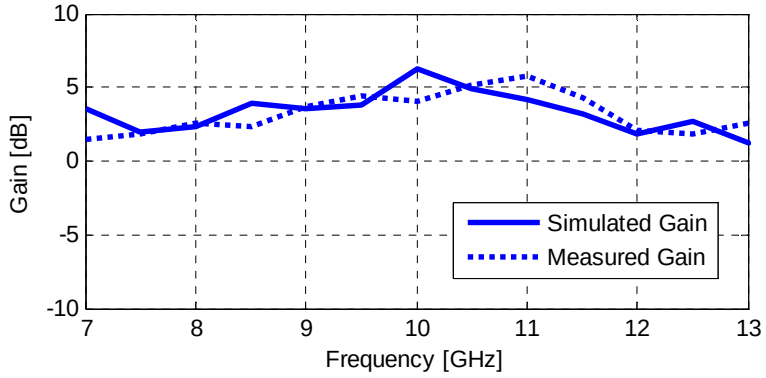

(b)

Figure B.5 Boresight realized gain of (a) the conventional array and (b) the Huang array

Secondly, the polarization purity is higher for the conventional array. In this case even along the H-plane a negligible amount of cross-pol level (< -30 dB for the entire front-plane) is notice due to the alignments of the two opposite elements together with the out-of-phase feeding technique.

Furthermore, we notice that the array patterns are almost symmetric along both principle planes for both array structures. Along the H-plane each element has symmetric geometry. Therefore, the radiation patterns are symmetric in this plane, even for an isolated element as shown in Chapter 2. Alike the H-plane, along the E-plane the radiating structures are not symmetric. Therefore, we noticed some asymmetry along the E-plane radiation pattern as shown. However, due to the sequential rotation the combined radiation pattern of these two elements will be again symmetric along the E-pane as demonstrated in Figure B.7.

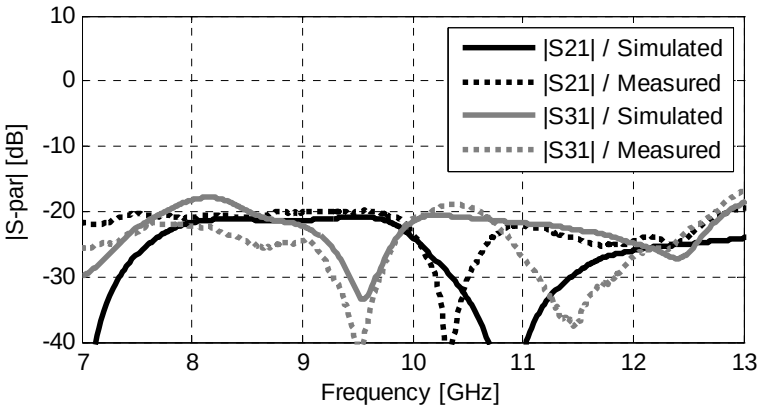

(a)

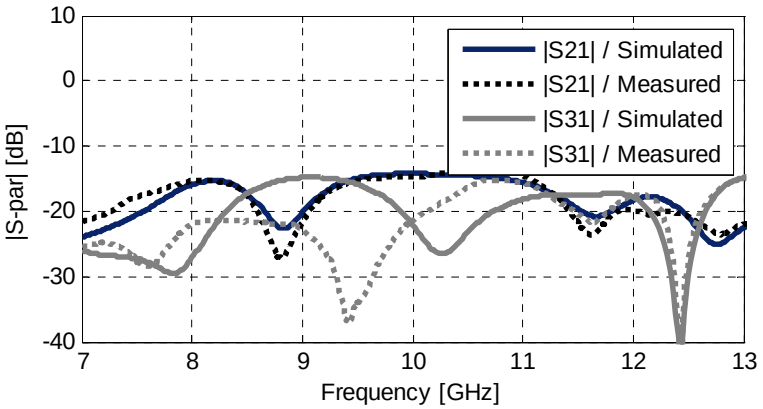

(b)

Figure B.6 Coupling between the elements for (a) the conventional array and (b) the Huang array

The antenna developed has been applied to polarimetric measurements of scattering from a sphere with a diameter of 2 cm placed 25 cm from the scan direction. Here, the conventional array was used. The linear scan was performed with 1 cm steps and a wideband transmit pulse (7 – 15 GHz) has been used. The measured signals in time domain are shown in Figure B.8. In the center region we notice large co-polarized reflected signal while the cross-polarization signal changes its polarity.

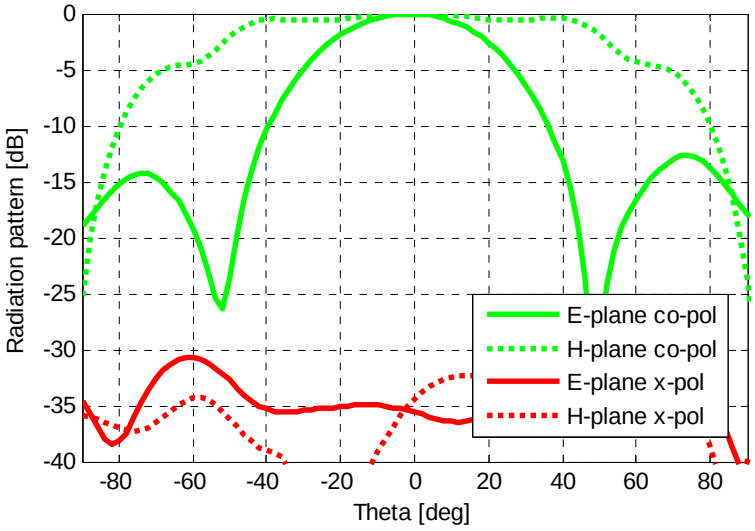

(a)

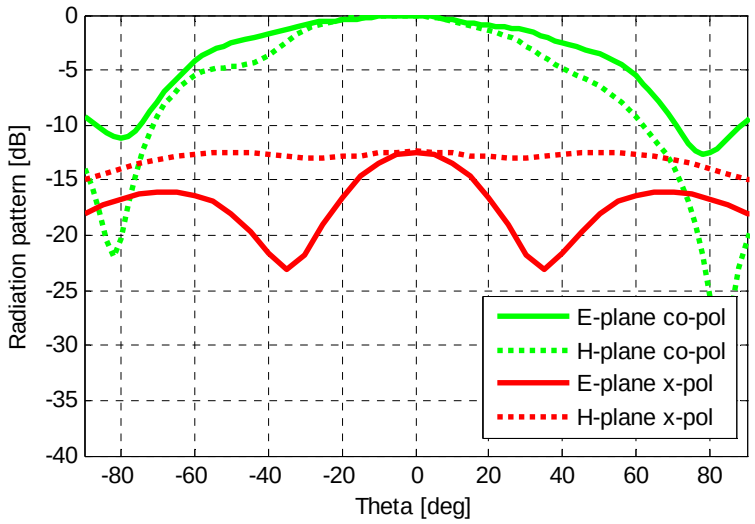

(b)

Figure B.7 Measured normalized radiation patterns at 10 GHz for (a) the conventional array and (b) the Huang array

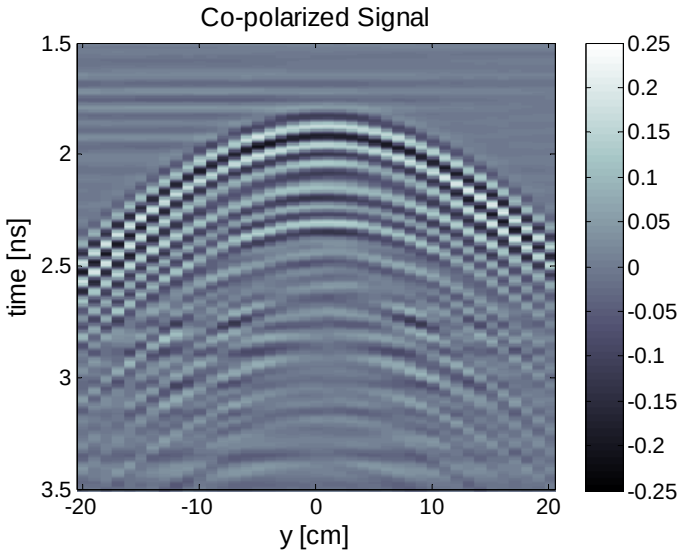

(a)

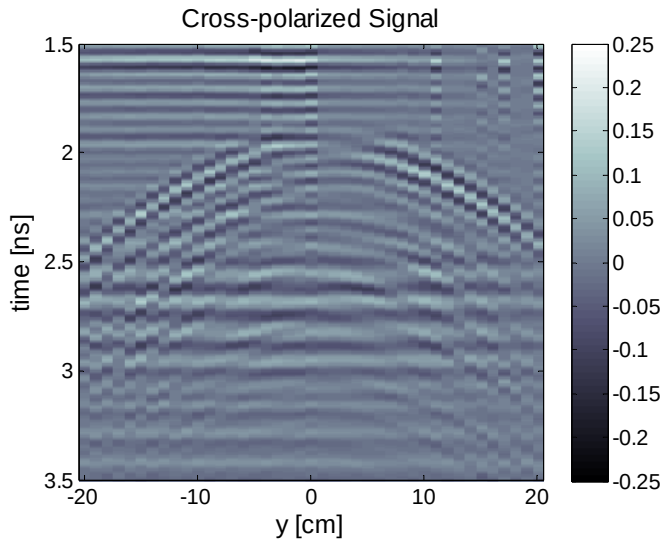

(b)

Figure B.8 Signals reflected from the sphere, (a) co-polarized signal and (b) cross-polarized signal

B.3 Conclusion

Two fully polarimetric planar arrays were designed and experimentally studied. The arrays consist of four electric-magnetic elements which are differentially fed. It is demonstrated experimentally that both arrays have about 40% fractional bandwidth and stable radiation patterns. Experimental results confirmed that the conventional array configuration provides better polarization purity and isolations while the Huang array arrangement offers a smaller sub-array size.

BIBLIOGRAPHY

[1] Y. Yang, “UWB Antennas and MIMO Antenna Arrays Development for Near-Field Imaging”, Ph.D. Thesis, Delft University of Technology: The Netherlands, Oct. 2011.

[2] A.G. Yarovoy, F. Roth, V. Kovalenko, L.P. and Ligthart, “Application of UWB near-field polarimetry to classification of GPR targets”, in F. Sabath, E.L. Mokole, U. Schenk & D. Nitsch (Eds.), *Ultra-wideband, short-pulse electromagnetics 7*, New York, USA: Springer Science + Business Media LLC, pp. 655-664.

[3] R. Maaskant, M. Popova, and R. van den Brink, "Towards the design of a low-cost wideband demonstrator tile for the SKA," *Proc. European Conference on Antennas and Propagation (EuCAP)*, Nov. 2006.

[4] J. Huang "A technique for an array to generate circular polarization with linear polarized elements", IEEE trans. on Ant. and Prop, AP-34, (9), pp. 1113-1124, 1986.

[5] P. S. Hall, J. Huang, E. Rammos, and A. Roederer, "Gain of circularly polarized arrays composed of linearly polarized elements," Electron. Lett., vol. 25, no. 2, pp. 124-125, Jan. 1989.

[6] Krytar. [Online] Available: www.krytar.com/pdf/4010265.pdf

APPENDIX C

ADDITIONAL ANALYSES OF THE E-SLOT ANTENNA

In Chapter 5 of this thesis the E-slot antenna has been introduced and used for variable impedance matching demonstration. The proposed single-layer element contains two parallel E-slots for dual band operation and provides the flexibility to control the resonance frequencies. In this section the impact of different antenna geometrical parameters on the operational bands, is presented.

C.1 Centre slot effect on the third harmonic

The geometry of the proposed concept is illustrated in Figure C.1. In this case the thickness of the substrate is set to 4.573 mm. In Figure C.2, the effect of the centre slot width on the third harmonic is depicted. By controlling the centre slot width we can influence the current path of the third harmonic. Increasing this value (Eslot in Figure C.1) will lead to a shorter current path for TM_{300} mode and thereby a higher resonating frequency. It is evident in Figure C.2 that the TM_{100} remains unaffected by this parameter variation. As a result the second frequency band can be reconfigured

---

The results presented in this section appeared in:

[C3] N. Haider, D.P. Tran, and A.G. Yarovoy, "Dual-band E-slot microstrip antenna with frequency tuning capability," *Proc. 7th European Conference on Antennas and Propagation (EuCAP)*, Gothenburg, Sweden, Apr. 2013.

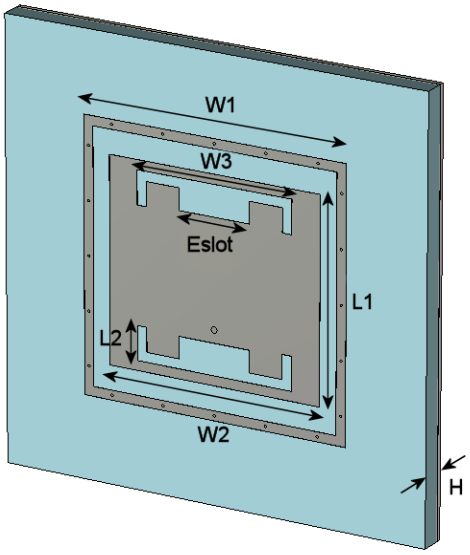

Figure C.1 The E-slot microstrip antenna geometry

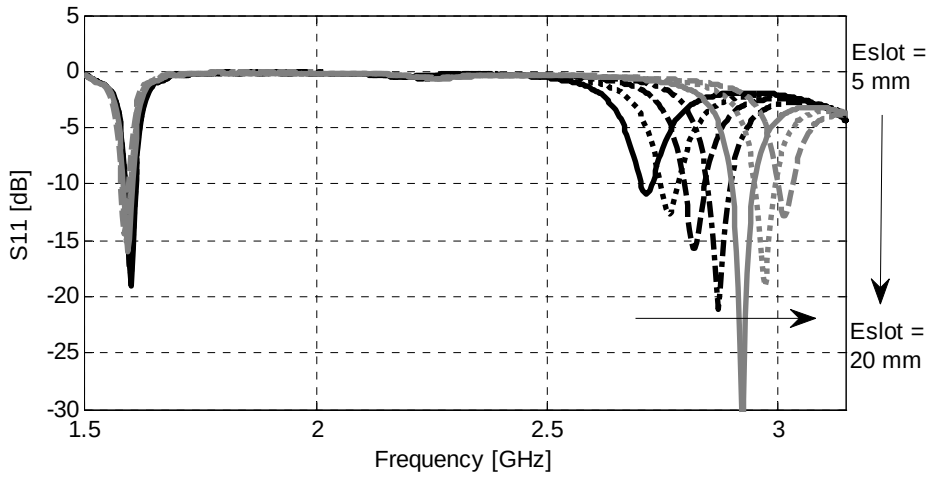

Figure C.2 The effect of Eslot on the third harmonic

independently either during the design process or during the operation by applying MEMS switches.

C.2 Antenna miniaturization and frequency tuning with additional notch

By adding notches at the centre of the element (see Figure C.3) the resonance frequency can be shifted towards the lower frequency band. The slots are located at the middle of the radiating patch where the current density of TM_{100} mode is the maximum and therefore the effect of the slots will be the utmost. In an array environment this miniaturization will help to reduce the element spacing and increase the scan angle.

The resonance frequencies of a single-band microstrip antenna and a dual-band E-slot microstrip antenna were modified by inserting notches at the center of the radiating patch as shown in Figure C.3. In Figure C.4 and Figure C.5 the effects of the notch lengths (Lslot in Figure C.3) on the operational bands are depicted. These notches can be then used for either miniaturization purpose or for frequency reconfiguration by placing RF-MEMS switches. For the dual-band antenna both the first harmonic (TM_{100}) and the third harmonic (TM_{300}) can be tuned by only changing the notch lengths.

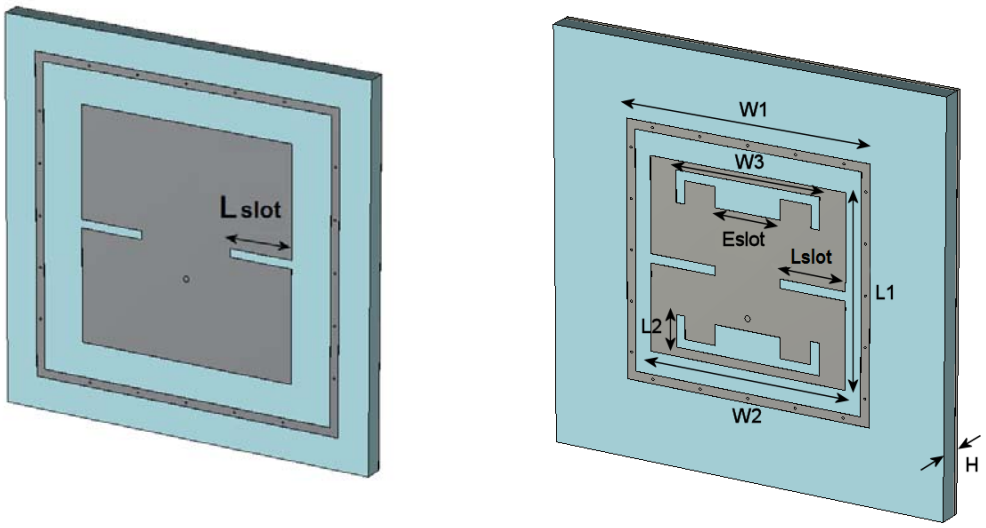

(a) (b)

Figure C.3 (a) Single-band microstrip antenna with notches, (b) Dual-band E-slot microstrip antenna with notches

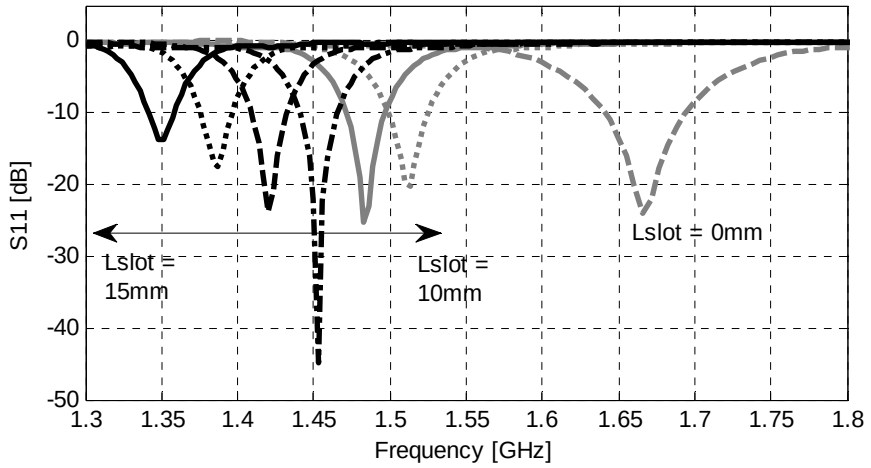

Figure C.4 The effect of notch length (Lslot) on the operational band of the microstrip antenna shown in Figure C.3(a)

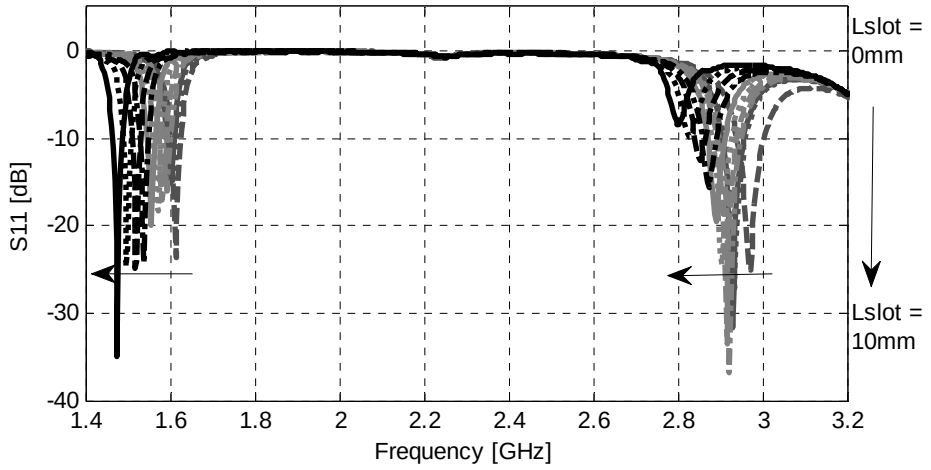

Figure C.5 The effect of notch length (Lslot) on the first and the third harmonics of the dual-band E-slot antenna shown in Figure C.3(b)

ABSTRACT

Sensors such as phased array radars play a crucial role in public safety. They are unavoidable for surveillance, threat identification and post-disaster management. However, different scenarios impose immensely diverse requirements for these systems. Phased array systems occupy a large space. In addition, if different antenna systems are needed for each function, the space required can be considerably large. For transportable platforms, such as ships and aircrafts, space and weight are critical parameters. Therefore, reconfigurable multi-band antennas are very attractive solutions for future multi-function sensor systems.

Within this research work three different approaches are investigated to realize antennas for reconfigurable phased arrays. Wideband antenna designs constitute the first approach. Integrating this type of antennas with frequency selective filters provide the opportunity for fine tuning within one radar band. The wideband operation of the antenna is achieved by the blind-via feeding section and the quasi electric-magnetic radiating structure.

The second approach involves the design of an antenna element with p-I-n diode switches. The switches are used to alter the antenna structure and thereby the operating frequency. Measured results verified the frequency reconfigurable capability of the antenna within L/S radar bands with frequency ratio more than 2:1. The planar structure, the back feeding mechanism, the compact size and the simple bias network made the proposed antenna suitable for array applications. The large frequency ratio and its usability in phased array applications made the design novel. Furthermore, for these frequency reconfigurable elements, a unique multi-scale array structure is introduced which can assure wide angle scanning for both frequency bands. The advantage of this novel array configuration is twofold: reduce the mutual couplings in the lower band, and increase the scanning volume for the higher band. A planar array demonstrator validated the proposed concept.

In the third approach the operational band of an antenna is tuned by variable-impedance matching. In this study, the standard 50 Ω matching is avoided and many advantages of variable-impedance matching are demonstrated. First, the principle is verified by tuning the frequency band of a microstrip antenna by an input-impedance tuneable CMOS RF-frontend. In the second design a novel dual-band E-slot antenna, with 2.5:1 frequency ratio, was designed. By changing the input-impedance the operating frequency of the antenna can be switched from L- to S-band. Variable-impedance matching provides few other advantages to phased array antennas. A scan-angle dependent impedance matching will assure low reflection coefficients for the entire scanning volume. On the other hand, it will reduce interfering and jamming signals coming from adjacent angles.

The outcomes of this research work have led to solid understanding of how we can realize frequency reconfigurable antennas for adaptive phased arrays. The results will be particularly valuable in developing future narrow or wide beam radar systems with frequency reconfiguration and angular filtering capabilities.

SAMENVATTING

Sensoren zoals phased array radar spelen een cruciale rol in openbare veiligheid. Ze zijn onmisbaar voor toezicht, dreigingen en ramp management. Echter leggen verschillende scenario's enorm uiteenlopende eisen op voor deze systemen. Phased array systemen bezetten grote ruimtes. Bovendien, als afzonderlijke antenne systemen nodig zijn voor iedere functie, zal de totaal vereiste ruimte aanzienlijk groter zijn. Voor verplaatsbare platforms, zoals schepen en vliegtuigen, is een laag gewicht en klein volume van belang. Daarvoor zijn herconfigurabele multi-band antennes een zeer aantrekkelijke oplossing voor toekomstige sensorsystemen.

Binnen dit onderzoek zijn drie verschillende aanpakken onderzocht om antennes te ontwerpen voor herconfigurabele phased arrays. Breedband antennes betreffen de eerste aanpak. Het integreren van dit soort antennes met frequentie afhankelijke filters zorgt voor een nauwkeurige afstemming binnen een radar band. De grote bandbreedte van de antenne is bereikt door middel van een blind-via voeding en de quasi electrisch-magnetische straling structuur.

De tweede aanpak heeft betrekking op het ontwerp van een antenne element met p-I-n diode schakelaars. Het schakelen wordt gebruikt om de antenne structuur en hiermee de frequentie aan te passen. Metingen bevestigen het vermogen om van frequentie te kunnen wisselen binnen de L/S radar banden met frequentie ratios die groter zijn dan 2:1. De planaire structuur, het voeden via de achterkant, zorgt voor een compact ontwerp en het simpele bias netwerk maakt de voorgestelde antenne geschikt voor array toepassingen. De grote frequentie ratio en de toepassing in phased array systemen maakt dit ontwerp uniek. Verder, voor deze herconfigurabele elementen, is een unieke multischaal structuur ontworpen welke er voor kan zorgen dat breedhoek scannen voor beide frequentie banden mogelijk is. Het voordeel van deze unieke aanpak is tweeledig: het reduceren van de onderlinge koppelingen in de lage bandbreedte, en het verhogen van het scanvolume voor de hoge band. De planar array demonstrator heeft de werking van het concept bevestigd.

Met de derde aanpak is de operationele band van de antenne instelbaar gemaakt door middel van een variabele-impedantie koppeling. Binnen deze studie is afstand genomen van de standaard 50 Ω impedantie koppeling en zijn verschillende voordelen bewezen van variabele-impedantie koppelingen. Ten eerste, het principe is geverifieerd met behulp van het instellen van de frequentie band van een microstrip antenne door middel van een input-impedantie instelbare CMOS RF-frontend. In het tweede ontwerp is gebruikt gemaakt van een unieke dual-ban E-slot antenne, met een 2.5:1 frequentie ratio. Door het veranderen van de input-impedantie is het mogelijk om het operationele bereik van de antenne te variëren tussen de L- en S-band. Het variabel koppelen van de impedantie heeft nog meer voordelen voor phased array antennes. Bij systemen met een impedentie die afhankelijk is van de scan-hoek zal het zorgen voor minder reflecties binnen het volledige scan volume. Daarnaast, zal het er voor zorgen dat er minder storing optreedt vanuit de overige hoeken.

De resultaten van dit onderzoek hebben geleid tot een grondig begrip over hoe we herconfigurabele antennes voor adaptieve phased arrays kunnen realiseren. De resultaten zullen met name waardevol zijn bij de ontwikkeling van toekomstige smal- of breedband radarsystemen met herconfigurabele frequenties en filter mogelijkheden met betrekking tot de richting.

ACKNOWLEDGEMENT

I am glad to have this opportunity to convey my appreciation to many colleagues, friends and family members. First of all, I would like to express my gratitude to my promotor, Prof. Alexander Yarovoy, for his guidance and support. His useful advice and expertise were extremely valuable in completing this research. His careful reading of the manuscript was of much assistance in improving the quality of this dissertation. I am indebted to him for providing me the opportunity to do my doctoral research under his supervision and for giving me the freedom to try my ideas.

I am grateful to Dr. Antoine Roederer for his very valuable support and critical remarks. I really enjoyed our many scientific (as well non-scientific) discussions and brainstorming. I have always been amazed by his great enthusiasm and interest for scientific work, even after working so many years in this field. It was a privilege to work with him. The support of Dr. Diego Caratelli is also highly appreciated. His passion for research work is really exceptional. I would like to thank him for his help and advice. I am truly glad that I had the opportunity to work with him.

This research work is funded by the STARS project and I would like to gratefully acknowledge this support. I also wish to express my appreciation to the project members from Thales, TNO, NXP and University of Twente for many useful discussions. I owe my gratitude to Mark Oude Alink and Eric Klumperink from the University of Twente for our joint research activities. Special thanks to Simon van den Berg, Frank van de Water and Ufuk Yalcin for their contributions in the measurement campaigns at Thales Nederland. I would also like to extend my gratitude to my defence committee members, Prof. Dauvignac, Prof. Vandenbosch, Prof. Gerini, Prof. Neto, Prof. Hoogeboom and Prof. Le Chevalier, for their constructive suggestions.

I wish to convey my thanks to many colleagues and friends in Delft. It was very special to meet and work with colleagues from so many different countries. Special

thanks to my office mates, Inna and Yuan, for many cheerful moments. Thanks to Dani Tran for always being kind and helpful. I really enjoyed our many discussions. I am glad to meet many amazing people at our research group: Tuen, Fotios, Alexey, Galina, Takuya, Xiaohua, Muge, Pascal, Jonathan, Xiadong, Bill, Shravan, Albert, Fred, Nikita, Alvaro, Prof. Ligthart, Prof. van Genderen, Dr. Krasnov, Dr. Nikookar, Dr. Kooij, Dr. Driessen, Dmitriy, Sharef, Shilong, Harun, Etienne and many others. Thank you all for the wonderful lunch breaks and fruitful discussions. I would also like to acknowledge the supports of Johan Zijderveld and Pascal Aubry during the antenna measurements, the supports of Paul Hakkart and Wil Straver with technical matters and the help of Minke van der Put with administrative issues.

As life does not only revolve around work, I must also thank all my friends for always being there for me. Special thanks to Michaela for sharing the experience and challenges of performing doctoral research (I really enjoyed our coffee or hot chocolate breaks), to Tiantian for the delicious Chinese dinners, Shams and Shampa for always keeping in touch, to Amora and Patricia for sharing the experience of being a mother.

I think it is not possible for me to express my feelings in words for my dear family. So I will keep it short. Thanks to my mother for her unconditional love, for supporting my study choice and for too many other things to mention here. I want to thank my father for showing how simple and satisfying life can be when we look beyond our own personal interests. Thanks to Julie and Natasha, for being wonderful sisters and for all the fun that we have together. I wish to thank my parents-in-law, Cyntha and Hennie, for their warm care and for treating me like a daughter. Special thanks to Hennie for his help in designing the cover of this book. Thanks to my husband Bas for his affection, constant support and for being a very caring father of our sons. Tobias and Rovan, you are the sunshine of my life and always will be.

LIST OF PUBLICATIONS

Journal Papers

[J1] N. Haider, D. P. Tran, A. G. Roederer, and A. G. Yarovoy, "Reconfigurable L/S band phased array", *Electronics Letters*, vol. 47, no. 23, pp. 1265 - 1266, Nov. 2011.

[J2] N. Haider, D. Caratelli, D. P. Tran, and A. G. Yarovoy, "Directive electric-magnetic antenna for ultra-wideband applications", *IET Microwaves, Antennas and Propagation*, vol.7, no.5, pp. 381–390, Apr. 2013.

[J3] N. Haider, D. Caratelli, and A. G. Yarovoy, "Circuital characteristics and radiation properties of an UWB electric-magnetic planar antenna for Ku-band applications", *Radio Science*. DOI: 10.1002/rds.20015, vol. 48, pp. 13–22, Jan. 2013.

[J4] N. Haider, D. Caratelli, and A. G. Yarovoy, "Recent developments in reconfigurable and multiband antenna technology", *International Journal of Antennas and Propagation*, vol. 2013, Article ID 869170, pp. 1-14, Jan. 2013, *Special Issue on Wideband, Multiband, Tunable, and Smart Antenna Systems for Mobile and UWB Wireless Applications*.

[J5] N. Haider, D. Caratelli, and A. G. Yarovoy, "Frequency reconfiguration of a dual-band phased-array antenna with variable-impedance matching", *IEEE Trans. Antennas Propagat.*(accepted for publication).

[J6] N. Haider, D. Caratelli, and A. G. Yarovoy, "Blind-via fence for bandwidth enhancement of planar probe-fed antennas", *IET Microwaves, Antennas and Propagation* (submitted).

[J7] N. Haider, A. G. Yarovoy and A. G. Roederer, "L/S-Band frequency reconfigurable multi-scale phased array antenna with wide angle scanning", *IEEE Trans. Antennas Propagat.* (submitted).

Conference Papers

[C1] N. Haider, B. Yang, D.P. Tran, and A.G. Yarovoy, "UWB antenna element for a full-polarimetric antenna array", *Proc. 4th European Conference on Antennas and Propagation (EuCAP)*, Barcelona, Spain, Apr. 2010.

[C2] N. Haider, D.P. Tran, and A.G. Yarovoy, "A new concept for frequency reconfigurable phased-array element", *Proc. Loughborough Antennas and Propagation Conference (LAPC)*, pp.1-4, Nov. 2011.

[C3] N. Haider, D.P. Tran, and A.G. Yarovoy, "Dual-band E-slot microstrip antenna with frequency tuning capability", *Proc. 7th European Conference on Antennas and Propagation (EuCAP)*, Gothenburg, Sweden, Apr. 2013.

[C4] N. Haider, A.G. Yarovoy, and D. Caratelli, "Frequency switchable L/S-Band antenna element", *Proc. 7th European Conference on Antennas and Propagation (EuCAP)*, Gothenburg, Sweden, Apr. 2013.

[C5] N. Haider, M. S. Oude Alink, D. Caratelli, E. A. M. Klumperink, and A. G. Yarovoy, "Frequency-tunable antenna by input-impedance-tunable CMOS RF-frontend", *European Microwave Integrated Circuits Conference (EuMIC)*, Nuremberg, Germany, Oct. 2013.

[C6] N. Haider, A. G. Yarovoy, D. Caratelli, W. Straver, J. Zijderveld, and A. G. Roederer, "Experimental verification of the frequency reconfigurable L/S-band phased-array antenna", *Proc. 35th ESA Antenna Workshop*, Noordwijk, The Netherlands, Sep. 2013.

[C7] D. Caratelli, N. Haider, and A. G. Yarovoy, "Analytically based extraction of Foster-like frequency-independent antenna equivalent circuits", *Proc. URSI International Symposium on Electromagnetic Theory (EMTS)*, Hiroshima, Japan, May 2013.

[C8] N. Haider, D. Caratelli, D.P. Tran, and A.G. Yarovoy, "Wideband electric-magnetic antenna for polarimetric applications", *Proc. 8th European Conference on Antennas and Propagation (EuCAP)*, The Hague, The Netherlands, Apr. 2014.

Book Chapters

[B1] D. Tran, N. Haider, P. Aubry, A. Szilagyi, I.E. Lager, A. Yarovoy, and L.P. Ligthart, “A novel directive, dispersion-free UWB radiator with superb EM-characteristics for multiband/multifunction radar applications”, in M. Matin (Ed.): “Ultrawideband communications – novel trends – antennas and propagation”, ISBN 978-953-307-452-8; pp. 351-384, Aug. 2011.

[B2] D. Tran, N. Haider, S. E. Valavan, I. E. Lager, A. Szilagyi, A. Yarovoy, and L. P. Ligthart, “Architecture and design procedure of a generic SWB antenna with superb performances for tactical commands and ubiquitous communications”, in M. Matin (Ed.): “Ultra wideband - current status and future trends”, ISBN: 978-953-51-0781-1, Oct. 2012.

[B3] D. Caratelli, A. Yarovoy, and N. Haider, “A novel class of reconfigurable spherical fermat spiral multi-port antennas”, in F. Sabath and E. L. Mokole (Eds.): “Ultra-wideband short-pulse electromagnetics 10”, Springer Verlag, ISBN 978-1-4614-9500-0, Dec. 2013.